UNIVERSITY OF SOUTHAMPTON

FACULTY OF ENGINEERING AND PHYSICAL SCIENCES

Chemistry/ECS

FABRICATION AND CHARACTERISATION OF INORGANIC MONOLAYERS FOR SEMICONDUCTORS AND DEVICES

By

Hamid Khan, MChem.

Thesis for the degree of Doctor of Philosophy

June 2019

UNIVERSITY OF SOUTHAMPTON

ABSTRACT

FACULTY OF PHYSICAL SCIENCES AND ENGINEERING

Chemistry/ECS

Thesis for the degree of Doctor of Philosophy

FABRICATION AND CHARACTERISATION OF INORGANIC MONOLAYERS FOR SEMICONDUCTORS AND DEVICES

Monolayers derived from layered materials exhibit electrical, magnetic and optical properties radically different to the bulk. Therefore, industrially-viable methods for fabrication of layered materials from precursors will find application in fields as diverse as electronics, fuel cells and light technology. In this thesis, several new avenues for 2D materials synthesis are explored.

A novel synthetic method for highly-crystalline micron-sized domains of monolayers of phase-pure MoS_2 by liquid atomic layer deposition (ALD). Single-crystalline MoS_2 with domain sizes up to 100 μm (among the largest reported) and an area of ~5,000 μm^2 is demonstrated and proved by optical and electron microscopy, Raman spectroscopy and photoluminescence (PL) characterisation. The new process combines liquid chemistry with discrete, layer-by-layer deposition of precursors for the first time. The quality of MoS_2 is comparable to that obtained by chemical vapour deposition (CVD). Hence, this method for MoS_2 production potentially provides a low-cost and large-scale route to 2D materials. An application for the technique is presented, involving development of an MoS_2—WS_2 heterostructure, aiming to exploit the unique optical properties of heterostructured materials in type II band alignment. A high-quality heterostructure is demonstrated, exhibiting good vertical coverage of the overlayer, as shown by XRD and Raman spectroscopy.

Hydroxide-mediated liquid exfoliation of SnS_2 is presented as a safe, high-quality alternative to lithium-ion intercalation. The resulting SnS_2 nanoflakes are shown to be monolayer and of good crystallinity, by optical microscopy (OM), Raman spectroscopy and x-ray diffraction (XRD).

The application of AFM to fundamental study of interlayer van der Waals (vdW) forces in layered materials is explored by combining the technique with liquid exfoliation.

Hamid Khan

Table of Contents

Table of Tables

Table of Figures

Table of Figures

Table of Figures

Table of Schemes

List of Accompanying Materials

1. Poster presentation:
   9th International Conference on Materials for Advanced Technologies (ICMAT), 19th-23rd June 2017, Singapore.
2. Poster presentation:
   2nd World Congress and Expo on Materials Science & Nanotechnology, 25th-27th September 2017, Valencia, Spain.
3. Journal article:
   Khan, H., Medina, H., Tan, L. K., Tjiu, W. W., Boden S., Teng, J. H., and Nandhakumar, I. A Single-Step Route to Single-Crystal Molybdenum Disulphide (MoS_2) Monolayer Domains. *Sci. Rep.* **2019,** *9*, 4142(1-7).

Academic Thesis: Declaration of Authorship

I, Hamid Khan, declare that this thesis and the work presented in it are my own and has been generated by me as the result of my own original research.

Fabrication and Characterisation of Inorganic Monolayers for Semiconductors and Devices

I confirm that:

1. This work was done wholly or mainly while in candidature for a research degree at this University;
2. Where any part of this thesis has previously been submitted for a degree or any other qualification at this University or any other institution, this has been clearly stated;
3. Where I have consulted the published work of others, this is always clearly attributed;
4. Where I have quoted from the work of others, the source is always given. With the exception of such quotations, this thesis is entirely my own work;
5. I have acknowledged all main sources of help;
6. Where the thesis is based on work done by myself jointly with others, I have made clear exactly what was done by others and what I have contributed myself;
7. Parts of this work have been published as: *See List of Accompanying Materials*

Signed: .....

Date: .....

Acknowledgements

First of all, thanks must go to my diligent supervisors, Dr Iris Nandhakumar and Dr Stuart Boden at the University of Southampton, and Dr Jinghua Teng at the A*STAR Institute of Materials Research & Engineering, Singapore. Their advice throughout the progress of this work has been indispensable. Equally deserving is Dr Henry Medina, for consistently sharing his sound knowledge and practical experience with me, to make sure that my laboratory time in Singapore was well-spent. Further thanks must go to Dr Sean O'Shea, Dr Deng Jie and Mr Norman Ang of A*STAR IMRE and my long-suffering colleagues Dr Kevin Huang Chung-Che, Mr Nikolay Zhelev and Ms Maria Gonzalez-Juarez in Southampton, who went above and beyond to help me to acquire important data at times of need.

Special thanks must go to all those who took the plunge with me in Singapore from October 2015 to October 2017, the hardy group that shall forever be known as the Teabugs. I am grateful to all of you for your inspired conversation, moral support, weekend downtime, and above all your tea breaks. In particular, I'd like to thank Dr Joanna Pursey for her iced lemon tea mornings, Dr Diana Teixeira (and her husband Nicolas), and soon-to-be Dr Elefterios Christos Statharas. All of you slogged it out with me. I am grateful also to my many other friends in Singapore who kept my sanity in a cage for me while I was busy doing other things: to Ms Ann Rebadavia and everyone involved with Arvo 2, one of the greatest quiz teams ever (ever to grace the banks of the Singapore River…on a Tuesday night…since November 2015). As a stranger in a foreign land, one can be overcome by the need to fit in. So thanks to the Singaporean lady who approached me at a bus stop one hot morning in the depths of March 2016 and asked if the next bus was going her way. That she regarded me as sufficiently knowledgeable of the local bus routes made me feel accepted in a foreign country! (It was going the other way.)

Thank you to my family, old friends including Dr David Williams, and all those I have known at the University of Southampton, particularly those involved in the university's Ballroom & Latin Dancing Society. Wednesday nights spent with you, whizzing all over the floor, has provided me with much-needed light relief for many years and a great deal of lasting friendships. Especial thanks must go to Mr Ollie and Ms Rosie Woods, who were still here when I returned from Singapore, and to Dr Chris Baker, who was partly responsible for the best Christmas of my PhD. They have become some of my very best friends over the time I have been tripping over the light fantastic! Thanks to everyone in the Nandhakumar and Stulz groups for their wit, wisdom and teatime levity. Speaking of tea, I don't know where any of us in Southampton Chemistry would be without the tearoom staff, Ann French and her many colleagues over the years, who work diligently to lighten our days for a few moments with freshly-made tea and coffee. Thanks also to others in Southampton who have eased considerably the tribulations of recent years: particularly Dr James Harrison and soon-to-be Dr Emma Chambers, for the regular dinner dates, and the

behemoths of the Sunday night quiz known as Team Arvoturf and, its successor, Limp Noddy Turf. In particular, James and Emma deserve special thanks for putting me up (and putting up with me!) in their home when I periodically had to return to Southampton towards the end of this PhD. For the same reason, I extend the same special thanks to Mr Steve Hayden and Ms Eleanor May-Johnson.

In the dying weeks of this campaign, I was really running low on funds and time, and so in an effort to speed up the process I took to scribbling bits of the thesis on the train and the bus. To that end, I would like to thank Transport for London, First Southampton, Bluestar and Southern Rail for their appalling punctuality. It gave me plenty of time to mull over my writing.

Last but not least, I'd like to yield the floor to the inimitable Paul Merton, wit extraordinaire, who coined this line about nanotechnology that I'd like this thesis to be remembered by when I'm gone:

> *"Isn't there a chance this technology could get so small that we won't be able to find it anymore?"*

HK

Definitions and Abbreviations

AFM	atomic force microscope/microscopy
ALD	atomic layer deposition
BSE	backscattered electron(s)
CB	conduction band
CHP	N-cyclohexyl-2-pyrrolidone
CMOS	complementary metal—oxide--semiconductor
CNT	carbon nanotube
CVD	chemical vapour deposition
DIBL	drain-induced barrier lowering
DMF	dimethyl formamide
DMSO	dimethyl sulphoxide
DoF	degrees of freedom
DTG	differential thermogravimetry
EA	electron affinity
EBL	electron-beam lithography
EC	European Commission
EDXS	energy-dispersive x-ray spectroscopy
EUV	extreme ultraviolet
FE	field emission
GI	grazing incidence
HER	hydrogen evolution reaction
ICP	inductively-coupled plasma
IPA	isopropyl alcohol
ISC	inter-system crossing

Definitions and Abbreviations

IUPAC	International Union of Practical and Applied Chemistry
LE	liquid exfoliation
LED	light-emitting diode
MA	methylammonium
MOCVD	metal—organic chemical vapour deposition
(MOS)FET	(metal—oxide—semiconductor) field-effect transistor
nD	n-dimensional
NLO	nonlinear optics/optical
NMP	N-methyl-2-pyrrolidone
OM	optical microscope/microscopy
PDMS	poly(dimethyl siloxane)
PL	photoluminescence
PMMA	poly(methyl methacrylate)
PPC	poly(propylene carbonate)
PVD	physical vapour deposition
QE	quantum efficiency
QW	quantum well
RIE	reactive-ion etching
RF	radiofrequency
SEI	secondary electron imaging
ssCVD	single-source chemical vapour deposition
STM	scanning tunnelling microscope/microscopy
TGA	thermogravimetric analysis
TEM	transmission electron microscope/microscopy
TMdC	transition metal dichalcogenide

UV-vis	ultraviolet—visible
VB	valence band
vdW	van der Waals
XRD	x-ray diffraction
0D	zero-dimensional
1D	one-dimensional
2D	two-dimensional
3D	three-dimensional

Chapter 1 Introduction

1.1 Background

1.1.1 Monolayers, nanomaterials and nanoscience

The world of nanoscience is burgeoning with apparently interchangeable terminology. Before considering anything else, it is important to define the terms that are pertinent to this work, such as 'monolayer', '2D material', 'thin film' and 'nanomaterial', the understanding of which will make future references to them comprehensible hereafter.

A monolayer is a closely-packed layer of crystalline material with single-molecule thickness. In this work, the term monolayer is used interchangeably with "2D *[two-dimensional]* material". A monolayer is an example of a nanosheet, which is a material with thickness ranging from ~1 nm to 100 nm. The prefix "nano-" denotes an order of magnitude such that 1 nm = 1×10^{-9} m. A nanosheet in turn is an example of a thin film, a material with a maximum thickness of several micrometres.

An order of magnitude, however, is inadequate as a definition of nanomaterials. The 'Nanomaterials Definition Facts Sheet' authored by the Centre for International Law explained the difficulty in defining nanomaterials. Too broad a definition would impose requirements on materials for which they were irrelevant. Too restrictive a definition would allow materials on the market for which specific risk assessments and control measures were not mandated even though they may be appropriate.[1] Nevertheless, there follows a standardised European Union definition of a nanomaterial, which seems to account for this difficulty:[2]

> "*A natural, incidental or manufactured material containing particles, in an unbound state or as an aggregate or as an agglomerate, and where, for 50 % or more of the particles in the number size distribution, one or more external dimensions is in the size range 1 nm – 100 nm.*
>
> *"In specific cases and where warranted by concerns for the environment, health, safety or competitiveness the number size distribution threshold of 50% may be replaced by a threshold between 1 and 50%."*
>
> **European Commission (EC) directive 2011/696/EU**

The EC directive provides a working definition of a nanomaterial that is sufficient for this study with the proviso that the lower threshold of the size range will be stretched to ~0.6 nm for convenience. This is a small change across the entire range but ensures that monolayer materials of

the sort discussed in this thesis will not be arbitrarily excluded from the definition.[3] The study of nanomaterials and the technologies used to manipulate them is called nanoscience.

1.1.2 From bulk to monolayer

Layered materials are solids with strong in-plane chemical bonds but weak, out-of-plane van der Waals (vdW) bonds. These layered structures are known as bulk, and their monolayer basal planes exhibit radically different optical, electrical and magnetic properties to the bulk.[4, 5] Some of these properties are listed below, and more detailed explanations of these properties are considered later.

Bismuth telluride, Bi_2Te_3, exhibits high thermal conductivity in the bulk, but this property is inhibited in the monolayer. That is to say it is a topological insulator, a material that is an electrical insulator in the bulk but has a surface/monolayer that is electrically conductive. Nano topological insulators have applications in the development of superconductors.[6]

The electronic properties of certain materials are inversely proportional to the number of layers, so bulk semiconductors exhibiting an indirect bandgap can become direct-bandgap semiconductors when reduced to few-layer flakes, such as molybdenum disulphide, MoS_2, and tungsten disulphide, WS_2.[5, 7] The change in electronic properties from bulk to monolayer is attributed to quantum confinement. Quantum confinement is a change in the electronic and optical properties of a material reduced to a sufficiently small size. For example, when the 3D electronic wavefunction of a bulk material is confined to two dimensions in the monolayer, the electron—hole pair interaction distance tends towards the excitonic Bohr radius, leading to band modification of the electronic structure and the amplification of hitherto-silenced electronic properties.[4] This is the case for MoS_2, which exhibits photoluminescence (PL) as a result of its direct bandgap in the monolayer. That will lead to applications in photodiodes (such as light-emitting diodes (LEDs) and photosensors) and photoconductors.[7-10]

Combining nanosheets of different materials, most often with graphene, creates hybrid heterostructures that exhibit enhanced properties or a combination of the properties of their constituents.[11] Monolayer MoS_2 and WS_2 exhibit PL, as well as evidence of ferromagnetism and hydrogen-evolving electrode properties, with potential in the fuel cell sector.[5, 12, 13] Sandwiching monolayer semiconductors between dielectrics, or vice versa, creates vertical heterostructures that have higher-quality contact points than lateral ones.[14, 15] For instance, the photoresponse of molybdenum ditelluride, $MoTe_2$, and PL in WS_2 are enhanced in heterostructures with graphene.[16, 17] Quantum confinement is again observed, and the band structure of the resulting quantum well (QW) can be tuned by the number of layers, as well as the choice of materials being combined.[18] This regime offers the prospect of enhanced quantum efficiency (QE) in optoelectronic and photovoltaic devices,[19,20] as well as potential in transparent and flexible electronics.[14]

One of the greatest challenges in nanoscience is to find ways to efficiently separate (exfoliate), synthesise and deposit layered materials to maximise monolayer properties, and to integrate new materials into existing technologies, particularly in optoelectronics.

1.1.3 Timeline of nanoscience

This short section gives an overview of the history of the field, giving some background and context to this project. It is useful for the overall narrative of the report to know about the world in which the work is being performed.

1948: John Bardeen, William Brattain and William Schockley at the AT&T Corporation's Bell Laboratories applied two gold point contacts to a germanium crystal and observed power amplification. They had discovered the transistor effect,[21] which would later be incorporated into devices for switching or amplifying a signal. The trio was awarded the 1956 Nobel Prize in Physics. Their "transistor" was macroscopic, but since then the transistor has become a revolutionary component of microelectronics, and modern transistors now exist on the nanoscale.

1959: In a lecture entitled 'There's Plenty of Room at the Bottom', the renowned physicist Richard Feynman challenged scientists to write "the entire 24 volumes of Encyclopaedia Britannica on the head of a pin".[22]

1974: The term "nanotechnology" was coined by Norio Tanaguchi of the Tokyo Science University:[23]

> *"Nanotechnology mainly consists of the processing, separation, consolidation and deformation of materials by one atom or molecule."*
>
> **Norio Tanaguchi**

Although electron microscopes existed at the time, they did not have the capability to effect the technology talked of by Feynman and Tanaguchi.

1981: Eric Drexler, a Massachusetts Institute of Technology engineer, coined the term "bottom-up" to describe the synthesis of nanomaterials by manipulation of individual atoms.[24] The scanning tunnelling microscope (STM) was invented by Gerd Binnig and Heinrich Röhrer at IBM Zurich, for which the pair were awarded half the 1986 Nobel Prize for Physics. The STM was the most advanced microscope yet invented, capable of lateral resolution to 0.1 nm and axial resolution to 0.01 nm, *i.e.*, atomic scale.[25]

1985: A team led by Sir Harold Kroto at Rice University synthesised the Buckminsterfullerene (see Table 1.1) from condensing carbon vapour, the first laboratory bottom-up synthesis of a nanomaterial.[26]

1986: Binnig went on to collaborate with Calvin Quate and Christoph Gerber on the invention of the atomic force microscope (AFM), which possessed sub-nanometre resolution, could be used to investigate insulating materials and was capable of atomic manipulation using a cantilever.[27]

1991: Sumio Iijima at Japan's NEC Corporation discovered the multi-walled carbon nanotube (CNT), a hitherto unknown carbon allotrope, comprising concentric tubes of single-layered nanosheets.[28] He went on to discover single-walled CNTs (see Table 1.1), which are stronger and lighter than aluminium.[29]

2004: Sir Andre Geim and Kostya Novoselov at the University of Manchester discovered graphene (see Table 1.1), a 2D sheet of carbon (*cf.* an unravelled carbon nanotube), by exfoliating layers of graphite.[30, 31] This paved the way for the discovery of other 2D materials by a variety of methods.

1.1.4 Dimensionality in nanoscience

Dimensionality is alluded to in discussions of so-called 2D materials. It provides a straightforward way of characterising nanomaterial structure.

An n-dimensional (nD) material is defined by growth in n physical dimensions; (3-n) of its dimensions are confined to the nanoscale. Thus, the flow of electrons in the material is restricted to n degrees of freedom (DoF). Table 1.1 summarises dimensionality, illustrated for convenience with different allotropes of carbon.[32]

Buckminsterfullerene, C_{60}, is a football-shaped carbon allotrope, leading to the common name of "buckyballs". Buckyballs are 0D nanomaterials because all three physical dimensions are confined to the nanoscale, and there are zero electronic DoF. Generally, 0D materials have all dimensions confined to <20 nm. Carbon nanotubes are 1D materials because growth is confined to one direction, and so there is one electronic DoF (*cf.* particle in a 1D box). The other two dimensions are generally confined to 10 nm. A nanowire has length greater than 200 nm, while a nanorod has length less than 200 nm. Graphene, a 2D material, is a conductive sheet of sp^2-hybridised carbon arranged in adjacent six-membered rings. Growth is confined to two physical dimensions, and there are two electronic DoF. Generally, a 2D material comprises a film of a single layer of molecules. Where the term "2D material" appears in this report, its technical definition will hence be clear. Finally, graphite and diamond are 3D materials because growth occurs in all physical dimensions and there are three electronic DoF. Graphite is a layered 3D allotrope of carbon, that is, it comprises stacked layers of graphene bonded by vdW interactions. Diamond is a non-layered 3D allotrope of carbon, that is, it comprises sp^3-hybridised carbon in a covalent network of tetrahedra. The difference between layered and non-layered materials will be crucial to this project.

Table 1.1 Dimensionality in nanoscience

Dimensionality	Morphology	DoF	Examples
0 (0D)	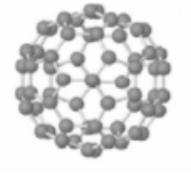	0	Buckminster fullerene
1 (1D)	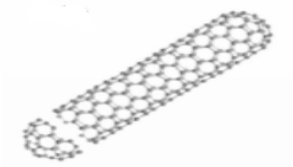	1	Carbon nanotubes Nanorods Nanowires
2 (2D)		2	Graphene
3 (3D)	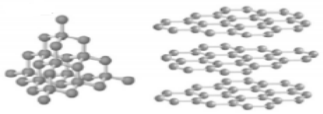	3	Diamond Graphite
Image reprinted from ref. [32], copyright 2007, with permission from Elsevier			

1.1.5 A word on graphene

Graphene is a single layer of graphite, first isolated in 2004 by Sir Andre Geim and Kostya Novosolev.[30, 33] They were awarded the Nobel Prize for Physics in 2010, and Geim was knighted for his work. And it was not without good reason, because the remarkable properties of graphene (as summarised below) revolutionised the future of electronics and cultivated the present interest in other monolayer materials.

In 2009, Andre Geim had this to say about his discovery:[33]

> *"It is the thinnest known material in the universe and the strongest ever measured. Its charge carriers exhibit giant intrinsic mobility, have zero effective mass, and can travel for micrometres without scattering at room temperature. Graphene can sustain current densities six orders of magnitude higher than that of copper, shows record thermal conductivity and stiffness, is impermeable to gases, and reconciles such conflicting qualities as brittleness and ductility."*
>
> **Sir Andre Geim**

Pristine graphene has unprecedented electronic properties, in particular an ambient electron carrier mobility of 1,500,000 $cm^2\ V^{-1}\ s^{-1}$, which is overwhelmingly superior to that of silicon, Si, at a mere 510 $cm^2\ V^{-1}\ s^{-1}$. In addition, graphene exhibits ballistic transport, that is, the charge carriers

(electrons) are mobile to several microns without scattering. Graphene has a thermal conductivity of 5,000 W m^{-1} K^{-1}, the highest ever recorded.[33]

Mechanically, graphene is the strongest material yet discovered, with a tensile strength of 130 GPa, compared to 400 MPa for A36 structural steel.[34]

Geim and Novoselov exfoliated graphene by mechanical exfoliation.[30] Although this method was crude, the breakthrough was extraordinary as a fundamental proof-of-concept that high-quality 2D crystals could be exfoliated and exist stably in ambient conditions. This observation triggered other groups to start looking into non-graphene 2D materials.

With all that is known about graphene, it may seem surprising that other materials were investigated so soon after its discovery. To understand why, consider band theory. Graphene's electronic band structure is that of a semimetal,[35] with discrete points of overlap between the full valence (VB) and empty conduction bands (CB) (Figure 1.1):[36]

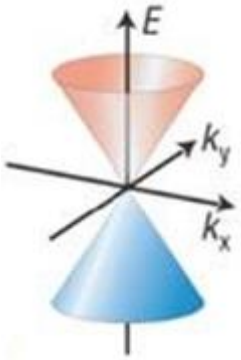

Figure 1.1 *Band diagram for single-layer graphene*

At discrete points in the Brillouin zone of graphene, known as K-points, the valence band overlaps with the conduction band. Thus, graphene has no intrinsic bandgap and is a semimetal. Image reprinted by permission from ***Springer Nature Customer Service Centre GmbH: [Springer Nature] [NATURE MATERIALS], ref. [36], COPYRIGHT*** *2007*

In Figure 1.1, the energies of the VB and CB formed respectively by the p_z bonding and anti-bonding orbitals of graphene is shown as a function of momentum space. Figure 1.1 shows a discrete point at which charge carriers from the VB can access the CB without crossing an energy barrier (a bandgap, E_B).[37, 38] This presents a problem for optoelectronic applications, which require materials to have a bandgap as a mode of switching the device on and off or generating light. Although it is possible to engineer a bandgap into graphene, this introduces fabrication complexity as well as a trade-off with carrier mobility that has, thus far, been considerable.[39, 40] For this reason, other materials have been considered that are not semimetals but semiconductors.

1.2 Semiconductors

Semiconductors – particularly inorganic monolayers semiconductors – have become promising for electronic, optical and magnetic applications. In contrast to semimetals, semiconductors possess small bandgaps that are overcome by applying a bias voltage. For comparison, metals are conductors, that is, they either have partially-filled CBs, or overlapping VBs and CBs.

Figure 1.2 shows the band structure of two generic semiconductors, one with a direct bandgap and the other indirect:

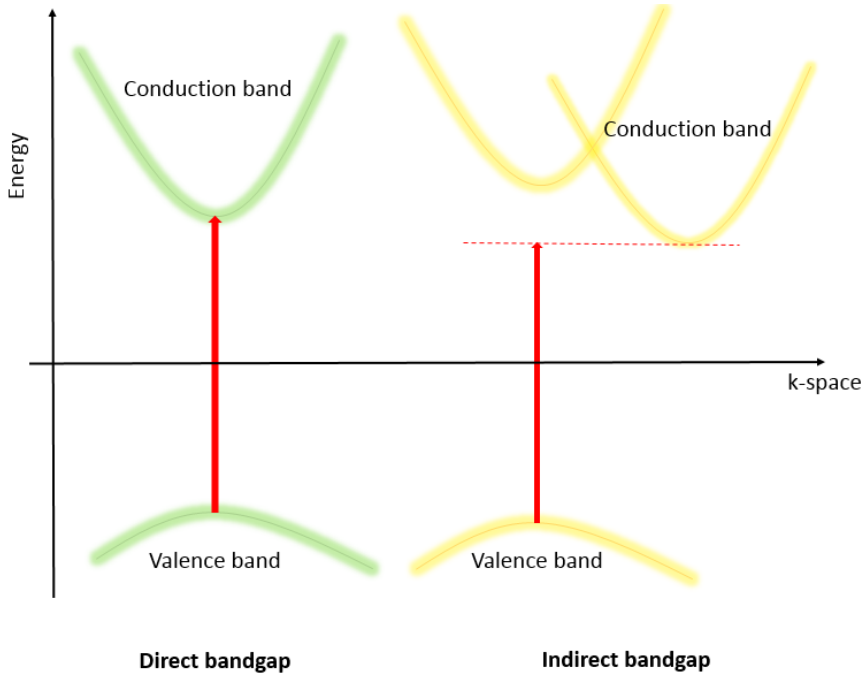

Figure 1.2 *Band diagram of direct (left) and indirect (right) semiconductors*

In the direct semiconductor, the minimum-energy state of the CB lies at the same crystal momentum as the maximum-energy state of the VB, so the electronic transition is direct. GaAs is a direct semiconductor. In an indirect semiconductor, the minimum-energy state of the CB lies at a higher crystal momentum than the maximum-energy state of the VB, so the electronic transition is indirect. Si is an indirect-bandgap semiconductor.

GaAs has a direct-bandgap electronic structure, while Si has an indirect-bandgap structure. An indirect bandgap is no barrier to the use of silicon in transistors, but makes it less suited to optical applications. For example, LEDs rely on the process of radiative recombination, whereby the absorption of a photon allows a CB electron to recombine with a VB hole and release its excess energy as light. This is possible in a direct-bandgap semiconductor because the relaxing electron does not undergo a momentum change, and so the process does not violate the principle of conservation of momentum. In an indirect-bandgap semiconductor, such a transition is difficult because the electron must pass through an intermediate state to transfer momentum to or gain it from the crystal lattice.

The idea of momentum change is best represented as in Figure 1.2, considering the electronic bands in k-space. This allows the momentum difference in an indirect bandgap to be visualised. The momentum difference must be accounted for by a non-radiative process in an indirect semiconductor.

It is possible to modify the electronic band structure of a layered material by varying the number of layers.[4, 5, 7] Materials with tuneable band structures have an advantage over silicon in photonics, because silicon is not a layered material, so its band structure can only be modified by bandgap engineering or complex chemistry such as doping.

Alternative families of materials to silicon and layered materials include the transition metal dichalcogenides (TMdCs). TMdCs possess a layered crystalline structure with the general formula MX_2 (M = TM in Groups 4-10; X = S, Se, Te), and many are direct semiconductors in the monolayer limit, specifically those derived from Mo and W. A typical TMdC structure involves a central metal ion sandwiched between two layers of chalcogenides in a hexagonal or trigonal prismatic coordination,[41] forming a basal plane. The bonding within a basal plane is strong and covalent, but interlayer bonding between basal planes is by weak van der Waals (vdW) forces. This allows cleaving of layers perpendicular to the basal plane, which gives rise to bandgap tuneability.

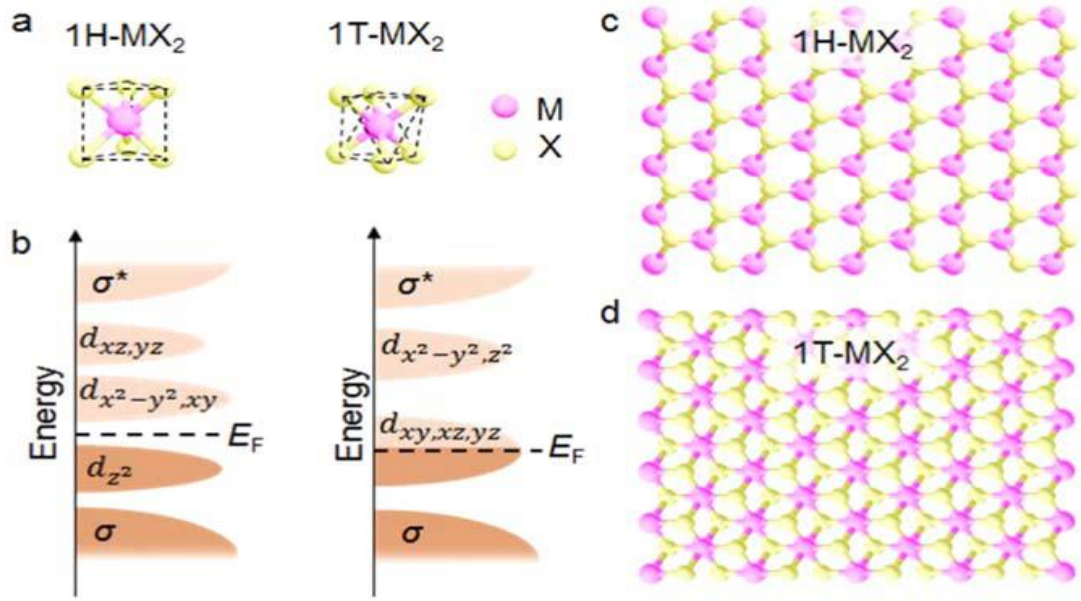

Figure 1.3 *Coordination regimes in TMdCs*

*The transition metal dichalcogenides MX_2 adopt hexagonal (1H) or trigonal prismatic (1T) coordination **(a)**. Each has consequences for orbital filling, band structure and electronic properties **(b)**, with the 1H phase being semiconducting and the 1T phase metallic. The two phases in plan, down the crystallographic c-axis **(c, d)**, possess different morphologies. Nanotechnology by Institute of Physics (Great Britain); American Institute of Physics. Reproduced with permission of IOP Publishing in the format Thesis/Dissertation via Copyright Clearance Center.*

The labelling of monolayer phases is explained thus: the letter, usually H or T in the case of TMdCs, represents the hexagonal and trigonal prismatic molecular geometries respectively, while the preceding number, usually 1, 2 or 3, represents the number of MX_2 units in a unit cell.[3, 42]

TMdCs have received considerable attention in the last 15 years owing to their exotic combinations of optical, electronic, magnetic and mechanical performance as compared to traditional semiconducting materials such as silicon, as summarised in Table 1.2.[43]

Table 1.2 Diverse properties of TMdCs, as in ref. [43]

Group	**M**	**X**	**Properties**
4	Ti, Hf, Zr	S, Se, Te	Semiconducting; Paramagnetic
5	V, Nb, Ta		Superconducting; Paramagnetic/ antiferromagnetic/diamagnetic
6	Mo, W		Sulphides/selenides semiconducting, tellurides semimetallic; Diamagnetic
7	Tc, Re		Small-gap semiconductors; Diamagnetic
8	Pd, Pt		Sulphides/selenides semiconducting and diamagnetic; Tellurides metallic and paramagnetic; $PdTe_2$ superconducting

Among the most fascinating properties of certain TMdCs, MoS_2 and WS_2 among them, is the bandgap tuneability as a function of layer thickness. For example, MoS_2 possesses an indirect bandgap of 1.29 eV in the bulk, which undergoes a gradual transition to a direct bandgap of 1.85-1.90 eV in the monolayer.[4, 7, 10, 38, 44, 45] This is attributed to quantum confinement of electrons in two dimensions and presents an advantage over non-layered materials. Indeed, that TMdCs can be cleaved into sub-nanometre layers at all is a considerable advantage over silicon for electronic applications such as transistors, and this will be discussed in depth in Chapter 3. Briefly, as the world of nanoelectronics moves "Beyond CMOS",[46] so too is there a need for component materials to move beyond silicon. Furthermore, the indirect-to-direct bandgap transition in TMdCs imparts the property of photoluminescence (PL), which is light emission from direct electronic excitation.[47] This is a crucial property for optoelectronic applications such as LEDs and photosensors.[7-10]

Another interesting property is bandgap splitting, wherein the band energy possesses several local minima or maxima, each of which can be accessed by a direct electronic transition associated with a particular electron spin.[48-50] The existence of such valleys has opened up the emerging field of "valleytronics", using the electron's association with a specific valley to transmit electronic signals. One way to do this is by exciting the ground-state electrons using circularly-polarised light, akin to a binary system where one valley represents a 1 state and the other a 0 state. As the valley states propagate through the whole material, they can only be destroyed by significant damage to the material, which reduces scattering, heat loss and signal degradation. This presents opportunities in advanced technologies such as quantum computing. Importantly, the properties of layer cleavage, bandgap tuneability, PL and bandgap splitting are not inherently present in silicon, presenting key advantages of the TMdCs over existing technologies. The unique electronic properties of some TMdCs are illustrated generally in Figure 1.4.[7, 51]

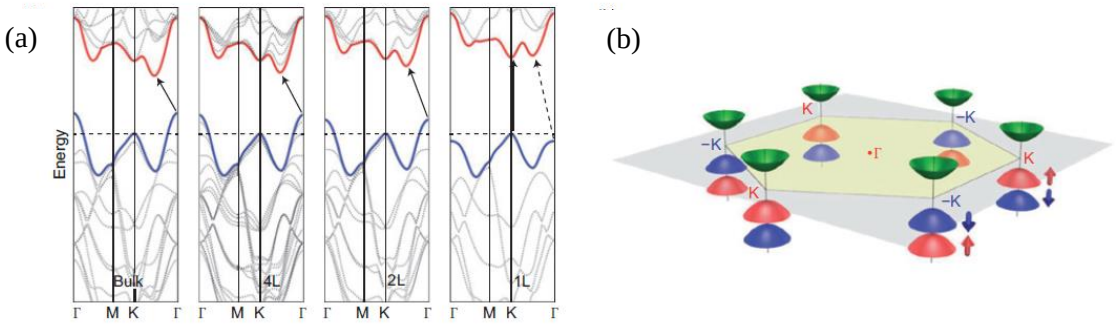

Figure 1.4 *Electronic properties of some TMdCs*

*In **(a)**, the energy dispersion undergoes a stepwise shift from bulk to monolayer (left to right). The red and blue lines indicate the VB and CB band edges respectively, and the solid arrows indicate the lowest-energy transition, which is indirect in all cases apart from the 1L case, where the indirect transition is represented by a dashed arrow. This gives rise to PL in many 1L-TMdCs. Image reprinted (adapted) with permission from ref. [7]. Copyright 2010 American Chemical Society. In **(b)**, the first Brillouin zone of a hexagonal TMdC exhibits six valleys illustrating the opposite splitting of the VB at the K and –K points, with each VB maximum associated with a particular electronic spin (up or down). This gives rise to valleytronic applications. Reprinted figure with permission from ref.[51]. Copyright 2012 by the American Physical Society.*

TMdCs possess advantages not only over silicon, but also graphene. While graphene is chemically inert, becoming appreciably reactive only after functionalisation with reactive moieties,[52] many Mo- and W-derived TMdCs are inherently reactive owing to their heterogeneous composition. The reactivity possessed by TMdCs opens up applications in energy, such as electrochemical catalysis. One key example of this is the hydrogen evolution reaction (HER, Equation 1.1) in fuel cells:[53]

$$2\,H^+ + e^- \rightarrow H_2 \qquad [1.1]$$

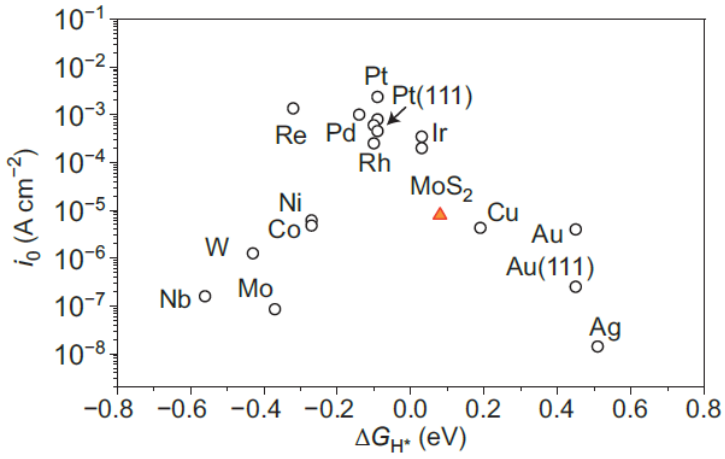

Figure 1.5 *MoS_2 in hydrogen evolution*

Volcano plot of exchange current density (i_0) as a function of Gibbs free energy (ΔG_{H^*}) of adsorbed atomic hydrogen for MoS_2 and pure metals, which is correlated to bond strength. Hydrogen evolution activity therefore reaches a peak at intermediate adsorption energies for several rare metals. MoS_2 and other TMdCs such as WS_2 possess catalytically active edge sites, with MoS_2 exhibiting HER activity near the top of the volcano, and are relatively inexpensive compared to precious metals. Image from ref. [53]. Reprinted with permission from AAAS.

Another family of note is the layered main group chalcogenides (MGCs). MGCs include those compounds of Group 13-15 metals with the chalcogens of Group 16 (S, Se, Te). A typical layered MGC has an MX_2-type structure arising from sp-hybridised metal—ligand covalent bonding.[54] As with TMdCs, so with MGCs. The bonding within a basal plane is strong and covalent, but interlayer bonding between basal planes is by weak vdW forces, allowing for cleaving of basal planes and bandgap tuneability.

The MGCs differ from the TMdCs in that they lack the rich d-electron chemistry, but many MGCs possess inherent electronic properties that make them useful for applications at wavelengths not accessible by TMdCs,[54] as shown in Figure 1.6.[55]

The favourable electronic properties of MGCs can lead to applications mainly in photovoltaics and photodetection (see Section 5.1). Briefly, the most common materials beyond silicon in photovoltaics are the TM oxides, such as ZrO_2 and TiO_2. Both are UV absorbers, but future photovoltaics may benefit from visible absorption capability. This naturally comes in the form of MGCs such as SnS_2. Chapter 5 will consider the application of MGCs in photovoltaics.

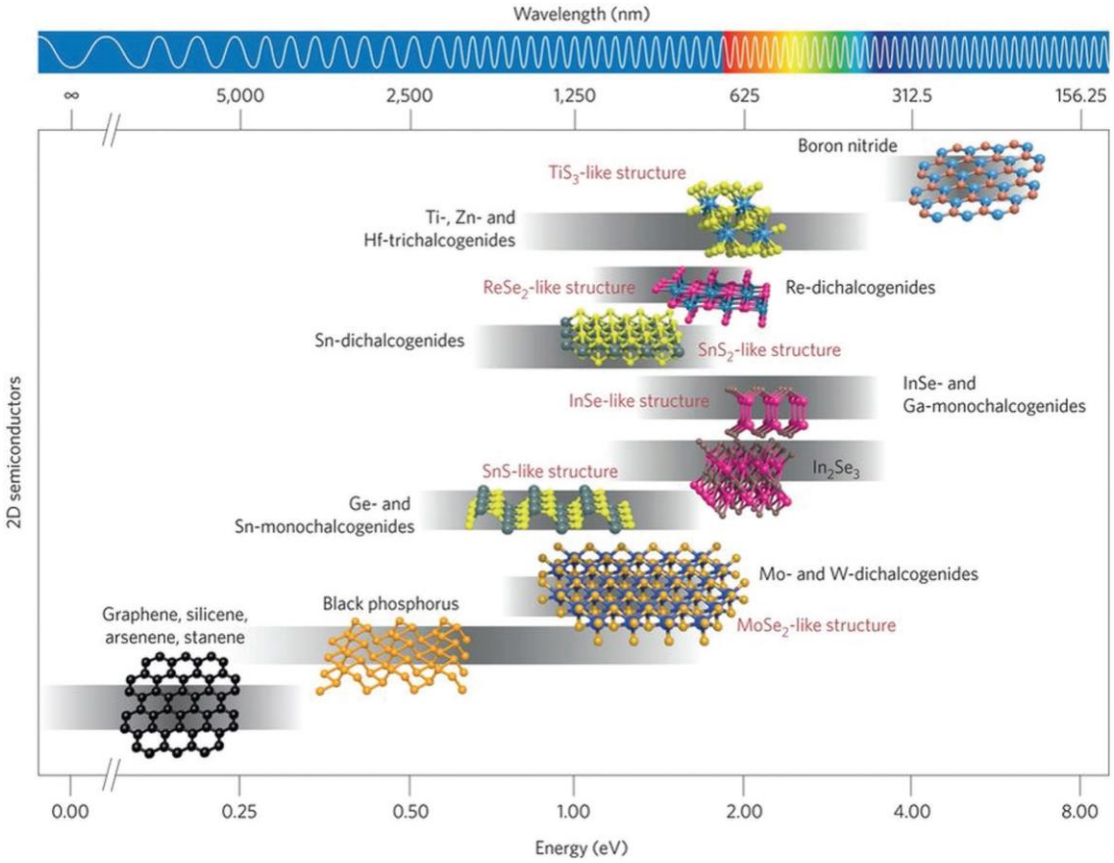

Figure 1.6 *Electronic comparisons between different chalcogenide families*

The grey horizontal bars indicate the range of bandgap values that can be spanned by changing the number of layers, straining, doping or alloying. The bandgap range of TMdCs is 0.8-2.0 eV, while that of MGCs is 0.5-3.8 eV, giving access to a wide variety of photonic and optoelectronic applications, particularly in the UV and IR regions. Image reprinted by permission from ***Springer Nature Customer Service Centre GmbH****: [****Springer Nature****] [****NATURE PHOTONICS****] **COPYRIGHT** 2016*

One area in which MGCs are preferred to TMdCs is nonlinear optics (NLO). NLO involves conversion of one frequency to another by superposition of two phase-matched light beams. Frequency conversion by an NLO-active crystal produces coherent light at frequencies where lasers perform poorly. For example, when two beams with frequencies ω_1 and ω_2 are introduced into an NLO medium, they interact nonlinearly to produce four distinct outputs: $2\omega_1$ and $2\omega_2$ by second harmonic generation, and $\omega_1 \pm \omega_2$ by sum and difference frequency generation.[56] Practical NLO materials should possess high second-order nonlinearity and wide optical transparency.[57] MGCs demonstrating NLO activity in the IR region are desirable because of their favourable optical transparency compared to traditional NLO materials, such as organic polymers.[58] NLO-active MGCs include GaX (where X = S, Se, Te), and these materials stand out from the TMdCs because TMdCs do not generally possess optical activity in the IR region, much less optical transparency.[56]

Further applications of NLO-active MCGs are extensive, and a thorough discussion is found in ref. [56] and references therein.

Overall, one sees that there is a need for inherently semiconducting materials for applications where it has not been possible to engineer a bandgap into graphene without substantial fabrication complexity and degradation of material quality. Moreover, it is necessary to consider families of layered direct semiconductors, as silicon, a non-layered indirect semiconductor, reaches the limits of its capabilities (see Chapters 3 and 5). The complementary TMdC and MGC families demonstrate favourable properties such as layered structure, bandgap tuneability, UV and IR optical activity, photoluminescence and optical nonlinearity that open up diverse applications inaccessible with present silicon-based technology.

1.3 Synthetic methods in nanoscience

There are two broad synthetic approaches for nanomaterials. Top-down syntheses start from macroscopic structures, whether bulk materials or patterns, and reduce them to the nanoscale. Bottom-up syntheses involve the aggregation of atomic-scale materials into nanomaterials, whether by self-assembly, through the use of interfaces or by surface reactions. Table 1.4 below summarises some of the techniques that will be discussed in this section.

Table 1.3 Bottom-up and top-down syntheses of nanomaterials

Top-down techniques	**Bottom-up techniques**
Mechanical exfoliation (“Scotch tape” method)	Physical vapour deposition
Liquid exfoliation	Chemical vapour deposition
Intercalation/exchange exfoliation	Atomic layer deposition
Photolithography	Liquid—liquid interface chemistry

1.3.1 Top-down synthesis

Top-down synthesis is the manufacture of nanomaterials by external control of macroscopic structures, either by shearing of bulk (known as exfoliation) or lithographic etching *via* a mask.

Geim and Novoselov exfoliated mono- and few-layer graphene from highly-oriented pyrolytic graphite (HOPG) by mechanical exfoliation.[30] They used strips of adhesive tape to peel off surface layers from the bulk. They then adsorbed these “flakes” onto a functionalised silicon substrate.[31] Not only graphene, but MoS_2, h-BN and $NbSe_2$ have been synthesised in this way. However, in every case, the technique has yielded a combination of nanosheets and thick films,[5] often with poor orientation. Thus, mechanical exfoliation suffers from poor reproducibility and lack of scalability,

which offers limited potential in industry. Others have tried to develop consistently reproducible methods.

First, there is a set of techniques for exfoliation into colloidal solutions (see Figure 1.7).[11] Several techniques are used to exfoliate mono- or few-layer flakes in this way.

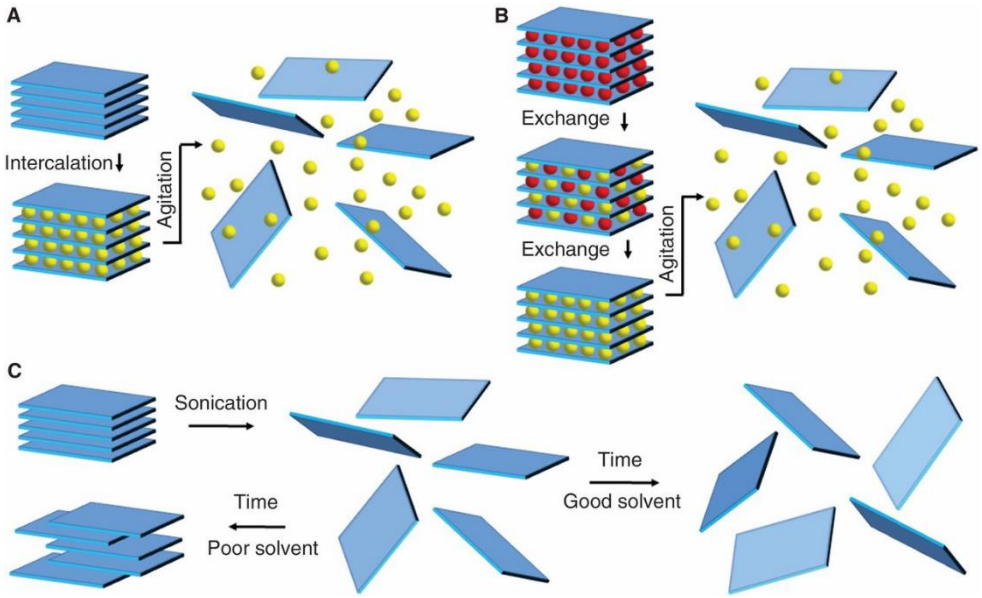

Figure 1.7 *Liquid exfoliation*

(a) *Ion intercalation. Insertion of ions into a layered materials breaks the vdW interaction, allowing for facile exfoliation by agitation.* ***(b)*** *Ion exchange. An ion-containing layered material is destabilised by substitution of the ions in its structure for bulkier ions of like charge, again allowing for facile exfoliation by agitation.* ***(c)*** *Solvent-assisted sonication. Sonication in solvents with surface free energy that closely matches that of the nanosheets results in solvent–nanosheet bonds that are thermodynamically stable with respect to the interlayer vdW interaction. Image from ref. [11]. Reprinted with permission from AAAS.*

Ang *et al.* used ion intercalation of graphene oxide with tetrabutylammonium cations to produce graphene monolayers.[59] However, the subsequent reduction process causes reaggregation and creates defects that render the monolayer substantially different to pristine graphene.[4, 11, 60] Liu *et al.* developed ion exchange whereby charge-balancing ions within the structure of a layered bulk material are exchanged for larger ions that break the interlayer vdW interactions.[61] They cited bulky anion (nitrate, sulphate, acetate, lactate) insertion into a chloride-containing layered double hydroxide. Ultrasonication uses sound waves to break apart layers using shear forces,[62] but not all materials contain ions in their structure, and shear forces can cause mechanical damage to the material or effect a phase transition to amorphous matter.

Solvent exfoliation involves sonication of bulk materials in different solvents with varying surface tensions. The effect is similar to ion intercalation in that molecules – solvent molecules in this case,

rather than ions – insert themselves between the individual layers of the bulk material and bind to the 2D nanosheets, thus breaking the vdW interactions between layers. It follows that the effect is strongest when the solvent–nanosheet interaction is greater than the interlayer vdW interaction, resulting in solvent-surrounded monolayers that are thermodynamically stable with respect to the bulk material.

The process can be performed with high throughput. Coleman *et al.* demonstrated the efficacy of this technique on transition metal dichalcogenides such as MoS_2 and WS_2 (NMP was judged the best solvent) and h-BN (IPA).[11] Solvent exfoliation does not suffer from the drawbacks of the other liquid exfoliation methods. Several materials have been produced by liquid exfoliation, and these are depicted in Table 1.5. For a more detailed discussion of the chemistry of liquid exfoliation, see Chapter 5.

Table 1.4 Liquid exfoliation

Material	**Solvent**	**References**
Graphene	benzyl benzoate	Hernandez *et al.* (2008)[63]
	fluoro-aromatics, pyridine	Bourlinos *et al.* (2009)[64]
	o-dichlorobenzene	Hamilton *et al.* (2009)[65]
	Water	Khan *et al.* (2010)[66]
		Cui *et al.* (2016)[67]
	chloroform, IPA	O'Neill *et al.* (2011)[68]
	NMP	Coleman *et al.* (2013)[69]
		Bracamonte *et al.* (2014)[70]
	dimethyl formamide (DMF)	Coleman *et al.* (2013)[69]
h-BN	PmPV* in 1,2-dichloroethane	Han *et al.* (2008)[71]
	DMF	Zhi *et al.* (2008)[72]
	IPA	Coleman *et al.* (2011)[11]
		Gao *et al.* (2014)[73]
		Ma and Spencer (2015)[74]
	ethanol + water	Zhou *et al.* (2011)[75]
	methanesulphonic acid	Wang *et al.* (2011)[76]
	Water	Lin *et al.* (2012)[77]
		Stengl *et al.* (2014)[78]
	IPA, followed by chloroform	Ma and Spencer (2015)[74]

Material	Solvent	References
	ethylene glycol	Stengl *et al.* (2014)[79]
	aq. ammonium hydrogen carbonate	Rafiei-Sarmazdeh *et al.* (2015)[80]
phosphorene	NMP	Brent *et al.* (2015)[81]
		Kang *et al.* (2015)[82]
phosphorene	DMF, dimethyl sulphoxide (DMSO)	Yasaei *et al.* (2015)[83]
	CHP	Hanlon *et al.* (2015)[84]
	ionic liquids	Zhao *et al.* (2015)[85]
TMdCs	NMP	Coleman *et al.* (2011)[11]
		Bang *et al.* (2014)[86]
	ethanol + water	Zhou *et al.* (2011)[75]
	aq. sodium cholate (surfactant)	Varrla *et al.* (2015)[87]
		Backes *et al.* (2016)[88]
		Gholamvand *et al.* (2016)[89]
	30% IPA (aq.)	Gerchman and Alves (2016)[90]
Bi_2S_3/Bi_2Se_3	Water	Ding *et al.* (2009)[91]
	NMP	Sun *et al.* (2014)[92]
	$[C_4mim]Cl$ **	Ludwig *et al.* (2015)[93]

*PmPV = poly(m-phenylenevinylene-co-2,5-dictoxy-p-phenylenevinylene)

**$[C_4mim]Cl$ = 1-butyl-3-methylimidazolium chloride

In addition to exfoliation is a set of techniques generally known as lithography, whereby a 2D material is etched on a substrate through a template mask. The term “lithography” is derived from the Greek for “lithos” (to write) and “graphein” (stone). There are many lithographic techniques. Photolithography, where light is focussed onto a photoresist, and electron-beam (e-beam) lithography, where the beam of light is replaced by electrons (which afford greater precision because they do not suffer from the Abbé diffraction limit of light) are the main two techniques. E-beam lithography is a point-by-point technique, directly writing on the substrate with a beam of electrons. In contrast, photolithography is a parallel technique in that the writing is not direct, but performed by the projection of parallel light beams onto a mask. Photolithography can be performed using many different wavelengths of light depending on the application. Photolithography is illustrated in Figure 1.8 and begins with coating of an oxidised Si substrate (wafer) with a photoresist.[94]

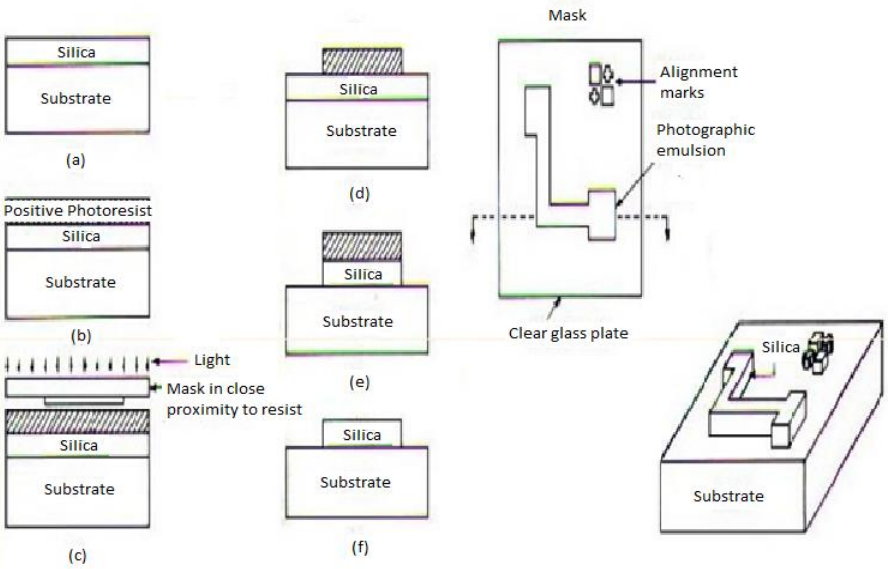

Figure 1.8 *Nanomaterials from photolithography*

(a) *Thermal oxidation of silicon wafer to form a silica (SiO_2) layer.* ***(b)*** *Spin-coating of photoresist on silica layer.* ***(c)*** *Mask held in close proximity to the photoresist and wafer exposed to light.* ***(d)*** *Application of developer washes away unpolymerised photoresist.* ***(e)*** *Silica under exposed sections removed, usually by plasma etching. Remaining photoresist protects covered regions of silica.* ***(f)*** *Remaining photoresist removed, leaving the pattern reproduced on the substrate. Image reproduced from ref. [94] under Creative Commons licensing.*

A photoresist is a light-sensitive organic resin, and there are two types: positive and negative. A mask with a pattern cut into it is placed just above the photoresist, and then the wafer is exposed to light, which initiates a photochemical reaction in the photoresist. If the photoresist is of positive type, then the areas exposed to light will undergo photolysis and become more soluble in a developing solvent. If the photoresist is of negative type, then the exposed areas will undergo photopolymerisation and become less soluble in a developing solvent. The wafer is then rinsed in a developer, which removes any unpolymerised photoresist. Then the exposed silica is removed by plasma etching, followed by the remaining photoresist. This leaves the exact pattern reproduced on the substrate.

With the exceptions of photolithography and liquid exfoliation, top-down techniques generally are expensive and slow, so unsuitable for large-scale commercial applications. Moreover, photolithography is a high throughput process but suffers from the optical diffraction limit, which limits its size resolution. This problem is overcome by using shorter wavelengths of light, such as extreme ultraviolet (EUV), but this increases the technical complexity of the process and introduces confounding factors such as secondary electrons.

1.3.2 Bottom-up synthesis

Bottom-up synthesis uses physical forces to combine atoms or molecules into layers.

Firstly, vapour-phase growth techniques involve the deposition of mono- and few-layer films of chemical onto a substrate, of which there are several examples.

In chemical vapour deposition (CVD), gaseous precursors are continuously introduced into a heated reaction chamber, where they adsorb onto a substrate and react. The products then remain on the substrate, while any by-products are desorbed and purged.[95]

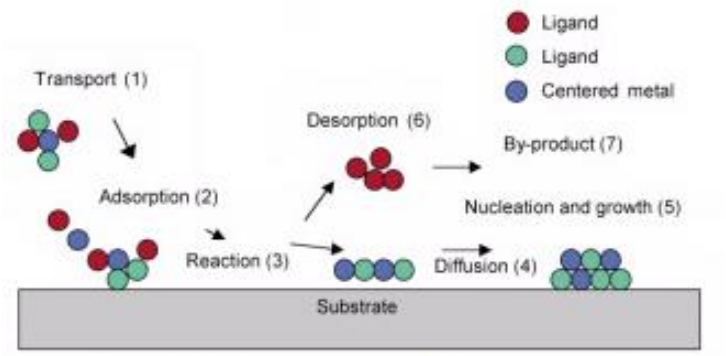

Figure 1.9 *Single-source chemical vapour deposition*

The single-source precursor contains the anion and cation moiety in the same molecule. It is transported via the carrier gas to the substrate, where it reacts. The products remain on the substrate, while the by-product desorbs and is purged. This is a continuous process whereby the film nucleates and grows. ssCVD is an advanced form of CVD that addresses some challenges in film purity that arise in traditional CVD, but it requires complex precursor design. Dalton transactions by Royal Society of Chemistry (Great Britain) Reproduced with permission of ROYAL SOCIETY OF CHEMISTRY in the format Thesis/Dissertation via Copyright Clearance Center.

There are several problems with CVD. Firstly, there is a tendency towards homogeneous pre-reaction in the gas phase, which then leads to random "snowing" of the material onto the substrate. This has an obviously negative effect on the morphology of the film; the uniformity of the film is difficult to control. Secondly, incomplete reaction or by-product desorption leads to dopant incorporation into the film. Thirdly, the most common chalcogen sources are hydrides, which are toxic. This imposes additional health and safety requirements that compromise the cost-effectiveness of the technique. Single-source (ss) precursors, which contain the metal and non-metal in the same molecule and offer clean thermal decomposition and limited pre-reaction, overcome some of these concerns because the reactive groups are held close to the substrate during reaction. However, ssCVD requires complicated precursor synthesis and environmental controls.

The most efficacious vapour-phase method is atomic layer deposition (ALD), whereby a film is grown by repeated exposure of a substrate surface to sequential pulses of gaseous precursors.[96] In contrast to CVD, the ALD reaction chamber is purged after each exposure to ensure that only discrete layers are deposited. The technique, shown in Figure 1.10, produces films with controllable thickness and a uniform coating because it benefits from self-limitation in that the adsorption of precursor onto substrate stops when all free sites on the substrate are occupied. It follows that the technique allows for nanocomposite synthesis. In these ways, ALD is superior to CVD for mono- or few-layer synthesis.[97]

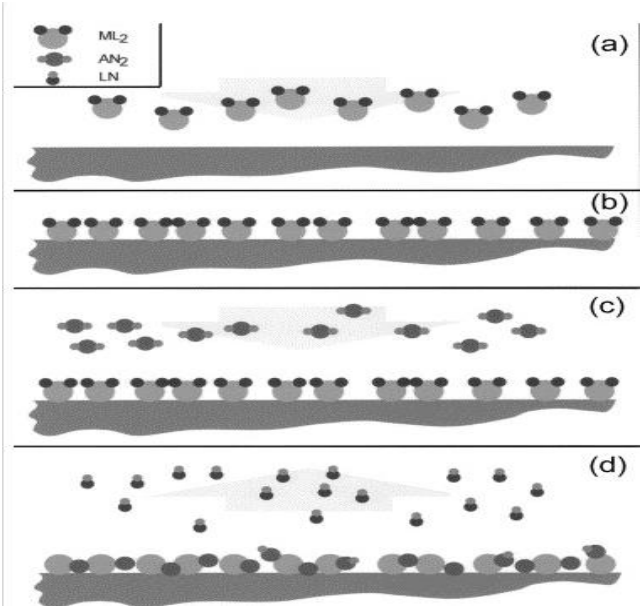

Figure 1.10 *Atomic layer deposition*

ALD is the successive deposition of discrete and controllable layers of different precursors (b-d) onto a functionalised adhesive substrate (a).[98] Note that ML_2 is a metal—ligand complex, and AN_2 is the anion source; thus LN is the waste by-product. It is easy to see how layers could build up to form a nanocomposite film, and also how a surface-mediated chemical reaction could occur. Reprinted from ref. [98], copyright 2002, with permission from Elsevier.

Much has been written on appropriate precursors for vapour-phase growth. Generally, precursors need to have the following properties:[97, 99, 100]

- High purity
- Clean decomposition without incorporating extrinsic impurities from ligands
- Moderate volatility allowing for mild conditions
- Gas-phase stability to prevent decomposition at the volatilisation stage before deposition
- Air- and moisture-stability
- Minimal toxicity
- Sufficient affinity for the substrate to ensure optimal adsorption and uniform morphology.

Physical vapour deposition (PVD) is the general name for a family of vacuum-based epitaxial techniques by which solid material is vaporised and deposited on a substrate in a vacuum chamber. This presents an obvious contrast to CVD, in which gaseous precursors are introduced to and reacted in the chamber under a carrier gas. Most PVD methods, such as pulsed laser deposition (h-BN, MoS_2)[101, 102] and sputtering (graphene and HfO_2, hafnia),[103, 104] are line-of-sight methods, that is, deposition occurs in the line-of-sight of ejection of material from a target plate, and sporadically elsewhere. For this reason, PVD generally does not produce as high-quality a film as ALD.

The second prominent bottom-up technique is liquid—liquid interface chemistry. This technique exploits the immiscibility of two solvents to effect a chemical reaction at the interface between them. Suppose that a TMdC material is desired. A complex TM—organic precursor is dissolved in an organic solvent, which is introduced to an inorganic chalcogenide compound in aqueous solution. The two precursors react at the interface, where a thin film is produced. The drawbacks of this technique are the need to design complexes and compounds with suitable solubility in given solvents and the impracticality of scaling.[105, 106]

The liquid-phase technique has advantages over the gas-phase technique in that it reduces the need for forcing reaction conditions, such as high vacuum and high temperature. This will reduce the cost and improve industrial viability of the liquid-based approach. However, one limitation of the liquid approach against gas-phase is that to promote interfacial reaction, essentially the opposite approach to liquid exfoliation is required: the precursor interaction must be more stable than the solvent—precursor interaction so that the precursor reaction or adsorption is favoured. Related to this is the incorporation of residual carbon impurities at the interface if organic solvent is used. The resulting loss of stoichiometry in the final film is detrimental to electronic properties.[107] Facilitating precursor adsorption and preventing interfacial impurities remain challenging in liquid chemistry will require careful control of reaction conditions such as solvent choice, concentration and solution temperature such that adsorption is favoured.

1.4 Aims of this thesis

The general properties of inorganic monolayers and their potential in electronic devices have been discussed in Sections 1.1.2 and 1.1.4 with reference to general problems with existing technologies involving silicon (low carrier mobility and indirect bandgap) and why graphene is not always an appropriate alternative. In subsequent sections, more application-specific problems with semiconducting silicon are presented. This poses two important questions. Firstly, which specific materials are of interest as alternatives to silicon-based materials? Secondly, how can novel materials be synthesised in an industrially viable way? The discussion and evaluation of the safest and most economical methods for producing the highest-quality results will continue.

Liquid atomic layer deposition will be presented as a novel route to large, single-crystalline domains of monolayer MoS_2. The background of the research will be discussed in relation to the field of nanoelectronics and the inability of silicon technologies to keep pace with the level of development. This is in part to do with inherent physical and chemical issues with silicon as a viable nanoelectronic material for future applications, which cannot be addressed in device fabrication alone. Therefore, the literature related to MoS_2 as an alternative to silicon and its synthesis will be presented. The novelty of the new synthetic approach will be twofold. It will rely on the introduction of a novel molybdenum-containing precursor, ammonium heptamoybdate tetrahydrate, *via* an aqueous dip-coating process that will be combined, for the first time, with layer-by-layer deposition analogous to traditional, gas-phase ALD. Monolayers grown by this new hybrid technique will again be reported for the first time. Achieving these outcomes will require fine control of several parameters. First of all, it will be necessary to modulate the initial thickness and coverage of the Mo precursor film. A range of deposition parameters such as solution concentration, substrate and deposition temperature will be explored in order to determine the optimal conditions for large-scale Mo precursor dip-coating Secondly, the deposition of the sulphur precursor will need to be controlled in order to achieve the thinnest MoS_2 films. This property will be important for applications, as will be explained in Chapter 3. Variable parameters will include the precursor itself, the sulphurisation temperature, atmospheric composition and gas flow, and post-annealing conditions (if used). The quality of the as-synthesised films will be examined according to the following figures of merit: domain size and morphology, film thickness, crystallinity. The domain size and morphology will be elucidated by optical microscopy (OM) and scanning electron microscopy (SEM). The film thickness will be determined by Raman and photoluminescence (PL) spectroscopy and AFM. The crystallinity will be confirmed by PL and transmission electron microscopy (TEM).

Given that many heterostructures of TMdCs are known to have unique properties (for examples, see Sections 1.1, 4.1 and 4.2), Chapter 4 details an approach to find an application for the above growth method by using it to design a heterostructure of MoS_2 and WS_2. The background of the research will be discussed in relation the field of heterostructures and their unique properties compared to single material films. The literature related to heterostructures of MoS_2 and WS_2 and their syntheses will be presented. The novelty of this new approach will rely on the application of an ALD-type process for heterostructure synthesis, which has never previously been reported. The same principles and figures of merit will be required as in Chapter 3, but the conditions will be need to be carefully controlled in order to select for the vertical heterostructure rather than lateral and to prevent alloying, as will be explained at the relevant point of the report. A characterisation of the heterostructure will be presented by SEM, energy–dispersive x-ray spectroscopy (EDXS), Raman spectroscopy, PL and x-ray diffraction (XRD).

The MGCs are similar to TMdCs except for the lack of d-electron chemistry. However, from a structural point of view, many MGCs adopt similar geometries to TMdCs. One such material is tin(IV) sulphide, SnS_2, and its layered structure will be exploited for liquid exfoliation. The background of the research will be discussed in relation to the field of photovoltaics. The literature related to SnS_2, its suitability for the application and its synthesis will be presented. The novelty of this project will again be twofold relying firstly on the use of aqueous solvent and secondly on the application of a hydroxide ion-mediated approach, neither of which has previously been reported for the exfoliation of SnS_2. Different concentrations of starting solution will be sonicated and centrifuged. These steps will require careful control of sonication time and temperature, as well as centrifugation rate and time. Samples will be characterised for yield and thickness. UV—visible spectroscopy will be employed for the former, making use of absorbance as a proxy for concentration. Raman spectroscopy will be the predominant method of thickness characterisation, exploiting the properties of the characteristic A_{1g} vibrational peak of SnS_2. Concentration and thickness information will be complemented by morphological data obtained by OM and SEM.

Chapter 2 Methods used in this Research

2.1 Synthetic methods

2.1.1 Dip-coating

Dip-coating is a conceptually simple process that involves suspension of a substrate in a solution of the desired coating, in this case the various precursors. It proceeds by five steps:[107-109]

1. **Immersion:** The substrate is immersed in a solution of the coating material.
2. **Start-up:** The substrate remains suspended in the solution and is then gradually pulled up.
3. **Deposition:** A thin layer of the coating deposits on the substrate by capillary action as it is withdrawn from the solution.
4. **Drainage:** Excess liquid is allowed to drain from the surface once the substrate is completely withdrawn from the solution.
5. **Evaporation/drying:** A volatile solvent can be allowed to evaporate naturally, or a less-volatile solvent such as water can be removed by drying in nitrogen.

These steps are shown in Scheme 2.1, which shows the stages of the process at which immersion, start-up, deposition, drainage and evaporation occur:

Scheme 2.1 The dip-coating process

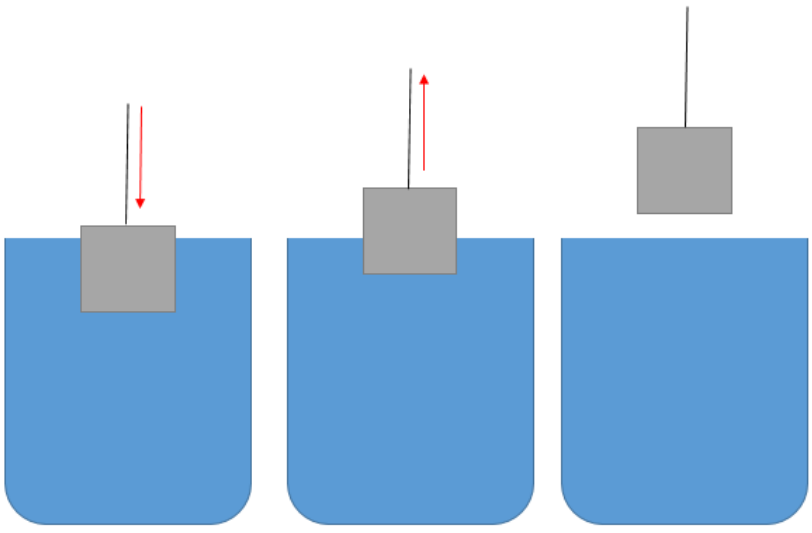

Steps 1+2 *Steps 3+4* *Step 5*

Figure 2.1 illustrates the mechanism of the film formation process as the substrate is withdrawn from the solution.[110]

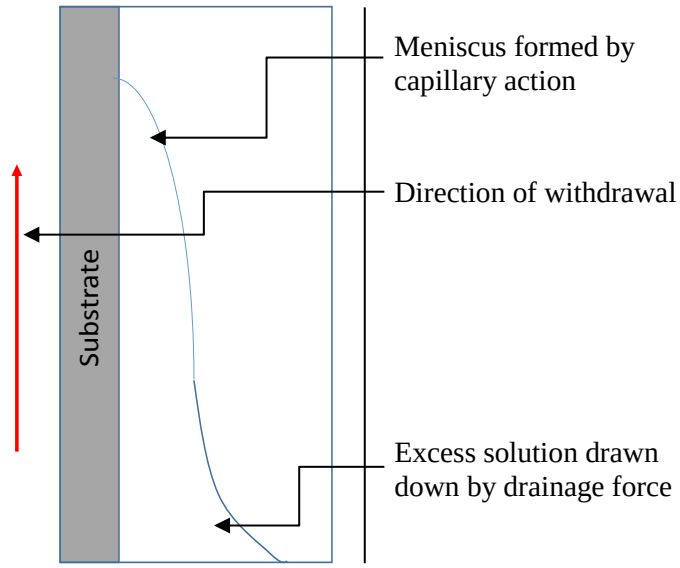

Figure 2.1 *Film formation by dip-coating*

The film is formed by gradual withdrawal of the substrate from the solution. As the substrate is pulled up, capillary action draws the solution up into a meniscus while drainage force draws it back down. The combination of these forces determines film thickness. Generally, slower withdrawal seems to lead to a thinner film.

If a mechanical dip-coater is used, the rate of removal of the substrate can be carefully controlled and, therefore, the thickness uniformity of the coated precursor can be modulated. However, if the process is performed by hand, human error makes it virtually impossible to control thickness uniformity in this way. That said, the results of dip-coating are dependent on several parameters that are consistent with the manual method. These include surface functionalisation, immersion time, solution concentration and number of cycles.

An unexplored area in dip-coating is the efficacy of solvent evaporation. If manual dip-coating is used and the effects of substrate-pulling cannot be reliably reproduced, then solvent evaporation may be one route to mimicking the effect. In a solvent evaporation regime, the substrate is suspended in the solution so that the top of the substrate is approximately level with the solvent. The solvent is continually heated to evaporation such that the level of solvent gradually decreases over time and the substrate is gradually exposed. One can think of this as the reverse of substrate-pulling, albeit a more time-consuming process. This technique has never been published but will be explored in this project.

2.1.2 Reactive ion etching

Reaction ion etching (RIE) is a high-resolution dry-etching process performed at low pressure. A typical setup involves a double-portioned vacuum chamber. A masked substrate, usually patterned by photolithography, is placed at the bottom of the chamber on an electrically-isolated conductive

wafer platter. In the top portion of the chamber, an inlet allows a vaporised etchant to enter, and outlets at the bottom allow excess to exit.

A radiofrequency (RF) field is applied at an electrode in the top portion of the chamber. The oscillation of the electromagnetic field ionises the etchant, generating an inductively-coupled plasma (ICP). Free electrons derived from the etchant are accelerated towards the substrate as a result of the oscillating RF field and deposit on the substrate surface. As electrons bombard the substrate, a negative charge accumulates at the surface. Meanwhile, the plasma develops a slightly positive charge due to excess ions. Thus, the positive ions in the plasma drift towards the substrate by electrostatic attraction and collide with the substrate surface. The resulting chemical reaction etches the substrate at the exposed areas.[111] The process is illustrated in Figure 2.1:

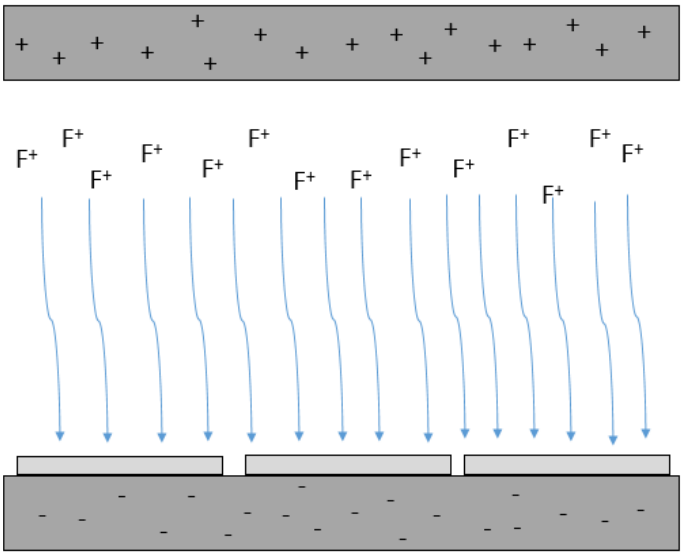

Figure 2.2 *Reactive-ion etching*

An oscillating RF field between two plates ionises the etchant parent molecule, creating a plasma, and drives electrons to the substrate, which creates an excess of positive ions at the top of the chamber. Therefore, plasma drifts towards the substrate, where the etching chemical reaction takes place at the surface.

The nature of etching as a chemical process means that it is necessary to be selective in the choice of etchant:[112-115]

1) An etchant must be reactive towards the substrate. For SiO_2 and Si, fluorides are common etchants, with sulphur hexafluoride and perfluorocyclobutane known to work well.
2) The byproduct of the surface reaction must be volatile with a low vapour pressure. This allows it to desorb from the surface and exit the reaction chamber *via* the outlet.

2.1.3 Electron-beam lithography

Electron beam lithography (EBL) is a high-resolution technique allowing for patterning of features just a few nanometres in lateral size. It uses a beam of electrons (e-beam) to "draw" a pattern on a pre-deposited resist. The resist reacts in a certain way on exposure to the e-beam: exposed regions of a positive resist become more soluble in a developer, while exposed regions of a negative resist become less soluble.[116]

The e-beam is produced by one of two sources. The first is thermionic emission, which involves heating a metallic filament, usually lanthanum hexaboride (LaB_6),[117-119] until the thermal energy imparted on the material overcomes the surface work function, leading to electron ejection. In contrast, a field emission (FE) gun is a cold source emitter – there is no heating involved. FE uses a metallic filament, such tungsten or tungsten-doped zirconia, W/ZrO_2, as a cathode, placing the filament in a large electrical potential gradient and focussing emitted electrons using anodic plates.[120]

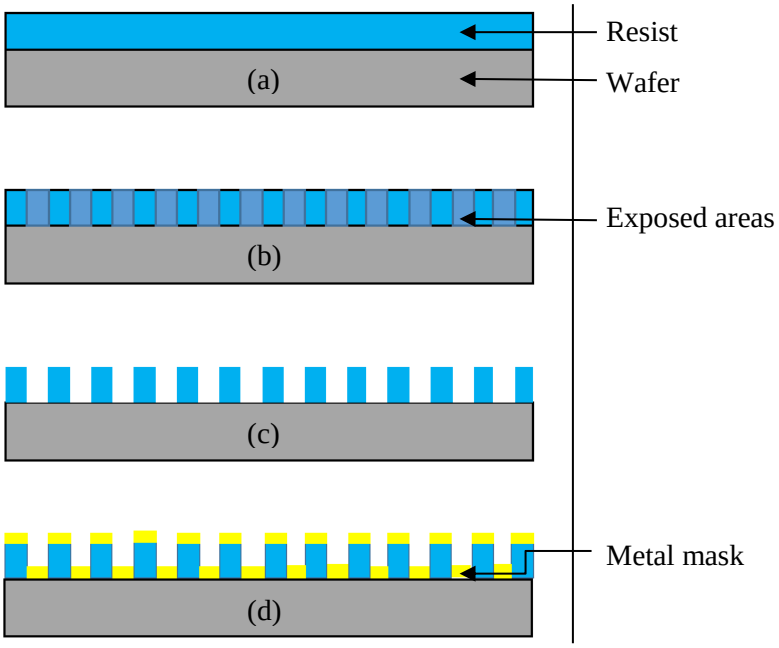

Figure 2.3 *Electron-beam lithography*

This figure shows a generic fabrication procedure. ***(a)*** *A wafer is coated with a resist.* ***(b)*** *The resist is exposed to an e-beam, with exposed areas undergoing either polymerisation or photolysis depending on the type.* ***(c)*** *Unpolymerised areas of the resist are removed in a developer.* ***(d)*** *Exposed areas are coated in a metal mask by e-beam evaporation, in preparation for further processing as required.*

After development, the remaining resist acts as a mask, which allows for bare regions of substrate beneath to be processed in whatever way is desired. Bare regions can be etched or they can be used for selective deposition, which is the process that will be used herein.

2.2 Characterisation methods

2.2.1 Thermogravimetric analysis

Thermogravimetric analysis (TGA) is a simple method of materials analysis, by which a known mass of sample is heated at a controlled rate and the change in its mass is measured over time. A corresponding plot of mass *vs* temperature provides details of phase transitions and thermal decomposition, with each such change denoted by a steep drop in mass at a given temperature. A derivative thermogravimetric (DTG) curve shows the first derivative of mass with respect to temperature, and this usually yields a sharp peak that can be used to pinpoint the exact transition temperature.

A simple setup comprises a precision balance with a programmable temperature control. The temperature can be increased at a constant rate, and the desired atmospheric composition and pressure within the TGA furnace can also be selected. The atmospheric control usually allows for ambient, inert, corrosive, carburising and redox gases, as well as a vacuum.

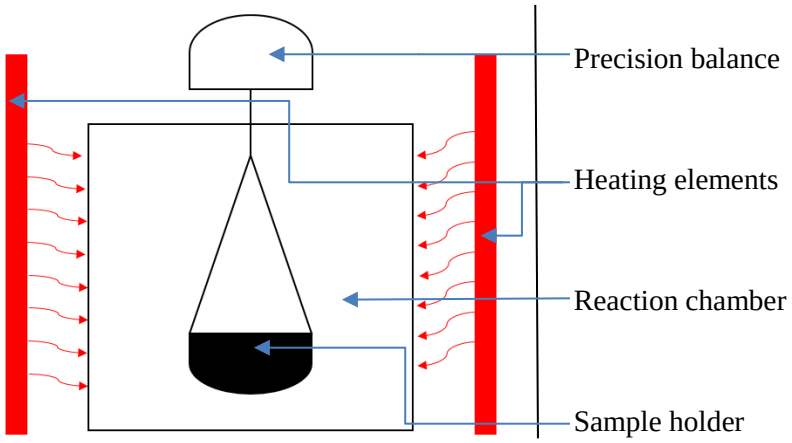

Figure 2.4 *Thermogravimetric analysis*

A standard TGA comprises a reaction chamber housing a precision balance. The atmosphere within the reaction chamber can be controlled, and it is heated by external heating elements with programmable temperature control.

TGA is used to elucidate the decomposition chemistry of the precursor in CVD/ALD.[121-125] This information can be used to understand the mechanism of the reaction in the chamber. For example, if it is known that a particular precursor A reacts with a precursor B to form a product C at a particular temperature T, then the TGA might reveal that at that temperature T, precursor A has decomposed to its base compound A_1. The product-forming reaction must therefore be between A_1 and B, rather than A and B.

Where TGA was used here, it was performed under the same conditions as – or the closest obtainable conditions to – the tube furnace setup. This involved a nitrogen atmosphere, for the most part, and a temperature of 800 ℃, obtained by heating the sample from room temperature at a ramp rate of 50 ℃/min.

2.2.2 UV-visible spectrophotometry

Ultraviolet—visible (UV-vis) spectrophotometry is a well-established non-destructive technique that is used to measure the absorbance of light by a sample in solution under broadband scanning.[11] The method makes use of the fact that, in general, absorbance of near-ultraviolet (near-UV) and visible light, at wavelengths in the range 180-750 nm, by a solution scales linearly with solution concentration. Of course, there are caveats to this, which will be addressed at the relevant stage of results discussion.

Chemical substances absorb over a definite region of the electromagnetic spectrum, and the active region over which absorbance occurs depends on the properties of the analyte in question. Absorbance can be influenced by the level of conjugation of bonding, the intrinsic electronic bandgaps and ligand—metal charge transfer, as well as ambient conditions such as pH. For this reason, the choice of solvent is particularly important. Solvent molecules may also absorb in the UV-vis region, particularly organic solvents, and such solvents have a cut-off below which solvent absorbance is indistinguishable from analyte absorbance. Preliminary solvent screening is employed to select solvents that do not interfere with analyte absorbance. Fortunately, water possesses an absorbance cut-off around 180 nm, so it is a good generic solvent that does not confound the absorbance peaks of any analyte.

Most UV-vis spectrophotometers have the key setup in common. A UV/visible beam of light is spectrally separated into its component wavelengths by a diffraction grating or prism. Each monochromatic beam is split into two equally intense beams (B_S and B_R) by a half-mirror/beam-splitter. The sample solution is contained in an optically transparent cuvette usually made of quartz. Beam B_S passes through this cuvette.

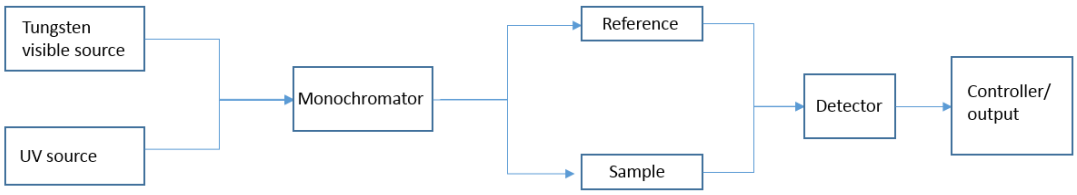

Figure 2.5 *UV-visible spectrophometer*

A standard setup involves two light sources with a changeover at ~350 nm. A monochromator selects for a single wavelength, allowing for broadband scanning.

To minimise the confounding effect of absorbance by the cuvette or the solvent, a background is taken before the experimental runs and subtracted from the experimental data. Beam B_R passes through this reference cuvette. At the detectors, the transmitted beam intensities are compared. The process is quickly repeated for all monochromatic wavelengths in the region desired. Some spectrophotometers do not have two pathways, so they use the same beam for the reference and sample measurements. In this case, the background is acquired before the sample measurement, and can then be stored by the controlling computer while the sample spectrum is acquired. The output in any case is a spectrum of detected absorbance against excitation wavelength.

Absorbance has no physical meaning, but it is defined with respect to a physical parameter, which is the transmittance T, where T is the fraction of incident light that passes through the sample (as measured at a detector):

$$T = \frac{I_t}{I_0} \qquad [2.1]$$

where T = transmittance

I_t = intensity of light at detector

I_0 = incident intensity of a given wavelength

And this yields absorbance A, as the inverse logarithm of transmittance:

$$A = -\log T \quad \text{or} \quad A = \log\left(\frac{1}{T}\right) \qquad [2.2]$$

Quantitative analysis of UV-vis absorbance is underpinned by two fundamental laws. The first is Beer's law:[126]

> *The intensity of a beam of parallel monochromatic light decreases exponentially with the number of absorbing molecules.*

The corollary of this law is that absorbance is proportional to concentration. The second law is Lambert's law:[127]

> *The intensity of a beam of parallel monochromatic light decreases exponentially as it passes through a medium of homogeneous thickness.*

The corollary of this law is that absorbance is proportional to optical path length. Combining the two laws yields the Beer-Lambert law, relating absorbance to concentration and absorbance path length:

$$A = \varepsilon c l \qquad [2.3]$$

where ε = molar extinction coefficient, $M^{-1} cm^{-1}$

c = concentration of known chemical, M

l = absorbance path length, cm

The quantity epsilon is commonly named the "molar extinction coefficient", but is more properly termed the "molar absorptivity". The molar extinction coefficient quantifies the propensity of a solution to absorb light at a particular wavelength, *i.e.*, high ε suggests strong absorption. It is no surprise that the value of this parameter varies from one chemical to another. In a study of 2D materials such as the one detailed in Chapter 5, molar concentration is potentially misleading. This is because of the difficulty in determining the molar mass of such materials. Instead mass-concentration, for example g L^{-1}, will be used. The molar extinction coefficient will therefore be referred to as the extinction coefficient. For UV-vis absorbance to be of any use, ε must be determined under the conditions pertinent to the experiment. To do this, the peak absorbance of several solutions of known concentration is plotted against wavelength. The optical path length is the length over which absorbance occurs, and this is commonly determined by the dimensions of the cuvette containing the sample solution. Most spectrophotometers take a standard cuvette of 1 cm. The extinction coefficient is then simply extracted from this plot as the gradient of the line of best fit. Once known, this value can be used to determine an unknown concentration of the same chemical. That is the way in which UV-vis absorbance will be used in this study.

UV-vis absorbance is a multifunctional technique. As well as information about solution concentration, a UV-vis spectrum can also be used in inorganic chemistry to extract the bandgaps of semiconductors.[11] This is done by extracting the absorption coefficient α from the raw absorbance data. The calculation will be set out in detail at the relevant stage. Suffice it to say that in studying materials that possess a bandgap characteristic of layer thickness, such as MoS_2, WS_2 and SnS_2, the ability to use UV-vis absorbance in this way is a useful diagnostic tool.

2.2.3 Optical microscopy

Optical microscopy (OM) is a simple, non-destructive and high-throughput technique for magnifying microscopic samples under illumination by visible light. It is often known as light microscopy and allows for rapid characterisation of few-layer materials.

Materials are identified by their optical contrast against the substrate surface, and this arises in one of two ways, either absorption of light or changes in the optical path length. The latter is important for materials such as h-BN, GaS and GaSe, large-bandgap materials that do not absorb in the visible region. This also gives rise to the thickness dependence of the optical contrast and means

that monolayers can be particularly difficult to see. However, 2D materials present the greatest possible optical contrast against the surface of 285-300 nm silicon dioxide thermally grown on silicon.[31, 128] This makes identification of monolayers practically trivial, even at low magnification.

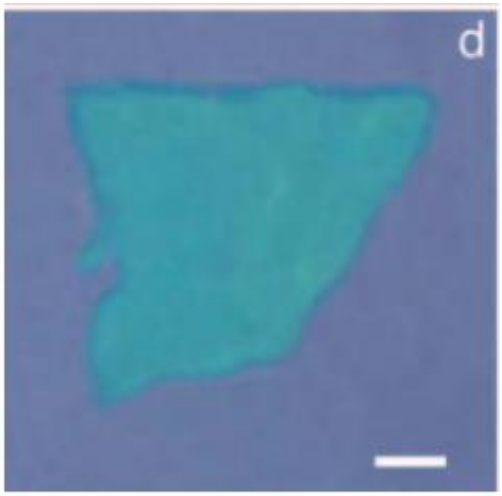

Figure 2.6 *Identification of 1L-MoS_2 on 300 nm SiO_2; scale bar = 1 μm*

In the study by Novoselov et al., the authors determined that the MoS_2 monolayer shows good contrast against the surface of 280-300 nm SiO_2 on Si when illuminated by an ordinary optical microscope. This is seen in the figure and presents a relatively straightforward way of performing an initial screening of samples for regions of potentially very thin material. Copyright 2005 National Academy of Sciences.

The monolayer MoS_2 in Figure 2.6 was obtained by Novoselov *et al.* and was easily identifiable by its optical contrast against a thermally-grown 300 nm SiO_2.[31] In their paper, they posited that regions of monolayers could be identified on a 1 cm^2 substrate in about 30 minutes, making this optical approach quite straightforward and high-throughput.

2.2.4 Raman spectroscopy

Raman spectroscopy is a vibrational technique that exploits the scattering of monochromatic photons from a laser source to identify a sample. Vibrations occur in the frequency range 10^{12}–10^{14} Hz, which corresponds to the near-infrared (near-IR) region of the electromagnetic spectrum. By accessing "virtual" molecular vibrational states, the significance of which is explained below, a laser source at a lower (visible) frequency can be used.

A beam of photons is an oscillating electromagnetic wave possessing an electric field of E. In a simple molecular case, the interaction of incident photons with the molecule induces periodic distortion in the molecule's charge distribution, known as an induced polarisation, P, and the molecule undergoes excitation to a virtual state known as an oscillating dipole. P depends not only on the incident E, but also on the molecule's inherent molecular polarisabilty, α, the relative

tendency of its charge distribution towards distortion, according to the Equation 2.4. For the purpose of visualisation, the quantity α can be viewed perhaps as analogous to classical strength. A leather ball, *cf.* a low-α charge distribution, will resist deformation upon application of tensive–compressive force, while a sponge ball, *cf.* a high-α charge distribution, will be highly deformable under an equal force.

$$P = \alpha E \qquad [2.4]$$

The induced dipole varies according to the instantaneous phase of the incident beam, so the charge distortion is oscillatory. Therefore, if the polarisation couples to a molecular vibrational state (mode), it gives rise to a characteristic molecular vibration frequency, υ_m.

The above process is true of molecular vibrations, but the characterisation of crystalline thin films is presented herein. The difference is that Raman spectroscopy of crystalline thin films does not measure polarisation of discrete molecules but periodic vibrations of the atoms within the lattice, and these lattice vibrations are known as phonons.[129] More discussion of the measured vibrations relevant to each material is found in Chapters 3, 4 and 5.

Whether the system in question is a discrete molecule or a lattice, there are three processes that can occur after the incident photon interacts with the system, illustrated in Figure 2.7:

1. Rayleigh scattering: The polarisation in an oscillating dipole does not couple to a vibrational mode. The incident photon with frequency υ_0 neither imparts energy to nor gains it from the oscillating dipole, and thus the molecule emits an elastic photon at the same frequency, υ_0. It follows that this process, which occurs for 99.9% of interactions, is Raman-silent and of no use in this spectroscopic technique. Unfortunately, only one in a thousand interactions is Stokes or anti-Stokes in nature.
2. Stokes scattering: The polarisation in an oscillating dipole in the ground vibrational state couples to the first excited vibrational state, causing a vibrational excitation. The incident photon with frequency υ_0 imparts energy to the oscillating dipole corresponding to the vibrational frequency υ_m, and thus the molecule emits an inelastic photon at a lower frequency than the incident photon, $\upsilon_0 - \upsilon_m$. It follows that this mode is Raman-active.
3. Anti-Stokes scattering: The polarisation in an oscillating dipole in the first excited vibrational state couples to the ground vibrational state, causing a vibrational relaxation. The incident photon with frequency υ_0 gains energy from the oscillating dipole corresponding to the vibrational frequency υ_m, and thus the molecule emits an inelastic photon at a higher frequency than the incident photon, $\upsilon_0 + \upsilon_m$. It follows that this vibrational mode is Raman-active. Anti-Stokes emission is typically even less intense than Stokes emission, because very few oscillating dipoles initially populate the first excited vibrational state.

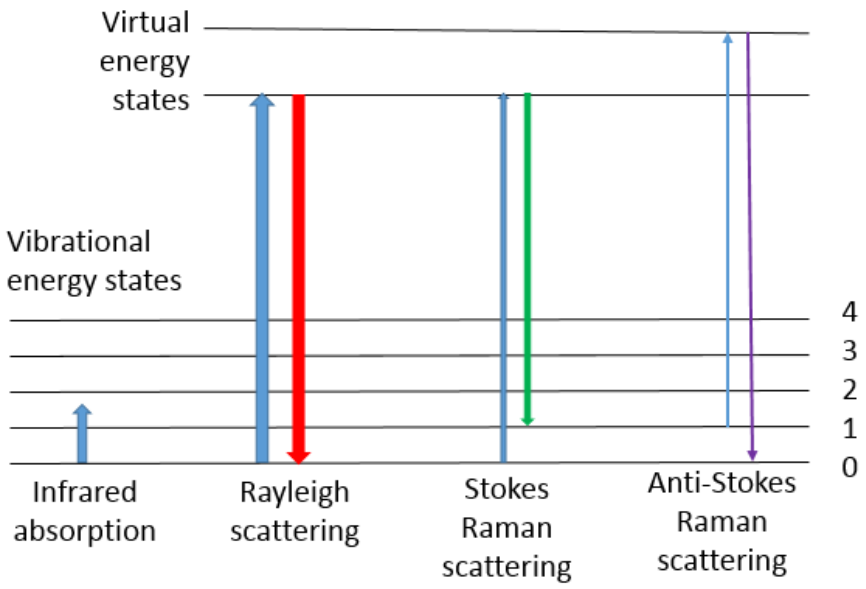

Figure 2.7 *The three processes that can occur in Raman spectroscopy*

Rayleigh scattering is emission at the same frequency as absorption. Stokes Raman scattering is emission at a lower frequency than absorption, following a vibrational excitation. Anti-Stokes Raman scattering is emission at a higher frequency than absorption, following a vibrational relaxation.

Inelastic emission arising from the latter two mechanisms is known as the Raman Effect, which gives its name to the spectroscopic technique. The Raman Effect is so named after the eminent Indian physicist Sir Chandrasekhara Venkata "CV" Raman,[130] who discovered it in 1928 and for which he was awarded the Nobel Prize for Physics in 1930.

Raman spectroscopy uses excitation energies much smaller than electronic transition energies, such that the virtual state occupied by the oscillating dipole is of a lower energy than the excited electronic singlet state. This reduces the likelihood of competing fluorescent pathways. However, as inelastic scattering is much less likely than elastic scattering, one problem in Raman spectroscopy is that the intensity of Rayleigh emission greatly exceeds that of Raman emission. Resonant Raman spectroscopy overcomes this by exciting a sample close to an electronic transition (a resonance) instead of a virtual state, such that vibrational modes close to the resonance are observed.[131] The intensities of those modes are much higher than in the non-resonant case. This is useful for studies of direct-bandgap semiconductors, where the excitation energy can be tuned to the bandgap, although it can introduce contaminating effects from fluorescence.

2.2.5 Photoluminescence

The IUPAC Compendium of Chemical Terminology defines photoluminescence (PL) as "luminescence from direct photoexcitation of the emitting species."[47]

Mechanistically, PL comprises electronic excitation of a ground-state electron (S_0) into its excited singlet state (S_1), as shown in Figure 2.8. That excitation is accompanied by a vibrational excitation, the energy of which is dissipated by a non-radiative transition. The non-radiative relaxation places the electron in the ground vibrational level of it S_1 state. Thereafter, the electron relaxes by radiative relaxation, either fluorescence or phosphorescence. The dissipation of some of the initial excitation energy by the non-radiative process means that fluorescence and phosphorescence occur at lower energies than the excitation.

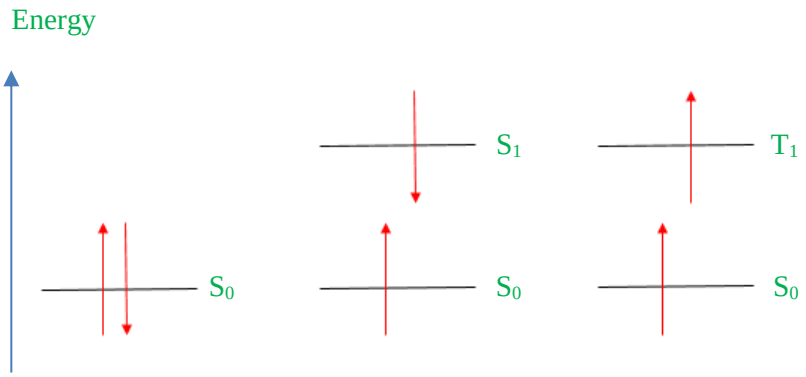

Figure 2.8 *Electronic energy levels in fluorescence and phosphorescence*

The energy level diagram is simplified as it does not show vibrational states, but it nevertheless captures the possible radiative relaxation mechanisms. The spin state is defined by the spin multiplicity, where S = singlet and T = triplet. In the singlet state, electron spins are paired, while in the triplet state, electron spins are parallel. Electrons are denoted by arrows, with the spin state defined as up or down. The subscript 0 denotes a ground state, and the subscript 1 denotes an excited state.

Fluorescence is the direct $S_1 \rightarrow S_0$ electronic relaxation, which takes place in a matter of nanoseconds or even faster. This is detectable by photoemission corresponding to the energy of the transition. Phosphorescence takes place after the S_1 electron undergoes a further radiationless process called intersystem crossing (ISC) into its triplet excited state (T_1), followed by $T_1 \rightarrow S_0$ relaxation. Figure 2.8 shows that ISC involves reversal of the electron's spin quantum number, so it is kinetically disfavoured relative to fluorescence, usually occurring over several seconds. This gives rise to the key observational difference between fluorescence, a lifetime of a few nanoseconds, and phosphorescence, a lifetime of several seconds or more.

Fluorescence as applied to semiconductors is specifically termed photoluminescence, and the photoemission energy corresponds to the material's bandgap. PL in the visible region (400–750 nm or 3.10–1.65 eV) is of particular interest to nanoscientists because it can be exploited for optoelectronic and photovoltaic devices.

The direct nature of the fluorescence process means that PL is limited to materials that possess a direct bandgap so as not to violate the principle of conservation of momentum (see Section 1.2). It follows that PL offers an experimentally straightforward method of determining the material's suitability for optoelectronic applications.

When supported materials are observed, PL intensity is substrate-dependent. That is to say, PL intensity is greatest upon excitation of monolayers grown on epitaxial substrates, such as sapphire or mica. On non-epitaxial substrates, such as silicon dioxide, PL is notably reduced. The direct bandgap of MoS_2 is 1.85-1.90 eV in the monolayer, [4, 7, 10, 38, 44, 45] which corresponds to emission wavelengths of 670-650 nm. Therefore, 532 nm excitation is sufficient for PL emission in MoS_2.

2.2.6 Scanning electron microscopy

The conventional light/optical microscope suffers from the Abbé diffraction limit of visible light, a consequence of the source wavelength. The Abbé diffraction limit, d, is the smallest separation distance at which two distinct objects can be mutually resolved; in other words, it is the best possible resolution that can be obtained using a given irradiation source:

$$d = \frac{\lambda}{2\, n \sin\theta} \qquad [2.5]$$

where λ = source wavelength

n = refractive index of medium

θ = half-cone angle subtended at the lens

Assuming a white light source with an average wavelength of ~500 nm, imaging in air using visible light is diffraction-limited to ~200 nm. The use of electrons as the illumination source substantially reduces the diffraction limit because the wavelength of the electron is some 100 thousand times smaller than that of visible light. This is the principle of electron microscopes, among which is the scanning electron microscope (SEM). The SEM has been able to access sub-nanometre lateral resolution, allowing for trivial visualisation of nanomaterials.

SEM is so-called because it produces a high-resolution image of a sample by raster scanning using a beam of electrons emitted from a metallic filament. The electron energy is not measured directly but calculated using the beam energy according to the following approximation:

$$E = \frac{1240}{\lambda} \qquad [2.6]$$

where E = beam energy/eV

λ = source wavelength/nm

An optical microscope exploits the sample's reflection and transmission of light to give contrast and compile an image, but an SEM uses scattered or emitted electrons from the sample.

There are a number of operating regimes of an SEM, named for the manner in which the electron beam is generated or the manner of imaging. For instance, the two types of SEM that are of relevance in this work are field emission (FE) and environmental (E) SEM.[132-134] An SEM produces a beam of electrons by thermionic emission. In contrast, an FE-SEM generates an electron beam by cold-source emission. See Section 2.1.3 for definitions of thermionic and field emission.

Upon interaction of the incident electron beam with the sample surface, a number of different processes may occur, each of which can be separately detected and analysed. They are briefly illustrated in Figure 2.9, but the most important ones for SEM are secondary electron emission and back-scattering.

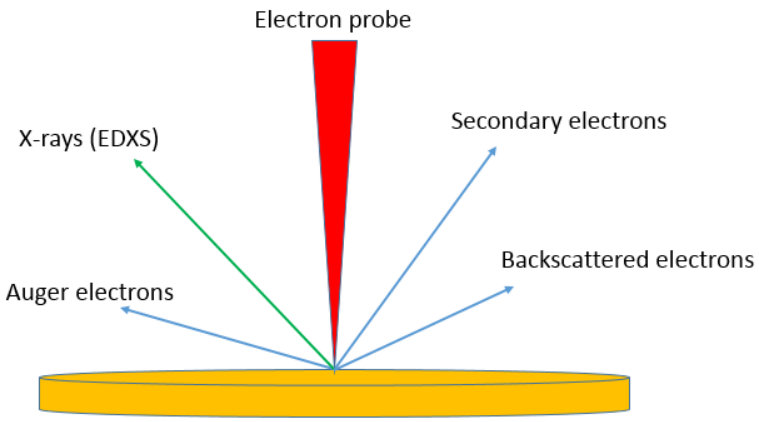

Figure 2.9 *Emission processes in SEM*

The Auger effect and X-ray emission will not be discussed here, although both are spectroscopically useful as characteristic tools (the latter is discussed in the next section). The processes most relevant to SEM are backscattering and secondary electron emission. Imaging can be performed in either mode, with most modern SEMs capable of switching between the two modes quite easily.

Secondary electron emission occurs when an incident electron collides with a core-shell electron and transfers its energy to the core-shell electron. Core-shell ionisation occurs if the kinetic energy imparted is greater than the core-shell electron's ionisation energy. The ejected core-shell electrons are known as secondary electrons. Detection of these secondary electrons allows an intensity map to be compiled, thus correlating image brightness to regions of the specimen. SEM conducted in this mode is known as secondary electron imaging (SEI) mode.

Backscattering is the reflection of incident electrons by the specimen. It is caused by elastic scattering of the primary beam electrons by an atomic nucleus. Heavier nuclei scatter more strongly than lighter ones, so backscattering can be used to obtain information about a specimen's chemical composition. SEM conducted in this mode is known as backscattered electron (BSE) mode.[135]

Regardless of the emission source and imaging mode, conventional or FE-SEM need to be conducted in high vacuum because a gaseous atmosphere absorbs and attenuates free electrons. An E-SEM allows imaging at lower vacuum by employing differential pumping, so that electron beam emission and sample imaging can be performed under different pressures. This is particularly useful for imaging liquid and large-bandgap semiconductors.[134]

As the technique relies on irradiation with electrons, non-conductive samples are generally poor specimens for SEM. This is because of the charging effect, which is the build-up of static charges at the sample surface. This creates bright hotspots that confound the imaging process, essentially masking morphological features. This effect is mitigated either by mounting the specimen to the sample holder using a conductive bridge of metallic tape (silver or carbon) or by sputtering a thin coating of Au on the surface. The latter process is, of course, destructive to the sample.

2.2.7 Energy-dispersive X-ray spectroscopy

Energy-dispersive x-ray spectroscopy (EDXS) is closely related to SEM in that it uses the same principle and can be performed using an FE-SEM, although EDXS analysis exploits x-ray emission rather than electron scattering.[136] Electrons emitted at the field emission gun irradiate the sample, as in SEM. Electrons incident on the sample may collide with a core-shell electron with sufficient kinetic energy to eject it from its shell, leaving behind a hole. A valence electron will then relax to fill the hole, emitting an x-ray with energy characteristic of the element. It follows that a number of electronic transitions may be possible depending on the initial interaction between the incident and core-shell electrons. The kinetic energy of the incident electron is therefore important, and this is proportional to the acceleration voltage at the field emission gun. Figure 2.10 illustrates the mechanism of x-ray emission in EDXS.

The electronic energy levels of the sample are denoted by the labels K, L, M, N and O with K being the innermost, lowest-energy shell and O being the valence shell. The same notation is used to label the emission lines observed in a typical spectrum. For example, the Kα-line occurs at the energy corresponding to x-ray emission arising from the 2p → 1s electronic relaxation; the Kβ-line, similarly, corresponds to the 3p → 1s transition; and the Lα-line is the 3d → 2p transition.

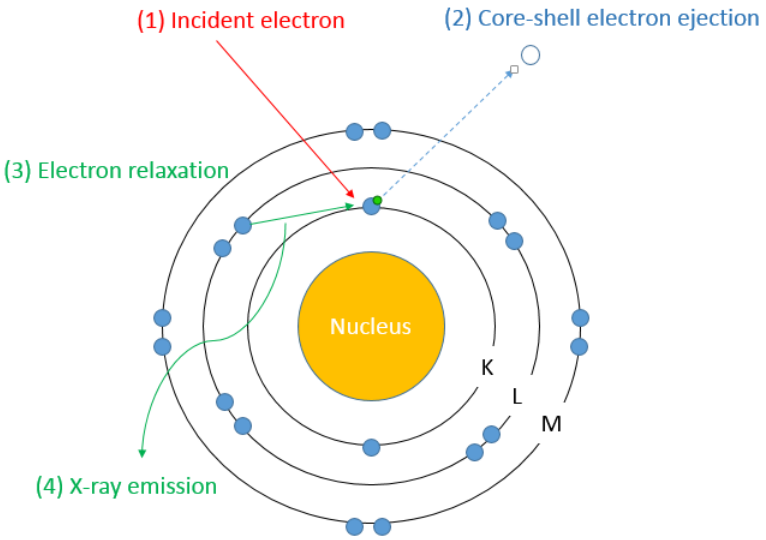

Figure 2.10 *Mechanism of characteristic x-ray emission in EDXS*

A sufficiently energetic interaction of the incident electron with a core-shell electron of an unspecified atom ***(1)*** *leads to secondary electron emission* ***(2)****, leaving behind a hole. An electron from a higher energy level relaxes to fill the hole* ***(3)****, releasing its excess energy in the form of x-rays* ***(4)*** *that are characteristic of the atom. This process is exploited in energy-dispersive x-ray spectroscopy for imaging specimens.*

2.2.8 Atomic force microscopy

To understand the advantages of the AFM, it is useful to explore the limitations of the STM and SEM (see Section 1.1.3). Typically, STM works by scanning a metal tip positioned over a surface. A bias voltage between the tip and the sample allows quantum mechanical tunnelling of the electronic wavefunction at the sample surface. The tunnelling current can be modulated by a feedback loop between the tip and the controller, allowing for angstrom-scale control of the tip—sample distance and, therefore, atomic resolution imaging.[25] For tunnelling current to flow, the sample surface must be conductive.

Non-conducting samples require coating, usually with gold film, for effective imaging under SEM. Otherwise, charging leads to artefacts in the image. As such, the technique is destructive to non-conducting samples because the as-prepared material cannot be retrieved after Au-coating.

The atomic force microscope overcomes the difficulty in imaging non-conducting samples by STM and SEM. With AFM, the sample is never charged and can be viewed as prepared. Instead, a morphological map is constructed from the variation of atomic forces between the cantilever tip and sample surface. Crucially, the technique is non-destructive.

The first AFM was invented in 1986 as the latest type of scanning probe microscope (SPM).[27] The SPM family of techniques, including the STM and SEM, are designed for high-resolution mapping

of the topographic features of a sample. In the AFM case, this is achieved using three-dimensional piezoelectric control of a cantilever that moves either the probe or the sample with nanoscale precision. In this way, a point-by-point scan can be carried out usually by raster scanning (one row at a time). Figure 2.6 shows a conventional AFM setup.[137]

The cantilever is usually a flat silicon plate with an atomically sharp tip. The tip tapers to a point and usually has a radius of a few nanometres at its apex. It is used to raster-scan a surface, and a feedback loop is used to control one of a number of parameters (depending on the desired mode). A map of the variation in atomic forces can then be constructed, allowing for high-resolution morphological characterisation. The feedback loop responds to deflection of the cantilever tip, as measured by a laser reflected off the back of the cantilever onto a photodiode, as in Figure 2.6.

Light reflected by the cantilever and incident on the photodiode is converted to current and positional changes in the photocurrent are used to modulate the feedback. Deflection of the laser beam at the photodiode depends on the angle of reflection of the laser beam by the back of the cantilever. This, in turn, depends on tiny deflections of the cantilever caused by the interaction between the tip and the sample. Figure 2.11 shows illumination from below the sample, but it is also possible to perform top-view/plan imaging from above the sample, which was useful for the work in Appendix C.

Feedback modulation can occur in several modes: contact and non-contact/tapping. In contact mode, the tip comes into hard contact with the sample surface and an image is constructed by one of two methods. For constant-force imaging, the height of the cantilever is continuously adjusted by the piezo controller Z in Figure 2.11. This ensures that the force between the tip and sample remains fairly constant. In constant-height imaging, the Z controller maintains the tip at the same height relative to the sample. This is useful for smooth surfaces, as the cantilever would catch on surface features, which would cause blunting and loss of resolution.

In non-contact mode, the cantilever tip is rapidly oscillated close to the sample surface by application of an AC voltage. This is an advantage for imaging soft samples as lateral forces such as drag can be eliminated.

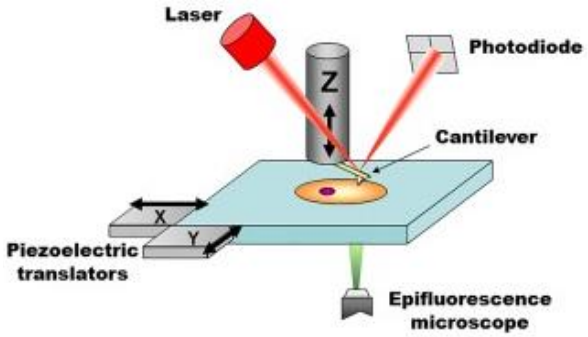

Figure 2.11 *Elements of an AFM setup*

In a typical setup for atomic force microscopy, a spring-like cantilever is carried by a holder that is mounted to a piezo controller. The controller drives the cantilever in the axial direction with respect to the sample that is mounted to a translation stage underneath the sharp cantilever tip. The interaction of the tip with the sample is therefore transduced into displacement of the cantilever. Detection of this motion is done by means of a laser that is reflected off the back of the cantilever, giving a very precise response to cantilever deflections. The reflected beam hits a photodiode, which converts the incident light signal into an electrical signal. An image can thus be constructed with resolution limited by the apex of the cantilever, which is usually of nanometre scale. Image reproduced from ref. [137] under Creative Commons licensing from Wiley Periodicals, Inc.

2.2.9 Transmission electron microscopy

A transmission electron microscope (TEM) exploits the transmission of electrons through a thin specimen in order to construct an image.[138] For this purpose, it follows that the sample needs to be ultrathin. Sample preparation can be achieved either by milling, which can be done mechanically using fine diamond film, or by wet chemical mounting onto a copper grid or holey carbon grid.

In most TEMs, the electron beam is produced by thermionic emission (see Section 2.1.3). The emitted e-beam is focussed and then accelerated at high voltage in a near-vacuum (~10^{-4} Pa to increase the mean free path) towards the sample. Acceleration through 100-200 kV provides the e-beam with sufficient kinetic energy to penetrate the sample and pass through. Electrons are then detected by a photographic film or a charge-coupled device (CCD) camera. The contrast in the image arises from differences in the interactions of different elements with the e-beam. Most commonly, the interaction that is of most significance is electron absorption by the material, and this depends not only on the elemental composition but also on the thickness.

A TEM image can be analysed by fast Fourier Transform (FFT), which generates a diffraction pattern in reciprocal space that encodes information about sample crystallinity. For a single crystal,

the resulting pattern is a series of concentric rings of dots, while a polycrystalline film generates a diffraction pattern of solid rings. An FFT diffraction pattern can be back-formed into a real-space image (inverse FFT), which is useful for studying interplanar d-spacings. This will be discussed in more detail in Chapter 3 and associated appendices, wherein the methodology for performing FFT analysis will be presented.

2.2.10 X-ray diffraction

X-ray diffraction (XRD) is a non-destructive, high-throughput technique for the phase identification of crystalline materials. The technique exploits the principle of Laué diffraction, by which crystalline materials diffract incident x-rays in the same way as a diffraction grating; each line in the diffraction grating is replaced by lattice planes in the crystal.

The interaction of incident x-rays with the sample is governed by Bragg's law, Equation 2.7:[139]

$$n\lambda = 2d \sin\theta \qquad [2.7]$$

where n = a positive integer

d = separation of lattice planes

θ = incidence/diffraction angle

Bragg's law is depicted in Figure 2.8, which shows x-rays incident upon a generic crystalline material, with like planes represented by imaginary lines through the atoms forming the plane.

According to Bragg's law, incident x-rays with an integer number n of wavelengths λ equal to the interplanar d-spacing are diffracted such that the angle of diffraction is equal to the angle of incidence. In practice, the wavelength is predetermined by the target source. Generation of x-rays occurs by the same principle as in EDXS, and a copper target is generally used. Core-shell ionisation of Cu leads to Kα-emission at a wavelength of 1.54 Å, corresponding to ~8,000 eV. Thus, the parameter that is varied instead of the source wavelength is the incidence angle. A goniometer is used to vary the incident angle across a range that typically spans 5-70° and reflections satisfying the Bragg equation are detected. The Bragg equation is satisfied when waves scattered from lattice planes interfere constructively, so they remain in phase since the difference between the path lengths of the two waves is equal to an integer multiple of the wavelength. This can be seen in Equation 2.7 and Figure 2.12.

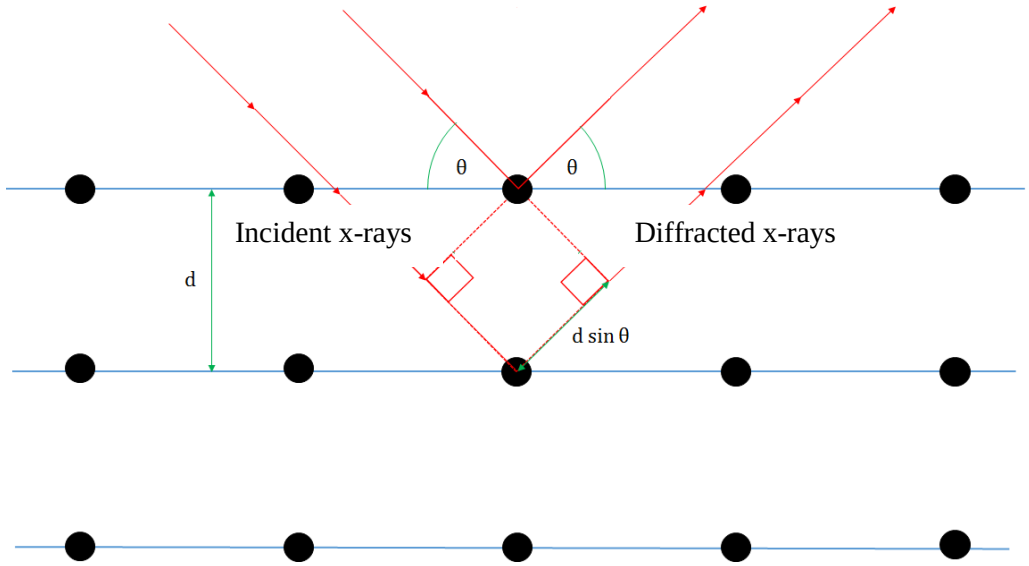

Figure 2.12 *X-ray diffraction by crystallographic planes according to Bragg's law*

Incident x-rays interact with lattice points in the crystalline film. When the Bragg condition is satisfied, x-rays are diffracted by an angle equal to the angle of incidence. The detector therefore measures the angle 2θ.

The output is a pattern of intensities of diffracted x-rays at angles of 2θ. This follows from considering the geometry in Figure 2.12. The angle θ is the angle between the incident x-ray beam and the crystallographic plane. When the Bragg equation is satisfied, it is also the angle between the crystallographic plane and the reflected beam. Thus, the angle between the reflected beam and the incident beam is, in fact, 2θ.

For thin film characterisation, x-ray penetration into the substrate can be minimised using grazing incidence, GIXRD.[140] Grazing incidence uses a very low angle of incidence (<3°), limiting penetration to less than 10 nm. In this case, the output 2θ is measured by moving the detector arm.

A complete pattern of diffractions across a range of angles is characteristic of a particular crystal lattice, and thus it can be compared to a database of the known lattices occupied by a range of phases in order to obtain the best fit. This is how XRD has been used in this research. Further processing, or indexing, of peaks can be used to obtain the Miller indices of a plane producing a particular reflection. This calculation involves the diffraction angle, but will not be discussed.

Chapter 3 Liquid Atomic Layer Deposition of Molybdenum Disulphide

3.1 Background and motivations

A metal—oxide—semiconductor field-effect transistor (MOSFET) is a three-electrode semiconductor device used to switch or amplify a signal. A MOSFET operates by the field effect, whereby the conductivity of a silicon channel between source (S) and drain (D) electrodes is modulated by a voltage to the gate (G) electrode. Figure 3.1 explains a MOSFET.[38]

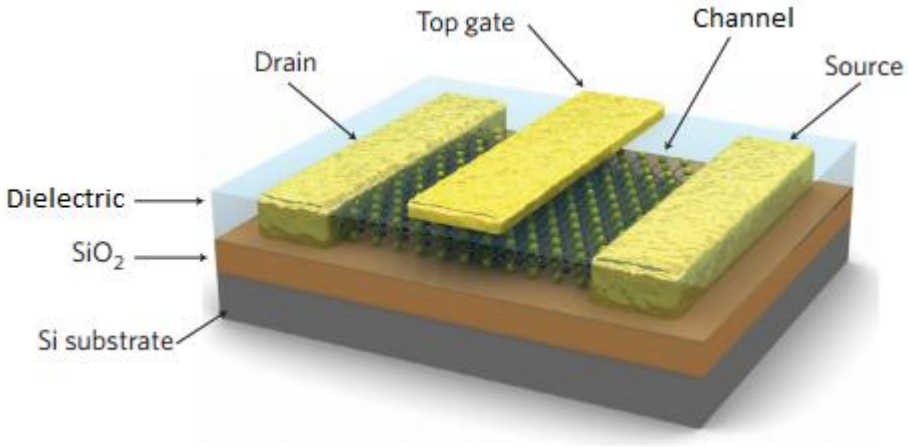

Figure 3.1 *A top-gated MOSFET*

This type of field-effect transistor is normally constructed on an oxide layer on a silicon wafer. The basic components are three electrodes, labelled the source (S), drain (D) and gate (G). Under the S and D electrodes are regions of similarly-doped semiconductor. Under the G electrode is a gate dielectric, most commonly SiO_2. Between the S and D regions is a semiconducting channel normally made of silicon. Reprinted by permission from ***Springer Nature Customer Services Centre GmbH: [Springer Nature] [NATURE NANOTECHNOLOGY], ref. [38], COPYRIGHT 2011***

Over the last 50 years, the number of transistors per integrated circuit has doubled roughly every 18 months, an observation known as Moore's Law.[141] As the size of individual transistors continues to decrease in accordance with Moore's Law, the efficacy of silicon-based materials as semiconducting channels and gate dielectric layers is being pushed to its limits.

In transistors, the semiconducting channel often has some dopant introduced to enhance its semiconducting properties. The type of dopant defines the majority charge carriers in the S and D regions of the transistor, which in turn define the type of MOSFET. In an n-MOSFET, the channel is p-doped and the S and D regions are n-doped, so the majority charge carriers are electrons (n-

type). In a p-MOSFET, the channel is n-doped and the S and D regions are p-doped, so the majority charge carriers are holes (p-type). A schematic is useful to illustrate the point (Figure 3.2).

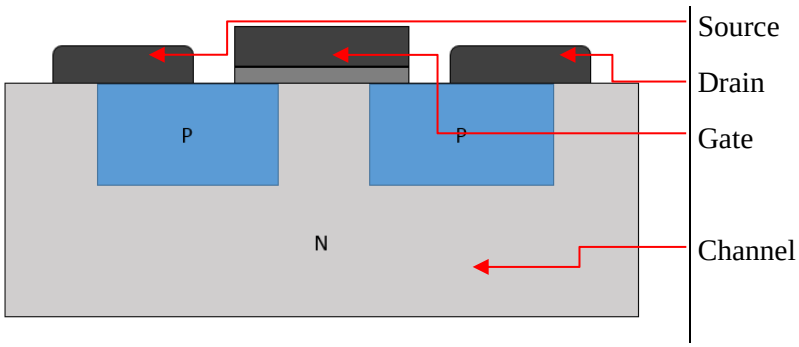

Figure 3.2 *Doping regime in a p-MOSFET*

Traditional MOSFET design utilises one of two doping regimes, either n- or p-type. In a p-MOSFET, the source and drain regions are p-doped, and therefore the majority charge carriers in a p-MOSFET case are holes. The reverse is true of an n-MOSFET.

Complementary MOSFETs (CMOSFETs) make use of a pair of transistors, in which there is a p-type channel contiguous with an n-type channel. This acts as a logic gate, in which a voltage at one of the devices switches the current in the complementary device. Integrated circuits comprise several million CMOSFETs. Semiconducting monolayers can be used as novel channel materials in MOSFETs.

The silicon MOSFET is only one design of transistor. Its main application is in microprocessors for high-performance computing, where the material quality, scalability and the ability to modulate the current have proven to be advantageous.

In short-channel MOSFETs – modern-day devices possess sub-30 nm channel lengths – the voltage at the D electrode V_D exhibits a modulating effect on the channel conductivity. In other words, the potential barrier to charge carrier flow is lowered by the application of V_D, so the phenomenon is known as drain-induced barrier-lowering (DIBL) and is obviously an unwanted effect because it compromises the ability to modulate the channel current by the V_G. DIBL is a quantifiable effect in that it manifests as a reduction in the device's threshold voltage V_T, the minimum value of V_G at which conduction through the channel can occur. To challenge this so-called short-channel effect, MOSFET technology has been advanced by the development of the finFET (see Figure 3.3), a non-planar (3D) device in which the channel (designed as a fin protruding out of the plane of the chip) is encased in the G electrode.[142]

The finFET has been a useful improvement on the existing MOSFET because the "wrapped-around" G electrode affords superior electrostatic control over the channel conduction compared to the planar structure, *i.e.*, DIBL is significantly reduced.[142] Nevertheless, changing the device architecture can only go so far with the current limits of the channel material.

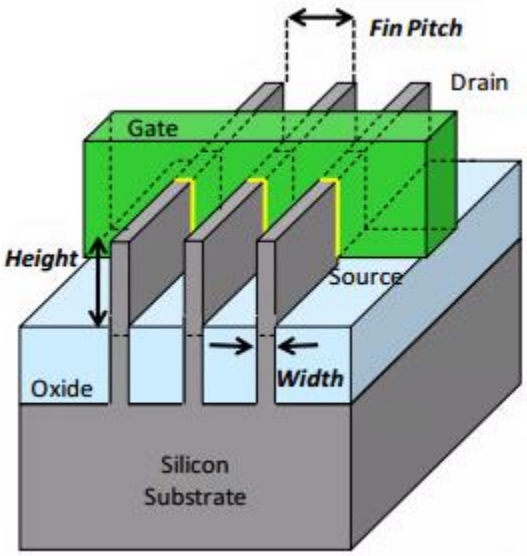

Figure 3.3 *A recent finFET design*

A finFET is designed to overcome challenges associated with the use of silicon as a semiconducting channel material in the MOSFET. The finFET incorporates all the recognisable features of a field-effect transistor, but with a 3D architecture that minimises short-channel effects and which can allow for the incorporation of additional features such as multiple gates. However, architecture can only go so far to mitigate problems inherent to the channel material. Image reproduced, with permission, from ref. [142]; © 2011 IEEE.

Silicon has traditionally been the semiconducting channel material in transistors. However, silicon suffers from one intrinsic drawback, which is its low breakdown field (E_{bd}), related to the highest bias voltage that can be applied to the device before the channel material loses its semiconductivity and becomes conductive. The breakdown field of a semiconductor is proportional to its bandgap by the following equation proposed by Wang:[143]

$$E_{bd} = 1.36 \times 10^7 . \left(\frac{E_B}{4.0}\right)^{\alpha} \text{ V cm}^{-1} \qquad [3.1]$$

where E_{bd} = material breakdown field

E_B = bandgap

α = exponent related to the band structure

The low breakdown field of silicon is, therefore, a consequence of the fact that silicon has only a small bandgap of 1.12 eV, which yields a breakdown field of 298 kV cm^{-1}. It is a problem in modern electronics, in which attempts to reconcile high-power applications with Moore's Law have resulted in the need for materials with higher breakdown voltages.

These limitations of Si as a viable material for next-generation nanoelectronics provides the motivation for the work outlined in Chapter 3. Nanoscientists now seek to move "Beyond CMOS",

a term coined by James Hutchby in 2002.[46] He forecasted the stage of nanoelectronics at which the rate of MOSFET scaling under Moore's Law could no longer continue, due to constraints imposed by the nature of the materials used. He stated that this would happen in the late 2010s. Inorganic monolayer semiconductors are the ideal candidates to replace silicon in Beyond CMOS transistors, because of their bandgap tuneability, thinness and good device performance, as well as the ability to tune properties by combination of monolayers into heterostructures.

3.2 Materials

Having addressed potential applications, gaps therein, and motivations, it is useful to consider which materials could fulfil the role that silicon can no longer perform. Table 3.1 depicts several 2D materials similar to MoS_2 with favourable properties.[144] All of the binary materials below are TMdCs and are calculated to have the same basal structure as MoS_2.

Table 3.1 Properties of MX_2-type semiconductors (ref. [144])

Material	Bandgap/eV	Carrier mobility/ $cm^2\ V^{-1}\ s^{-1}$
MoS_2	1.80	410
$MoSe_2$	1.50	150
$MoTe_2$	1.23	-
WS_2	1.90	-
WSe_2	1.74	250
WTe_2	1.14	-

In addition to the TMdCs above, hexagonal boron nitride (h-BN) is a promising material for high-temperature/high-power applications. It is isoelectronic and isostructural to graphene, and its 2D nanosheets possess a direct bandgap of 5.9 eV. The similarities do not end there: the h-BN unit cell has very similar lattice parameters to graphene. As a result, some have suggested h-BN–graphene hybrid films as a means of opening up a bandgap in graphene without introducing fabrication complexity or significantly compromising the carrier mobility of graphene. The large bandgap has also been investigated as a UV photoemitter.[145]

Monolayer MoS_2 has a direct bandgap of 1.85-1.90 eV, offering greater opportunity for high-power applications than Si owing to its larger breakdown field in accordance with Equation 3.1. [4, 7, 10, 38, 44, 45, 143] Monolayer MoS_2 has a breakdown fielding greater than 5 MV cm^{-1},[146] exceeding that of Si by nearly 20 times. It is noteworthy that even bulk MoS_2 has an indirect bandgap of 1.29 eV; the band modification occurs in films fewer than four layers thick and presents a second advantage of this material over Si.[4, 147]

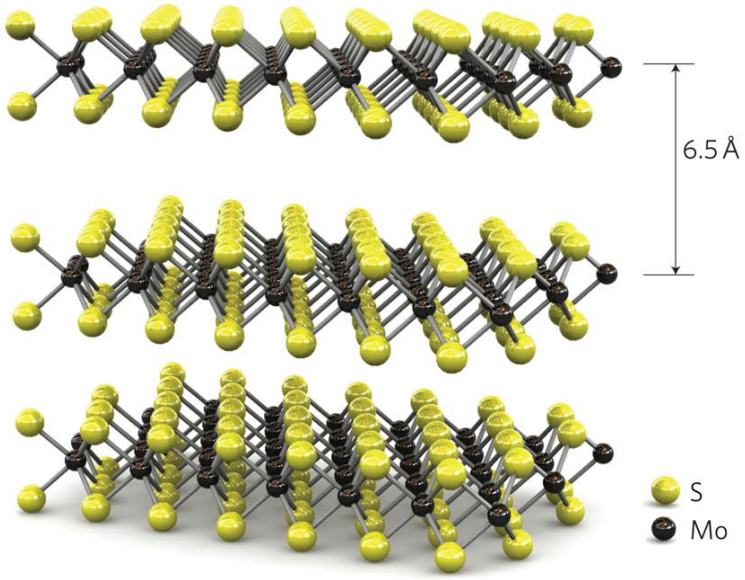

Figure 3.4 *MoS_2 structure*

The bulk material comprises layers of covalently-bonded, three-atom-thick, hexagonal sandwich structures of S – Mo –S. The interlayer spacing is 0.65 nm, and the thickness of a monolayer is ~0.6-0.7 nm. Reprinted by permission from ***Springer Nature Customer Services Centre GmbH: [Springer Nature] [NATURE NANOTECHNOLOGY], ref. [38], COPYRIGHT 2011****.*

Radisavljevic *et al.* designed a MOSFET incorporating single-layer MoS_2 as the channel semiconductor.[38] They used gold as the gate electrode and hafnia, HfO_2, as the gate dielectric. They observed carrier mobility through the channel of 200 $cm^2\ V^{-1}\ s^{-1}$, comparable to graphene nanoribbons. They anticipated that this could be improved with improvements in the synthetic and interfacial properties.

Amani *et al.* advanced the principle by synthesising MOSFETs with MoS_2/graphene heterojunctions to reduce contact resistance.[148] Contact resistance is electrical resistance at interfaces and is an acute problem in polycrystalline films in which many small crystals form grain boundaries. In principle, a contact material that introduces high carrier mobility at the heterojunction will reduce contact resistance.[9] Another way to minimise contact resistance is to reduce the number of contacts within the film by synthesising large single crystals.

Transistors are not the only application of MoS_2 and its family of materials. Splendiani *et al.* reported on emergent PL in ultrathin MoS_2 and expressed hope that the discovery would find applications in nanophotonic devices.[7] They produced MoS_2 flakes by surface exfoliation and adsorbed them onto a SiO_2/Si substrate. They used a 532 nm laser to effect ligand-to-metal electronic transitions, measured as photoemission. The strength of photoemission was inversely proportional to the number of layers, proving a transition from an indirect to direct bandgap on going from bulk to nano.

The ability to modulate the band structure by synthetic means will also find its application in transparent electronics, such as liquid-crystal displays and coatings, as shown by the work of Nomura *et al*.[149] It is predicted that PL of this nature is unique to transition metal-derived nanomaterials, which undergo rich d-electron chemistry, and it has been exploited by the likes of Li *et al.*, who synthesised a mechanically-exfoliated MoS_2 phototransistor.[8]

van der Zande *et al.* reported a phenomenon analogous to contact resistance occurring at grain boundaries in polycrystalline MoS_2 films synthesised by CVD.[150] They extolled the virtues of deposition-based synthesis *vs* exfoliation for producing the highest-quality crystals. They described the consequences of two types of boundary: tilt and mirror-twin. At a tilt boundary, the rotation axis of a crystallite is parallel to the boundary plane between it and an adjoining crystallite, resulting in a boundary resembling a bend with a dislocation (wedge) inserted between the crystallites. A mirror-twin boundary is a high-symmetry defect, in which a crystallite is a mirror image of an adjoining crystallite, resulting in periodically-shared lattice points. There was 50% quenching of PL at mirror-twin boundaries, but 100% enhancement at tilt boundaries. van der Zande's group constructed FETs from islands containing single grain boundaries and compared their electronic properties to those of FETs constructed with pristine crystal islands. They measured conductance across (perpendicular to) and along (parallel to) the grain boundaries. There was little variation in conductance in mirror-twin boundaries (with respect to the pristine system), but a 30% decrease in conductance both perpendicular and parallel to tilt boundaries.

In summary, ultrathin MoS_2 has found applications as a channel semiconductor in MOSFETs because of its bandgap and conductivity and optoelectronic devices because of its photoluminescence. Improvements can be made to these technologies by fine-tuning electronic structure, heterojunction properties and crystallinity. It has already been proven that post-exfoliation engineering can be used to tune the properties of graphene, but attempts can be explored to control properties at the synthetic stage.

For any long-term potential in replacing silicon as channel materials in high-power devices and optoelectronics, materials must have bandgaps much larger than that of Si. Therefore, MoS_2 and WS_2 (see Chapter 4) were chosen in the first instance.

3.3 Synthesis

The most-studied TMdC has been molybdenum disulphide, MoS_2, which possesses a direct bandgap of 1.85-1.90 eV in the monolayer. [4, 7, 10, 38, 44, 45, 143] However, realising the full potential of MoS_2 and other TMdCs for applications requires efficient and scalable synthetic routes.

The basal planes of layered materials are weakly bonded by vdW interactions, which allows exfoliation of individual layers. Graphene, MoS_2, WS_2, h-BN and black phosphorus are examples

of 2D materials that have been produced by exfoliation for research purposes.[11, 30, 31, 81, 85] The efficacy of exfoliation for applications suffers from the limited scalability of the process, which generally produces monolayers on the nanometre scale and is therefore only appropriate for small-scale proof-of-concept devices and fundamental elucidation of material properties.

Physical and chemical vapour deposition (P/CVD) have been studied for the synthesis of graphene, h-BN, HfO_2 and especially MoS_2.[102, 103, 150-172] CVD yields good-quality micron-scale single crystals, but larger films synthesised by CVD have suffered from defects arising from polycrystallinity.[162] It is preferable to achieve single-crystal growth in order to realise the potential of 2D materials, because this minimises contact resistance.[150, 173] The oxygen-assisted method developed by Chen *et al.* proved effective in CVD of single crystals up to several hundred microns in size.[152] However, the use of oxygen is known to have a deleterious effect on material quality, an effect acknowledged by the authors. They produced carefully controlled conditions that limited this oxidative effect, but that requirement clearly limits the generality of the oxygen-based process. CVD can be combined with seeding to promote nucleation. One alternative to this type of surface modification has been seeding. Traditionally, polymers, organic salts and reduced graphene oxide have been used as seeding promoters, but this introduces issues with incorporation of carbon impurities.[159, 162, 174, 175] One outstanding question is: to what extent can MoS_2 be used as a seed for itself?

ALD of TMdCs gives finer thickness control than traditional CVD and metal—organic CVD (MOCVD) because precursors are deposited discretely.[176-178] ALD does not require the complexity in precursor design that is often a problem in MOCVD, and therefore avoids the environmental and safety issues inherent to organometallic precursors.[159] Tan *et al.* performed the first MoS_2 ALD with readily-available precursors in 2014.[37]

Liquid-based techniques are used to react precursors at solution interfaces, which benefits from low cost and large volume.[179-181] However, they are generally difficult to control due to the stability of the solvent—precursor interaction and better suited to nanoparticles or porous materials.[182]

Liquid processing that is used to react precursors at solution interfaces has been combined with CVD to produce few-layer MoS_2, using either a single-source precursor solution or a solution of molybdenum precursor in a sulphur-based solvent.[107, 109, 183] Those processes have ultimately been CVD-type in nature and so suffer from the drawbacks of CVD.

In this chapter, a novel synthetic method is reported for the fabrication of 1L-MoS_2 single crystals with domain sizes up to 100 μm, which are among the largest reported with a single-substrate method.[151] This method combines liquid chemistry with ALD.[184] The technique combines the advantages of ALD and solution chemistry, yielding high-quality single crystals, in large volume and at low cost relative to liquid chemistry and ALD in isolation. The process benefits from readily-available precursors in contrast to MOCVD. This combination of liquid chemistry with the

discrete layer-by-layer benefits of ALD described herein has never previously been reported. Previous reports of liquid chemistry combined with CVD, such as that of Liu *et al.*, have yielded only trilayers.[107, 109, 183] The efficacy of liquid ALD to produce high-quality monolayers is demonstrated through detailed characterisation of the obtained material by OM, Raman spectroscopy, PL, SEM and TEM. Issues such as the solvent—precursor interaction are addressed by controlling deposition temperature so as to favour adsorption of the dissolved precursor.

In summary, the method developed in this chapter will aim to advance the field by providing a single-substrate, modification-free and low-cost route towards large, high-quality single crystals of MoS_2 by combining liquid and ALD-type techniques for the first time.

3.4 Characterisation

Each material has characteristic peaks in its Raman spectrum that indicate its nature and thickness. The important vibrational modes in MX_2 materials (M=Mo,W, V, Nb, Ta, Ti; X=S, Se, Te) are the in-plane E_{2g} mode and the out-of-plane A_{1g} mode (see Figure 3.5).[144]

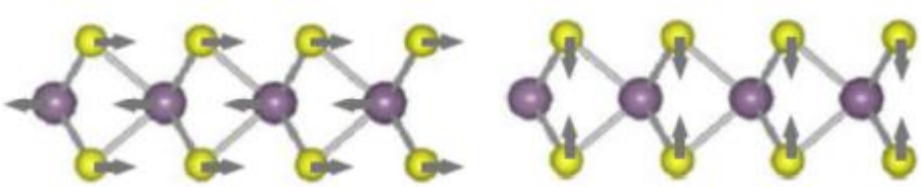

E_{2g} A_{1g}

Figure 3.5 *The two characteristic Raman phonons of MX_2 films*

The image shows a generic structure of a transitional metal dichalcogenide. Left is the in-plane E_{2g} mode, which is a periodic oscillation of the lattice in the basal plane. Right is the out-of-plane A_{1g} mode, which involves a periodic oscillation of X atoms normal to the basal plane. Reprinted from ref. [144], copyright 2011, with permission from Elsevier

The E_{2g} mode is an in-plane vibration of the X atoms in the lattice in opposition to the M atom. As a result, this phonon is not strongly influenced by interlayer vdW forces but does depend on Coulombic interactions between the heavy metal atoms. Therefore, in going from bulk to monolayer, the removal of interlayer shielding strengthens these interactions, and the characteristic peak corresponding to E_{2g} experiences a blueshift.[185] The A_{1g} mode is an out-of-plane vibration of the X atoms in the lattice independent of M. As a result, this phonon is strongly influenced by interlayer vdW forces as X atoms in adjacent layers oscillate periodically. The removal of layers weakens the vdW interactions, and the characteristic peak corresponding to A_{1g} experiences a redshift.[185, 186] The extent of the blue and red shifts in the peaks, as well as the resulting frequency gap between them, can confirm the identity of the material and the thickness of the film.[102, 187, 188]

For bulk MoS_2, the characteristic peaks occur at E_{2g} = ~383 cm^{-1} and A_{1g} = 408 cm^{-1}. [151-153, 160, 189] Small variations in these values may be expected depending on thermal and strain-related effects. Even accounting for those, the peak separation ($\Delta\bar{\upsilon}$) in the bulk is ≥24 cm^{-1}. Monolayers grown by vapour-phase techniques will yield $\Delta\bar{\upsilon}$ = 19.0-20.5 cm^{-1}, with variations again attributable to thermal or strain effects.[151-153, 160, 189]

For optoelectronic and photonic applications, good light emission is an essential property. The energy of PL depends on the material's bandgap, and in 1L-MoS_2 that is ~1.85-1.90 eV, corresponding to emission at ~670-655 nm. [4, 7, 10, 38, 44, 45] The bandgap-dependence itself makes PL a useful "diagnostic" tool for monolayers as the bulk material does not possess a direct bandgap and will not exhibit PL.

The variety of microscopy tools have proven to be very useful in morphological characterisation of TMdCs. Many single crystals of MoS_2 and structurally-analogous materials form striking single crystals that adopt a triangular-faceted morphology owing to their hexagonal lattice. Such a morphology lends itself well to trivial identification using OM and SEM in particular. Other morphologies of single crystals are known to exist, such as the hourglass, kite and butterfly facets, and each will be considered.

As described in the Methods chapter, SEM is dependent on the conductivity of the target sample. Non-conductive samples require sputtering usually with a thin gold layer in order to present a conductive surface to the SEM probe. MoS_2 is a semiconductor, so a piece of silver/carbon tape connecting the material to the metal sample holder was used to limit charging for the purpose of SEM. This is an advantage over gold sputtering as it allows the sample to be recovered undamaged after the characterisation is complete.

3.5 Experimental details

3.5.1 Substrates

The substrates used were thermally-grown 285 nm SiO_2 on Si-(100) known as **[1]** or c-cut (0001) sapphire known as **[2]**, purchased from University Wafer. Substrate **[1]** wafers had a thickness of 500 μm and resistivity of 0-100 Ωcm. Substrate **[2]** wafers were used either as-purchased or were pre-annealed at 1000 ℃ for 1 h in N_2 and 1400 ℃ for 1 h.

Before each experiment, 1×1 cm wafer dice were cleaned by sequential sonication (20 min.) in acetone, water and isopropyl alcohol (IPA), and dried in nitrogen or baked at 80 ℃ for 30 mins. In some cases, see T39 and T40, the final wash with IPA was followed by a 30-min. water dip to improve hydrophilicity and aid the precursor adsorption process from aqueous solution.

3.5.2 The molybdenum precursor

Thermal decomposition of the molybdenum-containing precursor, ammonium heptamolybdate tetrahydrate, $(NH_4)_6Mo_7O_{24}.4H_2O$ (CAS number 12054-85-2, purchased from Sigma-Aldrich at ≥99.999% purity), henceforth referred to variously as the "Mo/molybdenum precursor" or "ammonium molybdate", was studied by thermogravimetric analysis (TGA, Universal V4.5A TA Instruments). A small amount (~5 mg) of precursor was heated from room temperature to 750 ℃ at 50 ℃/min. in nitrogen (100 sccm/0.1 slm). The vendor specified 81.0-83.3% base MoO_3 in the as-purchased precursor.

The molybdenum precursor was introduced to the substrate by one of several regimes. In one case, the substrates were seeded (either from solution or by mechanical exfoliation) with MoS_2 in order to promote nucleation, and the Mo precursor was introduced by dip-coating thereafter. In a second case, the molybdenum precursor was introduced to the bare substrate by dip-coating. In a third case, the Mo precursor was introduced onto patterned substrates. All of these regimes are outlined in the following sections.

3.5.3 Substrate seeding

The seed crystals were obtained by two methods: mechanical exfoliation, and drop-casting from concentrated alcoholic solution:

a) Monolayer molybdenum disulphide (MoS_2, 92 g/mL ethanol solution purchased from 2D Semiconductors) was drop-cast as seed on four 1×2 cm dice of **[1]**, as outlined in Table A.1 in Appendix A. However, the concentration and solvent were changed thereafter.
b) Mechanical exfoliation was performed by the well-known tape method from a bulk crystal of MoS_2 (bought from 2D Semiconductors). Exfoliated crystals were seeded on **[1]**.

As well as being heated on a heating plate, substrates S5-10 were tilted at an angle ~30°, to prevent agglomeration of crystals by the coffee ring effect.

3.5.4 Dip-coating on bare substrates

Ammonium heptamolybdate tetrahydrate solution was manually dip-coated onto bare (untreated and unseeded) wafer dice at a range of temperatures, 40-90 ℃. Reaction conditions were achieved by suspending the dice in a pre-heated solution and maintaining the temperature throughout the deposition time. Dice were pulled out after various deposition times. See Scheme 3.1.

Scheme 3.1 Dip-coating setup

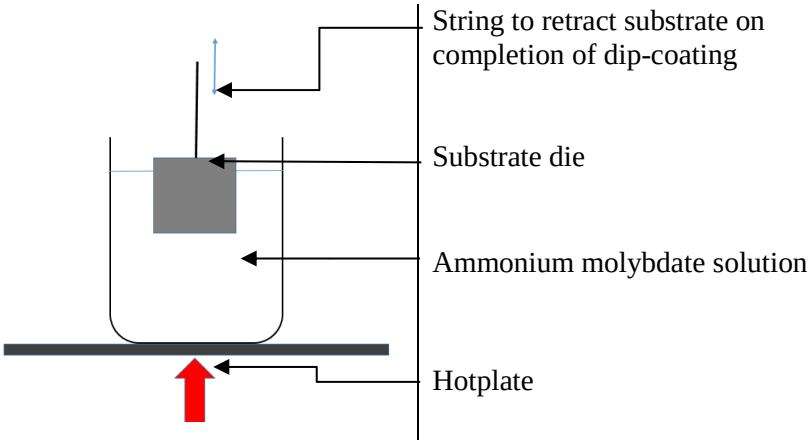

Dip-coating parameters were carefully controlled, and this is shown in Table A.2 (Appendix A.2). Different concentrations of precursor solution, dip-coating time/temperature and substrate were used to optimise the process as much as possible. A discussion of the step changes made will follow in later sections.

In the case of overnight dip-coating, see T39-40, the intended effect was to mimic mechanical substrate-pulling. Instead of pulling the substrate from the solution, the solution would gradually recede down the suspended substrate by evaporation, and thus it was presumed to be analogous in principle. With the solution maintained at 80 ℃ by the use of a heating plate modulated in a feedback loop with a temperature probe in the solution, an evaporation rate of 1.5 mm hour^{-1} was attained, leading to complete recession of the solution from the top of the 10 mm substrate in under seven hours. Literature shows that a slow substrate-pulling rate leads to deposition of a thinner film of precursor,[107] so the long evaporation time here was presumed to be beneficial to film quality.

3.5.5 Dip-coating on seeded substrates

On a selection of the seeded substrates (see Appendix A.3), the molybdenum precursor was dip-coated by the same method as outlined in Section 3.5.4. The substrates selected for deposition were S1-4 and S11. Those substrates were selected for having been seeded with few-layer MoS_2, as confirmed by SEM, which will be outlined in Section 3.6.

3.5.6 Substrate patterning

Cleaned dice of **[1],** see T23-25, were spin-coated (Brewer Cee® 300X spin-coated) with AZ5214 photoresist (2 drops) at 5000 rpm and backed at 90 ℃. AZ5214 is a positive photoresist, which means that unmasked areas exposed to light during photolithography are depolymerised.

Below is the square array mask viewed under OM. It is easy to see the dimensions of the squares, ~20 μm, and therefore the expected lateral dimensions of the resulting pillars. The inter-square "gap", ~30 μm, is also marked.

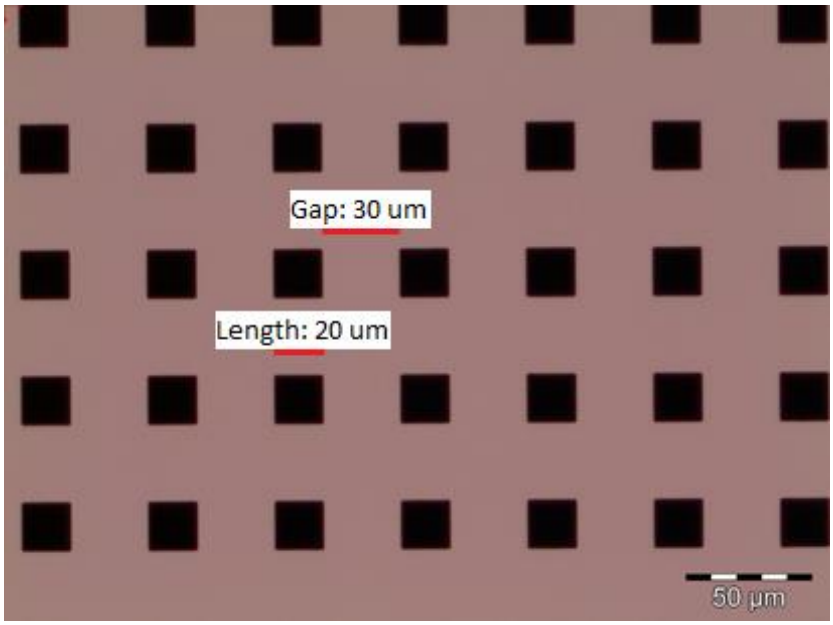

Figure 3.6 *Square array mask for photolithography of pillar pattern*

Optical image of the square array mask used for patterning SiO_2 substrates with pillars to exploit an edge-mediated growth effect. The pillars were patterned using photolithography with dimensions of 20 μm and a separation of 30 μm and then etched by reactive-ion etching.

Each substrate was patterned with the square array using photolithography, and the developed areas of the mask were washed with AZ400K developer to remove photolysed resist.

Reactive ion etching (RIE) was used to etch pillars into the unmasked areas of the substrate surface. The mask was necessary because RIE is a non-selective process. That is to say, etching occurs over the whole exposed surface. The etchant used for RIE was perfluorocyclobutane, C_4F_8 (see Figure 3.7), at a flow rate of 20 sccm. C_4F_8 is commonly used in SiO_2 etching.[112-114, 190] The temperature was maintained at 20 ℃, and the chamber pressure was 20 mT. The inductively-coupled plasma was generated at a power of 1000 W, and the etching power was 100 W.

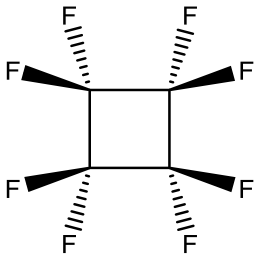

Figure 3.7 *Perfluorocyclobutane, C_4F_8*

This strained, highly-reactive molecule is used as a common etchant in reactive-ion etching of silicon/silicon oxide because it decomposes into radicals and ions, with fluorine plasma performing the etching.

The scheme below shows the expected cross-sectional appearance of the etched pillars.

Scheme 3.2 Patterned substrate (not to scale)

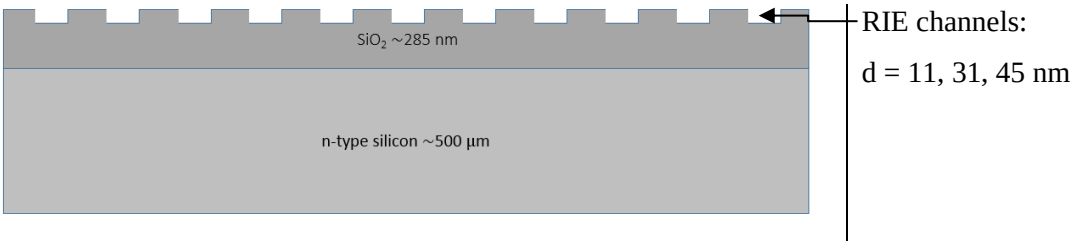

3.5.7 Improving hydrophilicity

The molybdenum-containing precursor is ionic and highly hydrophilic. Improving the hydrophilicity of the substrate could be one route towards achieving better adsorption and hence larger domains. Fresh dice, T35 and T36, were etched by sonication in aqueous KOH (0.2 M) for 30 minutes. T39 and T40 were prepared with an extra cleaning step: 30-min. sonication in water. Dip-coating of the Mo-containing precursor then proceeded by the method in Section 3.5.4.

3.5.8 Dip-coating of CS_2

Samples T41-T43 were prepared by sequential dip-coating of the Mo-containing precursor and the S-containing precursor. This would test the true liquid character of the new liquid ALD method. The Mo-containing precursor was dip-coated as per the optimal conditions in Section 3.5.4, while the volatile CS_2 was gently warmed to 30 ℃ and dip-coated for 20-25 min.

3.5.9 Comparison of substrates

Sapphire substrates T46 and T47 were used for comparison with the SiO_2/Si substrates.

T46 was pre-annealed at 1000 ℃ in Ar (100 sccm). The temperature was ramped up to the target temperature over 2 h then annealing proceeded for 1 h. Thereafter, the temperature was raised to 1100 ℃ in 1 h, followed by 1 h of tempering under the same conditions.[191] The furnace was allowed to cool naturally. T47 was used as received without pre-annealing.

Dip-coating of the Mo-containing precursor then proceeded by the method in Section 3.5.4; briefly, dip-coating at 80 ℃ for 15 mins.

3.5.10 Sulphurisation and annealing

Three annealing regimes were used to sulphurise the Mo precursor (see Scheme 3.3). Different annealing temperatures were tested, and some samples were post-annealed.

a) Precursor-coated substrates were sulphurised with sulphur flakes (CAS number 7704-34-9, purchased from Sigma-Aldrich, purity ≧ 99.99%). The substrates were placed inside a quartz tube within a tube furnace. The quartz tube was placed in the middle of the reaction tube, nearest the thermocouple. The sulphur flakes were placed in a ceramic boat upstream of the substrate container in the cooler part of the reaction tube. The tube furnace was purged in an N_2 atmosphere for 30 min. at a flow rate of 100 sccm. Temperature was ramped up to 600-800 ℃ at 50 ℃ $min.^{-1}$ and maintained for ten min. before natural cooling. Later experiments were performed in Ar atmosphere with a ramp rate of 20 ℃ $min.^{-1}$
b) Precursor-coated substrates were sulphurised with vapour-phase CS_2. Liquid CS_2 was fed into the tube furnace *via* a bubbling system under nitrogen.
c) A third regime involved suspension of the Mo precursor-coated dice in liquid CS_2 for 15 minutes of dip-coating followed by annealing for 1 h at 450 ℃, with a gas flow of 50 sccm Ar and 10 sccm H_2 in trace N_2. This was a liquid ALD in a truer sense as both precursors were introduced in liquid form.

The annealing parameters are outlined in Appendix A.4.

Scheme 3.3 Sulphurisation setup for each annealing regime

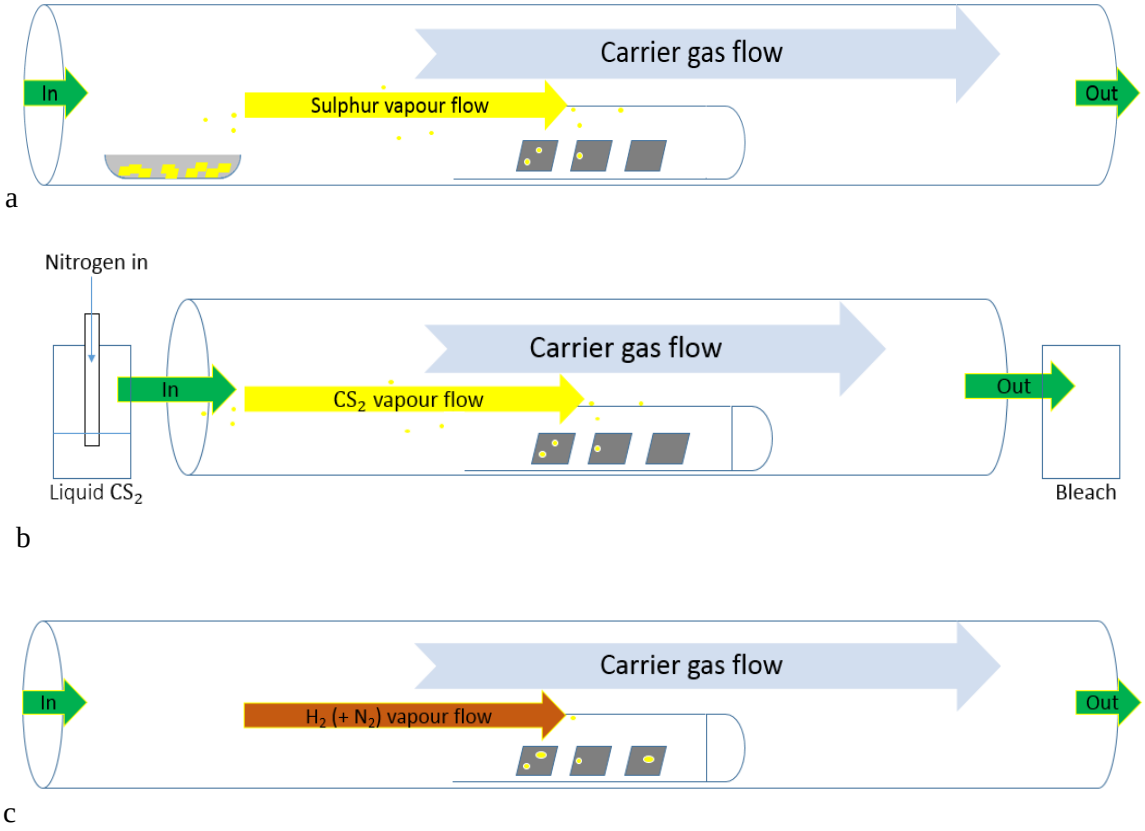

3.5.11 Characterisation

The characterisation of samples annealed in elemental sulphur proceeded as follows.

Regions of interest were identified by optical microscopy using an Olympus DX51 microscope with top-view imaging (DP12 digital camera system). Field-emission SEM (FE-SEM, JEOL FESEM6700x) was used to characterise morphology. Morphological and lateral domain size data obtained by SEM were complemented by thickness measurements from AFM (JPK NanoWizard® NanoOptics) in force modulation mode. Raman microscopy (Renishaw RL532C10 InVia microscope) was used to obtain further domain thickness information with a 532 nm 500 mW excitation source and a grating of 1800 lines/mm. Room-temperature PL spectra and maps were collected (WITEC photon scanning tunnelling microscope) at 532 nm excitation for a quantitative measure of crystal quality. An STEM (FEI Titan 80-300) at an operating voltage of 200 kV was used to visualise the nanostructure of the MoS_2 monolayers.

For SEM, samples were characterised as synthesised, supported on a 35 mm standard sample holder with carbon tape. The material was not coated with conductive film, but silver tape was used where required to reduce charging. Images were acquired in secondary electron imaging mode, at an acceleration voltage of 5.0 kV and working distances of 6.4-8.3 mm. In this mode, charging was low-level and acceptable.

For TEM, samples were prepared on TEM grids by the usual chemical transfer method. The as-synthesised films were cleaned by dipping in 2 M aqueous KOH for 5 min. at room temperature. A thin layer of polymethyl methacrylate with a molecular weight of 950,000 atomic mass units (PMMA-950) was spin-coated onto the samples at 2000 rpm for 30 s. The PMMA-coated films were etched in 2 M aqueous KOH at 75 ℃. The material films detached from the SiO_2/Si substrate after 20 min. The detached PMMA-coated films were collected on TEM grids, and the organic coating was removed by an acetone dip.

The characterisation of samples annealed in CS_2 proceeded as follows.

Samples were characterised Raman spectroscopy and PL. Raman spectroscopy (RL532C10 InVia microscope) was used to obtain thickness information with a 532 nm 500 mW excitation source and a grating of 1800 lines/mm. Room-temperature PL spectra and maps were collected on the same system at 532 nm excitation for a quantitative measure of crystal quality.

XRD was performed on a Rigaku SmartLab x-ray diffractometer, using a Cu Kα x-ray source at 1.54 Å. The 2θ range was 10-70°, and substrate dimensions of 10×10×0.5 mm were selected for sample alignment.

Sapphire-grown samples T46 and T47 were transferred to substrate **[1]** for optical characterisation. The transfer was performed by the usual chemical method. A thin film of PMMA-950 was spin-coated onto the as-prepared sample at 2000 rpm for 30 s. The PMMA-MoS_2 film was etched using 4 M KOH (aq) under gentle heating at 40-50 ℃. This caused the film to detach from the substrate in about 1 h. The film was rinsed with water to remove KOH residue and then transferred to a cleaned SiO_2/Si die. Finally, the PMMA-950 was removed by an overnight acetone dip. Characterisation was performed by OM, Raman and PL.

3.6 Results and discussion

3.6.1 TGA of Mo precursor

The thermal decomposition of the precursor under furnace conditions was used to understand the reaction chemistry during sulphurisation and annealing.

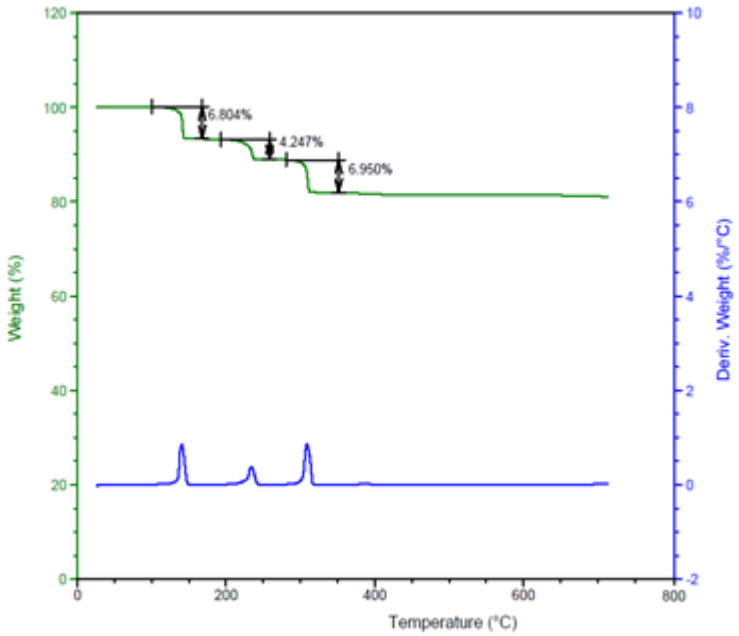

Figure 3.8 *TGA and derivative trace of Mo precursor*

The TGA trace shows a stepped decline in the mass of the Mo precursor starting from around 140 ℃ to 310 ℃. The trace of derivative weight percent with respect to temperature resolves the exact transition temperatures. After a series of NH_3 and H_2O loss steps, the final mass remained constant at 81.2% of the initial, corresponding to the manufacturer's stated base compound percentage of 80-83% MoO_3. TGA helps to understand the reaction mechanism by which MoS_2 is formed from the precursors.

Decomposition proceeds *via* three steps. These steps have been reported previously as loss of ammonia and water vapour and are shown in Scheme 3.4.[192]

In i), the mass loss to 93.2% at 140 ℃ corresponds exactly with ref. [188]. In ii), the mass loss to 88.9% at 230 ℃ corresponds very closely to the report in ref. [188] of 88.7% as a mixture of hexagonal and orthorhombic MoO_3. In iii), the mass loss to 81.9% at 310 ℃ again corresponds very closely to the report in ref. [162] of 81.2% as the metastable hexagonal phase transforms into the thermodynamic orthorhombic phase. The overall decomposition is not accompanied by reduction of molybdenum. The metal centres in ammonium heptamolybdate are in the +6 OS, and so is the metal centre in MoO_3.

Scheme 3.4 Decomposition of ammonium heptamolybdate tetrahydrate

i) 140 ℃: loss of 6.80% mass

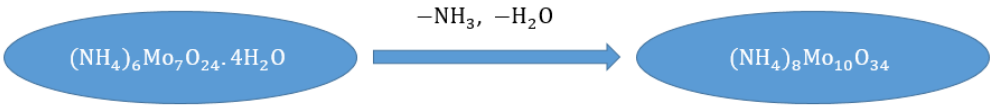

ii) 240 ℃: loss of 4.25% mass

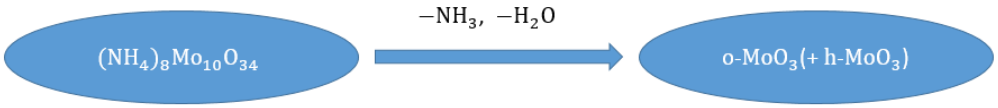

iii) 310 ℃: loss of 6.95% mass

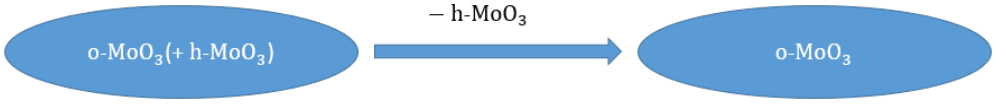

The product of thermal decomposition is orthorhombic MoO_3, a phase that is stable up to ~800 ℃. This is instructive for the sulphurisation step. Sulphur evaporates at 445 ℃, so under the temperature of the central heating zone of the reaction tube, sulphur vapour passes over the o-MoO_3 phase, and the overall reaction proceeds as in Equation 3.2:[193]

$$2\ MoO_3 + 7\ S \rightarrow 2\ MoS_2 + 3\ SO_2 \qquad [3.2]$$

Not shown in the figure is the behaviour of the precursor between 750 and 800 ℃. In this range of temperatures, a large drop in percentage mass was observed corresponding to thermal decomposition of the precursor. This was not depicted, in order to focus on the important mass-loss steps at lower temperatures. Nevertheless, it should be borne in mind during discussion of the sulphurisation parameters that o-MoO_3 was stable to thermal decomposition between 310 ℃ and 800 ℃.

3.6.2 Growth on seeded substrates

FESEM of seeds S1 and S3 were obtained to confirm that monolayer seeds had been deposited. Although other characterisation techniques are instructive, they were not available at the time of the experiments. Figure 3.9 and 3.10 show the SEM images obtained.

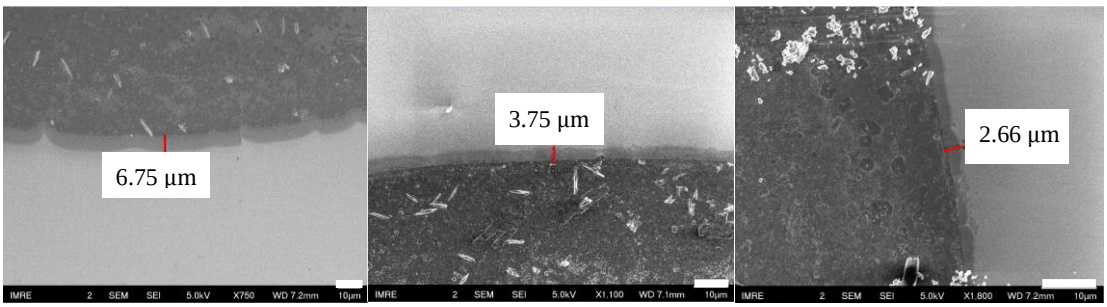

Figure 3.9 *Regions of S1 under different SEM magnifications; scale bars = 10 µm*

These images show an SiO_2 substrate with drop-casted MoS_2 seed via method (a) at 70 ℃. Note the stepped change in contrast at the edges of the seed crystal, possibly indicative of a bulk seed (dark region) tapering to thin edge layers (marked in red) varying in width from 2.66 to 6.75 µm.

The SEM images in Figure 3.9 show the seed "droplet" as dark patches presenting the greatest contrast against the grey substrate surface. However, at the very edge of the dark patches, there was a noticeable boundary region that presented a medium contrast against the substrate surface. The width of this boundary region varied from 2.66 µm to 6.75 µm. On the evidence of contrast variation, this region was presumed to be thinner than the inner regions of the seed droplet.

Figure 3.10, an SEM image of the seed crystal deposited on the room-temperature substrate, shows that a thin layer of seed was not present in this case. Again, the dark patch is the seed droplet, and the brighter region is the substrate. The absence of any region presenting a medium contrast against the substrate surface points to the lack of a thin boundary region.

The SEM images were consistent the expectation that at room temperature, drop-casting is an ineffective method for obtaining monolayer seed crystals. It is possible that at 70 ℃, the more rapid evaporation of the solvent helped to prevent agglomeration of the monolayers in the solution, which occurs when those layers settle over each other as the size of the drop-cast bubble decreases by evaporation. Nevertheless, it is extremely difficult to confirm the presence of monolayer seed crystals with SEM only. To be sure, Raman spectroscopy and AFM would be ideal characterisation techniques, but they were unavailable at the time of these experiments.

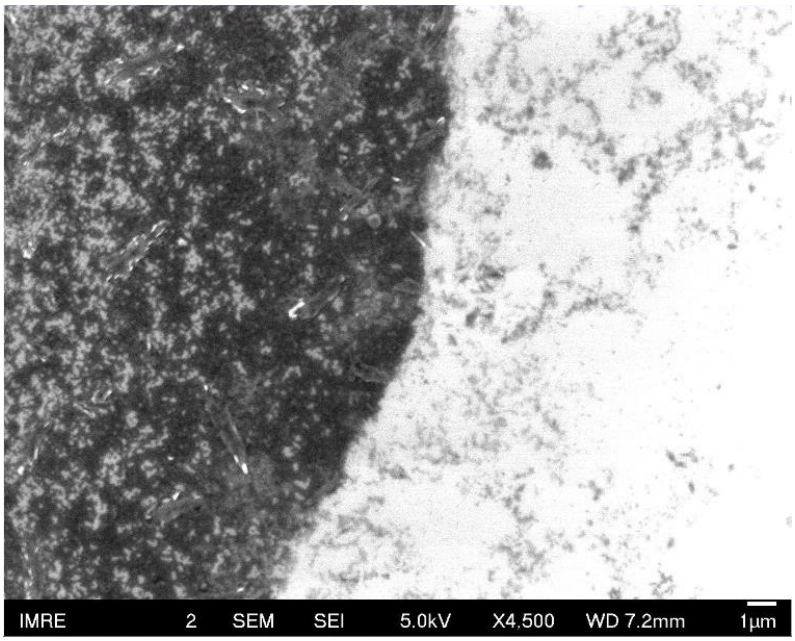

Figure 3.10 *Representative region of S3 under SEM magnification*

Image showing SiO_2 with drop-casted MoS_2 seed via method (a) at room temperature. Note there is no stepped change in contrast at the edge of the seed crystal (dark), so the potential thin seed layer at the edge did not exist in the room-temperature sample. This difference suggested a key temperature-related effect on seeding effectiveness.

In liquid exfoliation studies, where deposition of a droplet of solution onto a substrate for characterisation needs to be finely controlled in order to prevent agglomeration of monolayers, there is a well-known rule-of-thumb that the surface temperature of the substrate be 1.5 times the boiling point of the solvent.[194] This is an experimentally-determined route to rapidly evaporating the solvent before agglomeration can occur. Liquid exfoliation could be instructive in this case, suggesting that the surface temperature of the substrate even at 70 ℃, well below the boiling point of water, was too low to prevent agglomeration.

All four samples were observed under SEM after sulphurisation. Literature shows that high-quality conformal growth of MoS_2 from CVD and ALD results in micron-scale, triangular-faceted crystals.[150, 152, 173] In the SEM images (Figures 3.11-3.14), there was no evidence of these crystals, consistent with the conclusion that high-quality monolayers were not formed.

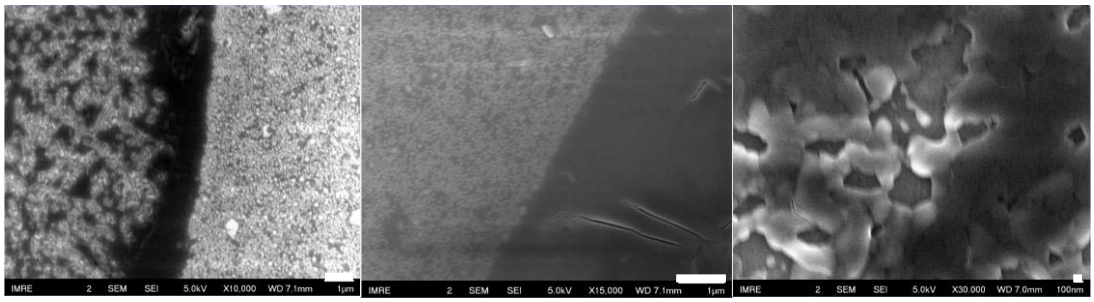

Figure 3.11 *Selected SEM images of regions of material on S1*

This sample was produced by growth of MoS_2 around an MoS_2 seed crystal deposited by drop-casting on the substrate 70 ℃. There was evidence of MoS_2 growth on this seeded substrate, judging by the abrupt changes in contrast in different regions of the substrate, which clearly differs from the clean substrate observed pre-growth in Figure 3.9. However, the nature or morphology of the material was unclear. There was no evidence of triangular-faceted single crystals in these SEM images. Scale bars (left to right):1 μm, 1 μm, 100 nm.

In Figure 3.21, there was evidence of random deposition of material.

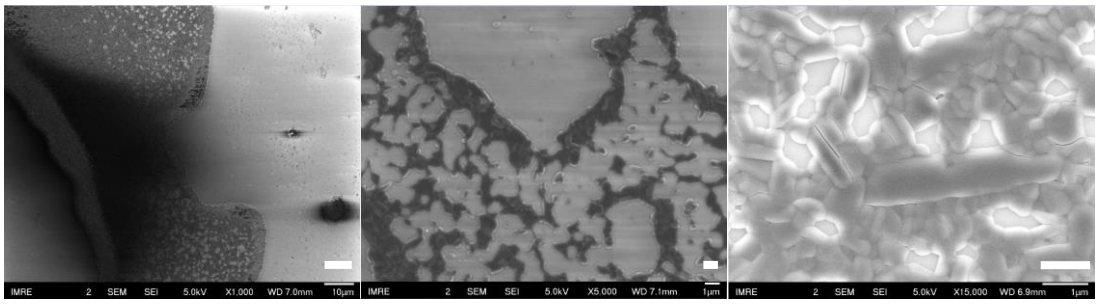

Figure 3.12 *Selected SEM images of regions of material on S2*

This sample was also produced by growth of MoS_2 around an MoS_2 seed crystal deposited by drop-casting on the substrate 70 ℃. Selected SEM images of regions of material on S2 show evidence of growth, but not of micron-scale triangles. In both this figure and the previous, growth appeared to occur at random sites on the substrate rather than at the seed crystal edges. Scale bars (left to right):10 μm, 1 μm, 1 μm.

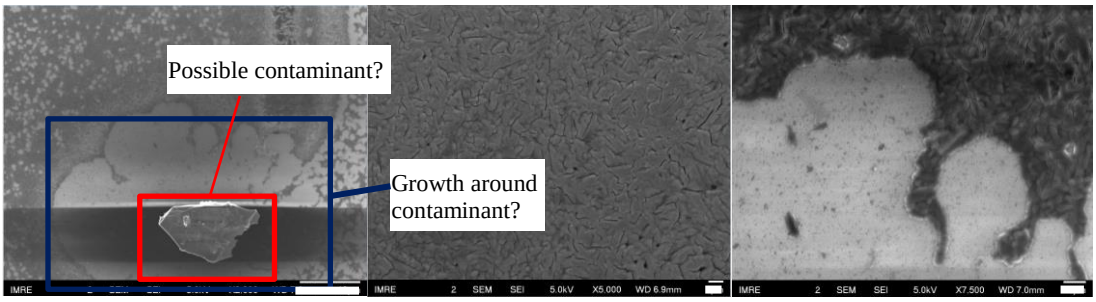

Figure 3.13 *Selected SEM images of regions of material on S3*

Selected SEM images of regions of material on S3. There was evidence of growth, particularly around a suspected contaminant. There was no visible difference in surface morphology between this sample and the previous two. Scale bars (left to right): 1 μm, 1 μm, 100 nm.

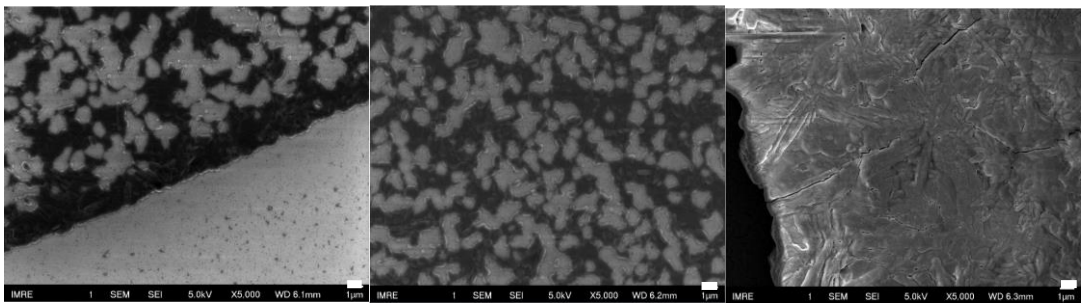

Figure 3.14 *Selected SEM images of regions of material on S4*

There was evidence of growth, and some of the resulting regions had different morphologies and likely thicknesses, as seen from contrast differences, but the nature of these is unclear without further investigation. It is unlikely that monolayers were deposited. Scale bars: 1 μm.

A significant problem was encountered in precursor deposition from aqueous solution. The Mo precursor adsorbed preferentially at apparently random sites on the substrate rather than in the intended sites around the seed crystals, particularly on S11 where the seed was dispersed around the substrate rather than in a single drop. The possible reasons for this are explained below:

(1) There was an energy mismatch between the precursor and the seed crystal. This could conceivably arise from the fact that the seed crystal is MoS_2 while the precursor is ammonium molybdate. And in that case, there are two possible solutions. Firstly, the seed crystal itself could be changed to ammonium molybdate. This would virtually eliminate an energy mismatch. A seed crystal of ammonium molybdate could be applied to the substrate using some epoxy, and the precursor then grown around it.

(2) Poor solvent-matching. The Mo precursor is hydrophilic, but the MoS_2 seed is hydrophobic. There is a repulsive interaction between the precursor solution and the seed crystal, greatly reducing the chances of deposition around the seed. The solution to this is

to use a less-polar solvent. MoS_2 is soluble in ethanol, but ammonium molybdate is insoluble in all alcohols, and only sparingly so in acetone. MoS_2 is soluble in a mixed solvent of 50% v/v ethanol/water. Due to lack of availability of ethanol, acetone was chosen in the first instance.

3.6.3 Growth on bare substrates

Optical micrographs as shown in Figure 3.15 demonstrate that regions of millimetre coverage of MoS_2 could be grown on bare dice from 0.13 g mL^{-1} aqueous solutions of ammonium molybdate in as little as 15 minutes by dip-coating followed by ten minutes of annealing, as evidenced by the triangular-faceted morphology that is well-known in CVD-type syntheses of 2D sulphides.

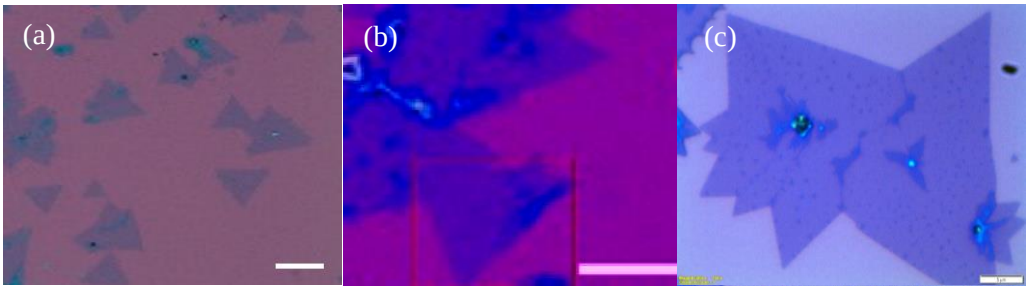

Figure 3.15 *Optical micrographs of MoS_2 grown from optimal dip-coating conditions.*

The triangular-and complex-faceted morphology was evidence of single crystals arising from initial dip-coating of the Mo-containing precursor from aqueous solution at 80 °C, the optimum dip-coating temperature of all the conditions explored in this study. In ***(a)*** *and* ***(b)****, standalone triangular-faceted can be seen. In* ***(c)****, the complex morphology is seen where several small crystallites grew into each other. Also visible in each image are the high-contrast nucleation centres at the centre of each crystal. Note that contrast was enhanced in post-processing using ImageJ to bring out the crystals, because the natural contrast of monolayers against the substrate is low. Scale bars (left to right) = 100 µm, 100 µm, 5 µm.*

Increasing the concentration up to 0.20 g mL^{-1} yielded mostly bulk and few-layer films, so dilute precursor solutions are preferable. This is attributed to nucleation density effects, and it is presumed, therefore, that there is a theoretical optimum concentration at which the nucleation density of incipient MoS_2 yields a modal coverage of monolayers.

Water was the best solvent because the precursor has the best solubility therein. Acetone and ethanol-water mixtures are poorer solvents for ammonium molybdate. The surface coverage was very poor when solvents other than water were used (see Figure 3.16), and this is attributed to poor nucleation density caused ultimately by poor dissolution of the ammonium molybdate in acetone or aqueous ethanol.

A selection of some 80 domains were sampled from six regions of growth to give a representative lateral size distribution of domain sizes (see Figure 3.17) estimated from OM. The size distribution was obtained after sulphurisation of two good samples dip-coated at 80 ℃, and confirms that large domains were obtained by this method, with a modal range of 15-50 μm and several single crystals exceeding 50 μm.

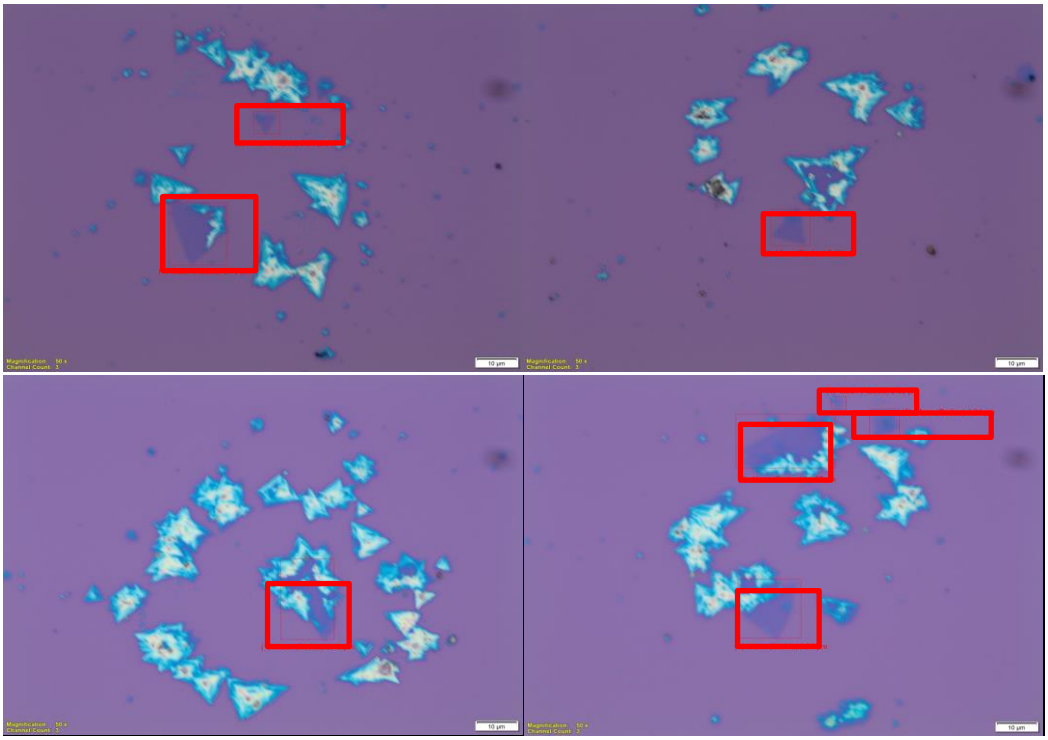

Figure 3.16 *Optical micrographs of MoS_2 grown from sub-optimal dip-coating conditions*

These images, from samples on which the Mo-containing precursor was dip-coated from acetone solution, clearly show poor surface coverage and low monolayer coverage as a proportion of total coverage. This was in evidence from the variation in contrast against the substrate surface, with thicker regions appearing brighter. Monolayer regions are highlighted as regions of low contrast in red boxes. Scale bars = 10 μm.

The largest crystals had diameters of ~100 μm and provided evidence of large-scale growth of the kind that has previously been achieved by traditional CVD, such as in the study by Jeon *et al.* (~120 μm).[151]

At deposition temperatures below 50 ℃ and above 80 ℃, the precursor did not sufficiently cover the substrate. This resulted in poor sulphurisation and a lack of good-quality domains. Near the water boiling point, it is possible that the kinetic energy of precursor molecules was greater than the adsorption energy at temperatures near the water boiling point leading to desorption. There may also be a complementary effect from re-dissolution of the precursor at elevated temperature.

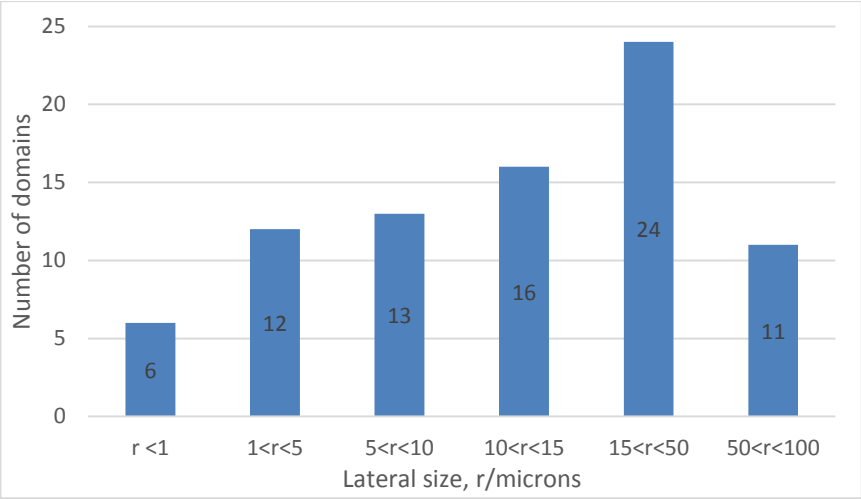

Figure 3.17 *Representative lateral size distribution of MoS_2 domains*

This was obtained by counting domains under a microscope. The samples used for this were grown by dip-coating 0.13 g L^{-1} of Mo precursor at 80 ℃, followed by ten minutes annealing in elemental sulphur at 800 ℃. Across these substrates, six regions of growth were sampled, giving a modal range of 15-50 μm (24 domains) with several crystals exceeding 100 μm (11 domains).

Field emission(FE)-SEM and AFM images, as shown in Figures 3.18 and 3.19, reveal straight-edged triangular-faceted morphology, as well as more complex geometries such as "hourglass" and "kite". These morphologies are consistent with previous reports of single crystals.[150, 154, 173, 195, 196]

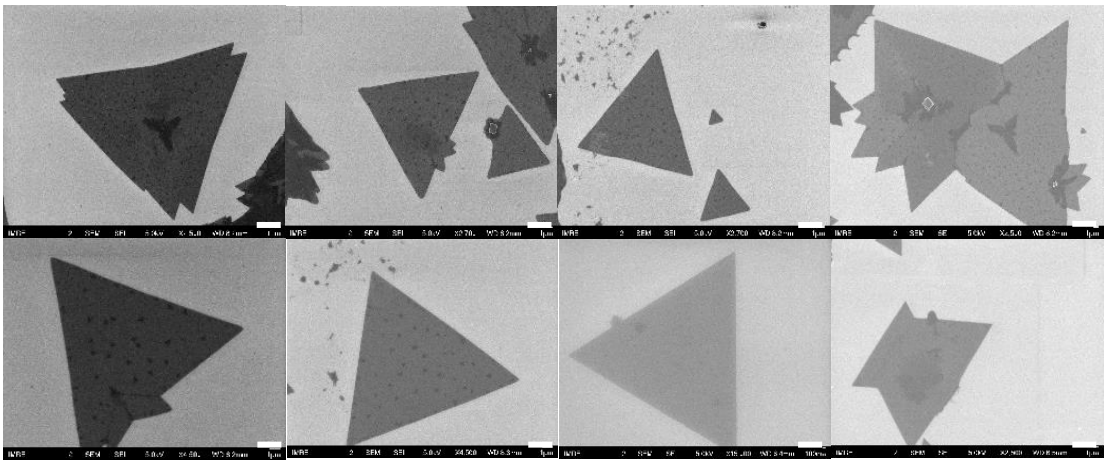

Figure 3.18 *FE-SEM images of MoS_2 single crystals; scale bars = 1 μm*

In these FE-SEM images obtained from the same samples described in Figure 3.17, the morphology of MoS_2 domains was quite clearly discernible. The triangular-faceted morphology is consistent with typical single crystals, and so too are the more complex "butterfly" and "kite" morphologies.

The straight-edged morphology exhibited by all of the crystals indicates that Mo-terminated single domains were synthesised by this method (S-rich conditions result in Mo-limited kinetics), while S-terminated crystals would be indicated by curved edges.[150, 196]

Layer thicknesses of 0.6-2.5 nm could be determined by AFM line profiling, which is consistent with 1-4L growth.[151, 153, 173] The image processing was performed on Gwyddion software.

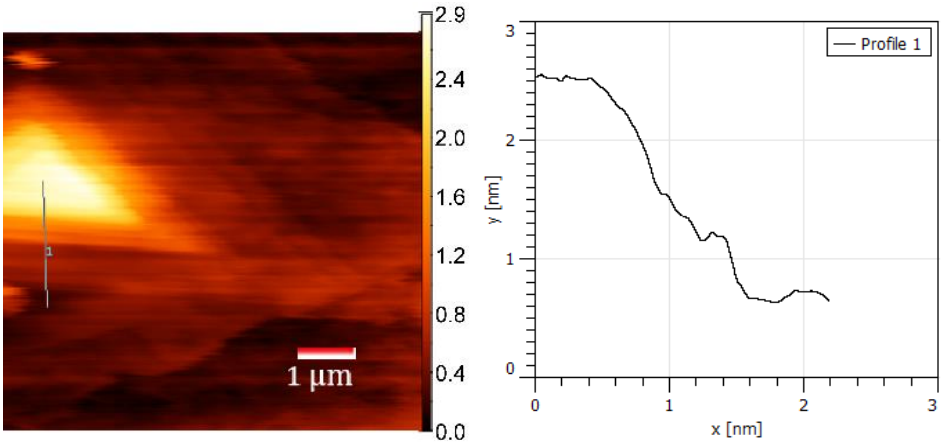

Figure 3.19 *False-colour AFM image and corresponding line profile*

In the image, acquired from a sample grown with 40 ℃ dip-coating, colour intensity corresponds to thickness. The line profile corresponding to line "1" in the image shows thickness decreasing from ~2.5 nm to ~0.6 nm, with a small plateau around ~1.2 nm. These thicknesses correspond to 4L, 2L and 1L respectively. The line profile is in agreement with the AFM image, as line "1" passes through regions of varying intensity indicating thickness.

The AFM image was acquired from a region of sub-optimal growth (note the small grain size), and this was chosen deliberately to demonstrate the propensity of this technique to produce few- and monolayer grains even when conditions are not optimised. Overall, the success of this simple growth method without pretreatment of the substrate or a nucleation promoter was a notable improvement on previous reports.[152, 158, 159, 175]

A clear relationship between dip-coating temperature and lateral grain size was observed. The largest crystals (r_{max}~100 µm) were grown by 80 ℃ dip-coating. At 70 ℃, crystals were much smaller (r_{max}~20 µm). At 50-60 ℃, crystals were smaller still with most crystals being sub-10 µm in dieter. The trend could be attributable to poorer precursor adsorption at lower temperatures.

These results suggest that dip-coating temperature was the key parameter in lateral domain size control, with a smaller contribution from dip-coating time, and that layer thickness was dependent on precursor solution concentration.

A previous report indicated a trade-off between the lateral and vertical diffusion rates of sulphur vapour over and into the precursor.[155] At low temperature, the rate of mass diffusion of sulphur

vapour over the sample exceeds the rate of mass diffusion into the precursor, which results in poor coverage. This situation is reversed at high temperature such that coverage is improved but films are bulk in nature. However, other authors have found no correlation between synthesis temperature and sample quality.[160] In this work, optimal sulphurisation parameters were ten minutes of annealing at 800 ℃ under nitrogen (100 sccm) with 1600 mg sulphur flakes. In contrast, 600 ℃ sulphurisation yielded poorer coverage and morphology. The work of van der Zande *et al.* showed that T<700℃ leads to incomplete reduction of MoO_3 due to the low electron affinity of sulphur.[150] This implies that increasing thermal energy ought to be beneficial for the reduction process, other chemical effects notwithstanding. Thus, the TGA of the precursor (see Section 3.6.1) indicated that 800 ℃ was likely to be the highest possible sulphurisation temperature.

There are two phases of 1L-MoS_2: the semiconducting 2H phase, which has a direct bandgap, and the metallic 1T phase. These two phases can be distinguished by Raman spectroscopy and PL. Only the 2H phase, being semiconducting, exhibits PL. The metallic phase, which by definition does not have a bandgap, cannot obviously exhibit PL. The presence of strong PL as in Figure 3.21 is therefore indicative of good-quality, phase-pure material.

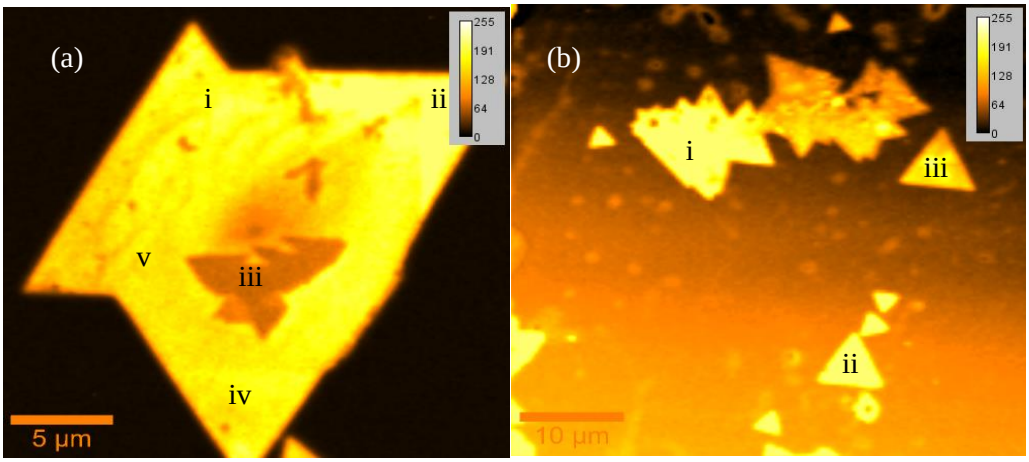

Figure 3.20 *PL maps acquired from two regions with good-quality monolayers*

These maps were acquired at 532 nm excitation from those samples grown at conditions subsequently determined to be the optimum for crystal size and quality, that is to say, dip-coating for 15 minutes at 80 ℃ from 0.13 g L^{-1} aqueous Mo precursor solution and sulphurisation in N_2 at 800 ℃ *for ten minutes. The maps show monolayer regions corresponding to the brightest parts of the images, as proven by Raman spectroscopy.*

PL maps in Figures 3.20 reveal mono/few-layer domains adopting the (2)H phase. This is corroborated by Raman peaks (see Figure 3.21) consistent with production of the H phase. Variation of PL intensity across a single domain can also be probed by Raman spectroscopy.

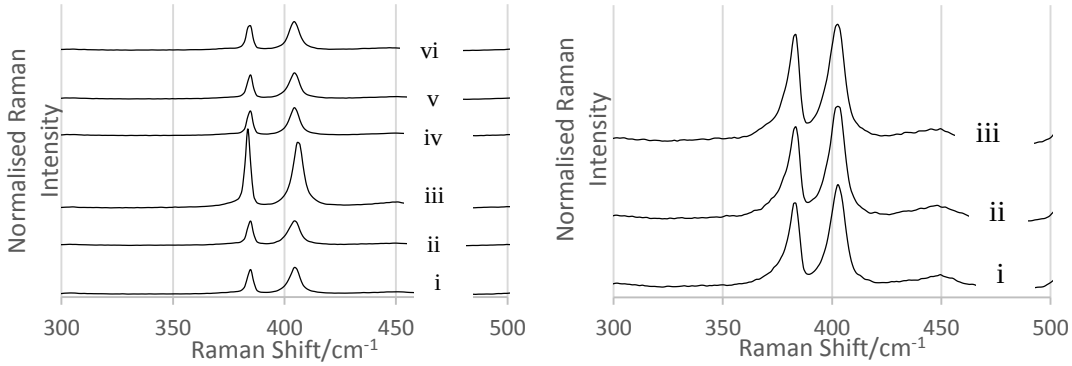

Figure 3.21 *Raman spectrum of each labelled point on the PL maps*

The spectrum on the left shows peaks corresponding to domain 3.20(a) and on the spectrum on the right shows the peaks corresponding to domain 3.20(b). The peaks were normalised to laser power to allow them to be plotted on the same graphs. The E_{2g} and A_{1g} characteristic peaks of MoS_2 were present at ~385 and ~405 cm^{-1}.

The H phase possesses a hexagonal lattice, and exhibits the two characteristic Raman modes of MoS_2: the in-plane E_{2g} and the out-of-plane A_{1g}, at ~382 cm^{-1} and ~407 cm^{-1} respectively.[151-153, 160, 189] The 1T phase possesses a tetragonal lattice and exhibits the same Raman modes, along with an additional intense mode at ~335 cm^{-1} that is forbidden in the 1H phase.[18] 1H is the thermodynamic phase, while 1T is metastable. Therefore, it is expected that any 1T-MoS_2 synthesised in the sulphurisation process was converted to 1H-MoS_2 during annealing. This is confirmed by the absence of a peak at 335 cm^{-1} in the Raman spectra (Figure 3.21).

The observed Raman shifts exhibit a well-known layer dependence. Specifically, CVD-synthesised MoS_2 monolayers on SiO_2/Si typically exhibit the characteristic vibrational modes with $\Delta\bar{\upsilon}$ around 19.0-20.5 cm^{-1}.[151-153, 160, 189] This was the range observed for most regions sampled across the domains in Figure 3.21 (see Table 3.2). The Raman spectrum of point iii suggested a layer thickness of 2-3L, and this could be due to overlayer growth. The thickness was corroborated by a drop in PL intensity at that point. Variation between $\Delta\bar{\upsilon}$ of the other, discrete monolayer domains is attributed to strain-related effects.[186, 197] Thermal diffusion also has a role in the shifting of vibrational energy,[198] and for this reason laser power was controlled at 10% of maximum output. Generally, characteristic peak separation increases with layer thickness up to the 5L limit; bulk MoS_2 exhibits $\Delta\bar{\upsilon} \geq 25.0$ cm^{-1}.

Important information about material quality is obtained from the ratio of peak intensities, I_A/I_E, between the A_{1g} and E_{2g} modes.[199] Cases in which $(I_A/I_E) < 1$, as shown in Table 3.2, indicate doping of the material, and this likely comes from oxide impurities relating to the substrate. This can explain the reduction in PL intensity across different monolayer regions of domains in Figures 3.20(a) and 3.20(b). Another possible explanation is the existence of grain boundaries, which are

known to quench PL by up to 50%.[148] With the exception of point iii, the domains sampled show good uniformity.

Table 3.2 Key Raman data acquired from domains in Figure 3.20

Figure 3.20(a)					
Region	$\mathbf{E_{2g}/cm^{-1}}$	$\mathbf{A_{1g}/cm^{-1}}$	$\mathbf{\Delta\bar{\upsilon}/cm^{-1}}$	**Layer thickness**	$\mathbf{\frac{I_A}{I_E}}$
i	384.9	404.3	19.4	1L	1.08
ii	384.9	404.3	19.4	1L	1.17
iii	383.6	405.6	22.0	2-3L	0.83
iv	384.9	404.3	19.4	1L	1.13
v	384.9	404.3	19.4	1L	1.08
vi	384.9	404.3	19.4	1L	1.01
Figure 3.20(b)					
Region	$\mathbf{E_{2g}/cm^{-1}}$	$\mathbf{A_{1g}/cm^{-1}}$	$\mathbf{\Delta\bar{\upsilon}/cm^{-1}}$	**Layer thickness**	$\mathbf{\frac{I_A}{I_E}}$
i	385.0	404.2	19.2	1L	1.08
ii	385.0	404.1	19.1	1L	1.10
iii	385.0	404.1	19.1	1L	1.05

Figure 3.22 shows representative PL spectra from MoS_2 regions of different thickness, including points ii and iii. A-exciton emission in the 1L case (blue) represents a greater than tenfold improvement in intensity over the 3L peak (red), and a threefold improvement over the 2L (green) peak. This observation of good-quality PL attested to the high crystallinity of the monolayer film and also suggested that the synthetic method incorporating aqueous dip-coating mitigated the incorporation of carbon impurities.

The monolayer spectrum in Figure 3.22 shows the A-exciton – which arises from the direct bandgap at the κ-point – at 665 nm (1.86 eV), and the weaker B-exciton is also well-resolved at 620 nm (2.00 eV). The latter peak arises from the κ-point band splitting due to the valence band spin—orbit coupling.[7] The splitting between the A- and B-excitons in the as-prepared monolayers was ~140 meV, which is in excellent agreement with the theoretical value (148 meV) for MoS_2 film.[200]

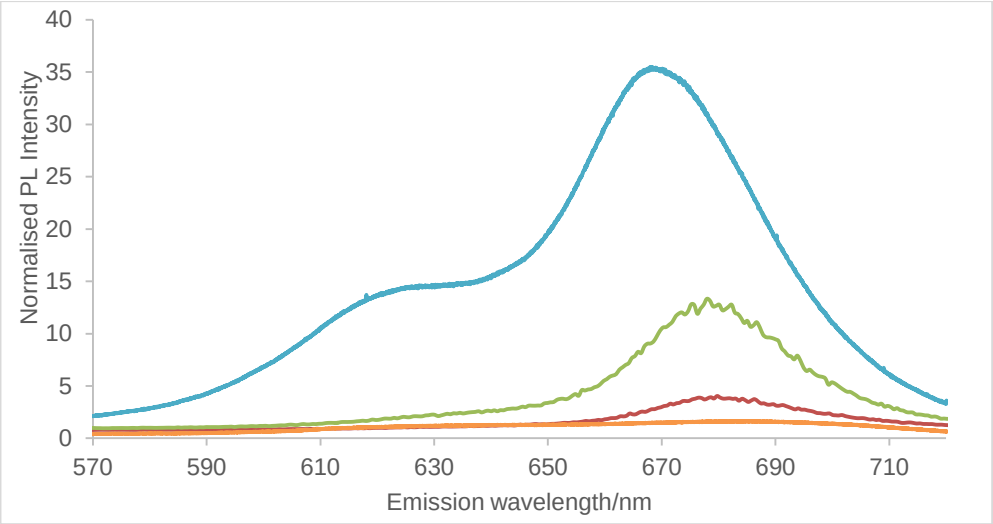

Figure 3.22 *Normalised PL spectra from different layer thicknesses of MoS_2*

PL spectra from regions of different thickness acquired at 532 nm excitation, normalised to laser power; (blue) intense peak at 668 nm corresponds to A-exciton emission at 1.86 eV in the ML limit; (green) redshift of the peak to 677 nm observed in the 2L limit along with large decrease in intensity; (red) further redshift in 3L limit yields weak emission at 680 nm; (orange) negligible PL in the bulk (>5L) limit.

The greater than tenfold improvement in intensity in the monolayer compared to the trilayer (35 against three), and threefold compared to the bilayer (36 against 12), is a feature of the gradual bandgap transition from indirect to direct. Another feature of this transition is the blueshift in emission energy with decreasing layer thickness, indicating that the band transition from an indirect gap of 1.29 eV to a direct gap of 1.86 eV is a gradual, incremental process.[201]

Previous reports show that 1L A-exciton intensity in mechanically-exfoliated samples is some 40% greater than 2L-PL intensity, and the obtained PL data are comparable to that.[7] These obtained data also compared well to the CVD results from the literature. For instance, Jeon *et al*. obtained roughly a fourfold improvement in 1L-PL intensity over the 2L condition.[151] The A-exciton energy at ~665 nm (1.86 eV) agrees with previous reports of monolayer MoS_2 PL emission.[4, 7, 10, 18, 38, 44, 45] The weaker B-exciton is also well-resolved in the monolayer on SiO_2 at ~620 nm (~2.00 eV) and is strong evidence for the excellent crystallinity of the as-prepared material.[200]

TEM provided further confirmation of crystalline monolayer formation (Figure 3.24). Fast Fourier transform (FFT) patterns confirm the hexagonal crystal structure of the material, complementing the Raman and PL data that show the 1H phase was synthesised.

The TEM images in Figures 3.23(a) and 3.23(b) show that defect-free crystalline structure was achieved over several nanometres, which is comparable to results obtained from CVD.[151, 152] The

diffraction patterns in FFT (insets) correspond to the (100) and (110) lattice planes of hexagonal MoS_2.[151, 162]

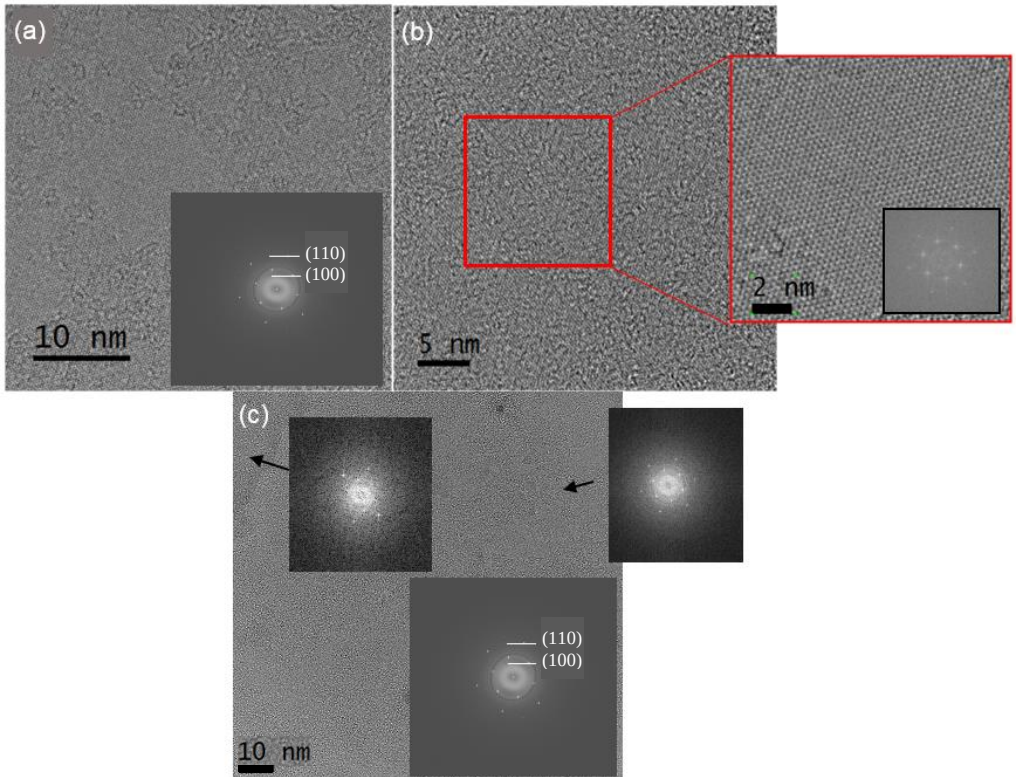

Figure 3.23 *TEM and FFT images of as-synthesised MoS_2*

(a) *A region exhibiting 1H phase purity, as confirmed by FFT (inset).* ***(b)*** *Magnification (red box) and FFT (inset) of crystalline region clearly show the hexagonal lattice pattern, consistent with 2H-MoS_2.* ***(c)*** *TEM image and FFT data (insets) from either side of a grain boundary in a large crystal. FFT of the entire region also shown (inset, bottom right). The author is grateful to Henry Medina and Weng Tjiu for assistance in obtaining these images.*

The interplanar d-spacings (Figure 3.24) between neighbouring planes were calculated to be d_{100} = 0.27 nm and d_{110} = 0.16 nm, which are in exact agreement with the reported spacings for hexagonal MoS_2.[162] Repeating the procedure over several more regions will be a way of demonstrating the reliability of these values.

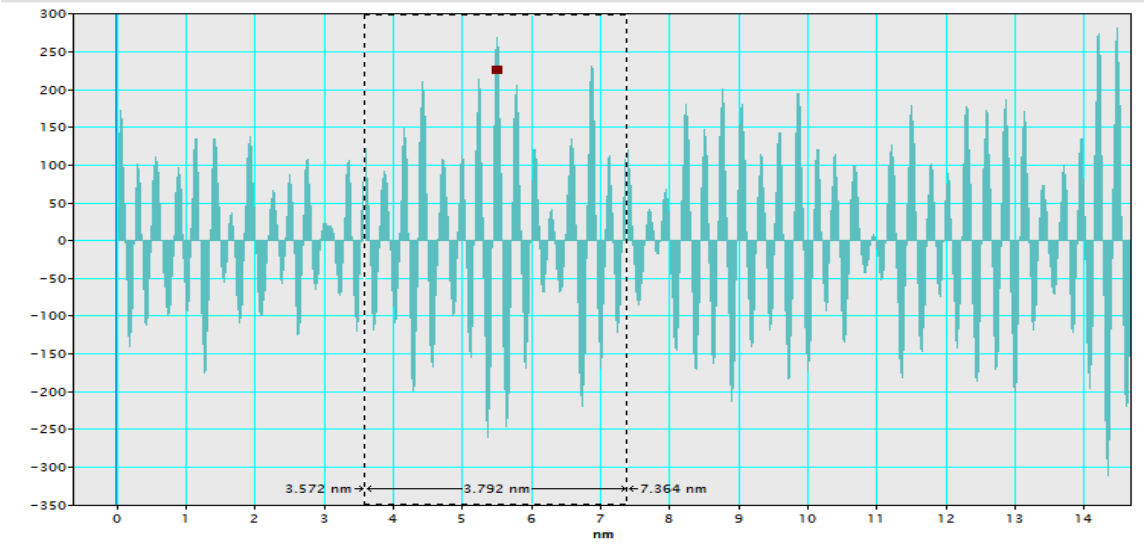

Figure 3.24 *Line profile of lattice planes observed by TEM*

A line profile obtained from an inverse FFT of TEM image 3.24(c) was used to calculate interplanar d-spacings in a lattice, using the difference between peaks. Full calculation of d-spacings is provided in Appendix A.5.

FFT was performed across an image of a grain boundary of a 100 μm complex-faceted crystal to determine its uniformity, as shown in Figure 3.23(c). Previous reports suggest that the butterfly, hourglass and kite morphologies can result from single crystal growth of 2D materials. FFT taken from small regions on either side of the grain boundary were compared to the FFT of the whole 100×100 nm region. The three patterns show the same set of six-fold-symmetrical diffraction points. Taken together, these patterns are consistent with single-crystalline monolayer growth.[152, 173] That supports previous reports of the complex morphologies of single crystals. This knowledge combined with OM and SEM images suggests that single crystals with lateral size up to 100 μm and area up to 5,000 μm^2 were synthesised by this method.

There was evidence of growth at the substrate edges, as shown in Figure 3.25. One might expect edge effects when using epitaxial substrates because of the decrease in nucleation energy at dislocations in the substrate's crystal structure or at a seed edge,[202, 203] but SiO_2 is amorphous. In a recent paper, Lee *et al.* proposed that the nucleation density at edges is lower than that at "inland" regions of the substrate, which favours growth of larger films, and this is a noticeable effect on the SiO_2 surface.[204] This could be one possible explanation for the edge effects at amorphous substrate edges. This edge-mediated growth provided the motivation for formulating patterned substrates because creating these edges was thought to limit the local nucleation density.

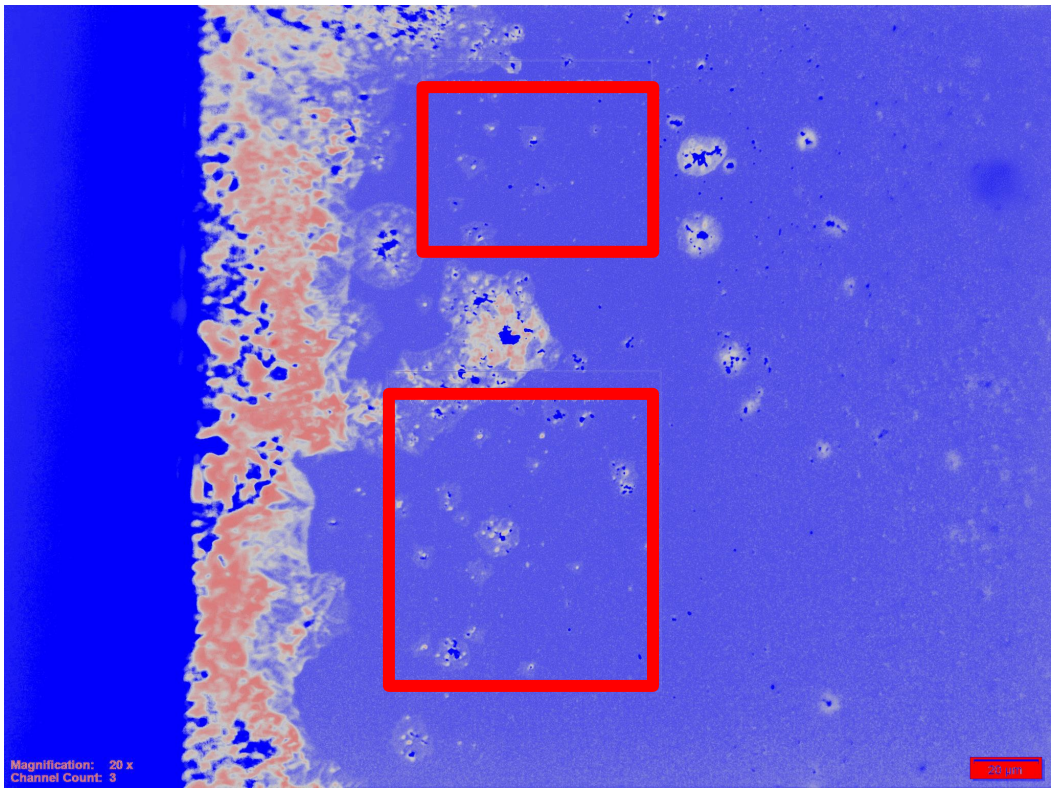

Figure 3.25 *MoS_2 growth at SiO_2 edge; scale bar: 20 µm*

The increase in material density at the edge of the substrate was clearly visible from differences in optical contrast. The red boxes indicate the more typical density of materials expected at inland regions. This sample was synthesised from dip-coating of 0.13 g mL^{-1} aqueous solution at 70 °C.

The nucleation density is evidently lower at lower concentrations. Lee's argument that lower nucleation density favours monolayer growth is one possible explanation of the consistent observation both in the literature and in this project that lower concentrations of the Mo precursor solution favoured monolayer growth.[107, 175] Furthermore, the growth of overlayers on top of the polycrystalline monolayer film in Figure 3.15(c) could be attributed to the edge effect, as these layers appear to have grown entirely along the crystalline defect at the grain boundary.

3.6.4 Growth on patterned substrates

In light of the results presented in the previous section, patterned substrates were fabricated with arrays of pillars of varying heights. The intention was to create many hundreds of "edges" in order to facilitate adsorption of the precursor.

Evidence of successful etching of pillars comes from OM and optical profilometry. Below is an OM image showing the 45 nm pillars after etching.

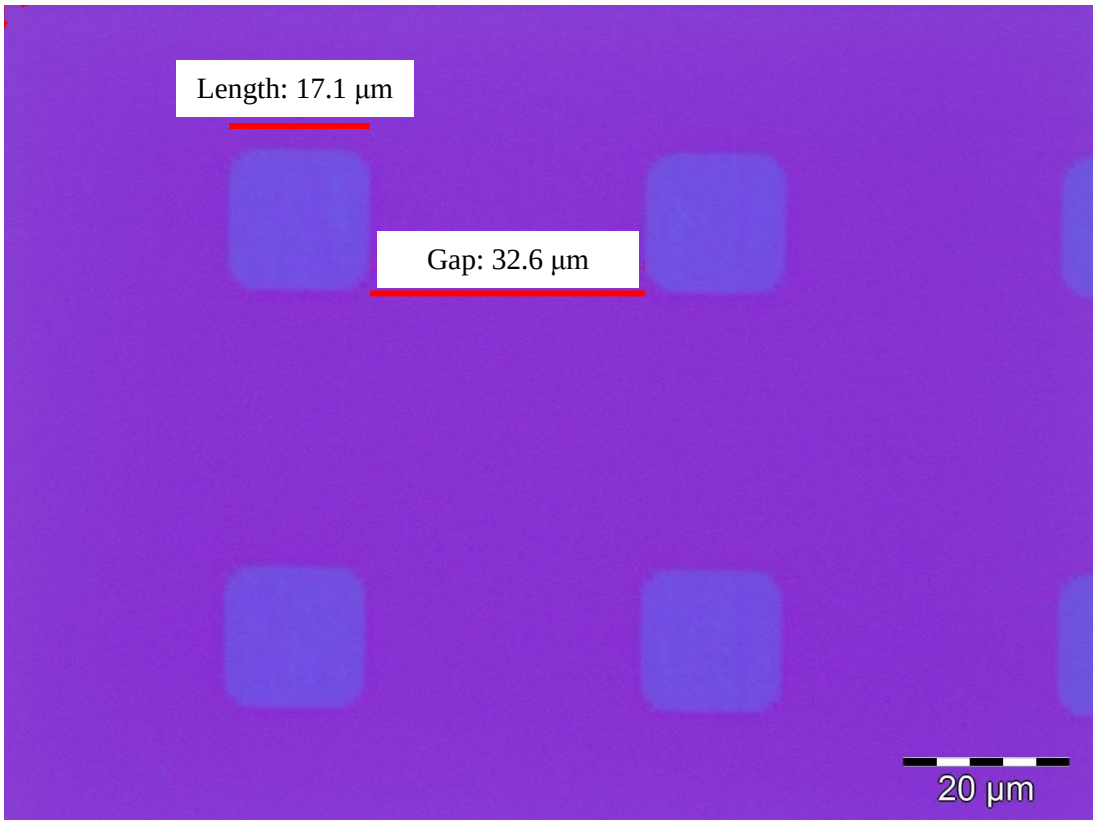

Figure 3.26 *OM image of patterned 45 nm pillars on SiO_2*

Many hundreds of "edges" were created by reactive-ion etching of photolithography-patterned pillars. The mask dimensions were 20 µm length and 30 µm separation. The OM images show a plan view of the patterned substrate post-etching, pillar surfaces visible as blue squares against the darker substrate surface.

Comparing the etched pattern to the square array mask (Figure 3.6), one sees clearly that the pillars were patterned at the points corresponding to the squares in the mask. The patterned pillars had somewhat rounded vertices while the mask had straight-edged squares with sharp vertices. The difference arises because the patterning is diffraction-limited to 2 µm. The diffraction limit means that sharp features cannot be patterned. For that, a higher-resolution technique such as electron-beam lithography would be required. However, this observation is redundant as the morphology of the patterns should not have presented an issue for the subsequent results.

Depth profiles of the patterned pillars were obtained using a stylus-controlled step profiler. The 10 nm pillars were obtained with 2 s etching and the 45 nm pillars with 15 s etching.

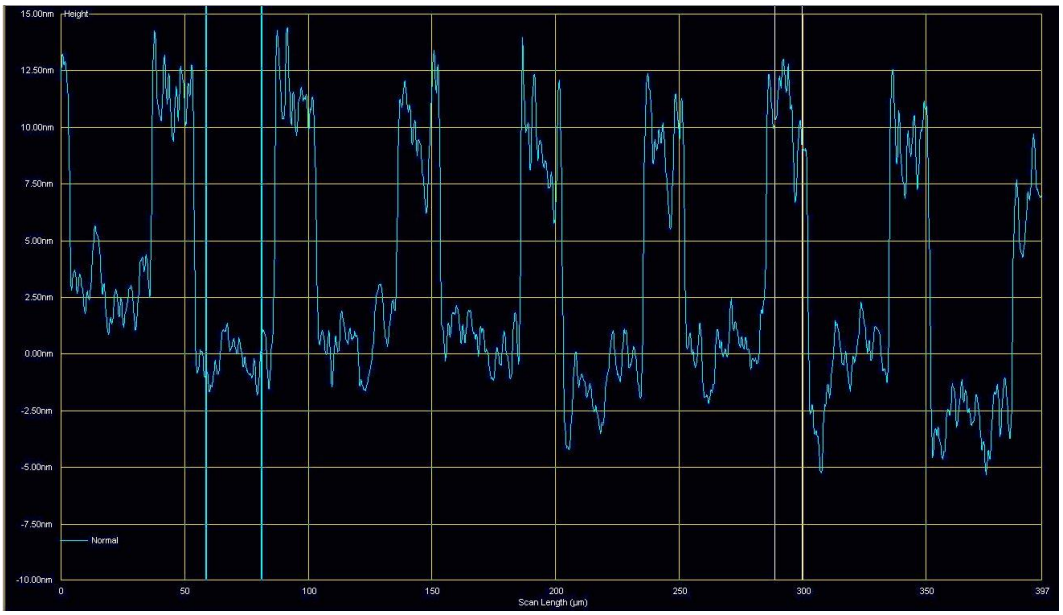

Figure 3.27 *Depth profile of 10 nm pillars*

Height of pillars after etching was obtained by optical profilometry. The height profile is seen as a blue trace across a 400 µm region, with a maximum at 7.5-12.5 nm and a minimum at -2.5-2.5 nm. The height of pillars in this profile therefore was in the vicinity of 10 nm.

Figure 3.27 shows the maximum of the line profile from 7.50 nm to 12.50 nm above the SiO_2 surface, and the minimum from 2.50 nm below to 2.50 nm above the wafer surface. The pillars evidently exhibited heights around 10 nm.

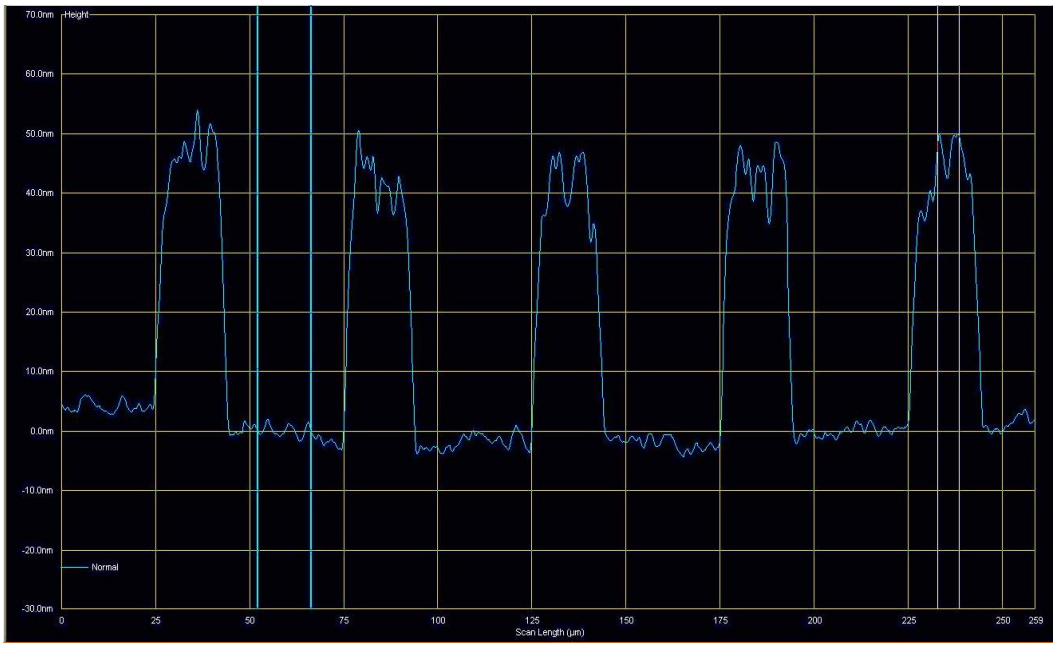

Figure 3.28 *Depth profile of 45 nm pillars*

Height of pillars after etching was obtained by optical profilometry. The height profile is seen as a blue trace across a 250 µm region, with maxima at 40-50 nm and minima at -2-5 nm. The height of pillars in this profile therefore was in the vicinity of 45 nm.

Figure 3.28 shows the maximum of the line profile from 40.0 nm to 50.0 nm above the SiO_2 surface, and the minimum from 2.0 nm below to 5.0 nm above the wafer surface. The pillars evidently exhibited heights around 42-50 nm.

The line profiles suggest that the patterning rendered the pillar and wafer surface quite rough. One does not see plateauing where the stylus passed over the pillar surface. However, it is important to note the limitations of the profiling technique, insofar as the stylus radius was 2 µm. Consequently, the technique is unable to resolve sub-micron features, which might give a false indication of the real roughness. AFM would offer better resolution.

Below are optical images of the material grown on the three patterned substrates. Figure 3.29 shows growth on substrate T23 (11 nm pillars):

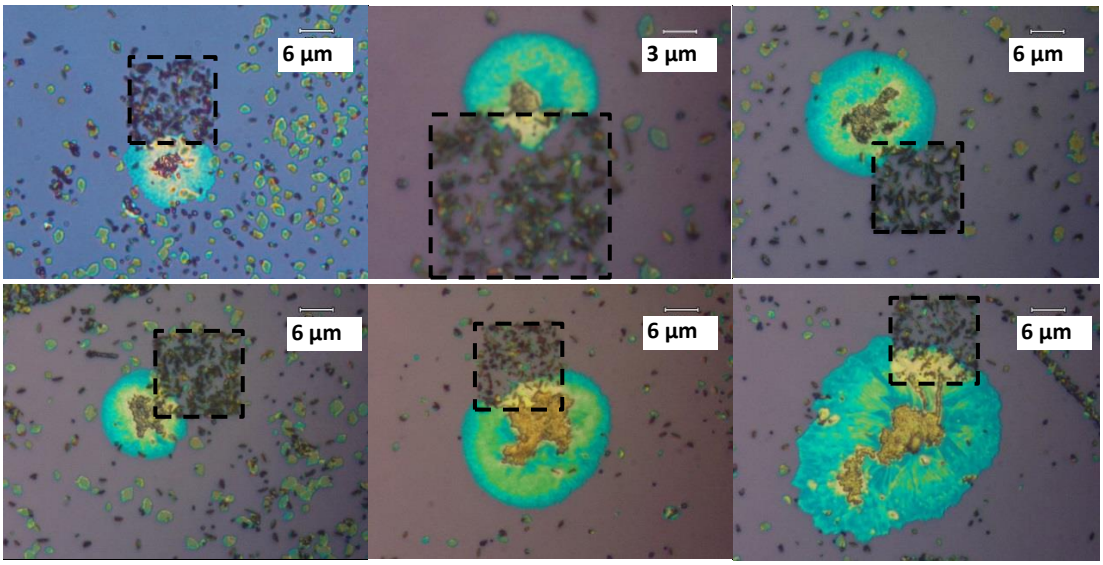

Figure 3.29 *Evidence of MoS_2 growth at 11 nm edges*

In the images above, the pillars are visible as square features on the substrate, labelled with dashed boxes. There was evidence of nucleation at the pillar edges and outward growth from there. The regions around the nucleation centre were thought to be thin, as evidenced by the light blue contrast against the substrate.

Growth on substrate T23 seemed to proceed somewhat as expected, with evidence in the images of micron-sized domains at the pillar edges. These are denoted by their stark optical contrast against the SiO_2 surface. There was growth also at other points, making the substrate appear "dirty", but clearly the largest and apparently thinnest domains were at the pillar edges. In the above images, the nucleation centres of the domains are at the pillar edges, confirming an edge effect, but this effect seemed so pronounced that the domains did not grow with uniform thickness. A peculiar observation is that there was growth of small, thick flakes on the pillar surfaces rather than at their edges, and this requires further investigation. One possible explanation for this was a meniscus

effect, as observed in dip-coating where the balance of cohesive and drainage forces leads to the formation of a thin coating as the substrate is withdrawn from the solution.[110]

Raman spectroscopy taken at different points of the above domains yielded confirmation of the material's thickness. In all cases, the spectra showed a combination of few-layer and bulk flakes.

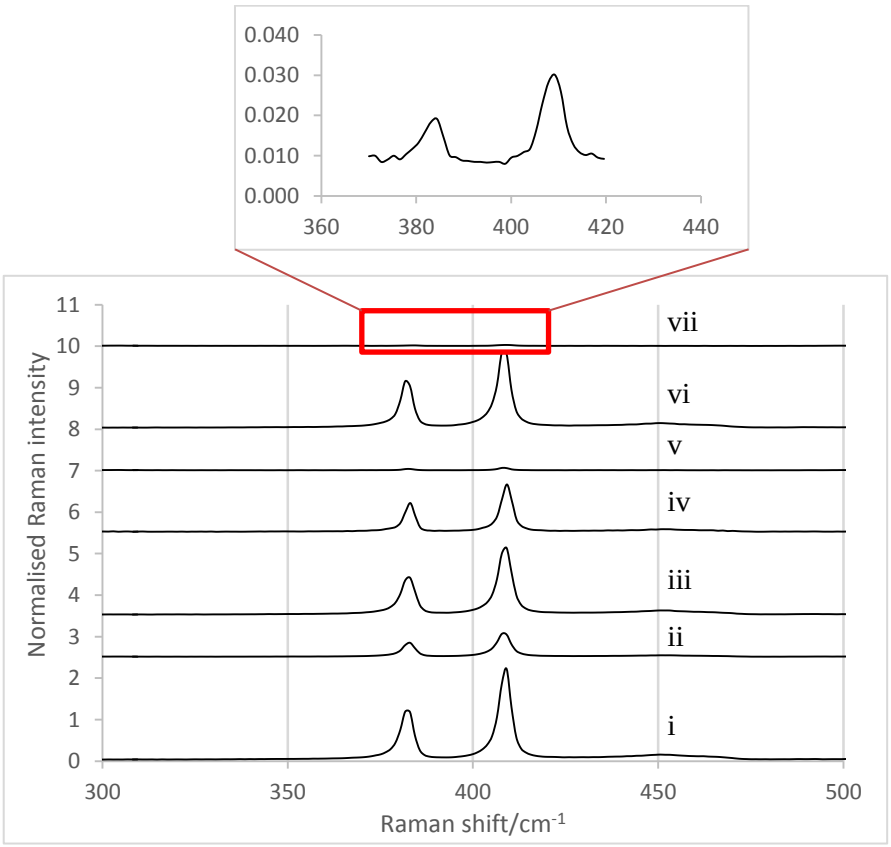

Figure 3.30 *Raman spectra of domains grown at 11 nm pillar edges*

The spectra show peaks corresponding to the E_{2g} and A_{1g} characteristic peaks of MoS_2 were present at ~385 and ~405 cm^{-1}. The peaks were normalised to laser power to allow them to be plotted on the same graphs. (Inset) Blown up spectrum vii for clarity.

The spectra show the expected characteristic Raman peaks of MoS_2, the E_{2g} mode around 383 cm^{-1} and the A_{1g} mode at around 407 cm^{-1}. These data confirm that crystalline MoS_2 was grown at the 11 nm pillar edges. Spectrum 3.30(i) showed the peaks with the greatest intensities, and this is usually attributable to thickness. Spectra (ii), (v) and (vii) exhibited the peaks with weakest intensities, so these were presumed to be the thinnest domains synthesised using the 11 nm regime. Confirmation of this can be seen in a tabulation of pertinent information in the above spectra. Table 3.3 quantifies the data in Figure 3.30.

Considering the table and the spectra together clearly shows that one difference between the 4L and 5L spectra was the absolute peak intensity. The 4L peaks are considerably weaker than the 5L peaks, and this follows from the fact there are fewer scattering centres in a thinner material.

However, the final column shows that for each few-layer case, the A_{1g} mode intensity considerably exceeded that of the E_{2g} mode, a sign of good crystallinity as discussed in Section 3.6.3.

Table 3.3 Key Raman parameters from Figure 3.30

Region	$\mathbf{E_{2g}/cm^{-1}}$	$\mathbf{A_{1g}/cm^{-1}}$	$\mathbf{\Delta\bar{\upsilon}/cm^{-1}}$	**Layer thickness**	$\frac{\mathbf{I_A}}{\mathbf{I_E}}$
i	381.7	409.1	27.5	Bulk	
ii	383.1	407.8	24.7	4L	1.61
iii	383.0	409.1	26.1	5L	1.78
iv	383.1	409.2	26.1	5L	1.62
v	383.1	407.8	24.7	4L	1.67
vi	381.7	407.8	26.1	5L	1.60
vii	384.4	409.2	24.8	4L	1.58
viii	381.8	407.9	26.1	5L	1.54

Figure 3.31 shows Raman maps corresponding to the E_{2g} and A_{1g} modes.

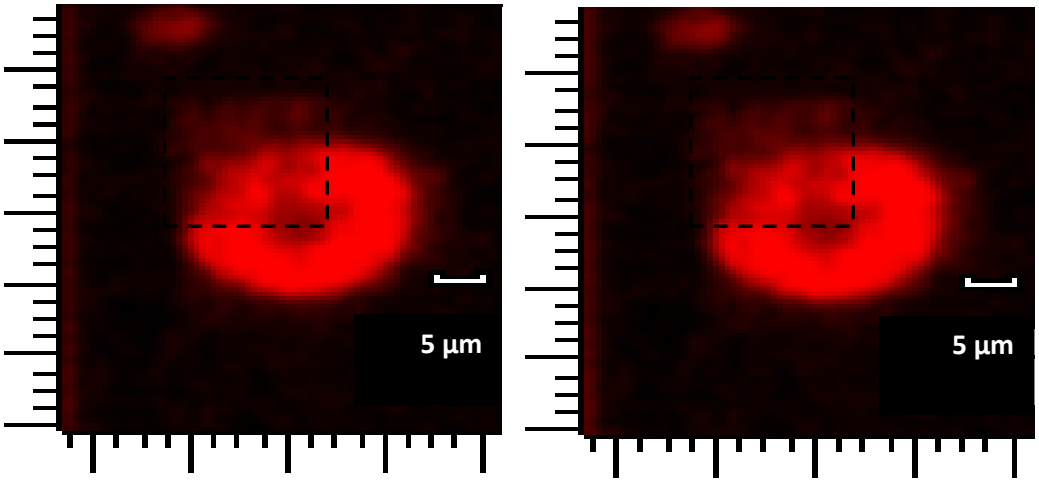

Figure 3.31 *Raman maps of 4L domain grown at 11 nm edges*

On the left is the E_{2g} Raman map taken at a 383.1 cm^{-1}. On the right is the A_{1g} Raman map taken at 407.8 cm^{-1}. Evidence of growth on the pillar surface (as well as the edge) came from the detection of Raman activity corresponding to each mode inside the region denoted by the dashed black boxes, as indicated by the very weak but detectable red region.

The Raman maps show the brightest regions corresponding to few-layer deposition. The monolayer/few-layer regions show up at the weakest intensity because they exhibit their brightest

intensity at shifted wavenumbers. Thus, it is possible that the thinnest growth took place on top of the pillars.

The PL spectrum below was taken from an edge-grown few-layer crystal (point ii in the Raman spectra) and is shown on the same plot as a good-quality monolayer spectrum (*cf.* Figure 3.22) for comparison. The spectra were normalised to the A_{1g} Raman peak.

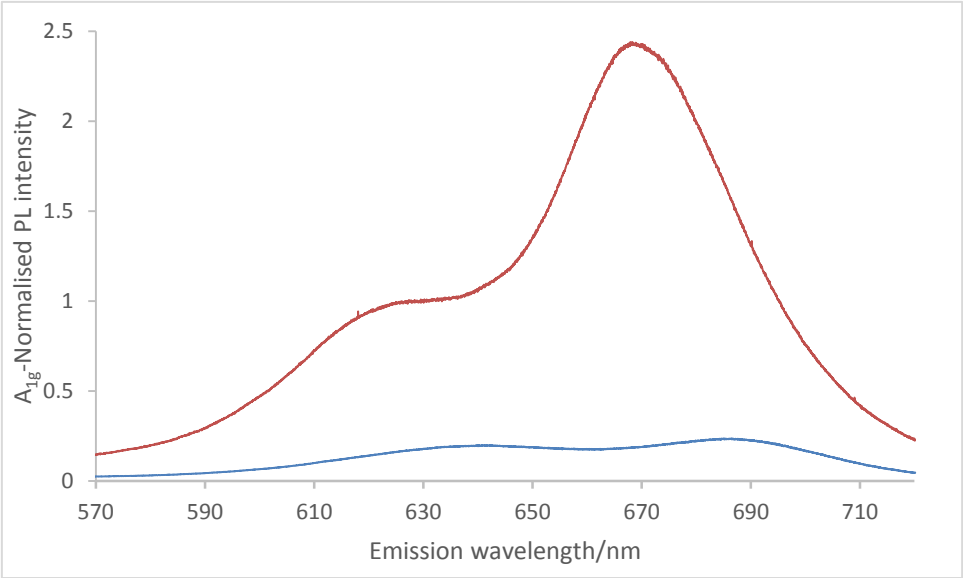

Figure 3.32 *Representative PL spectrum of 11 nm edge-grown crystal (blue)*

The edge-grown crystal spectrum (blue) is shown on the same plot as a good-quality monolayer spectrum (red) and both are normalised to the A_{1g} Raman peak. The PL spectra show a tenfold difference in peak emission intensity. This was consistent with the Raman spectra suggesting few-layer growth at the 11 nm edges.

The spectrum shows a roughly tenfold difference between the A-exciton peak monolayer peak and corresponding peak from the edge-grown crystal. This attests to the thickness of the edge-grown crystal. With reference to Figure 3.22 (see Section 3.6.3), one can say that the few-layer PL spectrum shown here corresponds probably to a four-layer case. Another clue is the virtual parity in intensity of the A-exciton compared to the B-exciton, with both appearing at a maximum of ~0.25. A good-quality monolayer PL signal would exhibit a substantial difference in intensities between the two peaks, and in the above spectrum one sees a 2.5-fold increase in the A-exciton intensity compared to that of the B-exciton in the 1L case. It is possible that the material that grew on top of the pillar surface was the same thickness as the edge-grown material but of poorer crystallinity.

Figure 3.33 shows growth on substrate T24 (31 nm pillars). These optical images show quite a different outcome to the previous case.

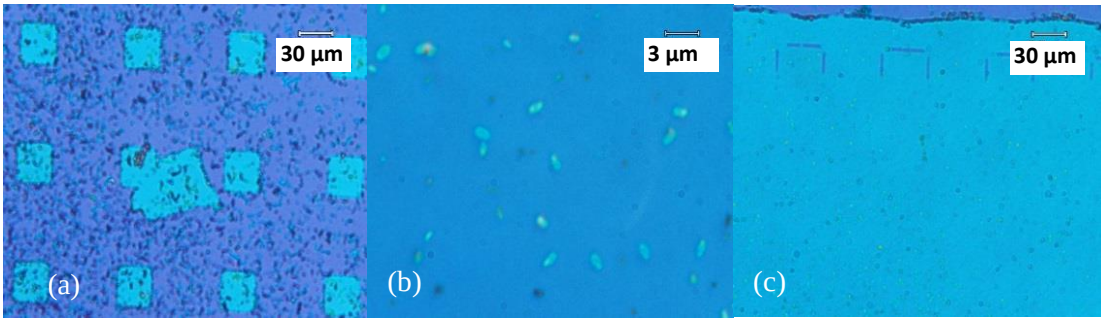

Figure 3.33 *Evidence of MoS_2 growth at 30 nm edges*

There was evidence of growth on top of pillars, seen in the difference in contrast ***(a)*** *between the tops of the square pillars and the substrate. However, there was also evidence of good coverage* ***(b)*** *around hundreds of microns* ***(c)****. This was seen in the uniformity of colour across the images. Raman spectroscopy confirmed that these light-blue regions were MoS_2.*

There was evidence of small-scale nucleation at the pillar edges leading to ~30 µm film, in contrast to the very small crystallites (1-3 µm) that grew in isolation of the pillars. There was evidence of large-scale growth (hundreds of microns) possibly by agglomeration of crystallites into a polycrystalline film, which was not observed in the case of 11 nm pillars. This is seen in the contrast of the material against the substrate; the material appeared light blue while the substrate was a darker blue/violet. From the OM images, the thickness of the polycrystalline film seemed comparable to the pillar height, suggesting a thin film around 5-6 layers thick. This is because the square edges of the pillars appear indistinguishable from the film surface, suggesting that the latter was flush with the former. Figure 3.34 shows the Raman spectra of MoS_2 on 31 nm-patterned SiO_2.

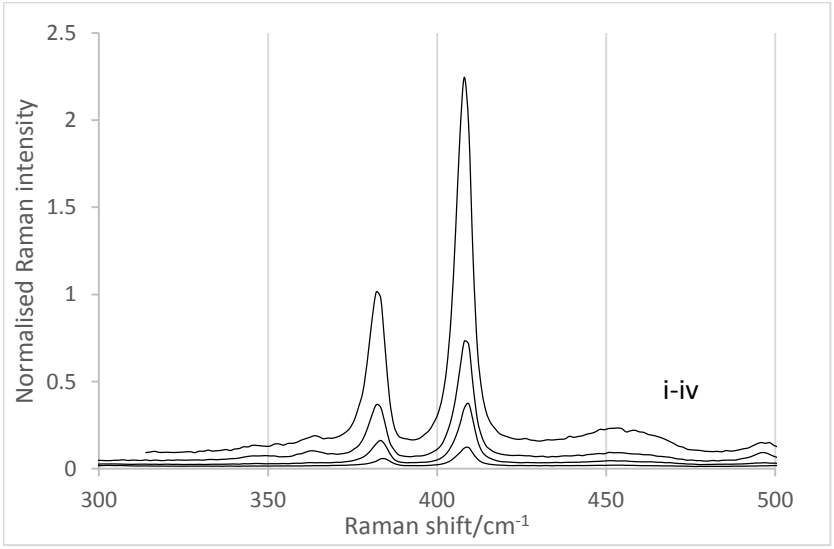

Figure 3.34 *Raman spectra of few-layer domains grown at 31 nm edges*

Spectra acquired from multiple regions at the edges and on top of pillars, normalised to laser power, exhibited peak separation corresponding to 3L-5L films, an improvement on the 11 nm case. Bottom to top: i-iv

The Raman spectra taken from various regions at edges (and on top) of the pillars showed $\Delta\bar{\nu}$ ranging from 23.4 cm^{-1} to 26.1 cm^{-1}, that is to say trilayer to bulk, as shown in Table 3.4. Note that the Raman peaks did not necessarily correspond to points in Figure 3.33.

Table 3.4 Key Raman parameters from Figure 3.34

Region	$\mathbf{E_{2g}/cm^{-1}}$	$\mathbf{A_{1g}/cm^{-1}}$	$\mathbf{\Delta\bar{\upsilon}/cm^{-1}}$	**Layer thickness**	$\frac{\mathbf{I_A}}{\mathbf{I_E}}$
i	384.6	408.0	23.4	3L	2.13
ii	383.8	408.9	25.1	5L	2.31
iii	382.0	408.1	26.1	Bulk	
iv	382.0	408.1	26.1	Bulk	

Raman spectroscopy confirmed the thickness of the 45 nm edge-grown material, as shown in Figure 3.35:

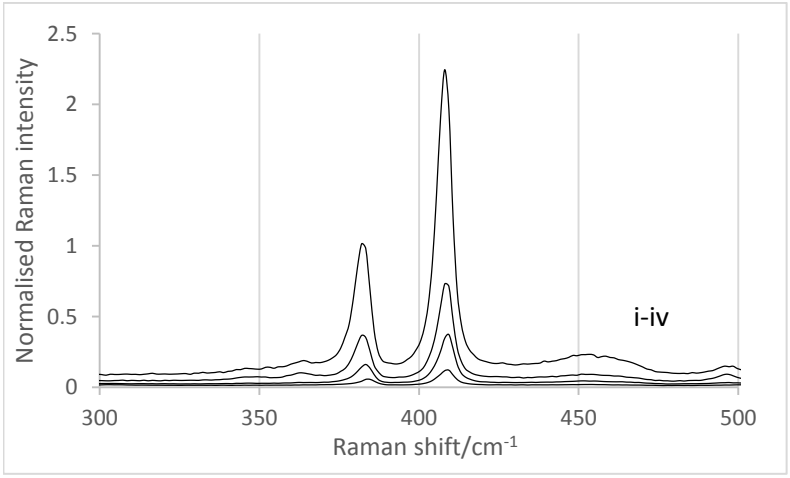

Figure 3.35 *Raman spectra of few-layer MoS_2 grown at 45 nm edges*

These spectra were acquired from multiple regions at the edges and on top of pillars and exhibited peak separation corresponding to 4L-bulk films, inferior to the 31 nm case. Spectra were normalised to laser power to allow plotting on the same graph irrespective of acquisition conditions. Bottom to top: i-iv

The Raman spectra taken from various regions at edges (and on top) of the pillars show $\Delta\bar{\nu}$ ranging from 24.6 cm^{-1} to 26.1 cm^{-1}, that is to say four-layer to bulk.

Table 3.5 Key Raman parameters from Figure 3.35

Region	$\mathbf{E_{2g}/cm^{-1}}$	$\mathbf{A_{1g}/cm^{-1}}$	$\mathbf{\Delta\bar{\upsilon}/cm^{-1}}$	**Layer thickness**	$\frac{\mathbf{I_A}}{\mathbf{I_E}}$
i	384.4	408.0	24.6	4L	2.08
ii	382.0	408.1	25.1	Bulk	
iii	382.0	408.1	26.1	Bulk	
iv	382.0	408.1	26.1	Bulk	

This suggests that the method afforded little control of thickness uniformity. One clear difference between the 11 nm, 31 nm and 45 nm cases was that the middle pillar thickness resulted in the growth of a larger and thinner film. The 11 and 45 nm cases resulted in small domains of 4-5L thickness, but the 31 nm case resulted in large films down to 3L thickness.

What these data show is that not only was there an edge-mediated effect on domain morphology, but that that effect could possibly be helpful in growing large-scale, phase-pure films by liquid ALD. This was in evidence from the 31 nm case, which resulted in a large-scale, optically uniform film extending over several hundred microns. Despite this, the film was few-layer in thickness, as confirmed by Raman spectroscopy. The optimum pillar height determined in this study was 31 nm as that afforded the thinnest films deposited over the largest area. It will be necessary to optimise the conditions in order to ensure reliable monolayer growth, but the method is clearly promising. There may very well be an optimum edge height at which large-scale monolayer growth is maximised. It will also be necessary to conduct further characterisation, particularly structural characterisation by TEM to show the crystallinity of the large film that was grown at the 31 nm pillar edges.

3.6.5 Improving hydrophilicity

The characterisation data presented in Sections 3.6.3 and 3.6.4 proved the efficacy of this new method for MoS_2 synthesis. One issue that remained, however, was the extent to which this technique could truly be defined as an ALD. Section 1.3.2 defines ALD as having two unique characteristics: (1) discrete, layer-by-layer deposition; (2) self-limiting precursor deposition related to the number of active sites on the substrate.

The first unique ALD characteristic was self-evident in that the precursors were introduced discretely in this method and the results clearly indicated monolayer deposition. After the Mo-containing precursor dip-coating process, the substrate was removed from the ammonium molybdate solution and drained of excess before the sulphurisation step. There was no free Mo source in the tube furnace concurrently with the sulphur source, which limited the potential for a

CVD-type pre-reaction and random snowing of the product. Furthermore, the temperature-modulated coverage observed during the dip-coating process clearly suggested solution-phase deposition of the Mo-containing precursor. In these two ways, the new process differed from CVD.

Demonstrating that the process conforms to the second unique characteristic of ALD is non-trivial as it requires a more detailed mechanistic study to show the surface chemistry that is taking place. A self-limiting reaction in this context is usually taken to mean a chemical reaction between the precursor and the substrate surface *via* dangling surface bonds or reactive moieties on the substrate surface.[37] Without the self-limiting nature, the process is more analogous to CVD, even though the dip-coating process is obviously not a vapour-phase deposition. However, treating the SiO_2 surface with concentrated acid or base could be used to initiate a surface reaction with the incoming molybdate ion, which also contains bridging oxide ligands. It follows, then, that such a reaction would be self-limiting due to the limited number of –OH surface groups.

The method thus outlined exhibited some of the characteristics of ALD and some of CVD, but not the full complement of characteristics that could adequately be used to place it in either category. Therefore, it is presently best described as a hybrid method that offers some advantages over both techniques in isolation. The potential to develop the surface-limiting nature of the method does, however, offer a route towards the eventual realisation of this method as a fully ALD-type process. This was the motivation for introducing KOH etching of SiO_2/Si in the substrate preparation.

The optical micrographs showed the expected triangular-faceted morphology of MoS_2 and some evidence of large-scale film deposition on the order of several hundred microns.

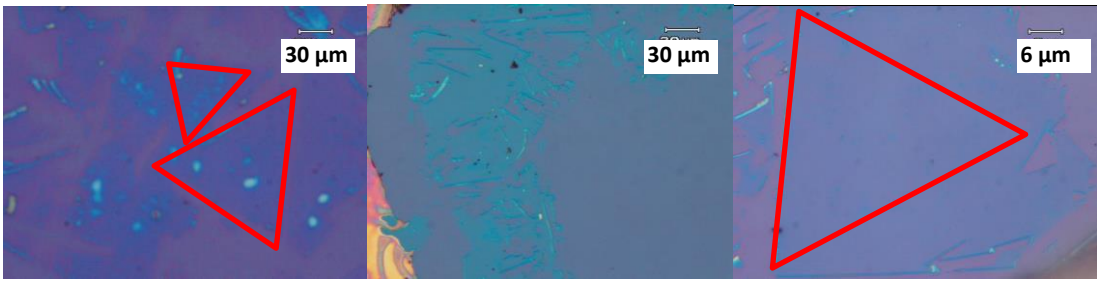

Figure 3.36 *OM images of MoS_2 on KOH-etched substrate T39 and T40*

The triangular-and complex-faceted morphology was in limited evidence from initial dip-coating of the Mo-containing precursor at 80 °C, the optimum dip-coating temperature of all the conditions explored in this study. In ***(a)*** *and* ***(b)****, standalone triangular-faceted can be seen. In* ***(c)****, the complex morphology is seen where several small crystallites grew into each other. Also visible in each image are the high-contrast nucleation centres at the centre of each crystal. Note that contrast was enhanced in post-processing using ImageJ to bring out the crystals, because the natural contrast of monolayers against the substrate is low. Scale bars (left to right) = 100 µm, 100 µm, 5 µm.*

The OM images showed regions of large and apparently thin films, the largest on the order of 120-150 μm in lateral size. Further characterisation by electron microscopy will elucidate the poly-/single-crystalline nature of these films. Large-scale counting of domains was not performed, but several regions showed films at least comparable in lateral size to single-crystalline domains synthesised on untreated substrates (see Section 3.6.3). One interesting observation was that monolayer coverage appeared to be greater as a fraction of the overall coverage, compared to the non-treated case. This was consistent with ALD-type behaviour.

Corresponding Raman spectra confirmed few-layer growth, with domains exhibiting the characteristic few-layer peak separations.

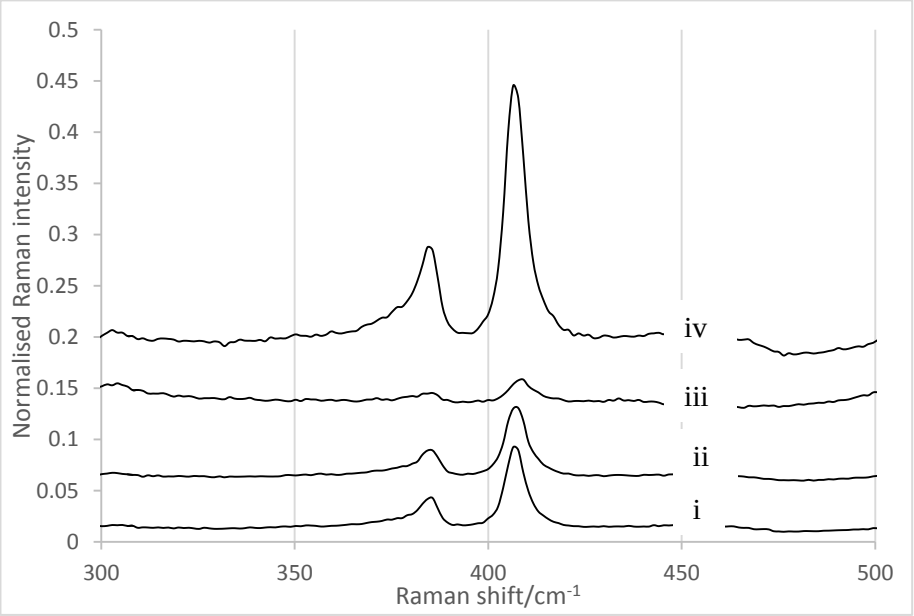

Figure 3.37 *Raman spectra of MoS_2 on KOH-etched substrates T39 and T40*

The spectra show peaks corresponding to the E_{2g} and A_{1g} characteristic peaks of MoS_2 at ~385 and ~408 cm^{-1}. The peaks were normalised to laser power to allow comparison on the same graph. Compared to spectra obtained from MoS_2 on bare substrates (Figure 3.20) and edge-grown MoS_2 (Figure 3.30), the I_A/I_{Si} ratio was notably improved. All other conditions being equal, this was attributed to a KOH-related effect, consistent with a surface reaction between the precursor and dangling Si-O bonds on the die surface, leading to good contact between the precursor and the surface.

The Raman spectra in Figure 3.37 were acquired from different regions on the substrates thought to exhibit characteristic monolayer contrast, as in the OM images in Figure 3.36. Tabulation of the Raman data indicated 1-3L domains.

Table 3.6 Tabulation of T39 and T40 Raman data

Region	$\mathbf{E_{2g}/cm^{-1}}$	$\mathbf{A_{1g}/cm^{-1}}$	$\mathbf{\Delta\bar{\upsilon}/cm^{-1}}$	**Layer thickness**	$\frac{\mathbf{I_A}}{\mathbf{I_E}}$
i	385.6	406.1	20.5	1L	2.16
ii	385.6	407.8	22.2	2L	2.05
iii	384.3	406.5	22.2	2L	2.15
iv	385.6	409.1	23.5	3L	1.52

The Raman data suggested that the MoS_2 films on KOH-etched substrates exhibited a good degree of crystallinity. This was inferred from the very high peak intensity ratios in the mono- and bilayer cases. Although this does not provide definitive confirmation of an ALD-type process, it may suggest a positive effect arising from pre-treatment of the substrate with an etchant to introduce the –OH surface moieties. The subsequent observation of good monolayer coverage and crystallinity was consistent with an ALD-type process owing to the surface-limited nature of ALD.

It was not clear from these results if the improved crystallinity was down to surface chemistry or the nature of the CS_2 precursor. A more detailed mechanistic study will confirm if surface treatment has moved this process any closer to true ALD character, but these results were promising and offer an interesting area for future work. For example, this may include characterisation of the precursor-coated substrate before sulphurisation in order to obtain information about the precursor binding energies on the substrate.

3.6.6 Dip-coating of CS_2

Data were conflicted on the efficacy of dip-coating CS_2. Some substrates exhibited no morphological or optical sign of the presence of MoS_2 (see Appendix A.6). In other cases, optical micrographs indicated generally good coverage after annealing at 450 ℃, as in Figure 3.38.

The OM images taken from sample T41 showed coverage on the order of ~20 μm with domains that gave the appearance of polycrystalline films. This was on account of the lack of obvious signs of the regular morphology of MoS_2 crystals (see Section 3.6.3), consistent with merging of single domains into larger films.

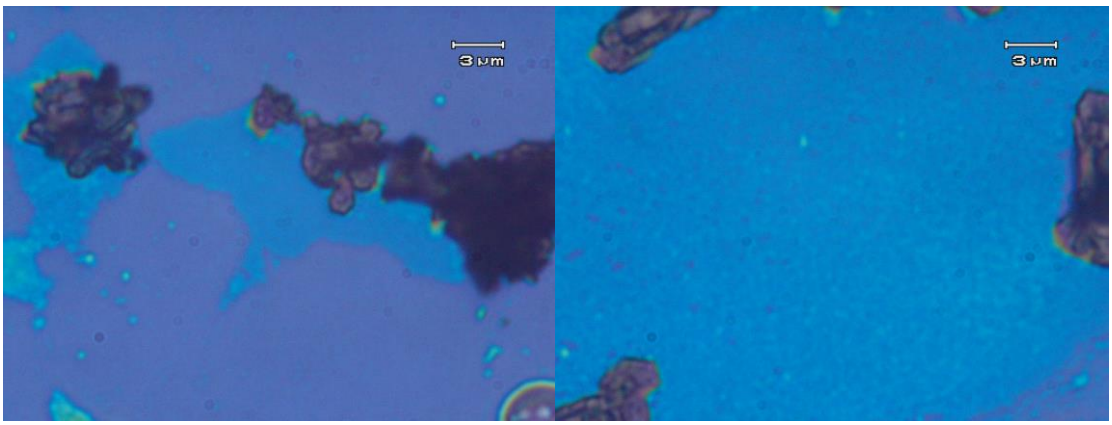

Figure 3.38 *OM images of MoS_2 grown by CS_2 dip-coating*

These images were acquired from a sample on which both the molybdenum-containing and sulphur-containing precursor were deposited by dip-coating, followed by low-temperature annealing. (Left) Indication of the contrast between the as-grown material and the substrate. (Right) Colour uniformity was consistent with good coverage across several microns, possibly polycrystalline MoS_2.

In addition, Raman spectroscopy showed evidence of mono- to few-layer MoS_2 formation.

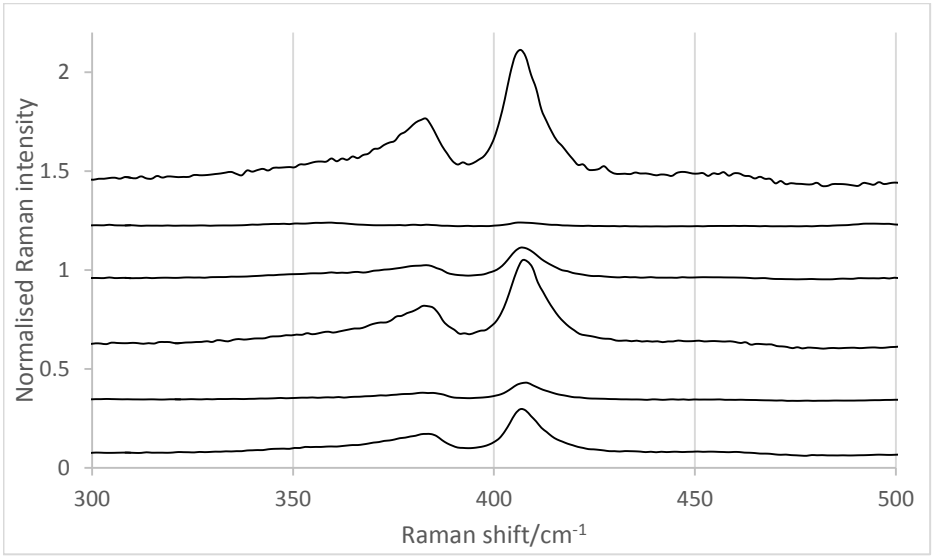

Figure 3.39 *Raman spectra of CS_2-grown MoS_2 films*

The spectra show peaks corresponding to the E_{2g} and A_{1g} characteristic peaks of MoS_2 at ~385 and ~408 cm^{-1}, including monolayer and few-layer peaks. The peaks were normalised to laser power to allow comparison on the same graph. The variation in peak heights attests to variable crystallinity, likely to be a consequence of low annealing temperature.

Raman intensity mapping of selected films showed excellent agreement between the OM images and vibrational data, as seen in Figure 3.40:

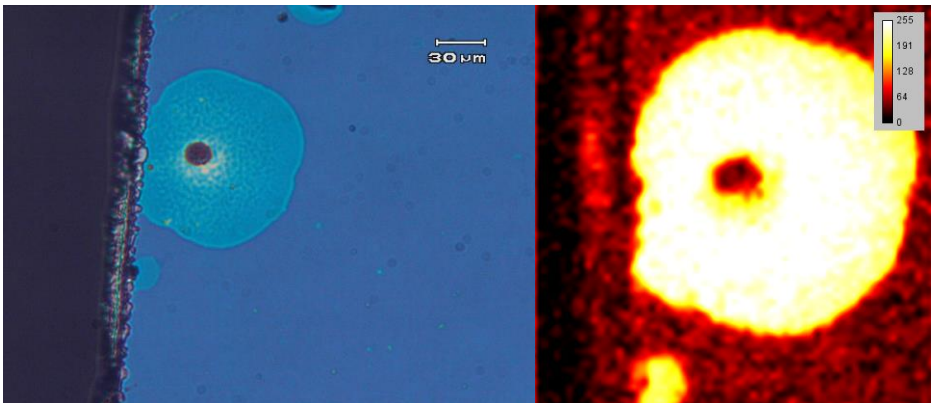

Figure 3.40 *A_{1g} Raman map of ~100 µm CS_2-grown film*

(Left) The OM image was typical of this sample, with variable crystallinity evidenced by the lack of recognisable facets. However, Raman mapping provided good evidence that MoS_2 with good thickness uniformity was grown by this CS_2 dip-coating method. In this case, the map corresponds to the A_{1g} mode of a bilayer. This is significant because it demonstrates the efficacy of using a low temperature (450 ℃ vs 800 ℃), which will be crucial for industrial viability of this method.

In Figure 3.40, the optical micrograph of a bilayer region is shown, alongside the corresponding Raman map of the A_{1g} mode at 406.6 cm^{-1}. The Raman map showed a high-intensity (high brightness) vibration corresponding to the bilayer A_{1g} mode.

The use of a growth temperature of 450 ℃ was chosen in order to offer a significant point of difference between the two sulphur sources: CS_2 and elemental sulphur. This is because 450 ℃ is well below the optimal annealing temperature in elemental sulphur for MoS_2. Raman mapping showed that large crystalline films were obtained at a much lower temperature simply by changing the sulphur source. This fact offers a clue as to the reactivity of CS_2 towards the MoO_3 intermediate. CS_2 has an EA of -1.46 eV, which is comparable to that of oxygen (-1.41 eV); however, sulphur (-2.08 eV) has a much lower EA than oxygen.[202] Therefore, it is possible that less forcing conditions are sufficient for Mo(VI)→Mo(IV) reduction to take place in the presence of CS_2 than are required in the presence of sulphur. The data also suggest that the dip-coated CS_2 did not desorb from the substrate surface before reaction, even though the compound is volatile. This is an unusual behaviour that could do with further investigation. It may be related to vapour pressure differences between the open atmosphere and the Ar atmosphere of the tube furnace. However, this was not observed across all substrates. Other examples showed no evidence of large-scale MoS_2 deposition, suggesting that CS_2 desorption had occurred.

3.6.7 Substrate-related effects: SiO_2/Si vs sapphire

CVD and ALD can be epitaxial and non-epitaxial. Epitaxial growth is that which occurs on crystalline substrates that adopt the same surface crystal structure as the target material. An

example of these is c-cut sapphire for MoS_2 growth.[107] Epitaxial growth generally gives the largest single-crystalline domains. This is because epitaxial nucleation is limited to specific orientations on the substrate surface, and so lateral growth of these nuclei then leads to merging of well-aligned crystallites, eventually forming a single crystal with no grain boundaries. In contrast, non-epitaxial substrates do not adopt the same surface crystal structure as the target material, and in some cases are entirely amorphous. An example of this is MoS_2 growth on SiO_2, which is amorphous. Nucleation occurs at random sites, and the resulting domains are therefore oriented randomly with respect to each other. This disfavours the formation of large single crystals, because of the introduction of grain boundaries, which abruptly disrupt the crystal lattice in occasionally useful but often deleterious ways.

One may wonder, then, if there is any benefit to non-epitaxial growth. In fact, characterisation of TMdCs on SiO_2 is easier than on sapphire or mica. Specifically, TMdCs on 285 nm thermally-grown SiO_2-on-Si exhibit maximum optical contrast against the surface of the substrate.[31, 128] This renders even monolayers easily visible at low magnification under a simple optical microscope.

It is possible to account for this using epitaxial substrates to grow the nanomaterial and then chemically transferring the as-synthesised film to SiO_2 for characterisation. However, this process is far from facile. For instance, desorbing the film from sapphire using an acetone dip requires a very long dipping time, and using basic or acidic solutions damages the material. Furthermore, sapphire substrates are dearer than silicon to begin with and substrate preparation is a difficult process. Sapphire is a much harder material than silicon, so wafer dicing, even using a diamond blade, is a resource-intensive process. A comparison of substrates is shown in this section.

Similar pre-annealing and tempering processes are known to improve smoothness in sapphire substrates, which encourages larger-scale epitaxial growth of the target material.

Figure 3.41 shows representative Raman spectra of domains grown on sample T46. Optical images were unavailable because the optical contrast between 2D materials and the sapphire substrate is usually too poor to afford good-quality images under OM.

The spectra in Figure 3.41 were normalised to the sapphire line at ~418 cm^{-1}. The sapphire vibrational mode at this Raman shift is quite intense, so one measure of the substrate effect is that the intensities of the MoS_2 A_{1g} and E_{2g} modes with respect to the substrate peak increased notably over the Si case.

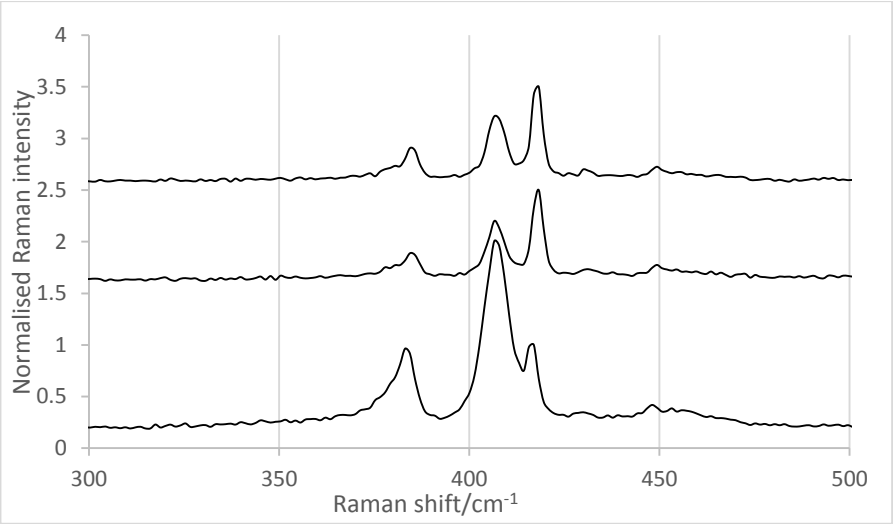

Figure 3.41 *Raman spectra of bilayer MoS_2 on sapphire*

The sample was grown under the previously-identified optimal conditions but on sapphire instead of silica. The spectra show peaks corresponding to the E_{2g} and A_{1g} characteristic peaks of MoS_2 at ~385 and ~405 cm^{-1}. The peaks were normalised to laser power to allow them to be plotted on the same graphs. In addition, there is the intense sapphire-derived peak at 418 cm^{-1}.

Optical characterisation on sapphire is practically impossible due to poor contrast. For this, the thin film was transferred to SiO_2. However, this process led to damage of the material. The first substrate was damaged in the spin-coating process, and the second was damaged during the acetone dip due to poor detachment. Good-quality optical characterisation and SEM could be a useful tool for a substrate comparison study, because it would clearly show domain sizes. TEM could then be used to determine the presence of grain boundaries and thus demonstrate definitively that growth on the sapphire substrate led to larger single crystals than that on SiO_2.

3.6.8 Post-annealing effects

Post-annealing was shown to have a deleterious effect on material quality for those samples grown on SiO_2 in elemental sulphur. Sample T19 was post-annealed in N_2 at 1000 ℃ (see Table A.2). This monolayer sample had given a high-quality PL signal before post-annealing, as evidenced by Figure 3.22. Figure 3.42 shows normalised PL emission from T19 after post-annealing. This sample had been synthesised under optimal conditions of dip-coating and sulphurisation as it had presented the best characterisation data before post-annealing was carried out.

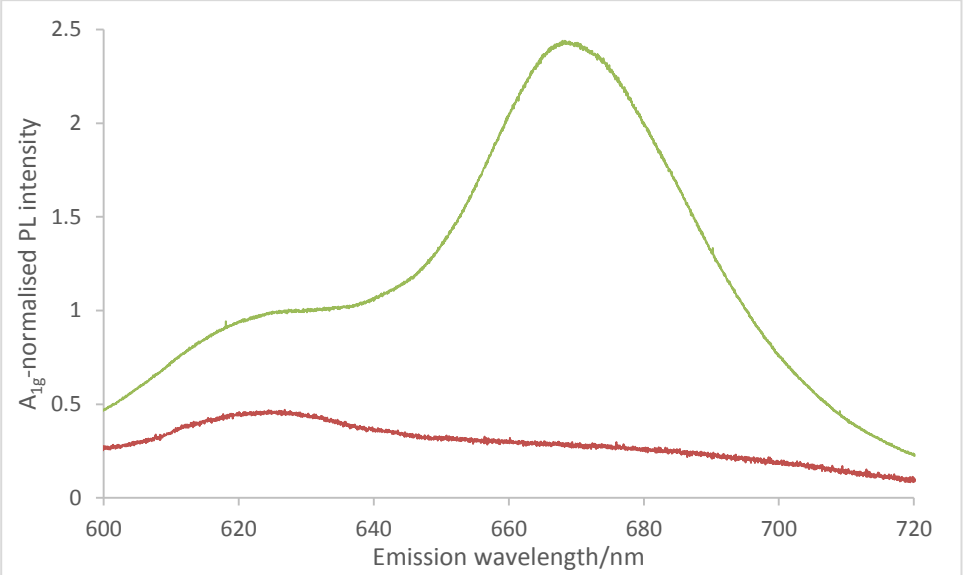

Figure 3.42 *Effect of post-annealing on PL emission of S-grown 1L-MoS_2*

The green spectrum show PL emission from the as-prepared monolayer T19 grown from 80 ℃ dip-coating of 0.13 g L^{-1} aqueous Mo precursor solution and ten minutes annealing in sulphur at 800 ℃. The red spectrum shows the corresponding emission after post-annealing in in N_2 at 1000 ℃. The drop in intensity is quite clear, pointing to ineffective post-annealing in this case. The data were acquired from the same point on the sample before and after post-annealing.

It is generally expected that the normalised PL intensity should increase after post-annealing, due to improved crystallinity.[107] However, the opposite was observed. Peak A-exciton intensity dropped more than tenfold in the post-annealed sample as compared to the case prior to post-annealing. The PL spectra above suggest a detrimental effect on material quality arising from post-annealing on SiO_2. Raman spectroscopy could corroborate this. Figure 3.43 shows Raman spectra from the post-annealed sample.

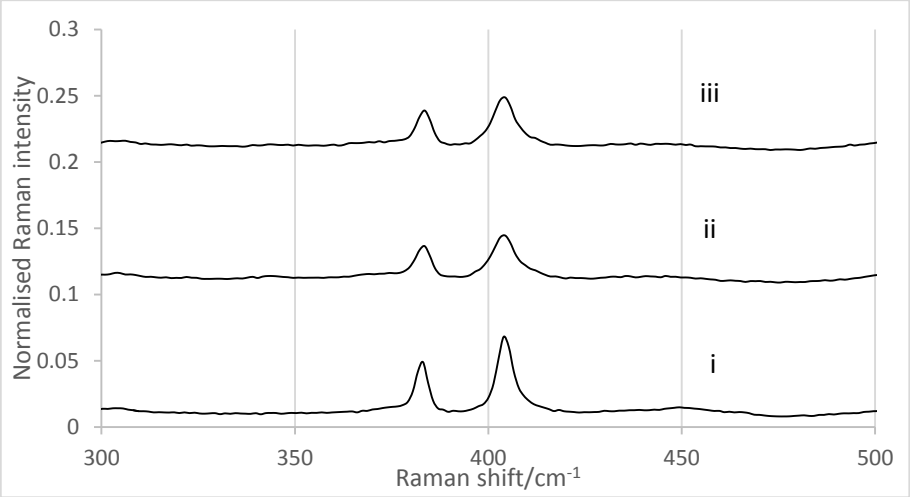

Figure 3.43 *Effect of post-annealing on crystallinity*

The sample was grown under the previously-identified optimal conditions, which gave good Raman and PL activity (see Section 3.6.3). After post-annealing in N_2 at 1000 ℃, the sample experienced degradation of crystallinity/purity. The spectra show peaks corresponding to the E_{2g} and A_{1g} characteristic peaks of MoS_2 at ~385 and ~405 cm^{-1}. The peaks were normalised to laser power to allow them to be plotted on the same graph. Although the correct peaks are present, the ratio of intensities shows loss of crystallinity.

Tabulating the relevant information from the above spectra yields important evidence about the effect of post-annealing on crystallinity.

Table 3.7 Key Raman data after post-annealing (*cf.* Table 3.2)

Region	$\mathbf{E_{2g}/cm^{-1}}$	$\mathbf{A_{1g}/cm^{-1}}$	$\mathbf{\Delta\bar{\upsilon}/cm^{-1}}$	**Layer thickness**	$\mathbf{\frac{I_A}{I_E}}$
i	383.1	404.0	20.9	2L	1.39
ii	383.7	403.4	19.7	1L	1.03
iii	383.5	403.3	19.8	1L	1.02

Comparing the monolayer peak intensity ratios between points ii and iii in Table 3.7 with the data from the same sample before post-annealing shows a drop in the ratio from a maximum of 1.17 (see Table 3.2) to a maximum of 1.03. As previously discussed, this ratio is indicative of crystallinity, so this evidence confirms that post-annealing had a detrimental effect on crystallinity.

The detrimental effect of post-annealing can be explained by considering the nature of the substrate. Accordingly, the effect can be attributed to the instability of SiO_2 at post-annealing temperatures, leading to a possible reaction between the substrate and the film.[107] Moreover, MoS_2 may be susceptible to doping by oxide impurities because of electron affinity considerations. There

is evidence of a SiO_2-dependent etching effect in MoS_2.[205] Therefore, at a temperature of 1000 ℃, it is likely that the combination of substrate instability and the material's susceptibility to oxide doping led to reduced quality of MoS_2 after post-annealing. It is possible to mitigate the oxidative effect. The use of a more stable substrate such as sapphire would be one way to do this, as it is stable at T>1200 ℃.[191] Such an approach was discussed in Section 3.6.7. However, another way to mitigate the detrimental effect of oxide doping is to anneal in a slightly reductive atmosphere.[128] This is because a reductive atmosphere disfavours oxidation. An atmosphere of forming gas, for instance, almost eliminates oxide impurities. This was the justification for using a 5% H_2 (in Ar) atmosphere for post-annealing in subsequent cases. In this case, the addition of H_2 did not, in fact, lead to an improvement in post-annealing outcomes. The ineffectiveness of H_2 here was likely a practical issue. Even when diluted and present in only low concentrations H_2 can react with the film.[107] For this reason, the gas was turned off at a temperature of 500 ℃,[206] and post-annealing proceeded thereafter only in argon up to 1000 ℃. The addition of hydrogen up to 500 ℃ was insufficient to prevent the loss of PL quality in the post-annealed film. In fact, this is still useful information. It is consistent with the conclusion that the PL degradation resulted from a phenomenon occurring at high temperature, and that may be the oxidative doping of MoS_2 arising from SiO_2 decomposition.

Structural information about the doping of the MoS_2 with oxide would be provided by TEM or XRD. These techniques would definitively identify any oxygen present in the surface species. XRD, as it is a crystallographic characterisation tool, would be particularly useful if oxygen was coordinated to molybdenum.

3.7 Conclusion and future work

A novel synthetic method for high-quality single-crystal monolayers of MoS_2 was presented in this chapter. The method successfully exploited dip-coating conditions as a low-cost and large-volume means of controlling layer thickness, and used sulphurisation and annealing to produce a highly-crystalline material. The optimum dip-coating parameters on SiO_2/Si were 15 minutes dip-coating from aqueous solution (0.13 g mL^{-1}) of ammonium helptamolybdate tetrahydrate at a solution temperature of 80 ℃. This was followed by optimum sulphurisation parameters of ten minutes in nitrogen at 800 ℃ in the presence of sulphur flakes followed by natural cooling. However, if the sulphur source was changed to CS_2 and introduced to the sample by dip-coating, it allowed a much lower annealing temperature (450 ℃) to be used, an important result for industrial viability because costs will be crucial. This result requires further investigation as it was inconsistently reproduced.

The thickness of monolayer domains was confirmed by Raman spectroscopy, PL and AFM. Many domains were found to be monolayer and of good crystallinity, leading to sharp Raman peaks and a large PL signal. The lateral size of the as-synthesised domains was confirmed by microscopy (OM

and SEM), resulting in an assessment of lateral size distribution that showed a modal range of 15-50 μm, with several domains exceeding 100 μm, comparable to reports of single-substrate synthesis. The high crystallinty of monolayers was confirmed by the quality of light emission at the direct 1L bandgap of 1.86 eV (known as the A-exciton). Finally, the single-crystal nature of the largest domains was confirmed by TEM. TEM also showed that the d-spacing between lattice planes corresponded exactly to the prior literature, further confirmation of the efficacy of this technique.

The novelty of this method lay in the unique combination of layer-by-layer, ALD-like deposition of successive precursors with liquid chemistry. This combination allows for deposition of a molybdenum-containing precursor without the forcing conditions of temperature, pressure and atmosphere required in traditional ALD. The use of a water-soluble precursor mitigated the effect of impurities on the final MoS_2 film. The method produced crystals comparable in lateral size and quality to CVD, the currently preferred method of monolayer growth, which is a good case for the efficacy of this new method. Previous work combined spin-coating with CVD and liquid-phase deposition on a treated substrate or has used different substrates. The unique combination of parameters in this study offers advantages that previous methods have lacked. These include practical simplicity, short annealing time and a single-substrate approach.

Table 3.8 summarises the key advantages obtained in this new method compared to existing techniques in the literature.

Table 3.8 Comparison between liquid ALD and existing techniques

Prior art	**References**	**Improvements in new method**
Surface modification or seeding	Refs. [159, 161, 162, 174, 175]	Bare, untreated SiO_2 surface gives good-quality crystals.
Two-substrate method	Ref. [205]	Single substrate improves efficiency.
Complex precursors	Ref. [161]	Commercially available precursors reduce cost and complexity.
Multiple deposition cycles	Ref. [37]	Single cycle improves efficiency.
Polycrystalline film	Refs. [18, 162]	Large single crystals better for optoelectronic applications.
Long/multistep annealing	Refs. [18, 37-38]	Single, short anneal gives good-quality crystals.

Although growth on bare substrates proved to be very successful for single crystal growth, the evidence from patterned substrates suggested that the edge effect played a role in promoting large-scale film growth over a region of several hundred microns. To this end, the optimal pillar height by RIE was 31 nm on SiO_2, leading to MoS_2 coverage over several hundred microns. The etching of several hundred pillars on the substrate multiplied the edge effect over a large area, leading to an improvement in film size compared to the bare substrate. However, the resulting film was few-layer in thickness and unlikely to be monocrystalline over such a large area. Structural characterisation by TEM could be used to confirm this. Improvements to this technique by optimisation of etching, dip-coating and sulphurisation parameters will be an interesting area of future work, and it is anticipated that large-scale monolayer exhibiting monocrystallinity over several hundred microns could thus be obtained.

How do the results herein advance the field? First of all, in the choice of materials, it is extremely promising that MoS_2 can developed as an alternative to silicon in optoelectronic technologies. MoS_2 possesses several advantages over silicon: a direct and tuneable bandgap and greater resistance to voltage-induced breakdown. The new method developed in this chapter was shown to preserve the favourable properties of crystalline monolayer MoS_2, demonstrated by photoluminescence and TEM, making this method ideal for the development of this and other materials for optoelectronic technologies beyond silicon. Second of all, present strategies for monolayer synthesis, even by the best CVD and ALD techniques, generally lead to polycrystalline films obtained with very harsh reaction conditions using complex precursors. Polycrystalline films are generally unsuitable for optoelectronic applications, due to the deleterious effects of grain boundaries on electronic properties, such as contact resistance. The method developed in this chapter thus contributes to the field in two ways. The introduction of a step performed entirely in the liquid phase can reduce the cost and increase the volume of production relative to traditional gaseous CVD and ALD. The synthesis of large single crystals will open up optoelectronic applications where the use of polycrystalline films has been suboptimal.

Another area for future work will therefore be to integrate these MoS_2 monolayers into devices such as transistors and LEDs. The sharpness of the contact between the film and the substrate will be crucial for electronic properties, and there was some evidence from Raman spectroscopy that surface functionalisation of the silica substrate by KOH helped to achieve this. However, it can be improved by carefully controlling the functionalisation parameters, such as etchant, concentration, temperature and dipping time. Another way to improve the surface contact in future may be to consider an epitaxial substrate. Results from growth on sapphire indicated that large single crystalline domains were obtained. This method is complicated by the need for careful transfer of the as-grown film from sapphire to SiO_2 for characterisation.

A future mechanistic study may focus on investigating the properties of the as-deposited molybdenum-containing precursor, which will include an investigation of the dip-coating process.

This was not possible here due to constraints on availability of characterisation techniques, but understanding the properties of the as-deposited precursor will lead to a clearer understanding of the mechanism, for instance, if final product is a few-layer film, then at which step has the greatest effect on the thickness? The use of manual dip-coating in this study introduced an element of human error, but the incorporation of a mechanical dip-coater in future work will help with industrial viability by improving reproducibility.

Chapter 4 Development of MoS_2–WS_2 Vertical Heterojunction Based on Liquid ALD

4.1 Background and motivations

A heterojunction occurs at the interface of two different, crystalline semiconductors, such as that in a composite material made by alternating two or more TMdCs. This is in contrast to a p-n homojunction, which occurs at the interface of two types of the same semiconductor, each type with a different doping regime. A heterojunction can be synthesised in a number of ways that will be discussed in Section 4.3. Heterojunctions offer a route towards accessing novel properties that arise specifically because of the quantum confinement of electrons in two materials with different band structures, such as band alignment and charge separation. In addition, some heterojunctions have exhibited enhanced thermal stability and improved light emission efficiency. A heterojunction occurs in heterostructured materials, of which there are two types: lateral and vertical.[207]

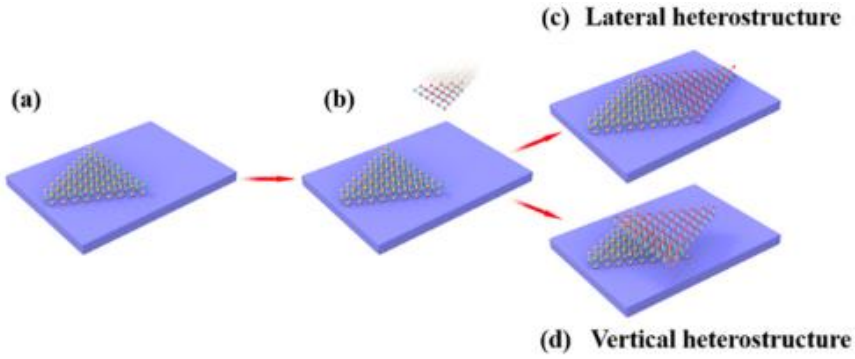

Figure 4.1 *Morphology of generic lateral and vertical heterostructures*

In the lateral heterostructure, the first material (a) is aligned in plane with the second material (b), creating a polycrystalline lattice (c), while in the vertical heterostructure, the contact is at the interface, creating an epitaxial, vdW-type arrangement of independent lattices (d). Image reproduced from ref. [207] under Creative Commons licensing.

In a lateral heterojunction, the unique optoelectronic effects can only be observed at the crystallographic boundary between the two materials. This presents a rather small surface area over which interesting chemistry and physics can occur.[16] The development of a vertical heterostructure, wherein the materials are deposited on top of each other rather than side-by-side, is one way of eliminating this issue. Provided that the contact at the interface is clean, the entire surface area of the materials can be utilised. The vertical heterostructure is also known as a van der Waals (vdW) heterostructure, because the interlayer bonding is vdW only, and it should be noted that these terms are used interchangeably in the literature.

vdW heterostructures based on TMdCs offer a route towards novel properties and applications, some of which are discussed in this section.[79] Firstly, there is a wealth of structural possibilities owing to a combination of any number of 2D materials. As the properties of heterostructures depend on the starting materials used and their alignment with respect to each other, this diversity of possible structures allows optical properties to be very precisely fine-tuned in a way that single layers do not allow.[208] For example, the highest carrier mobility in a graphene transistor has been observed in a heterostructure with h-BN (~60,000 $cm^2 V^{-1} s^{-1}$), a structural analogue.[209] Some heterostructures have exhibited unusual self-cleaning behaviour.[210] This property relies on attaining the cleanest possible interface between the heterostructured materials such that the affinity between the two interfaces is greater than that between crystal and surface contaminant. Thus, the contaminants are "pushed out" by the heterostructure in order to achieve the largest common interface. Among the most interesting of the unique properties of vertical heterostructures is the phenomenon of type II band alignment. This occurs where the CB energy maximum and VB energy minimum reside in different materials, leading to separation of photoexcited electrons and holes.[211] Such a charge separation has improved external quantum efficiency of photovoltaic cells.[16, 212, 213] In some vertical heterojunctions of $MoSe_2$ and WSe_2, the resulting interlayer excitons are tuneable and have unusually long lifetimes, ~1 ns, an order-of-magnitude improvement on conventional, intralayer excitons.[214] Hong *et al.* predicted that type II band-aligned heterojunctions could improve optoelectronic device performance due to long-lived excitonic states and femtosecond charge-transfer dynamics.[215] In-depth discussion of heterostructure properties is found in refs. [79] and [208] and references therein.

The unique properties of heterostructures, especially vertical heterostructures, described herein provide the motivation for finding a synthetic route that is low-cost and produces high-quality heterostructures in the correct configuration. This will open up an industrially viable route towards exploiting the properties of heterostructures.

4.2 Materials

Having addressed the background and possible applications, it is important to consider what materials could be conveniently used for a study of this nature. So far, much of the work on vapour-phase growth of graphene- and TMdC-based heterostructures has been limited to those materials with commensurate lattices.[15, 17, 20, 215, 216] Synthesis of heterostructures of non-lattice-matched 2D materials is complicated by strain-related effects and does not always lead to sharp interfaces. Therefore, there are consequences for the heterostructure's optoelectronic properties (as explained in Section 3.6.5). Careful choice of substrate is one way to improve vdW epitaxy of non-lattice-matched starting materials, and graphene and h-BN have shown some promise to this end.[217-222] However, such concerns can be sidestepped for the purpose of this study by limiting the

focus to lattice-matched materials. Fortunately, many TMdCs possess mutual lattice-matching, such as MoS_2 and WS_2, as shown in Table 4.1 where M is the metal and X is the chalcogen:[223]

Table 4.1 Lattice-matching in TMdCs (ref. [223])

Material	Lattice parameter/Å	M—X bond length/ Å
MoS_2	3.17	2.41
WS_2	3.17	2.41
$MoSe_2$	3.31	2.53
WSe_2	3.31	2.54
$MoTe_2$	3.54	2.72
WTe_2	3.54	2.73

The table shows that good combinations of materials are those that have the chalcogenide in common. The phenomenon of type II band alignment has led to interesting properties in MoS_2—WS_2 vdW heterostructures. Hong *et al.* observed ultrafast charge transfer (~50 fs) in the photoexcited heterojunction.[215] Specifically, the electron—hole pair separation occurred by p-type doping of MoS_2 VB holes into the WS_2 VB, as illustrated in Figure 4.2.

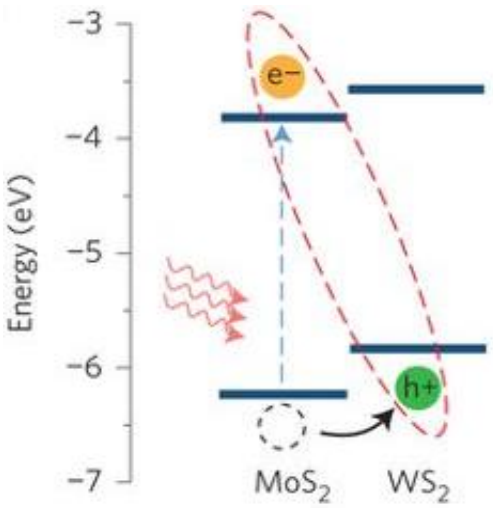

Figure 4.2 *Electron—hole pair separation in MoS_2—WS_2 vdW heterojunction*

Optical excitation of the MoS_2 A-exciton leaves behind holes in the VB. The small energy VB offset between the two materials can lead to p-type doping of MoS_2 VB holes into the WS_2 VB. This spatial localisation of charge carriers is a unique feature of certain heterostructures. Image reprinted by permission from ***Springer Nature Customer Services Centre GmbH: [Springer Nature] [NATURE NANOTECHNOLOGY] ref. 215 COPYRIGHT*** *2014*

The consequence of this charge separation is that photoexcited electrons are preferentially localised in the MoS_2 electronic bands, while holes preferentially bind to the WS_2 bands – a unique spatial separation of charges rather than only energetic separation.

The method developed in Chapter 3 applies to MoS_2. In light of the material considerations presented herein, investigating the development of an MoS_2—WS_2 heterostructure is a sensible application of that method.

4.3 Synthesis

Much like the 2D materials, vdW heterostructures have been prepared by mechanical exfoliation, including MoS_2—$MoSe_2$, MoS_2—WSe_2 and many others.[16, 211, 224-226] Conceptually, this is straightforward: two monolayers are exfoliated and brought into contact on top of the desired substrate. In practice, there are some complexities involved. In a typical procedure, shown in Figure 4.3,[79] a mechanically exfoliated flake is transferred onto the target substrate. This flake becomes the bottom layer of the heterostructure. The second mechanically exfoliated material is either dry-exfoliated as in the figure or transferred to a sacrificial polymer layer, such as PMMA. The PMMA—film is transferred to an optically transparent stamp such polydimethyl siloxane (PDMS) and lowered onto the bottom material under microscopic observation to ensure alignment. The polymers can then be removed by dissolution.[14, 214]

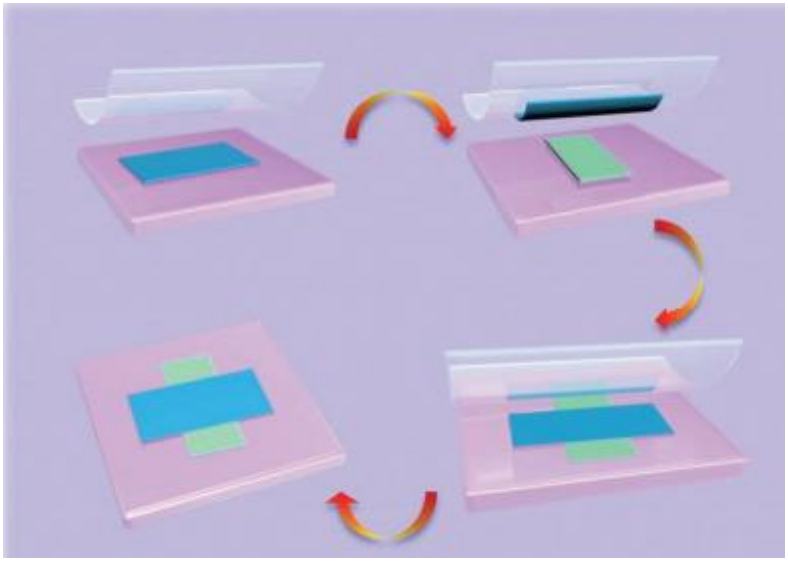

Figure 4.3 *Heterostructure synthesis by mechanical exfoliation*

A mechanically exfoliated flake is transferred to a second material. The transfer of the top material (blue) is aided by the use of PDMS backing in order to achieve a clean contact with the bottom material (green). The contact is achieved using an optical microscope and micromanipulators. Image reproduced from ref. [79] under Creative Commons licensing from J. Wiley & Sons, Inc.

This technique suffers from the many drawbacks of mechanical exfoliation, as have been previously outlined in Section 1.3.1. Additionally, the polymer removal process tends to leave residues, which affect the contact of atomic layers and hinders any subsequent processing such as further stacking. This has been overcome by a variation of the technique known as pick-and-lift, [164] which uses poly(propylene) carbonate (PPC) film as a second sacrificial layer that is removed by heating to soften as shown in Figure 4.4.[208, 227] However, scalability is an insurmountable problem in all mechanical exfoliation processes.

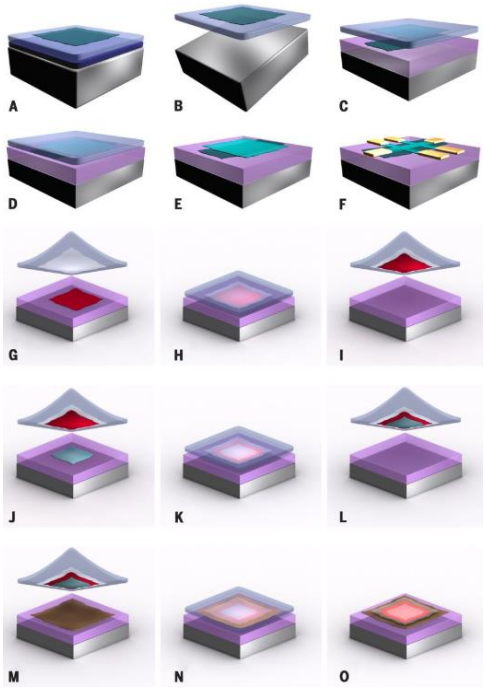

Figure 4.4 *Pick-and-lift technique*

A-F show the mechanical transfer technique, as previously explained, except that a 2D crystal is prepared on a double sacrificial membrane and removed from the substrate by dissolving only one membrane. In the pick-and-lift method, as-prepared crystal (B) is aligned on top of another (G). The strong, interlayer vDW interaction is used to lift both crystals at once using the second membrane. The process is repeated as desired (I-L), the stacked heterostructure is then transferred to a final substrate (M-N) and the second membrane removed (O). Image reproduced from ref. [208]. Reprinted with permission from AAAS.

Heterostructure synthesis by bottom-up, vapour-phase approaches has benefitted from scalability and clean contact. One method recently used is PVD (see Section 1.3.2).[19] This is a versatile process that exploits different volatilities of the target materials. For example, WS_2 boils at 1057 ℃ and WSe_2 at 1190 ℃. This allowed for a layer of WSe_2 to be deposited at the edges of WS_2.[228]

CVD allows for lower temperatures to be used with much greater control over deposition (see Section 1.3.2 for the limitations of PVD). CVD can be used for vertical and lateral growth.[219, 229-234] Lower temperatures can be used because it is not necessary to maintain a temperature above the material's boiling point. Controllability of the process is important in order to select for the vertical heterostructure rather than the lateral one (see Figure 4.5).[203]

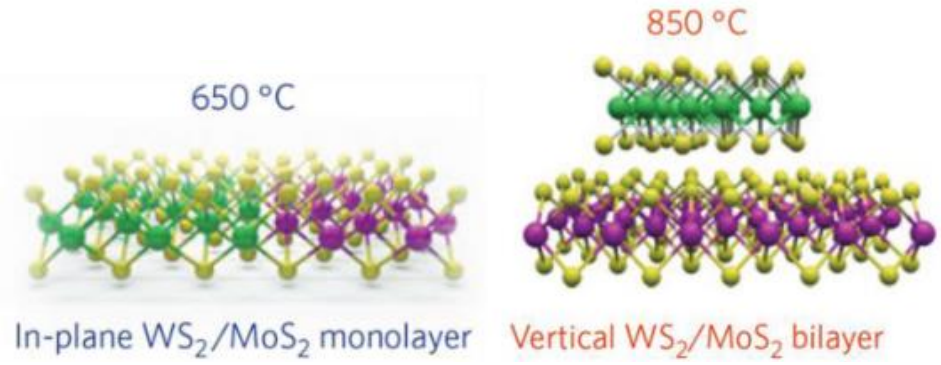

Figure 4.5 *Thermodynamic effect on contact morphology*

This figure shows the importance of annealing temperature for the morphology of the heterostructure. Using a low temperature, e.g., 650 ℃ in the case of a WS_2—MoS_2 heterostructure, produces an in-plane structure where the growth of second material can only occur at the crystallographic edge of the first, due to the seeding effect. In contrast, the thermal energy provided to the second material precursor at a high temperature, ~850 ℃, is sufficient to overcome the vertical nucleation barrier. Image reprinted by permission from ***Springer Nature Customer Service Centre GmbH: [Springer Nature]*** *[****NATURE MATERIALS****], ref. [203],* ***COPYRIGHT*** *2014*

Gong *et al.* demonstrated that MoS_2—WS_2 heterojunctions can be grown at 650 ℃. However, at such a low temperature, the nucleation and growth of WS_2 is extremely difficult to achieve, and so there is only limited potential for vertical growth of WS_2 by nucleation on top of MoS_2. In these conditions, the lateral/in-plane heterostructure dominates because of the reduction in nucleation energy at an existing crystal edge (seeding effect). Increasing the temperature up to 850 ℃, however, strongly favours the vertical heterostructure. This difference suggests that, at such high temperature, the thermodynamic barrier to vertical rather than lateral nucleation is overcome.[203] This points to thermodynamic considerations as being key to selectivity for the vertical or lateral heterojunction.

In a relatively young field, there are a few other syntheses of MoS_2—WS_2 heterojunctions by CVD.[215, 216, 235-237] At the time of writing, no process explicitly described as an ALD has been published in the field of TMdC heterostructures. The novelty of the method demonstrated in this chapter will be in the application of an ALD-type method to the synthesis of a TMdC heterostructure. This synthesis of MoS_2—WS_2 based on the method developed in the previous

chapter will require the less volatile component (WS_2) to be deposited first. That is because sulphurisation of tungsten requires a higher temperature than the thermal stability of MoS_2 would allow (see Section 3.6.1). Thus, sulphurisation of tungsten in the presence of any molybdenum-containing species would alloy the materials. As MoS_2 is thermally unstable at T > 800 ℃, this means that only MoS_2 can be deposited on top of WS_2 by ALD-type growth rather than *vice versa.*

It is expected that this method will advance the field by opening up layer-by-layer routes towards heterostructures, thereby overcoming the risks and complications of CVD (see section 1.3.2). The liquid component will be important for reducing the cost of heterostructure synthesis and improve the industrial viability.

4.4 Characterisation

Raman and PL spectroscopy are the optimum methods to probe the optical properties of heterostructures due to efficient, accurate and non-destructive measurements.

For a discussion of the characteristic Raman modes of MoS_2, see Section 3.4. The characteristic peaks of WS_2 occur at E_g = ~351 cm^{-1} and A_{1g} = ~420 cm^{-1}.[238, 239] Small variations in these values may be expected depending on thermal and strain-related effects. Even accounting for those, the peak separation ($\Delta\overline{\upsilon}$) in the bulk is ≥69 cm^{-1}. Monolayers grown by vapour-phase techniques will yield $\Delta\overline{\upsilon}$ = 61.0-63.5 cm^{-1}, with variations again attributable to thermal or strain effects. One may expect such effects in the WS_2 layer, grown on non-epitaxial SiO_2/Si. However, given the close lattice-matching of MoS_2 with WS_2, growth of the MoS_2 overlayer should be epitaxial, so strain-related effects should be minimised in the overlayer.

For optoelectronic and photonic applications, good light emission is an essential property. A discussion of A- and B-exciton emission in 1L-MoS_2 is found in Section 3.4. For WS_2, the A-excitonic peak occurs at ~2.03 eV with a shoulder peak also occasionally observed, attributed to a trion.[240-242] In both materials, the layer-dependence of the bandgap makes PL a useful diagnostic tool for monolayers as the bulk materials do not possess direct bandgaps and will not exhibit PL.

SEM of the heterostructure may be informative because of the different contrasts obtained from each material,[203] depending on layer thickness and the metal's atomic number.

Due to the bandgap, TMdC heterojunctions may undergo charging, so to minimise charging effects while preserving the sample, a thin piece of carbon tape or silver tape contacting the material edge with the underlying sample holder will be used to ground the heterojunction.

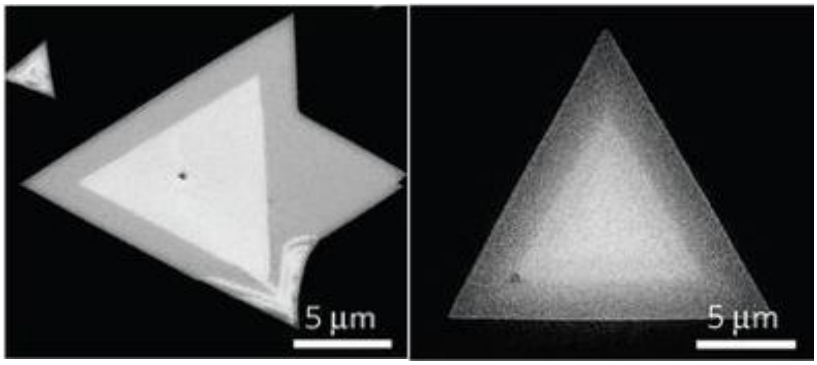

Figure 4.6 *SEM images of vertial (L) and lateral (R) heterostructure*

The vertical heterostrucuture was CVD-grown WS_2 on MoS_2, and the lateral structure was WS_2 at the edge of MoS_2. Variations in contrast identify the materials and the grain boundary between them. It is clear that the vertical heterostructure is easy to identify from contrast variation in SEM. Image reprinted by permission from ***Springer Nature Customer Service Centre GmbH: [Springer Nature]*** *[**NATURE MATERIALS**], ref. [203],* ***COPYRIGHT*** *2014*

XRD can scan an entire substrate in a very short space of time – about ten minutes per 1×1 cm substrate at a good resolution – and is very sensitive to crystallinity.

4.5 Experimental details

4.5.1 Tungsten deposition

Tungsten was deposited by plasma sputtering using a W target (99.999% purity). 1×1 cm dice of substrate **[1]** were used. The base pressure employed was 1.5×10^{-6} Torr and a working pressure of 1.2×10^{-2} Torr. A power of 40 W was used for 1 min. deposition time, and this was the lowest power that could be used while maintaining stable plasma.

4.5.2 Sulphurisation of W and annealing/post-annealing

Sputtered tungsten films were sulphurised under different parameters to determine optimal conditions for few-layer growth.

After initial characterisation, WS_2 film W3 was subjected to high-temperature post-annealing in order to improve crystallinity before heterostructure deposition. Post-annealing was performed in Ar + H_2. The temperature was ramped up to 600 ℃ in 23 min. and maintained for 30 min. in the presence of H_2, before the H_2 was switched off for the remainder of the post-annealing process. The temperature was ramped up to 1000 ℃ in 20 min. and maintained for 1 h in Ar, followed by

cooling back to 600 ℃ for a further 30 min. in the presence of H_2. This was followed by natural cooling in Ar.

Table 4.2 Tungsten sulphurisation parameters

Sample	**Carrier**	**Flow rate/ sccm**	**T./℃**	**Ramp rate/ ℃ min^{-1}**	**t./min.**
W1	N_2	~100	900	10	60
W2	Used for EDXS				
W3	N_2	~100	900	10	240

4.5.3 Vertical growth of MoS_2

On the as-grown sample WS_2 film W1, MoS_2 was grown by conventional CVD based on the process originally described by Huang *et al.*,[243] using $MoCl_5$ (supplied through a bubbler at a vapour pressure of 10^{-6} kPa) and H_2S (dissolved in Ar at 50:400 sccm). The carrier gas was Ar at 450 sccm, and both precursors were independently fed into the quartz reaction tube via an injection tube. The temperature was ramped to 850 ℃ at 10 ℃ min^{-1}, held at the reaction temperature for two minutes of deposition time, and allowed to cool naturally at the end of the process.

On the post-annealed WS_2 film W3, the ammonium heptamolybdate precursor was dip-coated from 0.1 g mL^{-1} aqueous solution. The solution was gently heated to 80 ℃ overnight, allowing solvent evaporation to proceed at a rate of 1.5 mm hr^{-1}. The dip-coated Mo-containing precursor was sulphurised in CS_2 under an N_2 atmosphere according to Scheme 3.1(b). The temperature was ramped to 750 ℃ at 10 ℃ min^{-1}. The sulphur-containing precursor was fed into the system via a nitrogen bubbler and the temperature maintained for 1 h. The tube furnace was allowed to cool naturally at the end of the process.

4.5.4 Synthesis outcomes

For clarity, the different samples are described below:

W1: W sputtered → Sulphurised in CS_2, 1 h → MoS_2 grown by conventional CVD as control

W2: W sputtered → Stored for several weeks and imaged by EDXS for signs of oxidation

W3: W sputtered → Sulphurised in CS_2, 4 h → Post-annealed in Ar + H_2, 1 h → MoS_2 grown by liquid ALD as per methodology described in Chapter 3

4.5.5 Characterisation

The sputtered tungsten films were characterised by OM using an Olympus DX51 microscope with top-view imaging (DP12 digital camera system).

Energy—dispersive x-ray spectroscopy (EDXS) was used to characterise the extent of oxidation of the as-prepared W film using an Environmental FE-SEM FEI XL30. Acceleration voltages of 5-15 keV and acquisition times of 30-60 s were selected, and Cu tape was used to ground the sputtered W film. These data were supplemented by XRD measurements acquired using a Rigaku SmartLab system. The x-ray source used was the Cu Kα-line at 1.54 Å. The 2θ range was 10-70°, and substrate dimensions of 10 × 10 × 0.5 mm were selected as sample alignment parameters.

WS_2 film was characterised by OM and Raman spectroscopy both before and after post-annealing. Raman spectroscopy was performed on a Renishaw RL532C10 InVia microscope with a 532 nm 500 mW excitation source and a grating of 1800 lines/mm.

Finally, MoS_2—WS_2 heterostructures were characterised by OM, Raman spectroscopy and XRD.

4.6 Results and discussion

4.6.1 Tungsten deposition by sputtering

Firstly, OM provided a very quick visual guide as to the success of W sputtering. Tungsten presents a good contrast against the surface of 285 nm SiO_2/Si (as in Figure 4.7):

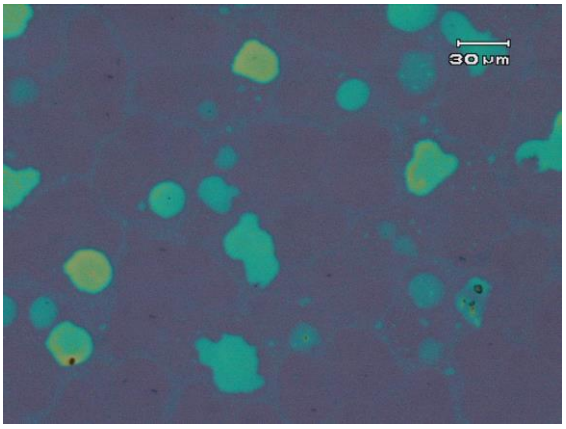

Figure 4.7 *OM image of as-sputtered W film W1 showed good optical contrast*

Tungsten was deposited on SiO_2 by plasma sputtering using a W target. OM images show small islands, ~20-30 µm, exhibiting good contrast against the familiar substrate surface. This was the morphology of sputtered tungsten.

In Figure 4.7, islands of tungsten are seen as light blue regions against the violet substrate background. Large-scale counting was not performed, so no definitive size distribution is available, but islands of ~30 μm are clearly visible in the image. Other regions of the substrate showed similar contrast and similar-sized islands.

To determine optimal sulphurisation parameters, it was important to know what was being sulphurised. Therefore, EDXS was performed to analyse the extent of oxidation, if any, of the as-prepared W film.

Tungsten exhibits two major x-ray peaks: the Lα-line at 1.774 eV and the M-line 8.396 eV. However, the former lies at the blue edge of the major Si peak, the Kα-line at 1.739 eV. The resolution of the apparatus was ~130 meV, so the two peaks are mutually unresolvable, especially given the overwhelming intensity of the Si peak. Therefore, the W Lα-line, although stronger in intensity than the M-line, was not considered to be helpful in this case (Figure 4.8). Only the M-line (Figure 4.9) will be considered in the discussion. The penetration of incident X-rays is proportional to the acceleration voltage. A high acceleration voltage therefore leads to a more intense Si peak with respect to the W peak. It is possible to mitigate the effect of Si and "bring out" the W Lα-line by using a low acceleration voltage. In practice, however, the minimum acceleration voltage at which any x-ray emission can be detected is 5 kV. Even at 5 kV, the Si line was of substantial intensity.

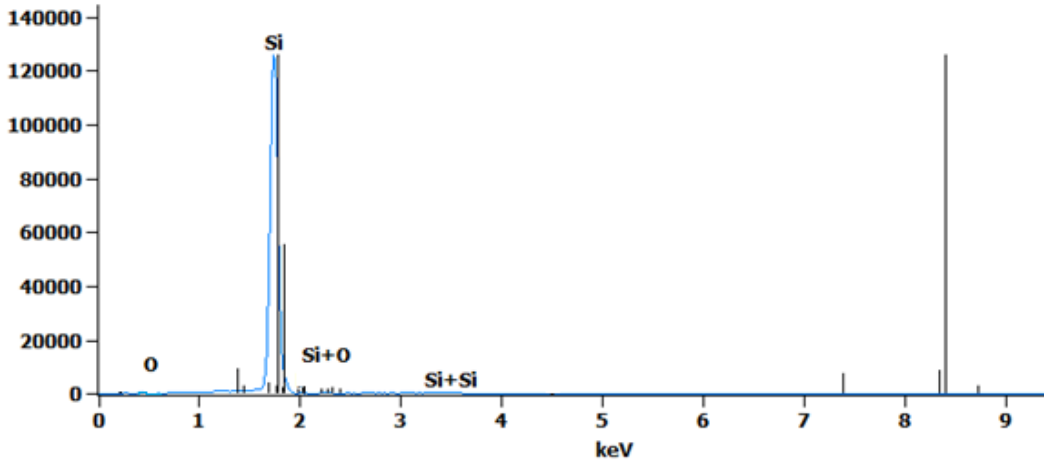

Figure 4.8 *EDXS spectrum of as-sputtered W film W2*

The acquired spectrum is shown as a blue trace. The sharp lines are the predicted peaks arising from Si and W. The predicted W Lα-line can be seen at 1.774 keV close to the Si Kα-line at 1.739 keV, along with the W M-line at 8.396 keV. The W Lα-line was difficult to resolve against the Si line, so it was not a useful diagnostic of W deposition in this case. Instead, the M-line was used to prove that W was present.

In the EDXS spectrum in Figure 4.8, the experimental trace is superimposed over the predicted Si and W peaks, highlighting the difficulty of resolving the W Lα-line. The W M-line, in contrast, was present in this spectrum, albeit very weak. Zooming in on the high-energy region will show this (Figure 4.9). However, it is also clear that if one predicts the position of the O peak at 0.525 eV, no experimental peak was observed that corresponded to the O line.

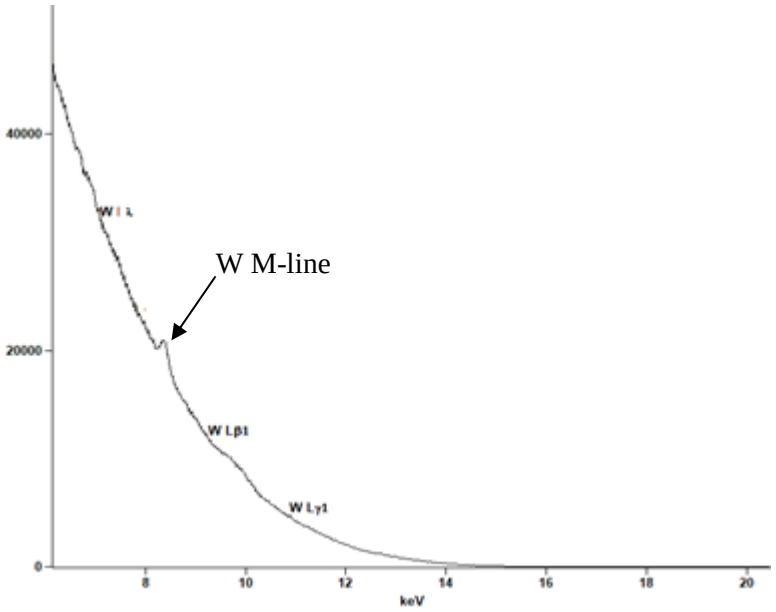

Figure 4.9 *W M-line in EDXS spectrum of sputtered W film*

Zooming in on a narrow range of x-ray energies shows the W M-line at 8.394 keV, close to the expected value. It was a very weak signal, and this was attributed to the thin film having few scattering centres. The presence of this line confirmed W deposition on the SiO_2 substrate by sputtering.

Looking at the spectrum in Figure 4.9, it is clear that the W M-line was present at 8.394 eV. It was very weak, and this followed from the fact that a thin film has few scattering centres. However, the detection of that peak confirmed W deposition by sputtering. This spectrum was compared to an SEM image of the entire island (Figure 4.10):

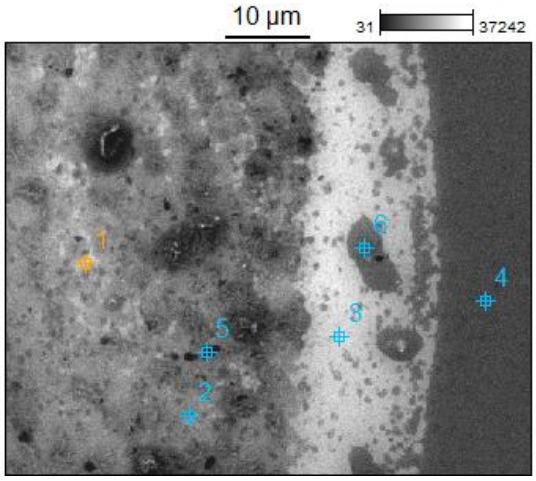

Figure 4.10 *SEM image of as-prepared W island*

Each labelled point 1-6 corresponds to a point spectrum acquired in EDXS mode. The regions of different brightness are indicative of charging, the implications of which will be explained in the discussion.

The spectrum of W was, in fact, taken from point 6. Looking at the SEM image, one notes that the regions corresponding to the presence of tungsten were dark. This is because W is metallic, so does not undergo prodigious charging. If one considers the spectrum of a brighter region, point 1 or point 3, there is a clear difference in the low-energy region:

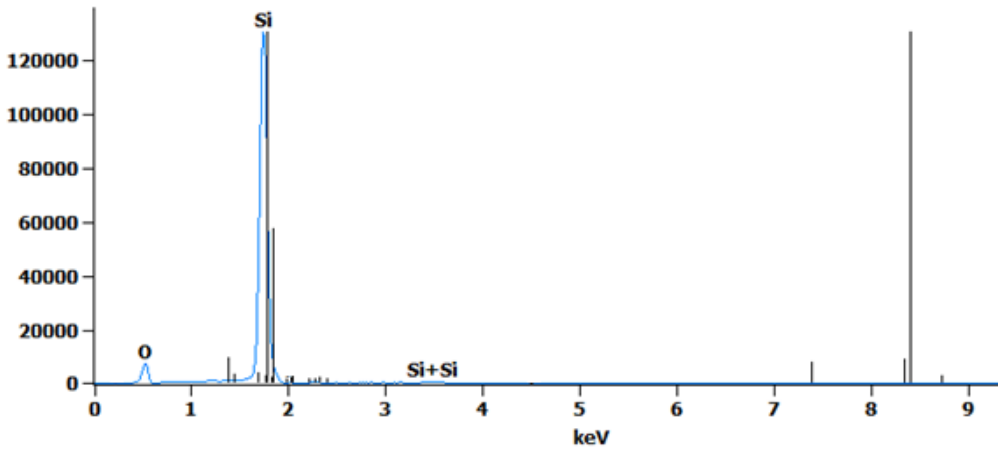

Figure 4.11 *EDXS point spectrum of as-sputtered W film W2, point 3*

The acquired spectrum is shown as a blue trace. The sharp lines are the predicted peaks arising from Si and W. The predicted W Lα-line can be seen at 1.774 eV close to the Si Kα-line at 1.739 eV eV, along with the W M-line at 8.396 eV. An interesting additional peak can be seen, which was at 0.525 keV. This was attributed to oxygen and was evidence of oxidation at point 3, consistent with expectations of charged/bright regions.

The EDXS spectrum in Figure 4.11 showed an acquired peak at 0.525 keV that was not predicted to arise either from Si or W. This peak is the oxygen Kα-line and was therefore attributed to oxidation of the tungsten film. As tungsten oxide has a wide bandgap, it can undergo charging much like an insulating layer, and this means that oxidised regions of the tungsten film would show up as brighter than the purer metallic film. This was confirmed by consideration of the complementary EDXS spectra and SEM morphological data, with regions showing an oxide x-ray peak consistently showing up brighter in SEM. Taken together, the data confirmed deposition of a thin film of W by sputtering, followed by partial oxidation under storage in ambient conditions.

4.6.2 Sulphurisation of W

The order of film deposition is important in heterostructure synthesis. WS_2 requires a higher annealing temperature (850-950 ℃) than MoS_2 (700-800 ℃). It follows that depositing MoS_2 first would not necessarily lead to a good quality heterostructure comprising discrete layers of each material, due to the risk of alloying under the higher annealing temperature of WS_2. For this reason, it was necessary to deposit WS_2 first and then grow MoS_2 vertically on top. In general, the material requiring the higher annealing temperature must be deposited first in an ALD-type process.

Raman spectroscopy and XRD were used to confirm the presence of WS_2 after sulphurisation as outlined in Section 4.5.2. Raman spectra acquired from WS_2 film W3 are shown in Figure 4.12:

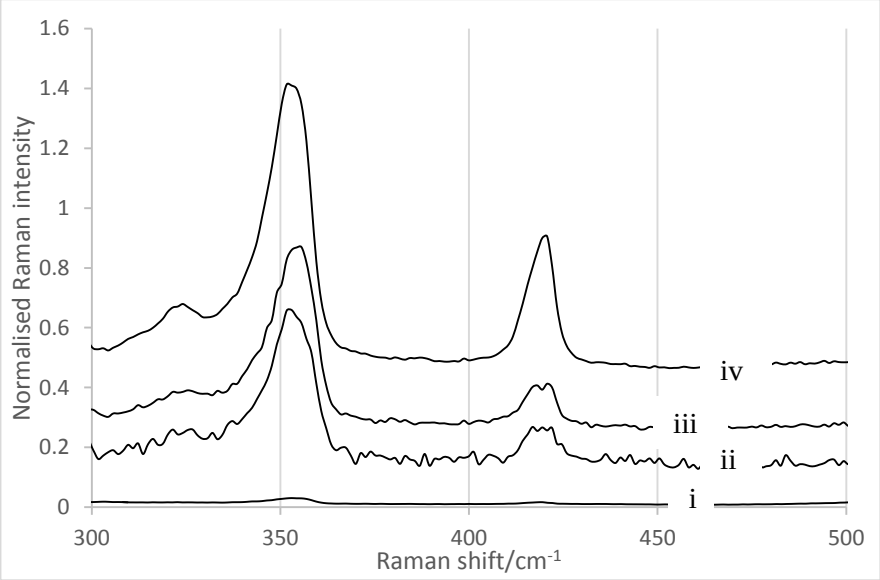

Figure 4.12 *Raman spectra of as-synthesised WS_2 film W3*

The sample was WS_2 grown by sulphurisation of sputtered W in CS_2/N_2 for 4 h. Spectra show peaks corresponding to the E_{2g} and A_{1g} characteristic peaks of WS_2 at 351 cm^{-1} and ~420 cm^{-1}. The peaks were normalised to laser power to allow them to be plotted on the same graph irrespective of acquisition conditions.

The Raman spectra showed the expected vibrational modes of WS_2: the E_g at ~353 cm^{-1} and the A_{1g} at ~420 cm^{-1}.[238, 239] However, spectra i to iii also showed an additional peak at ~326 cm^{-1}, which was attributed to residual oxide.[244] Tabulation of the E_g and A_{1g} peaks suggested variable thickness.

Table 4.3 Key Raman data of as-prepared WS_2 film W3

Region	E_{2g}/cm^{-1}	A_{1g}/cm^{-1}	$\Delta\bar{\nu}/cm^{-1}$	Layer thickness
i	355.6	419.4	63.8	2
ii	353.0	419.6	66.6	3-4
iii	353.0	419.6	66.6	3-4
iv	351.7	420.7	69.0	Bulk

The characteristic peak separation of the monolayer is 61.0 cm^{-1}, increasing to 68.0-69.0 cm^{-1} in the bulk. Therefore, the observed separations were diagnostic of 2-4L, with some bulk also present.

XRD was used to show crystallinity and for phase-identification. Consider the XRD pattern of as-synthesised WS_2 film (Figure 4.13) before post-annealing or dip-coating of the Mo precursor.

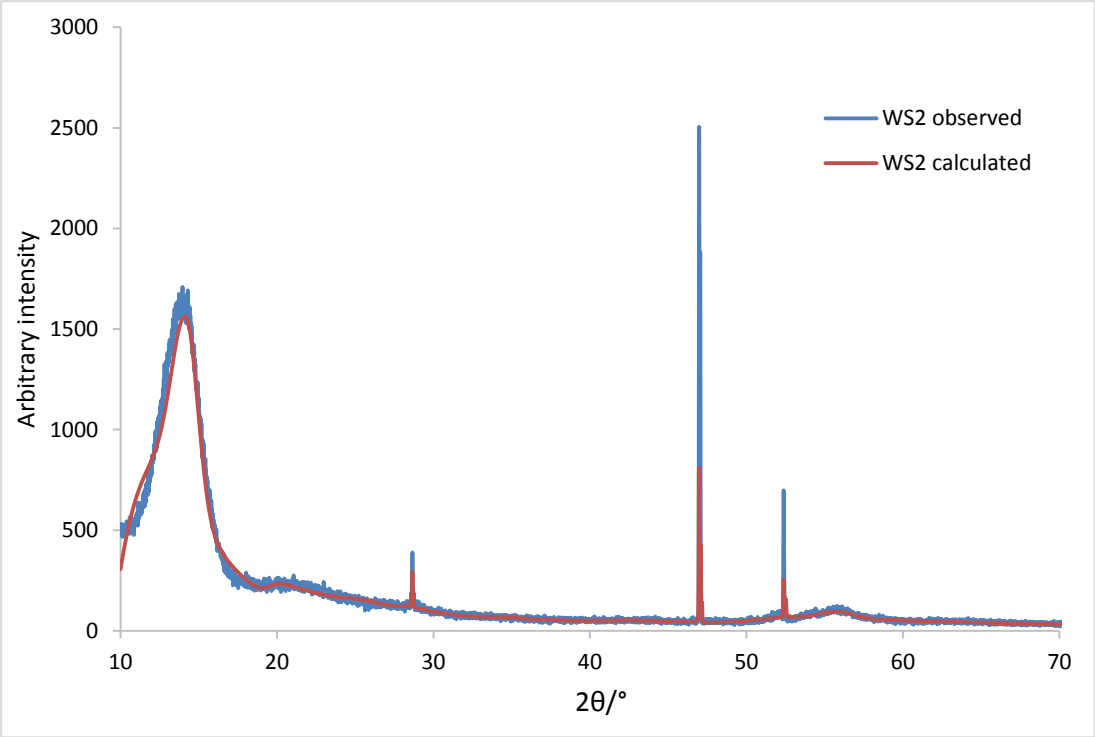

Figure 4.13 *XRD pattern of as-synthesised WS_2*

Pattern acquired using Cu Kα-line (λ = 1.54 Å) as X-ray source. Acquired pattern compared to peaks arising from 3R-WS_2 using PDXL2 software. The acquired and predicted patterns were an exact match indicating 3R-WS_2 synthesis under the conditions used.

The XRD data clearly indicated an exact match between the acquired spectrum and the predicted pattern for the 3R phase of WS_2. The 3R phase is metastable, so post-annealing should effect a phase transformation to the thermodynamically stable 1H phase. This is an area that can be considered during process optimisation.

4.6.3 Effect of post-annealing on WS_2

In contrast to the MoS_2 case, post-annealing of WS_2 was thought to be conducive to crystal quality. This was evidenced by the monolayer PL spectrum in Figure 4.14, which showed photoluminescence from WS_2 after post-annealing. This proved the positive effect of post-annealing in this case, as a result of the stepped process involving H_2. However, this this did not definitively prove the 3R → 1H phase transformation.

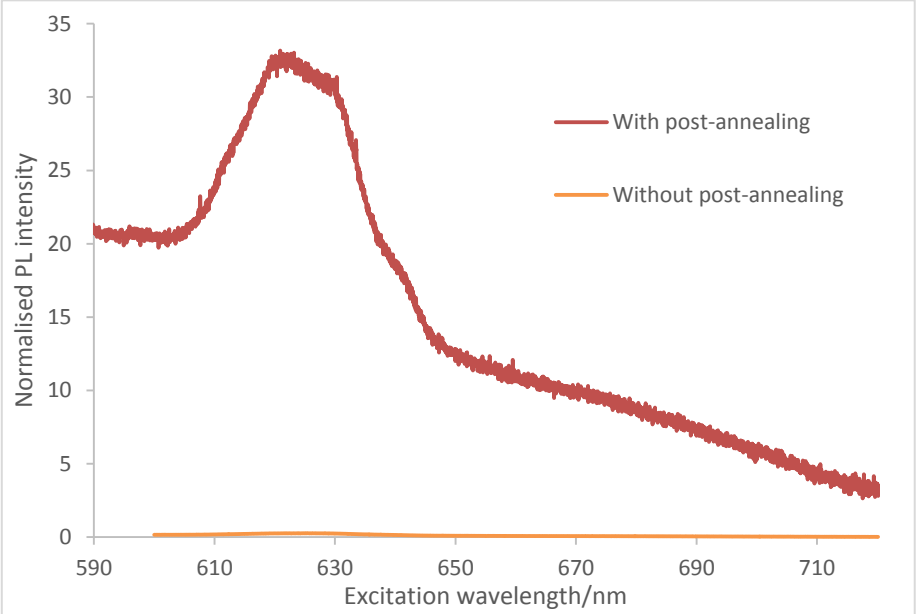

Figure 4.14 *PL spectrum of post-annealed monolayer WS_2 film W3*

Evidence of the positive effect of post-annealing came from comparison of the material's PL properties both with and without post-annealing. Spectra were normalised to laser power to allow comparison irrespective of acquisition conditions. Detection of strong photoluminescence at 621 nm (2.00 eV) after post-annealing was consistent with crystalline WS_2, proving the effectiveness of post-annealing due to the 35-fold improvement in PL intensity.

The monolayer spectrum sat on a rather large background. The presence of a background in the PL spectrum is usually attributed to fluorescence contamination. Nevertheless, the A-exciton was present at 621 nm (2.00 eV). There was a further peak forming a shoulder to the A-exciton. This second peak, occurring at 631 nm (1.96 eV), is attributed to an n-type trion or charged exciton.[245] Unlike an exciton, which is an electron—hole pair, the trion is an excitation comprising two

electrons and a hole. The trion peak in monolayer WS_2 arises due to the intrinsic n-type nature of 1H-WS_2, and a spectrum such as the one in Figure 4.12 was therefore typical for excitation at 532 nm due to photoinduced doping.[242] Although possibly of general interest for applications, this observation is unlikely to be of any synthetic consequence. The observed PL emission was consistent with highly crystalline monolayer WS_2, attesting to the efficacy of post-annealing in this case.[242, 245]

The necessity of hydrogen can be demonstrated by considering that reduction of tungsten(VI) to tungsten(IV), as is required when going from WO_3 to WS_2, is complicated by the low electron affinity of sulphur compared to oxygen. In contrast, hydrogen has a greater electron affinity than both, so hydrogen is able to reduce WO_3 more effectively than sulphur. Precedents in the literature, for example in the selenisation of MoO_3 and WO_3, suggest that hydrogen forms a non-stiochiometric intermediate with the respective metal oxide.[202, 246] It is plausible that a similar mechanism was involved here. Overall, the addition of a small amount of hydrogen at the beginning and end of post-annealing might have been able to improve the crystallinity of the final product by accessing the tungsten(IV) oxidation state. An alternative explanation is that WS_2 is more stable to oxidation than MoS_2. This demonstrated the importance of understanding the extent of oxidation of the sputtered tungsten film, as the presence of oxygen is an important factor in determining appropriate annealing/post-annealing conditions.

4.6.4 Vertical growth of MoS_2

After MoS_2 growth on the same sample, the XRD pattern of the as-grown WS_2—MoS_2 heterostructure showed strong peaks corresponding to the 1H phase (Figure 4.15).

The XRD data clearly indicated an exact match between the acquired spectrum and the predicted spectrum for the 1H phase of MoS_2. It is interesting that the software did not highlight any peaks from the WS_2 layer underneath the MoS_2. This is a good result as it implies a 3R → 1H phase transition in WS_2 under post-annealing. Due to the close lattice-matching of MoS_2 and WS_2, one would not expect to see large differences in the XRD patterns arising from the same phase of both materials.

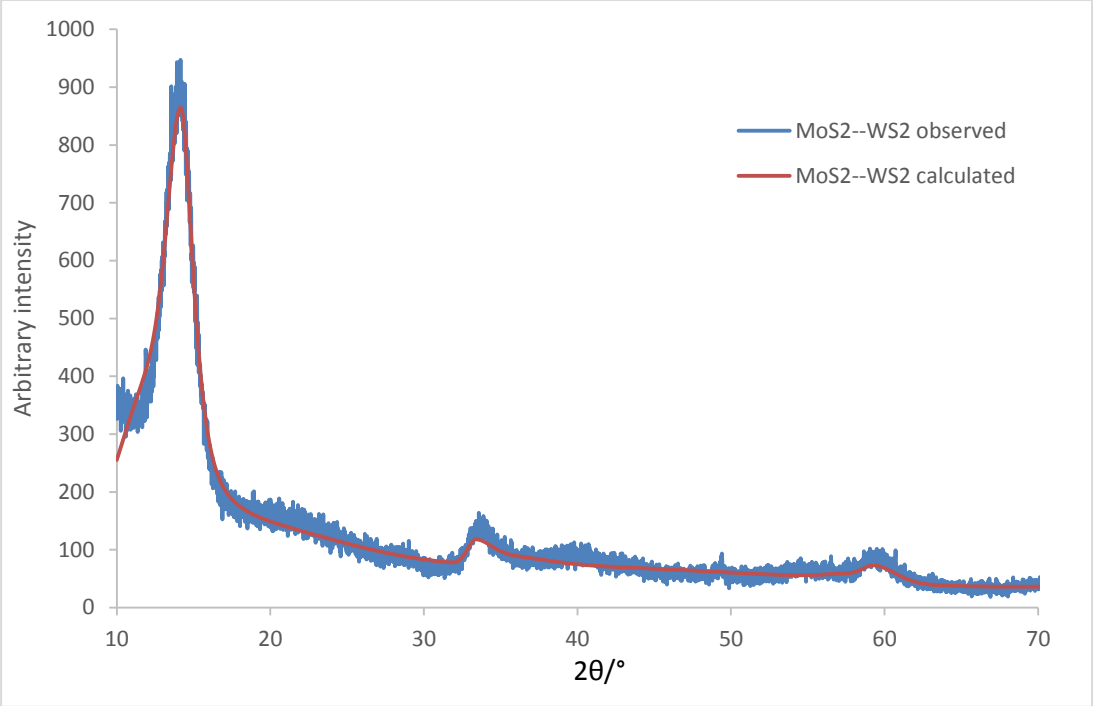

Figure 4.15 *XRD pattern of as-synthesised WS_2—MoS_2 heterostructure W3*

Pattern acquired using Cu Kα emission (λ = 1.54 Å) as x-ray source. Acquired pattern matched peaks arising from 1H-MoS_2 using PDXL2 software. The acquired and predicted patterns were an exact match, indicating 1H phase synthesis. The pattern was consistent with 1H-1H heterostructure synthesis due to the close lattice-matching of the two materials.

In theory, peak intensities could be improved by post-annealing. However, the efficacy of post-annealing heterostructures is uncertain because too high a temperature risks alloying the two discrete species, while too low a temperature is as good as no post-annealing at all.

These data compare favourably to the CVD-synthesised heterostructure W1. Consider first the Raman spectra of the CVD-grown heterostructure, showing the two major modes of MoS_2 (Figure 4.16).

There was a remarkable consistency in peak positions. In the above spectra, two strong peaks are present: either 385.5 cm^{-1} and 405.2 cm^{-1}, or 386.9 cm^{-1} and 406.6 cm^{-1} (depending on the spectrum being viewed). In both cases, the peaks at 385.5 cm^{-1} and 386.9 cm^{-1} were consistent with the E_{2g} mode, and the peaks at 405.2 cm^{-1} and 406.6 cm^{-1} were consistent with the A_{1g} mode. In the absence of a peak at 335 cm^{-1}, these spectra implied 2H phase-pure MoS_2 growth.

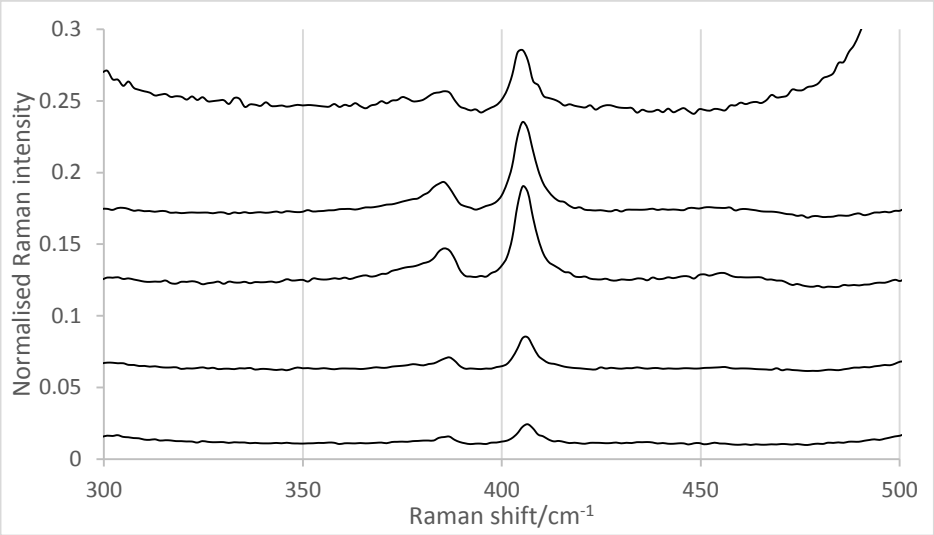

Figure 4.16 *Raman spectra of as-grown WS_2—MoS_2 heterostructure W1*

These Raman spectra were acquired from the CVD-grown heterostructure. The peaks exhibited a remarkably consistent peak separation of 19.7 cm^{-1}, suggesting good coverage of monolayer MoS_2 on top of WS_2. Spectra were normalised to laser power to allow direct comparison irrespective of acquisition conditions.

The peaks exhibited the characteristic $\Delta\bar{\nu}$ = 19.7 cm^{-1}, which was consistent with monolayer MoS_2. No WS_2 peaks could be observed (see Figure 4.12), indicating good coverage of a vertically nucleated monolayer MoS_2 on the WS_2 surface.

The CVD-grown heterostructure W1 offered PL comparable to that in the literature (see Figures 4.17 and 4.18),[215] but crystallinity of W3 (Figure 4.18) could be improved to yield better PL. This is an area for future work.

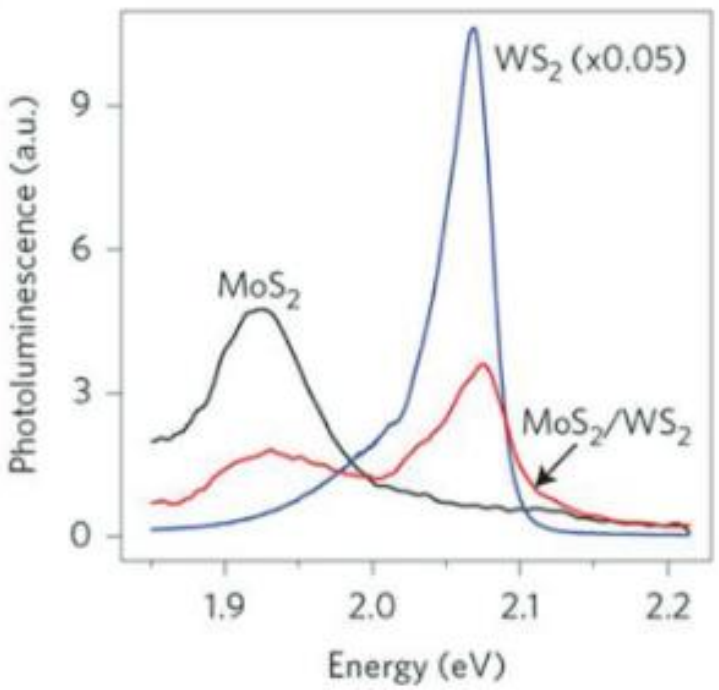

Figure 4.17 *PL emission from 1L MoS_2, WS_2 and MoS_2—WS_2*

Heterostructure PL shows characteristic peaks of both constituent materials, exhibiting a strong peak at ~2.07 eV arising from the WS_2 A-exciton and a weaker MoS_2 A-exciton peak at ~1.92 eV. The exact peak positions and intensities depend on doping and crystallinity, but this serves as a good general approximation of where to find the relevant peaks. ***Springer Nature Customer Service Centre GmbH: [Springer Nature]*** *[**NATURE NANOTECHNOLOGY**], ref. [215],* ***COPYRIGHT*** *2014*

In the experimental spectra taken from W1 (Figure 4.18(a) and 4.18(b)), the A-excitonic peaks occurred in the positions consistent with an MoS_2—WS_2 vertical heterostructure. The WS_2-derived A-exciton emission occurred at 612 nm (2.03 eV) and the MoS_2-derived A-exciton emission at 653 nm (1.90 eV).

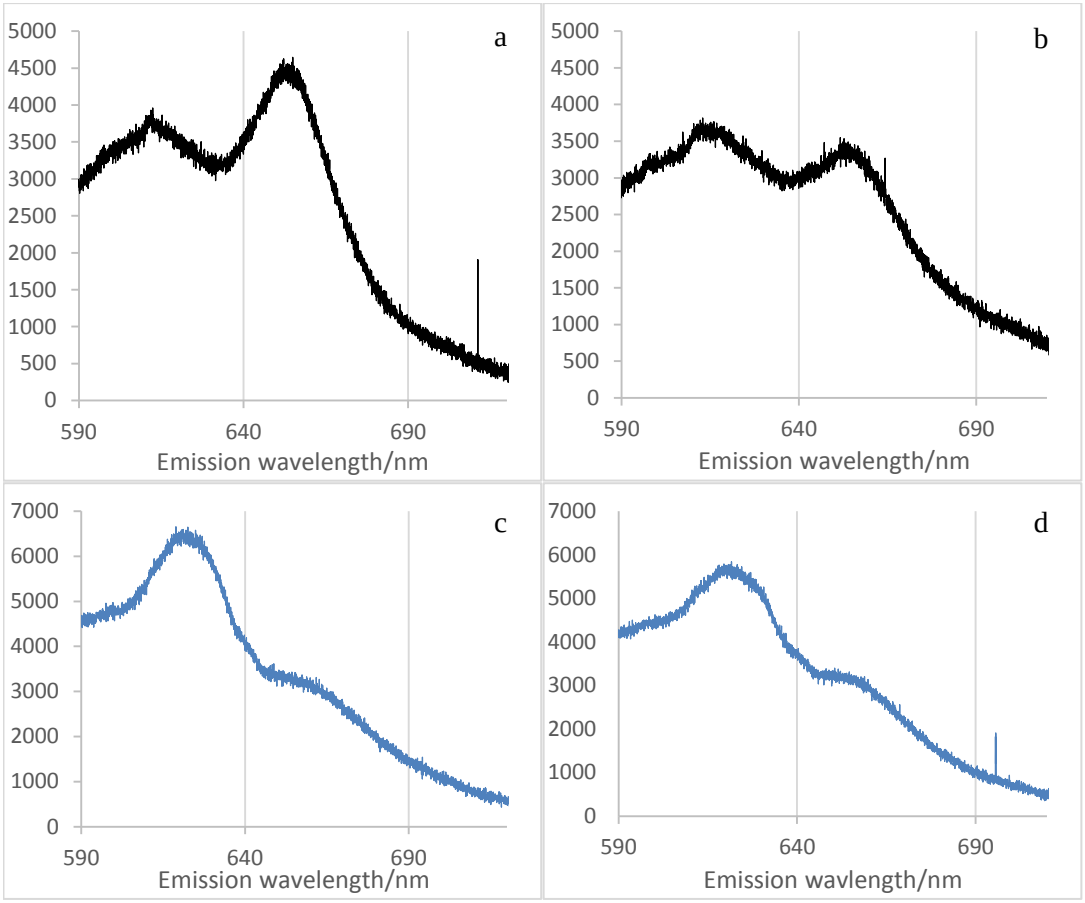

Figure 4.18 *PL emission from CVD heterostructure W1* ***(a, b)*** *and as-grown W3* ***(c, d)***

Spectra ***(a)*** *and* ***(b)*** *were acquired from two regions of the CVD-grown heterostructure W1, while spectra* ***(c)*** *and* ***(d)*** *were acquired from two regions of the liquid-grown heterostructure W3. The top spectra were consistent with the MoS_2—WS_2 heterostructure with WS_2-derived A-exciton emission at 612 nm (2.03 eV) and the MoS_2-derived A-exciton peak at 653 nm (1.90 eV). In contrast, the bottom spectra suggested contradictory outcomes, although they did show some evidence of heterostructure formation.*

In the experimental spectra, the top row in black shows the expected behaviour of the MoS_2 and WS_2 excitons of the CVD heterostructure (Figure 4.18(a) and 4.18(b)), in accordance with the literature spectrum (Figure 4.17). In the bottom spectra, showing PL from the ALD heterostructure, there are some notable differences. The two apparent A-excitonic peaks occured at 661 nm (1.87 eV) and 621 nm (2.00 eV) in Figure 4.18(c), but 650 nm (1.91 eV) and 621 nm (2.00 eV) in Figure 4.18(d). These values were contradictory. In the former case, the peaks were somewhat redshifted with respect to the literature values for the heterostructure and aligned closely with the A- and B-excitons of monolayer MoS_2 (see Section 3.6.3), although the higher-energy B-exciton would usually exhibit lower intensity. In the latter case, the lower-energy peak was consistent with the expected heterostructured MoS_2 emission, but the higher-energy peak was redshifted with respect to the expected heterostructured WS_2 peak. Literature suggests that a peak at 650 nm (1.91 eV) is

also observed at lateral interfaces,[203] but it is of stronger intensity than was observed here. It is possible that some lateral growth of MoS_2 could have occurred at WS_2 edges. This was expected to be minimal, due to the favourable conditions for vertical nucleation. In addition, WS_2 band structure might have been affected by a strain-related redshift attributed to the non-epitaxial substrate. For these reasons, the peaks could not be unambiguously assigned, and the PL emission from the W6 heterostructure was deemed inconclusive. Nevertheless, the WL PL emission was consistent with monolayer growth. Literature shows that a slow substrate-pulling rate leads to deposition of a thinner film of precursor,[107] so the long evaporation time here used as equivalent was thought to be beneficial to film quality in at least one sense.

One sometimes sees a third exciton peak that is derived from neither of the materials in isolation but from interfacial n-type doping of WS_2 VB electrons into the MoS_2 VB, as in Figure 4.19:[216]

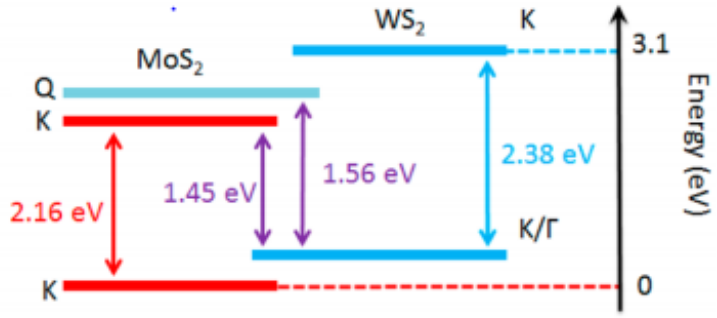

Figure 4.19 *Third excitonic peak arising from WS_2—MoS_2*

The VB of MoS_2 is close in energy to that of WS_2. The expected offset is around 0.7 eV. This is small enough to induce n-type interfacial doping of the MoS_2 band structure in a good-quality heterostructure, leading to excitonic emission at 1.41-1.45 eV, a third PL peak. Image reprinted (adapted) with permission from ref. [216]. Copyright 2016 American Chemical Society.

The n-type behaviour is attributed to the small VB offset of ~700 meV between the two materials.[216] Thus, the interlayer-derived excitonic emission occurs at a longer wavelength than the first two peaks, around 875-855 nm (1.41-1.45 eV).[214] However, this is not always observed. PL effects in WS_2 are particularly dependent on excitation power and intensity, so it is possible that the same dependence exists in the heterostructure. Alternatively, the absence of the interlayer excitonic peak may attest to poor contact.

Issues related to ambiguity of PL emission or absence of expected peaks could be addressed by post-annealing in forming gas to improve the general crystallinity and specifically the quality of the interfacial contact.[16]

4.7 Conclusion and future work

In this chapter, an application of the TMdC synthesis developed in Chapter 3 was successfully demonstrated for the development of an optically active MoS_2—WS_2 heterostructure. Sputtered tungsten was sulphurised in CS_2 for 4 h and post-annealed by a stepped method in a reductive atmosphere. The resulting WS_2 thin film was used as an epitaxial substrate for liquid ALD of MoS_2, leading to a clean WS_2—MoS_2 vertical heterostructure.

The heterostructure conformed to the desired vertical rather than lateral configuration, and this was achieved by controlling the order and temperature of material deposition. Characterisation was performed by Raman and PL spectroscopy as well as XRD and EDXS.

XRD performed on the bottom WS_2 layer aligned closely with the 3R phase pattern. Post-annealing of the bottom WS_2 layer was shown to be effective using PL spectroscopy and XRD to confirm the direct bandgap transition in the post-annealed monolayer, confirming a high-quality monolayer. This highlighted the efficacy of the stepped post-annealing approach using dilute H_2 as a high electron affinity reductant.

Comparison of the liquid-grown and CVD-grown heterojunction suggested a cleaner interface in the latter, as evidenced by PL. The stepped post-annealing approach may offer a route towards improving the contact between the liquid-grown MoS_2 phase and the underlying WS_2 without the risk of alloying.

The novelty of this method lay in the first demonstration of an ALD-type process of heterostructure synthesis. This process benefits from a solution-phase precursor deposition step leading to a potential reduction in production costs and improvement in volume when the process is scaled up. As well as this, the process benefits from straightforward, commercially available precursors unlike traditional CVD.

This work will advance the field by providing a new, alternative route towards heterostructures that benefits from lower cost than existing CVD-type techniques, readily available precursors and less forcing conditions.

One issue in this work has been the quality of the liquid-grown sample against a CVD-grown reference, as measured by PL. PL quality from the liquid-grown sample was inconsistent with that of a vertical heterostructure. This indicated that either the quality of the interfacial contact was poor or that the structure was not fully of vertical configuration. Future work may focus on improving the contact between the monolayers, as well as developing a true liquid ALD using liquid-phase tungsten deposition using self-limiting precursors. The materials thence grown may offer device performance comparable to those materials grown by existing CVD technologies.

Chapter 5 Exfoliation of Tin(IV) Disulphide (SnS_2) by Lithium-Free Intercalation

5.1 Background

In a solar cell, photons interact with semiconducting materials. There are three possibilities for the interaction of the photon with the material:

1. Reflection off the surface.
2. Transmission through the material.
3. Absorption if photon energy is greater than the semiconductor's bandgap.

The third process is the most important for the photovoltaic effect, which is the generation of current in response to absorption of light. The photon is absorbed if the following condition is satisfied:

$$h\nu > E_b \qquad [5.1]$$

where h = Planck's constant

ν = frequency of incident photon

E_b = bandgap of semiconductor

Upon absorption of an incident photon, valence band electrons in the crystal lattice absorb the energy and "jump" the bandgap into the conduction band. The electron leaves behind a hole, which allows other electrons to move freely by diffusion, thus propagating the hole through the network of covalent bonds. In turn, excited electrons diffuse towards a rectifying p-n junction, usually created by two doping regimes in silicon, and accelerate through a potential difference. A simplified classical analogy to this might be that of a ball accelerating as it rolls down a hill. The acceleration through the potential generates an electromotive force that thus converts some of the incident light energy into electrical energy.

Concerns around the use of silicon once again crop up in the solar energy sector, and these have been previously discussed (see Sections 1.2 and 3.1-3.2). Existing alternative materials that have shown photovoltaic potential, such as TiO_2 and ZnO, absorb primarily in the UV region, in which lies only 4% of available solar energy. In contrast, 43% of solar energy incident on the Earth lies in the visible region.[247] This is clear when one considers a solar spectrum.[248]

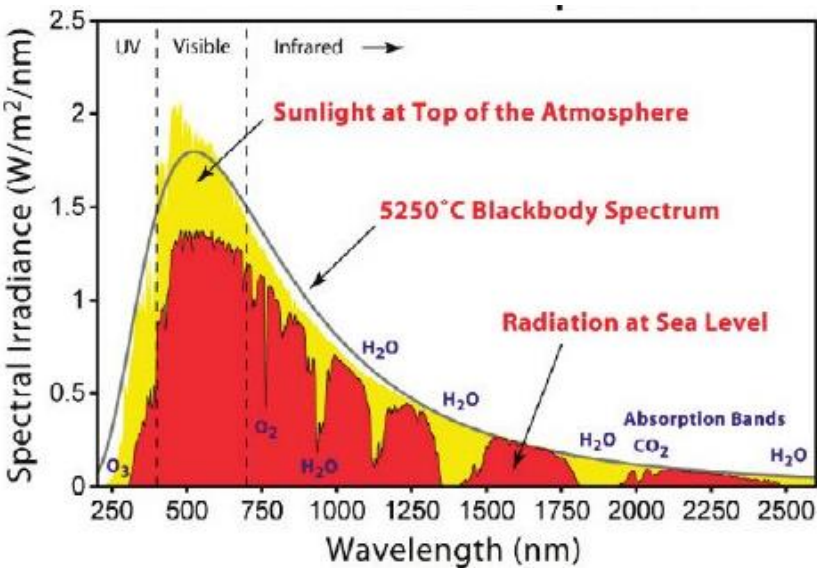

Figure 5.1 *Flux of sunlight incident on Earth*

The solar spectrum approximates black-body emission, with the highest irradiance in the visible region. The spectrum suggests that materials which absorb in the visible region may offer advantages in solar energy not presently available using UV absorbers such as TiO_2. Spectrum reprinted from ref. [248], copyright 2011, with permission from Elsevier

Figure 5.1 shows the flux of sunlight incident on the Earth at different wavelengths. Note the difference in irradiance, whether at the top of the atmosphere or at sea level, between the UV and visible regions. Peak irradiance at sea level is ~1.4 W m^{-2} nm^{-1} at 500 nm, and ~1.0-1.2 W m^{-2} nm^{-1} across the visible region. In contrast, maximum UV irradiance occurs at ~0.5 W m^{-2} nm^{-1}. Materials that absorb in the visible region will therefore present a viable alternative both to silicon and to UV absorbers. For example, tin(IV) sulphide, SnS_2, is an Earth-abundant,[249] non-toxic compound with a bandgap in the visible region.[247]

Materials absorbing in the visible region have been able to rival TMdCs in some optoelectronic applications such as photodetectors, exhibiting a superior response time compared to TMdCs.[250, 251]

Related to this is photocatalysis, a process that is increasingly important in the environmental sector, for instance in the degradation of organic pollutants in water intended for drinking.[252] Industrial scaling-up of photocatalysis in this way will benefit greatly from visible light-driven materials as opposed to UV absorbers.

The limitations discussed of Si and UV-absorbing materials for photovoltaic and other applications provides the motivation for developing a viable route towards alternative materials.

5.2 Materials

Having considered applications and motives, the discussion turns to suitable materials for advancing the relevant technologies where existing materials are inappropriate. Of course, it is possible to tune the light-absorbing properties of photovoltaic materials, by doping and strain engineering.[192, 249] Pure TiO_2 has a bandgap of 3.2 eV, but its visible-light activity has been predicted to increase by doping the pure material with lead selenide, PbSe, quantum dots,[253] and has been demonstrated by co-modification with iron and nitrogen.[254] Photocatalytic properties have been altered by modification with metallic nanoparticles and heterojunctions, [255, 256] and functionalisation with conjugated organics.[257] Band modification in this way, although reliable and scalable, is a challenging, resource-intensive process that requires careful control of conditions to ensure purity.[258] Bandgap engineering has also been reported to have a deleterious effect on solar cell stability.[259]

Among the most promising developments in photovoltaics have been the lead halide perovskites,[260] an example of which is methylammonium (MA) lead bromide, $CH_3NH_3PbBr_3$, which has a bandgap of 2.18 eV.[261]

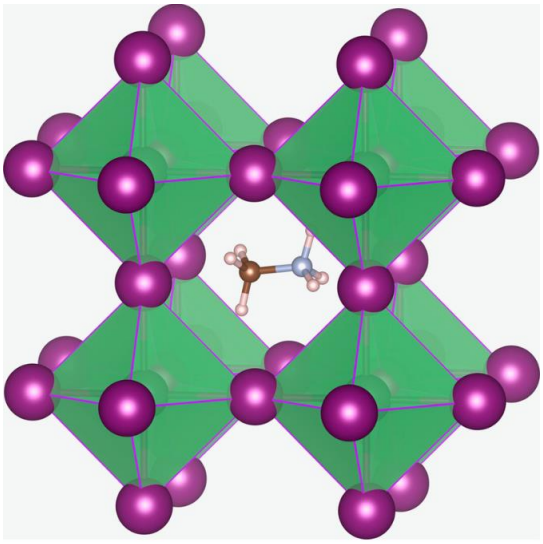

Figure 5.2 *Crystal structure of lead halide perovskite*

The central methylammonium cation is coordinated to eight PbX_6 octahedra where X = I, Br, Cl. An alternative unit cell is possible wherein the lead halide is in the centre of the structure and is coordinated to eight methylammonium cations. However, such a representation would simply be a translation of the same crystal structure. Lead halide perovskites have been investigate for photovoltaic applications due to high efficiency. Image reproduced from ref. [260] under Creative Commons licensing from Springer Nature.

Exfoliation of Tin(IV) Disulphide (SnS_2) by Lithium-Free Intercalation

MA lead halide perovskites now offer a light-to-electricity conversion efficiency in excess of 22% in solar cells, among the highest reported.[262] However, there are numerous concerns about the environmental and safety implications of lead (see ref. [263] and references therein) and the chemistry of perovskites,[263] particularly their instability towards oxidation and thermal and photo-induced degradation,[264-268] and the difficulty of bandgap tuneability.[263]

Instead of the above, layered materials that have an intrinsic visible-region bandgap will present a lower-cost alternative to band engineering of UV absorbers and fewer chemical concerns than lead-based perovskites. As previously discussed, the bandgap chemistry of many layered materials is much easier to tune than that of perovskites, and this presents another advantage of such materials.

SnS_2, is an MX_2-type IV-VI semiconductor. Apart from the TMdCs, a related family of layered materials is the IV-VI semiconductors. These are compounds of Group IV metals with Group VI chalcogens. The family is not as well-studied as the TMdCs, particularly not by liquid exfoliation. That leaves plenty of scope for exploration in this study. The IV-VI family is isoelectronic to the Group V elements, giving them one more valence electron than silicon.

Like a number of metal(IV) chalcogenides, bulk SnS_2 crystallises into the hexagonal CdI_2 crystal structure, of the form S-Sn-S with the Sn atom octahedrally coordinated to six nearest-neighbour S atoms.[269] The material possesses two polytypes depending on the layer stacking. 2H-SnS_2 is the metastable, kinetic product of bulk synthesis and dominates bulk structures at T<800 ℃, while 4H-SnS_2 is the thermodynamic product dominating at T>800 ℃.

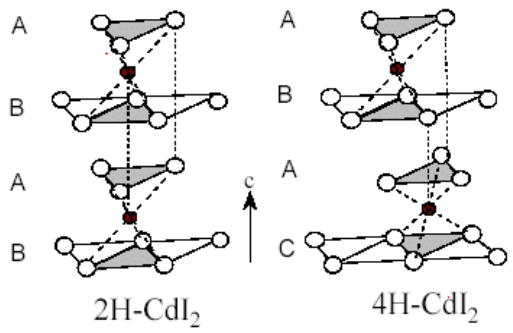

Figure 5.3 *The two polytopes of SnS_2, conforming to CdI_2 crystal structure*

In the figure, reproduced from ref. [269], showing a cross-section of the crystal structure (i.e., c-axis in the plane of the page), Sn is represented by filled circles and S by hollow circles. In the 2H polytype, layers stack in the form ABAB, with tin and sulphur atoms in one layer lying directly below the respective atoms in the layer above. In the 4H polytype, layers stack in the form ABAC, with sulphur atoms in one layer offset by 60° relative to those in the layer above. Additionally, the tin atom in a layer of 4H-SnS_2 lies below a sulphur atom from the layer above. SnS_2 is a visible absorber. Reprinted from ref. [269], copyright 1996, with permission from Elsevier.

Irrespective of the phase, the interlayer spacing is 5.90 Å, and this is an important detail in relation to liquid exfoliation because it will affect the degree of ion intercalation.

SnS_2 has the potential for application in the energy, catalysis and environmental industries. Its structure and absorbance properties present two considerable advantages over the present silicon technology. The first advantage is that SnS_2 is a layered material, in contrast to silicon. Therefore, the resulting confinement of the electronic wavefunction in a monolayer limits the electronic degrees of freedom to the basal plane of SnS_2, leading to a large, direct bandgap. The second advantage offered by SnS_2 is its absorbance in the visible region. In contrast to materials such as TiO_2, which absorb in the UV region, and lead-based perovskites, which present challenging environmental issues, SnS_2 offers the potential to capture a greater percentage of incident solar energy using a relatively non-hazardous material.

5.3 Synthesis

Layered materials can be cleaved into their constituent nanosheets by processing in a specific solvent with surface tension close to that of the bulk material. Surface tension is the attraction of surface liquid molecules to the bulk liquid by cohesion. It is a property which tends to minimise surface area. The solvent is such that the solvent—nanosheet interface energy exceeds the interlayer interface energy. This minimises the enthalpy of mixing (Equation 5.2) and, by extension, the enthalpy of exfoliation.

$$\frac{\Delta H_{mix}}{V_{mix}} = \frac{2}{d}(\delta_{mater.} - \delta_{sol.})^2 \phi \qquad [5.2]$$

where $\frac{\Delta H_{mix}}{V_{mix}}$ = volume-specific enthalpy of mixing

d = thickness of flake

$\delta_{mater.} - \delta_{sol.}$ = surface tension difference between material and solvent

ϕ = dispersed material volume fraction

By sonication or shearing, the dissolved material is cleaved into solvent-surrounded layers that are thermodynamically stable with respect to the bulk. The dispersion is centrifuged to separate flakes of different thicknesses, and the thinnest flakes are decanted in the supernatant. The process is known as liquid exfoliation (LE) and has been used to extract monolayers from many materials. For further processing, the exfoliated flakes can be adsorbed onto a substrate.

The first LE of a 2D material was performed on graphene by Hernandez, *et al.*[63] They found that benzyl benzoate solvent provided the highest-quality nanosheets and a yield of 0.01 mg mL^{-1}.

Perhaps the seminal work on LE was that of Coleman *et al.*[11] They demonstrated LE (Figure 6.1) of several TMdCs, primarily MoS_2 and WS_2 (NMP was the best solvent for both), and some non-TMDs such as h-BN (isopropanol, IPA). The lateral size of the exfoliated MoS_2 and WS_2 crystals ranged from 50 nm to 1 μm, while that of the exfoliated h-BN crystals ranged from 100 nm to 5 μm. It is important to note that the processing conditions in each case, such as initial concentration, centrifugation rate and sonication time, were different in order to optimise dispersion.

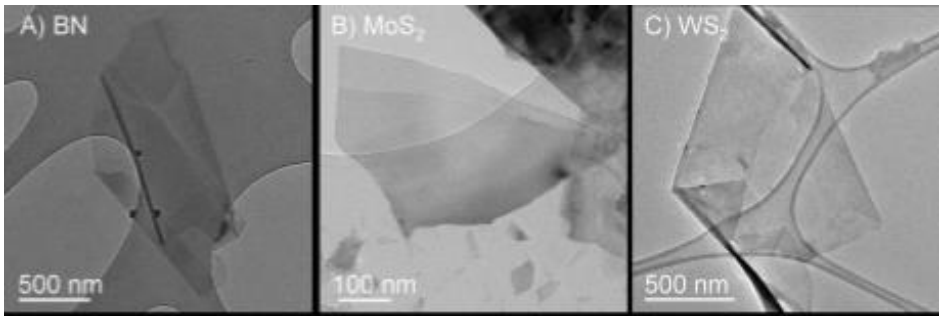

Figure 5.4 *TEM images of exfoliated flakes of* ***(a)*** *h-BN,* ***(b)*** *MoS_2 and* ***(c)*** *WS_2*

Flakes were obtained from sonicated dispersions of the bulk layered materials in appropriate solvents, followed by decantation of the supernatant. Note that the size of flakes in the region of 500 nm – 1 μm . Image from ref. [11]. Reprinted with permission from AAAS.

Suitable solvents must fulfil two criteria:

1. They must disperse the material for a sufficient period of time.
2. The dispersed material must be highly exfoliated.

They found that these were solvents with dispersive, polar and H-bonding moieties. Not all surface energy-matched solvents will dissolve a given solute.[69] For this, the Hansen solubility parameters are required, and they are defined as follows, taking into account the three bonding components (Equation 5.3):

$$\frac{\Delta H_{mix}}{V_{mix}} = \left[\left(\delta_{D,sol.} - \delta_{D,mater.}\right)^2 + \frac{1}{4}\left(\delta_{D,sol.} - \delta_{D,mater.}\right)^2 + \frac{1}{4}\left(\delta_{H,sol.} - \delta_{H,mater.}\right)^2\right]\phi \quad [5.3]$$

where δ_i is the square-root of the dispersive ($i = D$), polar ($i = P$) and hydrogen-bonding ($i = H$) components of the surface free energy of the solvent (sol.) and material (mater.).

Below are other materials exfoliated by Coleman's group:

$MoSe_2$, $MoTe_2$, $TaSe_2$, $NbSe_2$, Bi_2Te_3, $NiTe_2$

In all of these cases, the best solvent was N-cyclohexyl-2-pyrrolidone (CHP). However, the choice of solvents was limited to those previously considered for MoS_2, WS_2 and h-BN, and the processing conditions were not optimised.[11]

The group used UV-vis absorbance spectra as a proxy for the amount of dispersed matter in the centrifuged solutions. This works because of the Beer-Lambert law (Equation 2.3).

Since Coleman's paper, many other groups have followed suit, and a few predated his study. Several key findings in the field of 2D material liquid exfoliation are summarised in Table 1.2.

NMP and CHP are compatible with many nanomaterials. However, both have high boiling points (203 ℃ and 284 ℃ respectively). DMF also has a high boiling point of 153 ℃. This makes processing of the disperse material difficult. Coleman *et al.*, in their study on graphene, addressed this by substituting NMP and DMF for IPA and acetone, solvents with lower boiling points (83 ℃ and 56 ℃ respectively). They observed much lower levels of dispersion due to incompatibility between the surface parameters of the solute and solvent, but accounted for this by optimising processing conditions (*i.e.*, increasing centrifugation time and rate).[69] This illustrates the trade-off between solvent compatibility and practical realities, necessitating compromise conditions, as in the papers by O'Neill *et al.*,[270] Stengl *et al.*,[78] and Gerchman & Alves among others.[90]
Dispersions of nanosheets possess broad distributions of size and thickness,[271] as shown in Figure 5.5. The lateral size range is 20 nm to 5 μm, while the thickness range is 1 to 30 layers. For various applications mentioned in ref. [271], these polydisperse solutions of nanosheets with varying and uncontrollable thickness are unsuitable.

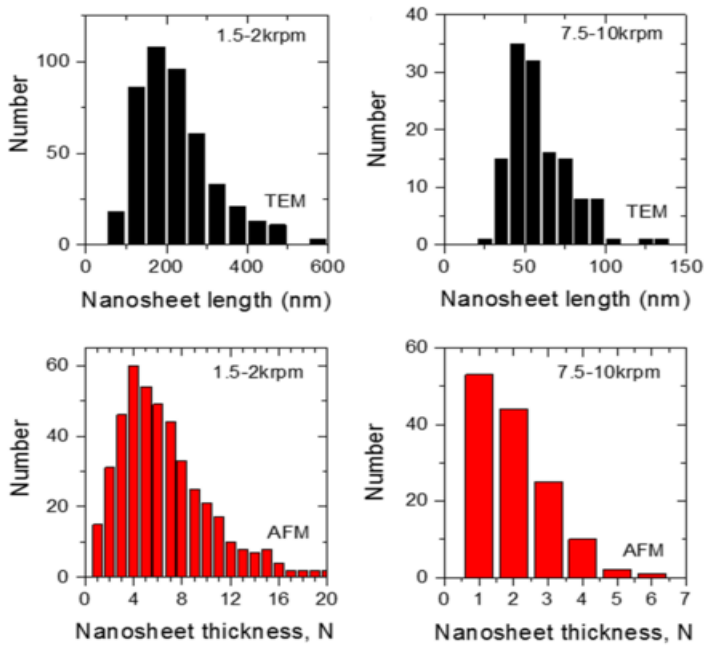

Figure 5.5 *Liquid-exfoliated WS_2 nanosheets centrifuged under different regimes*

Top row – Typical distribution of lateral grain size by liquid exfoliation, measured by TEM. Bottom row – Typical distribution of grain thickness by liquid exfoliation, measured by AFM. Lack of size selectivity makes application of exfoliated flakes quite challenging. Image reprinted (adapted) with permission from ref. [271]. Copyright 2016 American Chemical Society.

The cascade method employed by Backes *et al.* yielded a near-monodisperse solution of WS_2 comprising 75% monolayer by volume.[271] However, the absolute yield of the material was not clear, nor was the grain size.

One common method to improve exfoliation yield is ion intercalation, whereby ions are forced into the gaps between layers. The interaction between the ion and the nanosheet stabilises the exfoliated sheet by reducing its surface energy relative to the non-intercalated case. As the interlayer spacing is usually sub-nm, only a limited number of ions can be used for this purpose. The general methods have been discussed elsewhere (see Section 1.3.1).

A well-known approach is lithium ion intercalation, the Li ion being sufficiently small to intercalate many layered materials. The bulk materials is dissolved in a solution of *n*-BuLi in hexane, heated to 100 ℃ and allowed to react for 48-72 hours, producing Li_x[mater.]. The process can be performed under stirring in an inert atmosphere without heating, as in several studies on TMdCs.[44, 272, 273] Li-intercalated TMdCs are exfoliated by reaction with water, with the consequent evolution of H_2 gas forcing layers apart.[274] Recently, the techniques of pure solvent exfoliation and lithium intercalation were married by introducing a sonication step (see Figure 5.6).[11,275]

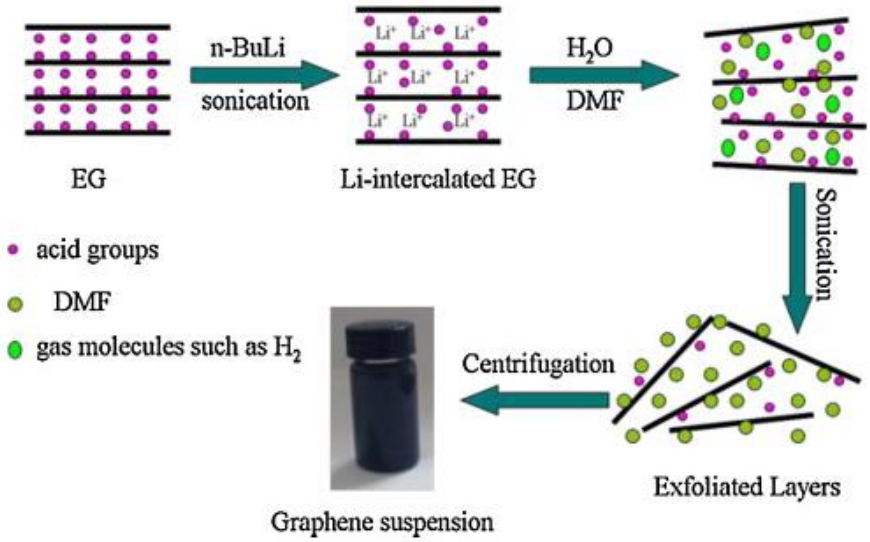

Figure 5.6 *Setup for sonication-assisted lithium intercalation exfoliation of graphene*

A mixture of graphene and 0.5 M n-BuLi in hexane was used. Sonication of the mixture resulted in lithium intercalation between layers, weakening the interlayer attraction and expanding the material. Drying and subsequent sonication in H_2O/DMF evolved hydrogen gas, with the resulting rapid volume expansion forcing layers apart. Scheme reprinted from ref. [275], copyright 2013, with permission from Elsevier.

The shock waves generated by sonication are effective in perturbing and fragmenting TMdCs, reducing the reaction time to roughly three hours with intercalants.[276] As well as being safer than the heating process, sonication is more appropriate than water-based techniques for some materials that are sensitive to degradation in oxidative conditions.[84, 277]

There are two practical difficulties in lithium intercalation. The first stems from the inability to control the degree of intercalation: too little results in a low yield of monolayers, but too much results in decomposition of the bulk material into ion-bound nanoparticles. Electrochemical exfoliation using a lithium anode and a cathode coated in bulk material was developed as an alternative. This process makes use of lithium discharge under the application of a voltage, wherein the degree of subsequent intercalation can be precisely controlled by modulating the voltage.[278]

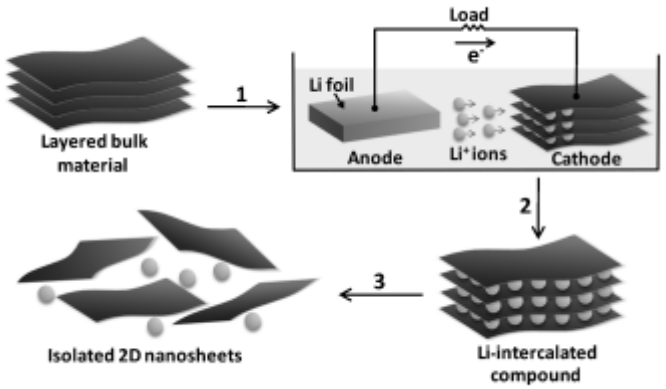

Figure 5.7 *Setup for electrochemical exfoliation of graphite*

Electrochemical intercalation was designed to overcome difficulties in controlling the degree of lithium intercalation during exfoliation. The anode was made of lithium, and the cathode copper coated in a slurry of graphite. The electrolyte was 1 M $LiPF_6$ in a mixture of equal parts ethyl carbonate and dimethylcarbonate. The current density for the process was 0.05 mA cm^{-2}. The intercalated bulk material was sonicated in ethanol and centrifuged to separate residual bulk matter. The advantage of the technique is that lithium intercalation is precisely modulated by an applied voltage. Image reproduced from ref. [278] under Creative Commons licensing from J. Wiley & Sons, Inc.

Although monolayer yield has been reported as high as 92% by the method in Figure 5.7, it is an inherently cumbersome process and not easily scalable. Lithium ion intercalation has been observed to effect an unwanted phase change in MoS_2 from 2H to 1T.[44] As previously noted (see Section 3.6.3), the 1T phase is metallic, and so does not exhibit the useful properties of MoS_2. The exfoliated flakes then require high-temperature annealing to reform the 2H phase. This is a problem that rather diminishes the gains from a process that ought not to require extreme conditions.

The second problem of lithium intercalation is more difficult to overcome and arises from the inherent safety risks associated with lithium ions. One such hazard is that lithium reacts violently with water in a highly exothermic process. Compounds such as n-BuLi are highly toxic and pyrophoric in air. Thus, very careful handling is required, and lithium-based compounds are generally required to be stored and handled in gloveboxes, which compromises the practicality of using the lithium intercalation method.

The difficulties in precisely controlling lithium intercalation and the safety risks of lithium ions have led to the development of alternative intercalation methods.

Hydroxide ion intercalation overcomes the safety risks because aqueous hydroxide solutions present only a moderate health and safety risk that can be mitigated by good laboratory practice. Water can be used as a low-risk and convenient solvent for hydroxides, which is not the case where lithium ions are involved. Hydroxide ions, like lithium, have an effect on material properties. To

study this, the amount of hydroxide needs to be controlled. Fortunately, this is straightforward because the concentration of hydroxide can be calculated from the pH of the solvent solution.

Liquid exfoliation by ion intercalation has previously been applied to a number of materials, and these have been discussed in Section 1.3.1. Specifically, base intercalation has been explored for the exfoliation of graphene,[279] black phosphorus and carbon nitride (C_3N_4).[280] The addition of sodium hydroxide, NaOH, increased the exfoliated yield as much as 20-fold with respect to the hydroxide-free case. There is some evidence that the nature of the base is largely irrelevant, suggesting that pH is the most important factor; stable graphene dispersions have been reported using tetramethylammonium hydroxide, potassium hydroxide and sodium carbonate intercalants,[281] as well as ammonia.[282] Hydroxide-assisted exfoliation of MoS_2 has been reported with a yield of 65% at pH 14,[86] compared to 15% in pure solvent.[11] Bang *et al.* compared the effects of LiOH, NaOH and KOH observing that exfoliated yield was inversely proportional to the cation size, suggesting a role for the cation as well as the anion.[86]

Of the photovoltaic materials capable of absorbing in the visible region, SnS_2 is known to dissolve readily in basic solutions, making it an ideal candidate for hydroxide-mediated exfoliation. Therefore, it was initially chosen for this study.

There is little prior art on the liquid exfoliation of SnS_2, and much of it has settled for obtaining non-uniform thickness distributions, *e.g.*, for TiO_2 sensitisation. Zhang *et al.* demonstrated liquid exfoliation in ethanol solvent at a starting concentration of 1.67 g L^{-1}, obtaining mixed dispersions of mono-to-few-layer flakes in the vicinity of 200 nm lateral size.[258] They made no further attempts at optimisation, nor did they comment on yield. Fu *et al.* also used ethanol and were able to obtain monolayers, although this required an infeasibly long sonication time (48 h), and the modal size distribution of monolayer flakes was only ~2-4 nm.[250] Shen *et al.* determined that 1:4 IPA:water mixed solvent was a good solvent for SnS_2 exfoliation;[283] however, this was based purely on solubility parameters, and there is an issue of long-term stability arising from the mixed-solvent approach, usually due to the volatility of one component of the solvent.[194] A single-solvent approach would almost always be preferable for that reason. There is, therefore, a great deal of scope for novel results in the field of SnS_2 liquid exfoliation.

The method investigated for SnS_2 exfoliation herein will advance the field by providing a safe, scalable and less chemically damaging alternative to lithium intercalation. The development of a method towards SnS_2 will open up possibilities in light-based applications (see Section 5.1) not presently demonstrated in the literature.

5.4 Characterisation

Like MoS_2 and WS_2, SnS_2 exhibits characteristic Raman vibrational modes: the E_g at ~205 cm^{-1} and the A_{1g} mode at ~315 cm^{-1}.[250, 284] Unlike MoS_2 and WS_2, however, the peaks do not exhibit reliable $\Delta\bar{\upsilon}$ contraction in the monolayer. A different approach is required, and this involves the normalisation of the peaks to the Si line at 521 cm^{-1}. Doing this allows the relative intensities of the few-/monolayer peaks to be compared directly to the bulk peaks. For SnS_2, there is a systematic and predictable relationship between the peak intensity and the layer thickness. It becomes apparent then that only the A_{1g} is diagnostic of the monolayer. This is because the E_{2g} mode is a weakly-intense vibration in the bulk (seven times weaker than the A_{1g})[285] that weakens further in the monolayer, a phenomenon that can be explained by the reduction of scattering centres. The A_{1g} does, of course, weaken also, but it is of sufficient intensity to begin with that it is still resolvable against the background even in the monolayer. To that end, the expected peak intensity ratio between the A_{1g} line and the Si line, I_A/I_{Si}, is 0.02 in the monolayer, increasing to 0.96 in the bulk.[250, 284] The ratio is diagnostic of the monolayer and will be used in characterisation.

The bulk (indirect) bandgap has been reported as 2.18-2.44 eV.[247, 286] However, the monolayer possesses a large, direct bandgap of 2.68 eV,[285] corresponding to PL emission at ~460 nm, which is detectable in the blue-indigo region of the visible spectrum. However, PL presents practical difficulties because excitation with a 532 nm, 633 nm or 785 nm laser source would be insufficient. It would require excitation in the UV region.

The above methods rely on a material supported on a substrate, and SiO_2/Si dice are the ideal candidates for this, as previously explained (see Section 2.2.3).

For this project to achieve its aim, the relative effects of changing pH will need to be quantified in terms of the yield of material. Thus, a method for analysing material concentration in the as-prepared solutions of material is necessary. UV-vis spectroscopy is the ideal candidate for this because the Beer-Lambert law can be used to calculate the concentration of SnS_2 in the basic solutions provided that the molar extinction coefficient, ε, is known (see Section 2.2.2). Fortunately, it is possible to calculate ε using an aqueous control solution of known SnS_2 concentration. Formulating dilute solutions of aqueous SnS_2 by serial dilution of a starting solution allows absorbance data to be plotted against UV-vis absorbance, in which case ε is the gradient of the line of best fit. This is a standard procedure for calculating molar extinction coefficients, and the obtained value of ε is then applied to every subsequent Beer-Lambert calculation.

5.5 Experimental details

5.5.1 Control solvent

Aqueous SnS_2 (10 g L^{-1}) was prepared by sonication for 2 h in a Decon FS100b ultrasonic bath (35-45 kHz, 75W). UV-vis absorbance spectra were obtained at five concentrations prepared by sequential dilution: 100%, 50.0%, 10.0%, 5.0% and 2.5%. The optical path length (*i.e.*, quartz cuvette width) was 1 cm. The excitation range was 900-190 nm with a source changeover at 350 nm. The accumulation time was 0.5 nm s^{-1} against a reference of pure water acquired at 1.0 nm s^{-1}. Data were acquired on a Varian CARY 300 Bio UV-vis spectrophotometer.

Additional solutions were derived at 7.5% concentration (by redilution of three-quarters of the 10% solution) and 1.0% concentration (by redilution of two-fifths of the 2.5% solution).

5.5.2 Basic solvent preparation

Two stock solutions of aqueous base were prepared, at pH 9.0 (± 0.5) and pH 13.0 (± 0.5) respectively. The solutions were prepared respectively by dissolving KOH in deionised water and gently sonicating for 15 minutes. The pH was tested using pH paper to give a reading accurate to within 0.5 units. Incremental adjustments were made where necessary by adding small amounts of KOH or by further dilution.

5.5.3 Sonication and centrifugation

Sample SnS_2 solutions were prepared at a concentration of ~10 g L^{-1} in each basic solvent. The solutions, including the control, were sonicated for 6 h, with samples taken at every 2 h interval. At each interval, five aliquots (~1 mL) of each sample solution were taken. The first of these was not centrifuged, the second was centrifuged at 800 rpm for 20 minutes, the third at 1600 rpm for 20 minutes, and the fourth at 2400 rpm for 20 minutes. The fifth was subjected to cascade centrifugation, whereby the supernatant resulting from 800 rpm centrifugation was re-centrifuged at 1600 rpm, and the supernatant resulting from that was re-centrifuged at 2400 rpm. The tables below therefore show the full dataset, 45 solutions prepared under unique conditions of pH, sonication time and centrifugation speed.

Table 5.1 Liquid exfoliation parameters – aqueous

cent. speed/rpm sonication t./h	0	800	1600	2400	Cascade
2	**E0-0**	**E0-1**	**E0-2**	**E0-3**	**E0-12**
4	**E0-4**	**E0-5**	**E0-6**	**E0-7**	**E0-13**
6	**E0-8**	**E0-9**	**E0-10**	**E0-11**	**E0-14**

Table 5.2 Liquid exfoliation parameters – pH 9

cent. speed/rpm sonication t./h	0	800	1600	2400	Cascade
2	**E1-0**	**E1-1**	**E1-2**	**E1-3**	**E1-12**
4	**E1-4**	**E1-5**	**E1-6**	**E1-7**	**E1-13**
6	**E1-8**	**E1-9**	**E1-10**	**E1-11**	**E1-14**

Table 5.3 Liquid exfoliation parameters – pH 13

cent. speed/rpm sonication t./h	0	800	1600	2400	Cascade
2	**E2-0**	**E2-1**	**E2-2**	**E2-3**	**E2-12**
4	**E2-4**	**E2-5**	**E2-6**	**E2-7**	**E2-13**
6	**E2-8**	**E2-9**	**E2-10**	**E2-11**	**E2-14**

5.5.4 Characterisation

A single drop of each as-prepared solution was pipetted onto pre-cleaned SiO_2/Si substrate dice for characterisation. The dice were pre-heated to 150 ℃ (50 ℃ above the boiling point of the solvent)[194] to ensure rapid evaporation of the solvent and prevent agglomeration of flakes by the coffee-ring effect. The remaining solution was kept back for UV-vis analysis. The substrate-supported flakes were used for characterisation by OM, Raman spectroscopy and XRD. It was not possible to perform photoluminescence due to practical difficulties of performing UV excitation.

UV-vis measurements were carried out by drawing a specific volume of solution from the top of each solution (thus omitting large sediment) and diluting it to a known factor in order to prevent

saturation of the detector. In the analysis of absorbance data, peak absorbance was simply multiplied by the dilution factor in order to obtain the "actual" absorbance.

5.6 Results and discussion

5.6.1 SnS_2 extinction coefficient

It is crucial to know the mass-specific extinction coefficient, ε, of SnS_2 in order to calculate the yield from liquid exfoliation. UV-vis absorbance data obtained from the control sample (see Section 5.5.1) were used to calculate ε. First of all, the raw data obtained at 2.5%, 5.0% and 10.0% concentration are plotted for clarity in the range 800-200 nm. Higher concentrations resulted in saturation of the detector and were not selected for analysis.

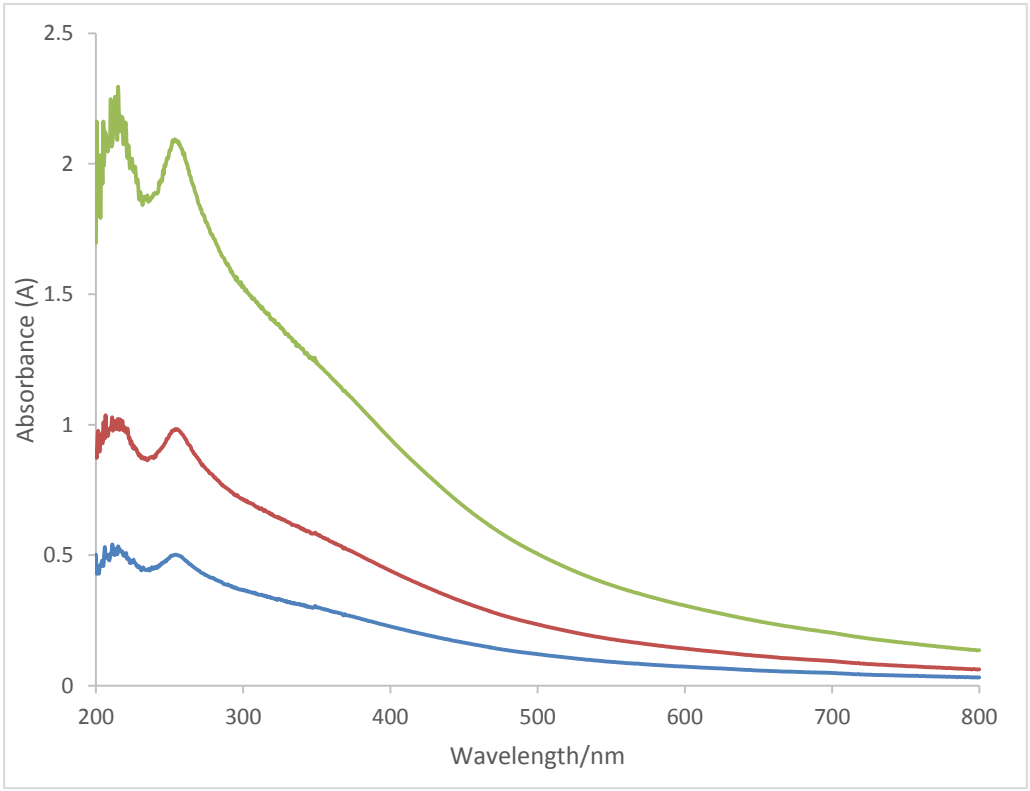

Figure 5.8 *UV-vis absorbance of aqueous SnS_2*

Spectra were obtained at 10.0% (green), 5.0% (red) and 2.5% (blue) of initial concentrations. Solutions were prepared by serial dilution of 10 g L^{-1} mother solution sonicated for 2 h. The absorbance peak at 250-255 nm is quite pronounced, which can be used to calculate the extinction coefficient.

The most distinct absorption peaks appear at 250-255 nm, and the maximum absorbance (A) at these wavelengths was plotted against the absolute concentration. The spectra confirmed that the choice of solvent was appropriate because the UV absorbance cut-off of water (~190 nm) did not interfere with the absorbance of the material. The spectra also showed that the main peaks had

shoulder peaks developing at their red edges, and the shoulders corresponded to absorbance in the visible region around 400-450 nm. These peaks will be important for applications but were not selected for analysis here.

The peak absorbance allows for ε to be extracted as per the Beer-Lambert law (Equation 2.3), which defines the absorbance at a given wavelength as a function of the solution concentration. The Beer-Lambert law shows that the gradient of the plot is the extinction coefficient, provided that the path length is constant. A common path length is 1 cm.

The table below shows the peak absorbance of each solution at 254 nm, including absorbance of solutions at 7.5% and 1.0% initial concentration.

Table 5.4 Peak absorbance of aqueous SnS_2

[SnS_2](aq)/g cm^{-3}	**Absorbance @ 254 nm**
0.0001	0.2067
0.00025	0.5020
0.0005	0.9840
0.00075	1.4998
0.001	2.094

A plot of the above data allows ε to be extracted.

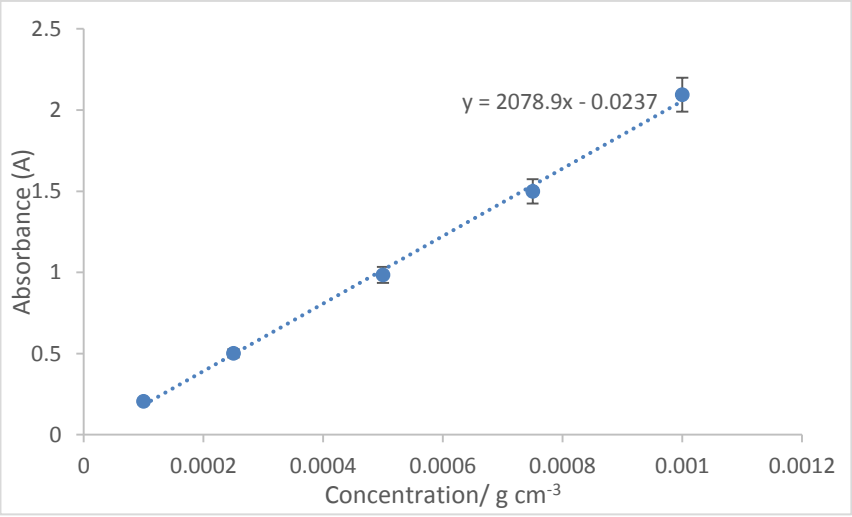

Figure 5.9 *Determination of the extinction coefficient of SnS_2 at 254 nm*

Plotting peak absorbance against concentration for a constant absorbance path length presents a linear relationship between the two variables such that ε is extracted as the gradient of the line of best fit. The error bars were obtained by performing linear regression on the raw data and obtaining the 95% confidence intervals.

These data offer a precise value for the molar extinction coefficient, and an explanation of error extraction is provided in Appendix B.1:

$$\varepsilon = 2100 \pm 170 \text{ g}^{-1} \text{ cm}^2$$

In an ideal case, one may prefer to use independently prepared solutions rather than a serial dilution. This is to ensure that errors in the starting solution concentration do not filter down into the dilutions leading to a systematic error. However, this was not done here. The reason for using a serial dilution was to preserve the starting material. It is not expected that this will have a substantial effect on the outcomes of this project, because relative values of concentration will be sufficient for determining the optimal conditions.

In this project, the effect of pH on the UV-vis absorbance was thought to be variable, but this will be discussed where necessary. For that reason, the extinction coefficient calculated here was presumed to be the extinction coefficient in every subsequent concentration calculation.

As a further point of interest, these UV-vis data will be instructive to the research community in solvent-scanning. A solvent is inappropriate for UV-vis spectroscopy if it has an absorbance cut-off at a longer wavelength (lower energy) than the peak absorbance wavelength of the material or close to it. This rules out solvents containing phenyl groups, double-bonding and large atoms such as chlorine or sulphur. These and similar solvents, were they found to be good solvents for SnS_2, would not be appropriate choices as they would limit the scope for UV-vis absorbance analysis.

5.6.2 Analysis of as-prepared solutions

It is important to note some caveats when analysing UV-vis absorbance of nanosheets. Firstly, flakes that correspond to the wavelength of the excitation source can cause scattering of light. This phenomenon is known as Mié scattering. It is not a problem for very small objects such as nanoparticles less than 200 nm in size, and nor is it a problem for larger flakes greater than 800 nm. In those cases, the size of particles lies outside the range of the spectrophotometer. Unfortunately, liquid exfoliation tends to produce a large number of flakes with lateral sizes of hundreds of nanometres. It will be important to consider the effects of scattering on the absorbance. Scattering affects absorbance indirectly by increasing the optical path length, the quantity ‘l’ in the Beer-Lambert law. Therefore, greater scattering will increase observed absorbance relative to a hypothetical non-scattering case in which only the concentration of species affects absorbance. Secondly, the extent of scattering is inversely proportional to a power of incident wavelength, as per the approximation (Equation 5.4):

$$A \propto \lambda^{-n} \quad [5.4]$$

where A = absorbance

λ = incident wavelength

n = an exponent that takes a value between 1 and 4 in the scattering case

The implication of Equation 5.4 is that there could be anything between an inverse linear and inverse fourth-power relationship between the absorbance and the incident wavelength in the scattering case.

Overall, then, there is a confounding effect on absorbance of nanoflake solutions, arising from scattering of incident light by particles corresponding to its wavelength. Therefore, UV-vis absorbance of a given solution cannot be assumed to have a strict linear relationship with concentration.

According to Coleman *et al.*, there is an experimental method to determine whether a scattering component is present in the absorbance. This involves plotting the spectra on a log—log scale. The Coleman group found that a straight line in the longwave region indicated scattering. This is in accordance with the relation in Equation 5.5 such that the following approximation is true:

$$\log(A) = -n \log(\lambda) \quad [5.5]$$

Equation 5.5 is simply a linearisation of 5.4 and shows that the gradient of the linear portion of a log—log plot of absorbance against wavelength will yield the value of the exponent n. This method worked for WS_2, MoS_2 and h-BN, and accordingly it may be sufficiently generic a method to be applied to other materials.

The UV-vis absorbance data are plotted below. The plots show the effect of changing pH for a given set of sonication and centrifugation parameters. Each plot shows three UV-vis absorbance curves, each acquired at different pH under a given set of sonication and centrifugation conditions.

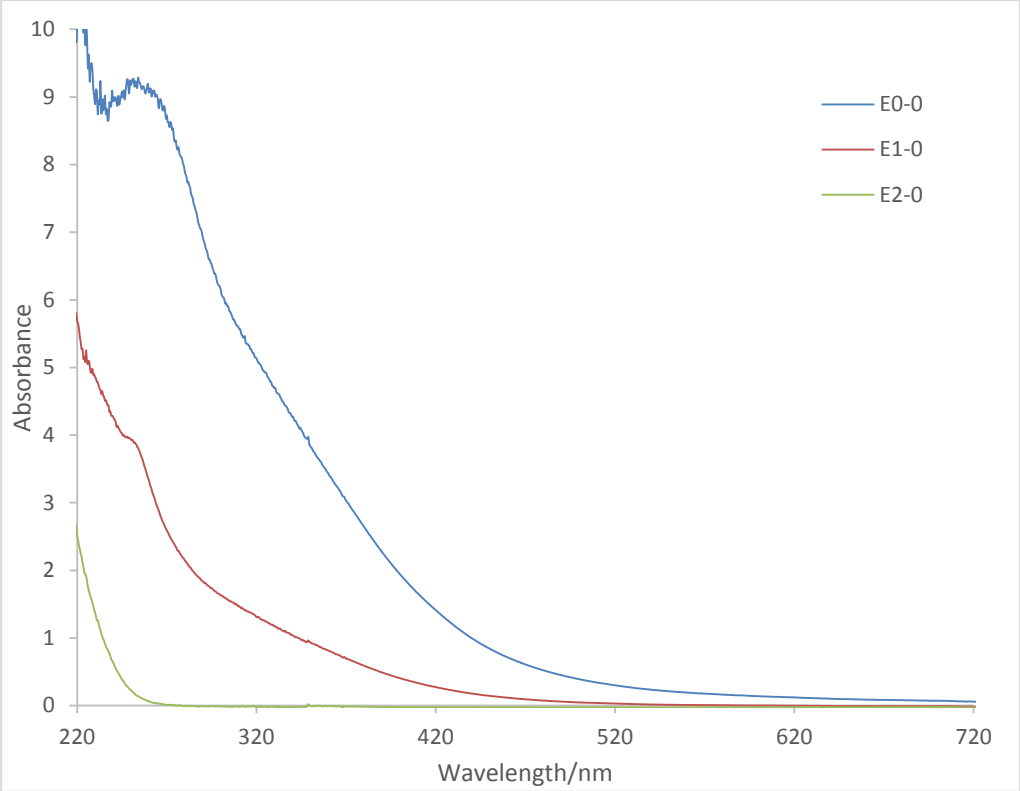

Figure 5.9 *UV-vis absorbance data for SnS_2 (aq.) at 2 h sonication*

Control (blue), pH 9 (red) and pH 13 (green) solutions at 10 g L^{-1} sonicated for 2h and data acquired before centrifugation. As pH was increased, so absorbance decreased. Given all other conditions were the same, the reduction in absorbance was likely attributable to the changing pH. Yields are not directly estimable from absorbance, due to possible effects of scattering.

Figure 5.9 shows the effects of two hours of sonication. The control solution exhibited a maximum absorbance of ~9.3 at 254 nm, and absorbance at the same wavelength was observed in the pH 9 solution, although the maximum was ~3.9. No peak was seen in the 250-255 nm region for the pH 13 solution. It is important to note that as the sonication and centrifugation parameters were identical, differences in absorbance can most likely be attributed to pH effects. The corresponding log—log plots were used to quantitatively assess the effect of Mié scattering:

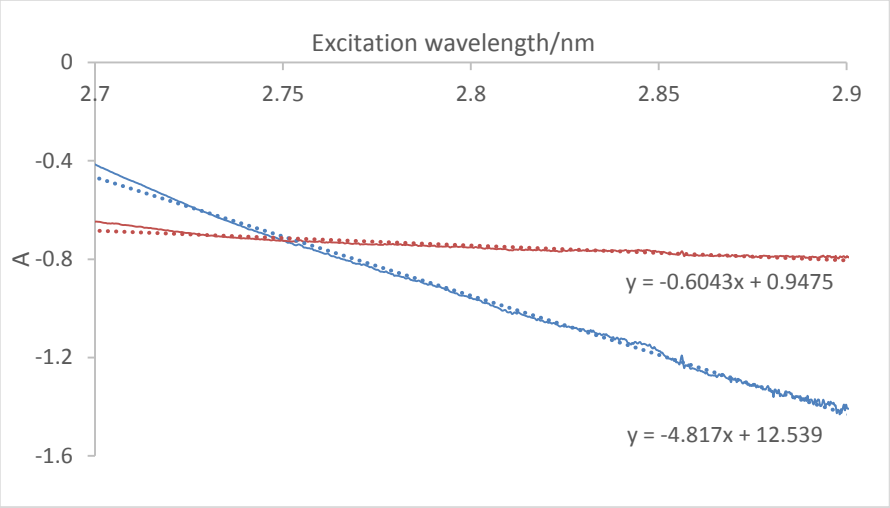

Figure 5.10 *Determination of scattering effect in 2h-sonicated solutions*

Plotting the E0-0 UV-vis spectrum (blue) and E1-0 UV-vis spectrum (red) in the longwave region on a logarithmic scale linearised absorbance and allowed the effect of scattering, n, to be extracted from the gradient of the line of best fit. An n-value of 1-4 indicated scattering.

The value of the exponent n was determined from the gradients of the lines as 4.80 ± 0.02 for E0-0 and 0.60 ± 0.02 for E1-0. The numbers suggest that solutions E0-0 and E1-0 were unaffected by scattering under their synthetic conditions. However, Figure 5.10 did not show a prodigious background from E2-0 absorbance, so it was not included in Figure 5.11.

Assuming full dissolution and negligible scattering, using the extinction coefficient calculated in the previous section 6.6.1 yields concentrations of 4.40 ± 0.40 g L^{-1} (control) and 1.90 ± 0.16 g L^{-1} (pH 9), *i.e.*, ~44% and ~19% yield respectively based on the starting concentration of 10 g L^{-1}. The extent to which it is reasonable to neglect scattering effects is dependent on the interplay between parameters. Flake size is inversely proportional to sonication time: longer sonication yields smaller flakes. Therefore, the assumption is more likely at least to be a close approximation at short sonication times. OM was used to roughly judge the size distribution of as-exfoliated flakes as a way to provide confirmation.

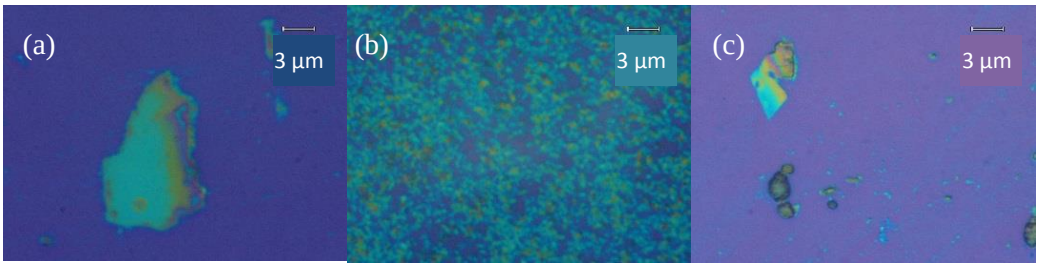

Figure 5.11 *Selected OM images of as-deposited SnS_2 flakes from solution E0-0*

The control sample was used to determine the size distribution of flakes after 2 h sonication. Flakes were deposited on SiO_2 as in Section 5.5.4 and observed under optical microscopy. Many flakes, identifiable as light blue regions against the dark substrate, were micron scale, indicating that it was reasonable to neglect the effect of scattering.

The OM images in Figure 5.11, all acquired at the same magnification, showed a mixture of thick and thin, large and small, flakes. This is evidenced by the differences in optical contrast even within the same flake. In image (c), the large, dark flake on the order of 3-5 µm shows that bulk material remained in the solution without centrifugation. The images suggest that sub-micron flakes were not present in the dispersion in great quantity, so the assumption in the concentration calculations holds true for E0-0. However, the smaller flakes are more difficult to see without higher magnification, which compromises resolution.

The OM images can be complemented by Raman data. Although it is a sensitive technique, Raman is most effective when particle size is greater than the laser spot size. This is because crystal edges act as defects, leading to elastic backscattering of electrons, which has previously been shown to broaden certain Raman peaks.[287] In practice, at the magnifications achievable on the equipment available, spot size is 1-2 µm. The spot size could be effectively reduced by reducing laser power, but this would be unlikely to help very much because it would make weak monolayer signals susceptible to noise. A laser power of 10% maintained a small spot size while providing sufficient resolution of weak signals.

Raman spectroscopy of deposited flakes from solution E0-0 shows a combination of bilayer and multilayer flakes, suggesting that these were suboptimal conditions without any centrifugation. Below is an example of a bilayer Raman spectrum.

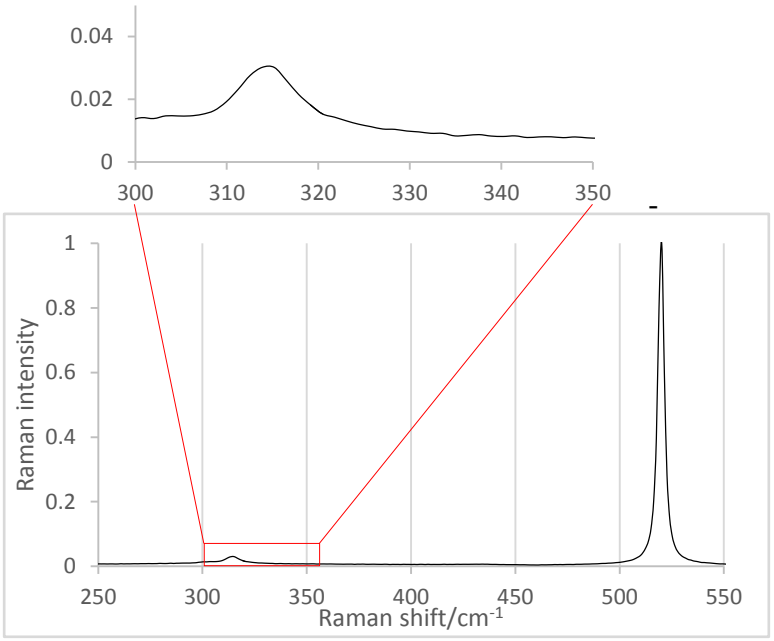

Figure 5.12 *Raman spectrum of flake from solution E0-0 supported on SiO_2*

Spectrum acquired from the control solution, normalised to laser power, shows a peak at 315 cm^{-1} corresponding to the A_{1g} phonon in the bilayer. (Inset) The layer thickness is confirmed by blowing up the material peak such that its intensity relative to the Si-line can be resolved: 0.03 corresponds to 2L-SnS_2.

For comparison, see Figure 5.13 for the bulk SnS_2 Raman spectrum. The intensity of the A_{1g} mode in the bulk starkly illustrates the importance of the intensity ratio for the thickness characterisation of this material.

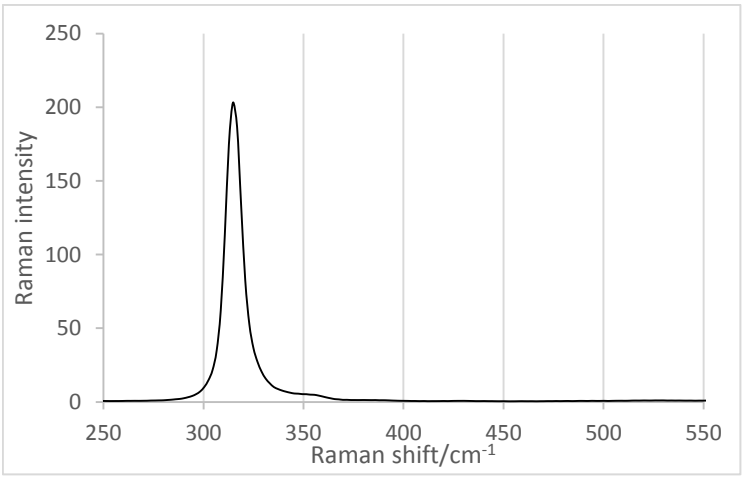

Figure 5.13 *Raman spectrum of bulk SnS_2*

In contrast to the few-layer spectrum, the bulk spectrum exhibits a much larger ratio of the A_{1g} intensity with respect to the Si line. Commonly, the ration in the bulk exceeds 0.96. This is a straightforward method of inferring layer thickness from Raman spectroscopy.

Figure 5.13 represents quite an extreme case. It shows the Raman spectrum of the as-received bulk crystal without any exfoliation. The peak ratio in this case is ~200, but a ratio greater than or equal to 0.96 denotes bulk.[250, 284] The spectrum highlights very clearly the effect of thickness on A_{1g} peak intensity, showing why it is diagnostic of the monolayer.

Solution E1-0 showed the effect of the same sonication time but in pH 9 solution rather than pure water as solvent.

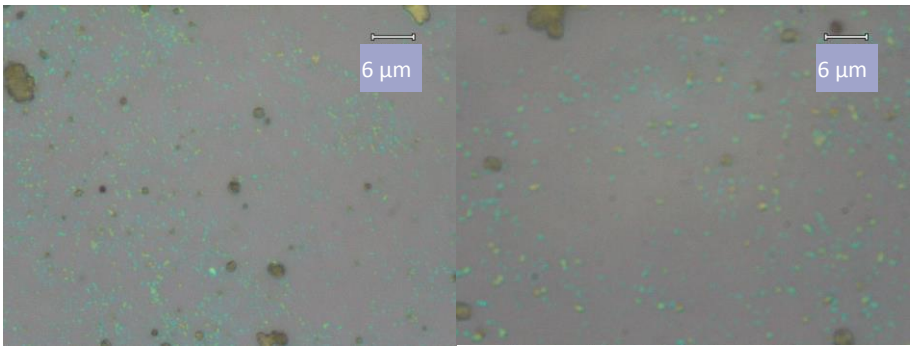

Figure 5.14 *Selected OM images of as-deposited SnS_2 flakes from solution E1-0*

These images show the effect of changing pH. Comparing these images to those in Figure 5.12, one sees that changing solvent from water to pH 9 solution, while keeping all other exfoliation conditions the same, led to a more uniform dispersion of flakes, which are identifiable as blue specks against the dark substrate.

One notable difference between the OM images in Figures 5.11 and 5.14 was that the latter figure showed a more uniform dispersion of particle size. The large flakes present in the aqueous solution after 2 h sonication were not present in the pH 9 solution, even without centrifugation. The flakes in the latter figure were still micron-sized, suggesting few-layer thickness, but minimal scattering. Again, it is important to note that while smaller flakes might have been present, this was difficult to corroborate, due to the limits of magnification and resolution.

Solution E2-0 still offers a useful comparison of pH effects. The corresponding substrate was prepared by deposition of as-prepared flakes after 2 h sonication at pH 13 (and no centrifugation). Thus, it is a direct comparison with sample E0-0. The possible effects of pH are discussed in the Section 5.6.5.

XRD of many different substrate-supported samples provided further confirmation of the presence of SnS_2 across a range of exfoliation conditions at pH 9. An example XRD pattern is shown in Figure 5.15. It was acquired from sample E1-14 and shows the observed pattern and the calculated SnS_2 pattern.

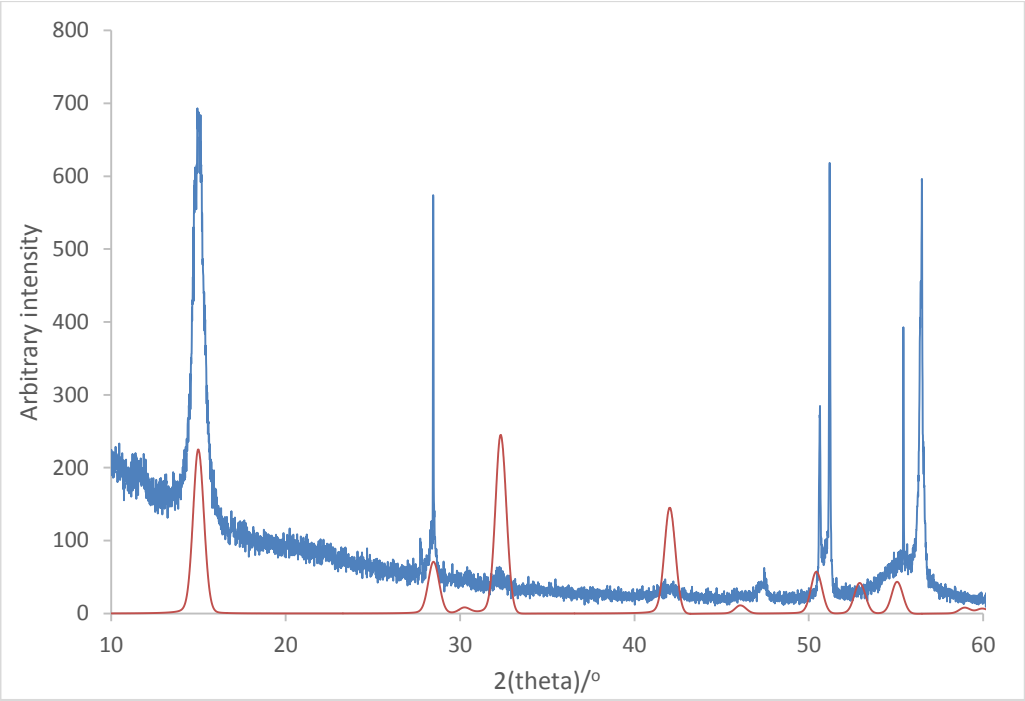

Figure 5.15 *XRD pattern from E1-14 flakes (blue) and calculated SnS_2 pattern (red)*

XRD pattern of sample E1-14 (pH 9, 6 h sonication, cascade centrifugation) shows good agreement between the experimental and calculated sample (using PDXL2 software). The positional agreement provides evidence of good-quality exfoliation without chemical damage to the flakes. Peak height does not agree in all cases but may be affected by flake thickness.

The observed and calculated patterns exhibited a good overlap of low- and mid-angle peaks, confirming that SnS_2 was produced at pH 9. One also sees at the high-angle end of the pattern, $2\theta>50°$, that there were peaks that obviously did not conform to the expected SnS_2 pattern, although it is possible that some peak shift had taken place due to strain-related effects in a monolayer on an amorphous substrate or defects arising from the exfoliation process. This may explain the poor fit between the intense peak at $2\theta = 56.5°$ and the nearest calculated SnS_2 peak. A consideration of the species present in the starting solutions suggested a possible reaction between SnS_2 and hydroxide ions, yielding products such as SnO, SnO_2 or $Sn(OH)_2$. No characterisation data exist for tin(IV) hydroxide, as it is an unstable species that readily oxidises in ambient conditions. In fact, some of the high-angle peaks could be fitted to an SnO XRD pattern, as in Figure 5.16.

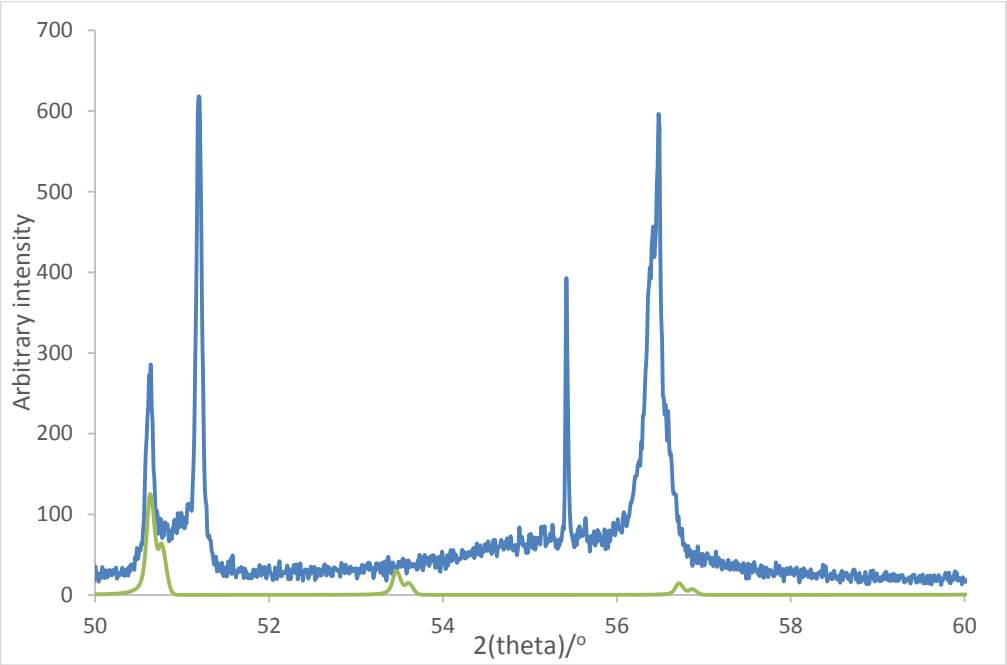

Figure 5.16 *High-angle XRD peaks (blue) correspond to SnO impurities (green)*

Comparison of high-angle experimental peaks from sample E1-14 with calculated SnO pattern (using PDXL2) showed good agreement at 50.6° and 56.5°. This suggested a possible, but very limited, chemical reaction of SnS_2 with the hydroxide ions at pH 9.

The reflection at 2θ = 50.6° was attributable to SnO, while the calculated peak at 56.6° was observed as a shoulder to the SnS_2-derived peak at 56.5°. In fact, performing Raman spectroscopy over many regions did not indicate that SnO was present in anything other than trace amounts at pH 9.

Monolayers of SnS_2 were detected from as-deposited regions of every sample at pH 9, attesting to the favourability of the hydroxide-mediated approach. Example monolayer spectra taken from various samples are reproduced in Figure 5.17:

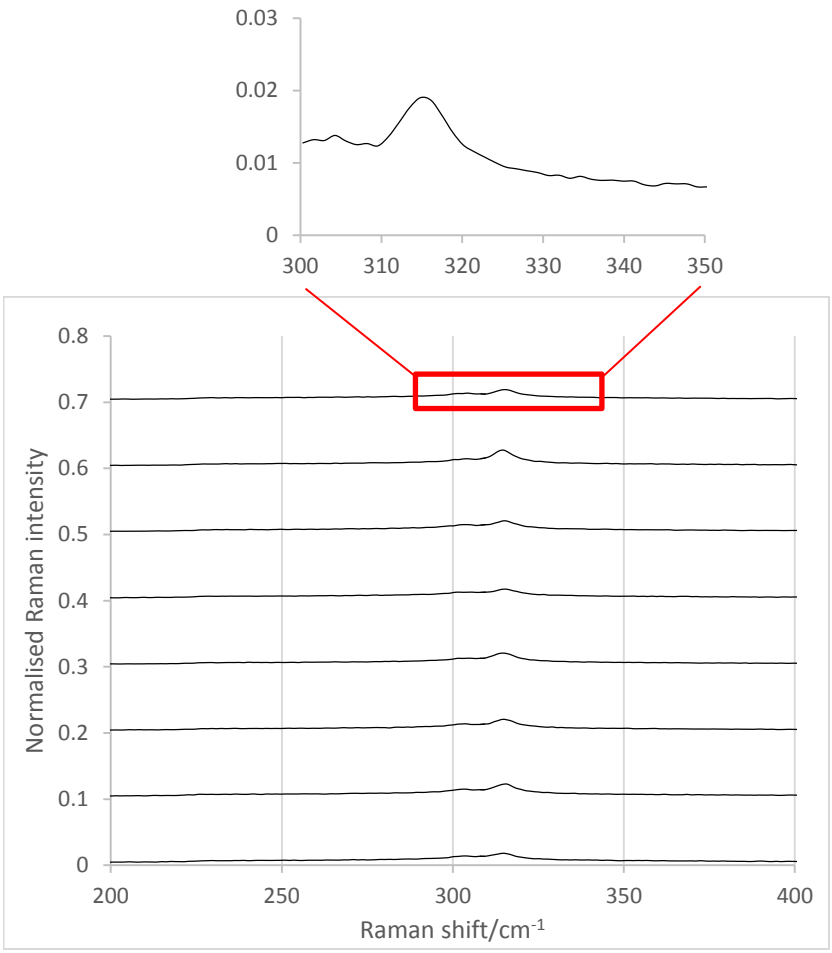

Figure 5.17 *Selected 1L Raman spectra from pH 9 samples*

These are amalgamated Raman spectra acquired from several samples at pH 9. Spectra normalised to laser power for plotting on the same graph irrespective of acquisition conditions. The presence of an A_{1g} phonon at 315 cm^{-1} indicated that monolayer SnS_2 was obtained across a range of possible conditions at pH 9. (Inset) The blown-up spectrum confirms the characteristic monolayer peak I_A/I_{Si} ratio of 0.02.

In the spectra in Figure 5.17, the A_{1g} vibrational mode of SnS_2 can be seen as a weak peak. The intensity of each peak relative to the Si-line at 521 cm^{-1} was 0.02, a clear indication of monolayers. Notwithstanding the monolayers present in each sample, the morphology of deposited flakes varied considerably between different conditions. An example of this was the contrast in appearance between flakes deposited from E1-1 and E1-14, and this will be shown in the next section.

5.6.3 Screening of all solutions – aqueous and pH 9

UV-vis absorbance analysis was applied to each solution as per the Beer-Lambert law and scattering estimation. The tabulation of samples therefore shows the percentage yield for a given set of parameters. In Table 5.4, data from the aqueous solution and the pH 9 solution are shown. Where percentage yield could not be reliably calculated, it was not shown. Where the absorbance

was affected by Mié scattering, the n-value is shown. This implies the corresponding yield was an overestimate.

Table 5.4 Percentage yields and scattering from aqueous and pH 9 solutions

	0	**800 rpm**	**1600 rpm**	**2400 rpm**	**Cascade**
2h	43%, 19%	44% (3.40), 27%	39% (3.00), 29%	44%, 35% (1.40)	43%,
4h	44%, 96%	44% (4.00), 71%	11%, 49%	9%, 51%	
6h	44%, 87%	7% 88%	6%, 130%		4%, 74%

In the table, the first percentage in each cell denotes the yield from aqueous solution, and the next one is the percentage yield from pH 9 solution. Data from pH 13 were not included, and this omission will be explained in the next section.

According to the table, the best conditions for yield were 4 h sonication at pH 9 (E1-4), giving 96% yield, and 6h sonication at pH 9 followed by centrifugation at 800 rpm (E1-9), giving 88% yield. However, the Raman data suggested that monolayer yield was not maximised. Few-layer flakes persisted in solution E1-4, while the monolayer count was very low in E1-9. This was confirmed by OM. In fact, the best Raman spectra, in the sense of the highest count of monolayers detected, resulted from 4h sonication at pH 9 followed by centrifugation at 800 rpm (E1-5, Figure 5.20). In the case of E1-9, it is possible that monolayers were too small to detect under the magnification possible using the Olympus microscope. Techniques such as SEM may afford a better picture of which of the solutions E1-5 and E1-9 offered a greater monolayer yield.

Conditions E1-5 resulted in 71% yield, importantly with a high degree of monodispersity. This represented >27% increase in yield with respect to the corresponding conditions without hydroxide. Conditions E1-9 offered an even greater improvement in yield against the aqueous conditions. The yields obtained here using hydroxide were comparable to literature,[86] attesting to the efficacy of the method for SnS_2 liquid exfoliation.

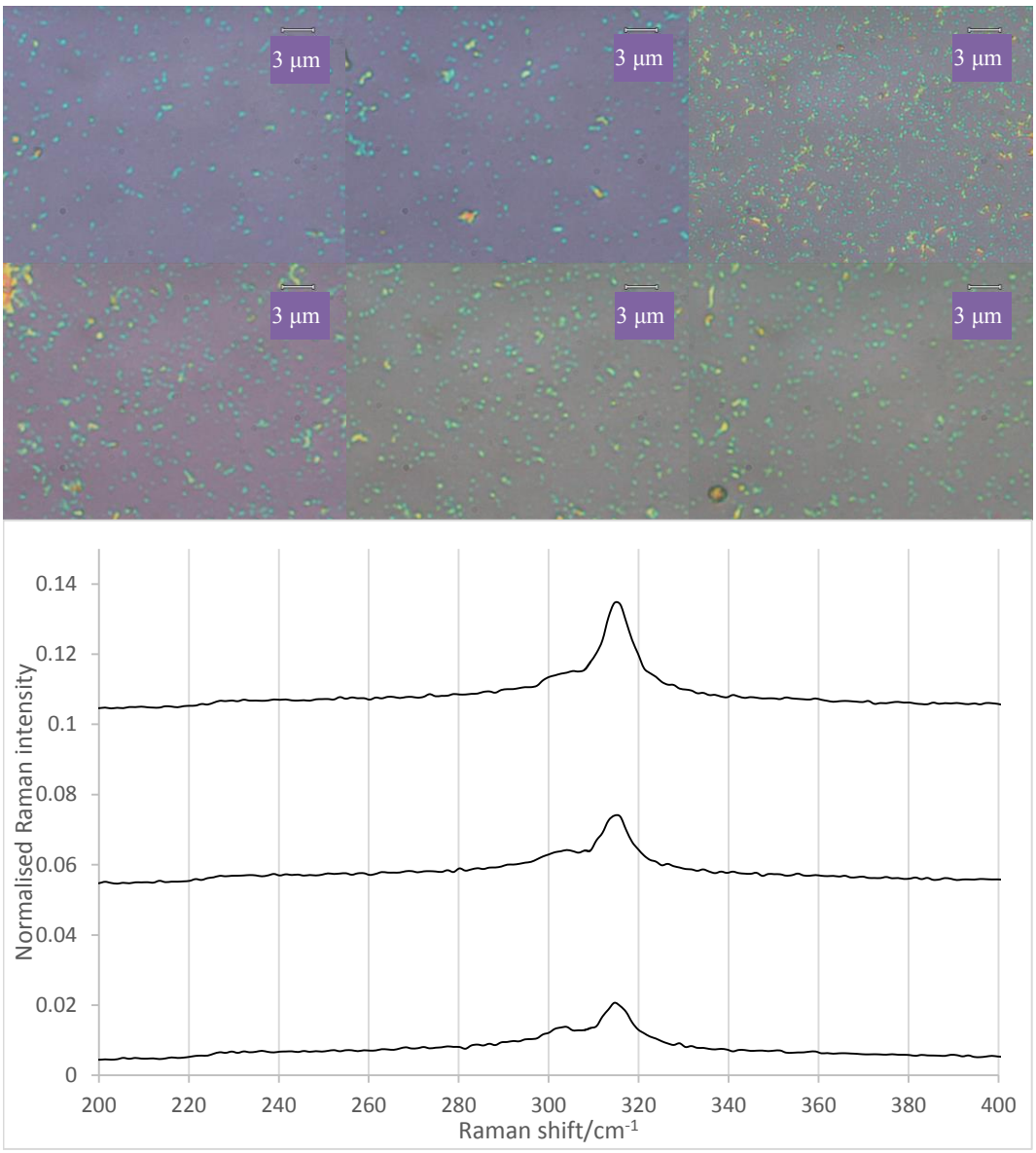

Figure 5.18 *Representative characterisation data from E1-5*

OM images of micron-scale dispersion from E1-5 (pH 9, 4 h sonication, 800 rpm centrifugation), scale bars = 3 µm, showing regions of uniform monolayer flakes. Spectra normalised to laser power to allow plotting on same graph irrespective of acquisition conditions. Note the good degree of monodispersity indicated by similarly-coloured flakes. UV-vis absorbance indicated 71% yield.

The data in Figure 5.19 contrast with those from E1-9. Notably, the OM images suggested fewer observable monolayers as a proportion of the entire dispersion (Figure 5.20).

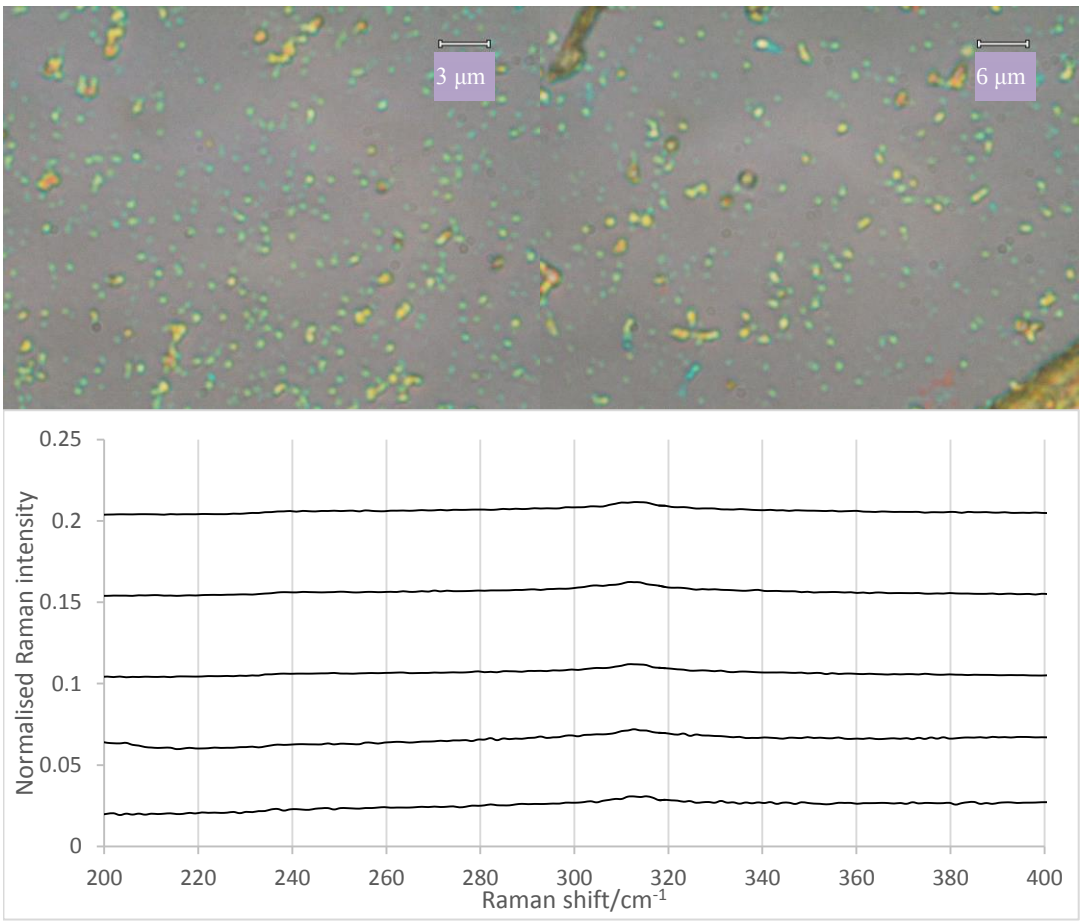

Figure 5.18 *Representative characterisation data from E1-9*

OM images of micron-scale dispersion from E1-9 (pH 9, 6 h sonication, 800 rpm), showing regions of uniform monolayer flakes (315 cm^{-1}). Spectra normalised to laser power to allow plotting on the same graph irrespective of acquisition conditions. Note the non-uniform dispersion here, indicated by the flakes of differing contrast against the background. UV-vis absorbance indicated 88% yield, which contradicts the Raman data showing a low monolayer count. It may be that monolayer flakes were too small to detect in this case compared to E1-5 due to longer sonication time.

The Raman data confirmed monolayer SnS_2, but the OM images seemed to contradict the higher yield. It is likely that 6 h sonication time played a significant role in breaking the lattice perpendicular to the basal plane, thus resulting in monolayers too small to be observed by conventional microscopy. Such monolayers, sub-micron in lateral size, would not prodigiously affect the background of the UV-vis spectrum, so this explanation is consistent with the data. That suggests it was entirely possible that E1-9 did, in fact, contain a higher monolayer yield. SEM could be used to confirm this.

The exponent n varies with flake size,[288] and the tight range of n-values at 800 rpm (n = 3.40-4.00) suggests that roughly the same size of flake was selected for at the same centrifugation speed,

while higher centrifugation speed selected for a different size (n = 1.40 @ 2400 rpm). This was entirely consistent with expectations, because that is the purpose of centrifugation at greater speeds.

In general, one sees that yield increased with the presence of hydroxide for sonication times longer than 2 h. The solvent provides the medium allowing the ions to intercalate into the interlayer gaps. As previously discussed, the interlayer distance in SnS_2 is ~0.60 nm, but the ionic radius of the hydroxide ion is 0.11 nm,[289] allowing easy intercalation. The ion insertion then causes expansion of the interplanar spaces, facilitating exfoliation by sonication.[290]

The yield obtained from absorbance of solution E1-10 (pH 9, 6 h sonication, 1600 rpm centrifugation) suggested a concentration of 130%. This is clearly nonsensical, but there is a possible explanation for it. If the UV absorption at the peak wavelength of 254 nm arose from an optical bandgap, then a degree of aggregation of nanoflakes could have an effect on the electronic wavefunction, changing the size of the bandgap. This in turn would break the linearity of the Beer-Lambert law by affecting the absorbance through a variable other than concentration. The corresponding change in the extinction coefficient would result in a misleading calculation of the absolute concentration. The anomalous yield did not appear in any other case, but further work may focus on elucidating the nature of the anomaly and the extent to which it applies to other yields.

5.6.4 Cascade centrifugation

To analyse the efficacy of the cascade centrifugation method, the UV-vis absorbance of the solution subjected to cascade centrifugation (E0-3) was plotted alongside that after 2400 rpm centrifugation (E0-12):

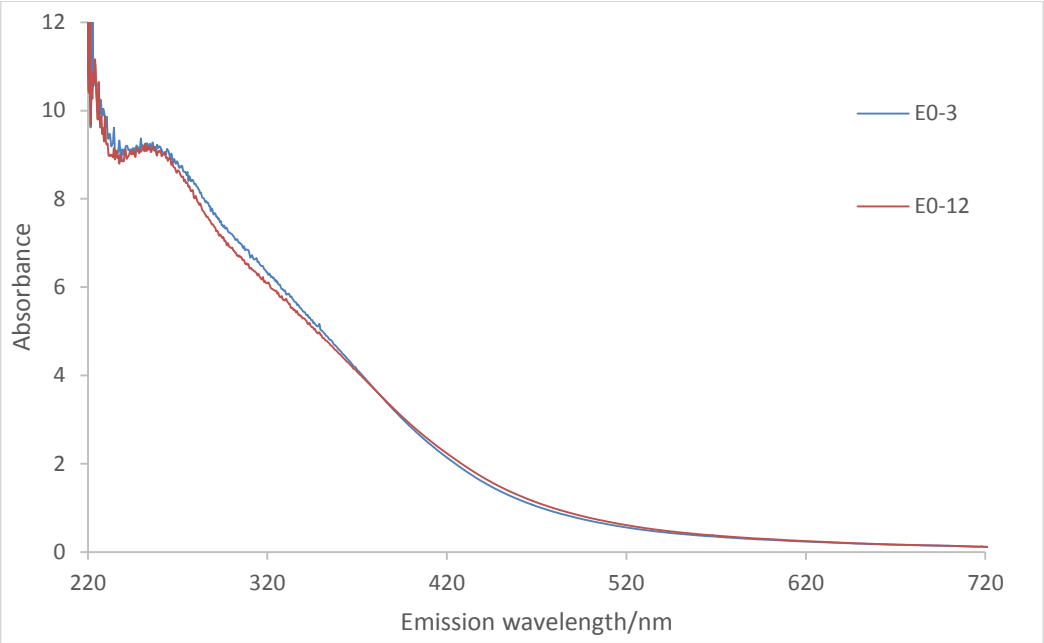

Figure 5.19 *Effect of cascade centrifugation on yield*

UV-vis absorbance spectra of aqueous solutions sonicated for 2h. E0-3 was centrifuged at 2400 rpm, and E0-12 was centrifuged by the cascade method.

The spectra look remarkably similar, so much so that they are almost superimposable. According to the figure, the peak absorbance occurred at ~9.3 for E0-3 and ~9.2 for E0-12. This suggested that, if anything, the cascade method had a marginally detrimental effect on yield. However, to estimate yield, the n-values also need to be known.

Comparison of n-values between 2400 rpm- and cascade-centrifuged solutions after 2 h sonication showed:

E0-3 (2400 rpm): $n = 4.50 \pm 0.02$

E0-12 (cascade): $n = 4.90 \pm 0.02$

As per the Coleman study, these values suggest that these absorbance spectra were not affected by Mié scattering. Accordingly, absorbance was assumed to have scaled linearly with concentration according to the Beer-Lambert law. The yields therefore corresponded to 44.3% (E0-3) and 43.7% (E0-12). Accounting for the effect of volumetric error in the molar extinction coefficient value, the slight difference in yield between the 2400 rpm and cascade methods was insignificant: $(44.3 \pm 3.8)\%$ compared to $(43.7 \pm 3.9)\%$. However, it is important to note that this is not a general indictment of the cascade method, because these solutions were prepared under specific conditions of solvent, concentration and sonication time, all of which affect the yield before the centrifugation step. Other conditions give a more favourable view of the cascade method. For evidence of this,

cascade centrifugation of E1-14 (pH 9, 6 h sonication) yielded an absorbance peak at ~15.7 and n = 4.10 ± 0.01, a yield of 74%.

The cascade method had a notable effect on the uniformity of the monolayer dispersion, as evidenced by OM images. Figure 5.20 showed few-layer SnS_2 flakes deposited on SiO_2 from solution E0-3 and E0-12.

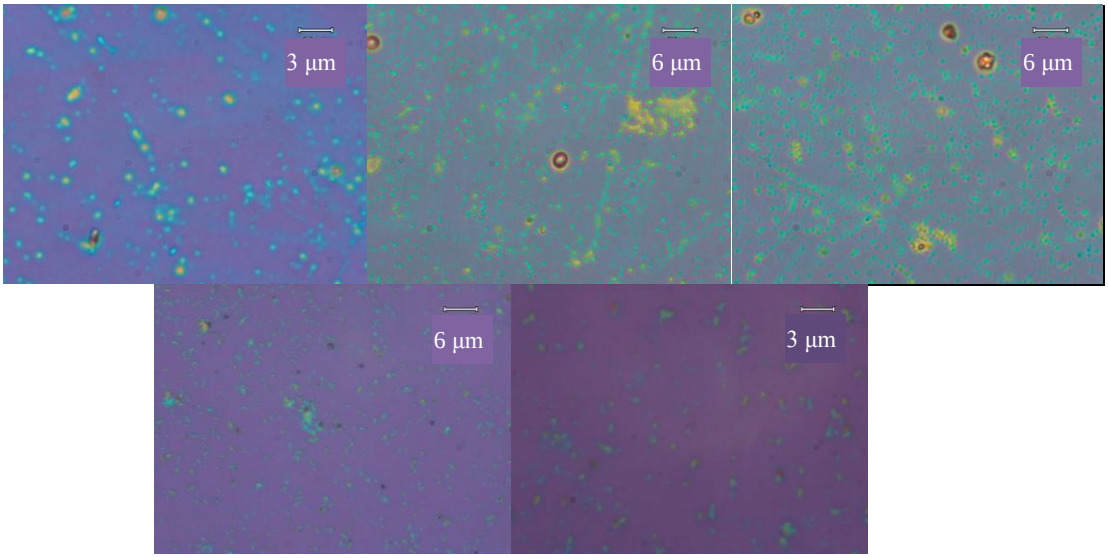

Figure 5.20 *Dispersion from E0-3 and E0-12 – effect of cascade centrifugation*

(Top row) Dispersion of SnS_2 on SiO_2 from E0-3; (Bottom row) Dispersion of SnS_2 on SiO_2 from E0-12. E0-3 (aqueous, 2 h sonication, 2400 rpm) flakes showed a larger size distribution compared to E0-12 (aqueous, 2 h sonication, cascade) flakes. Given that other conditions were the same, this difference was attributed to the size selectivity of cascade centrifugation.

The images in the top row, acquired from as-deposited flakes from solution E0-3, showed a good dispersion of high-contrast flakes. This is indicative of thickness, a sign that the solution likely contained a mixture of few-layer and monolayer flakes. It is unlikely that thicker flakes would be present given the high centrifugation speed. One sees that the contrast of the flakes from E0-12 on the bottom row was much lower against the substrate, even at higher magnification. The flakes in the latter case did not show as large a size distribution as the flakes from E0-3. This is to be expected as a consequence of the greater selectivity of cascade centrifugation for smaller flakes.

The same effect was observed comparing the OM images of E1-11 (pH 9, 6 h sonication, 2400 rpm centrifugation) and E1-14 (pH 9, 6 h sonication, cascade centrifugation):

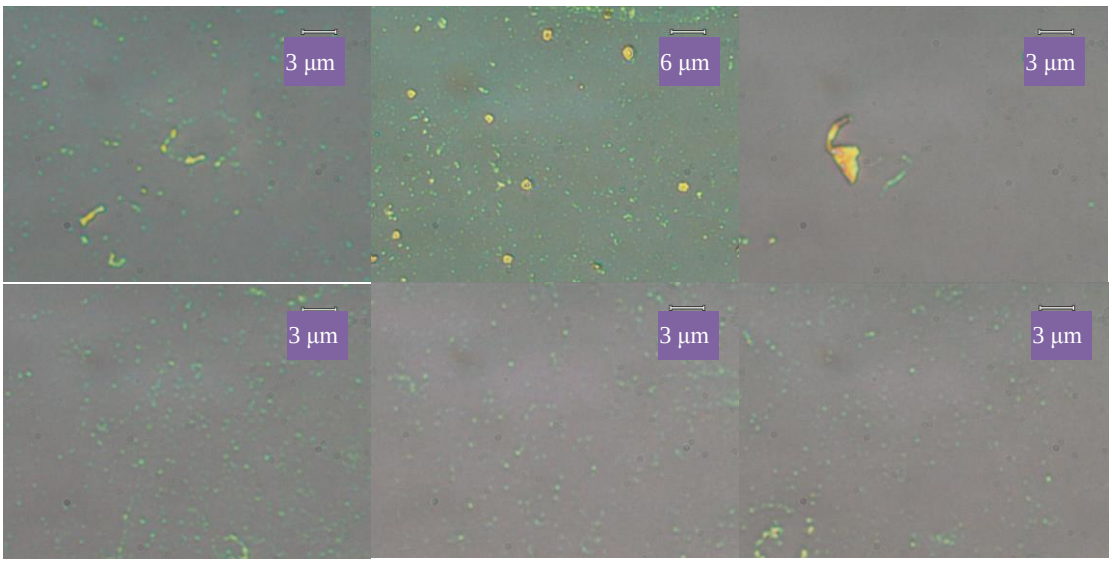

Figure 5.21 *Dispersion E1-11 and E1-14 – effect of cascade centrifugation*

(Top row) Dispersion of SnS_2 on SiO_2 from E1-11; (Bottom row) Dispersion of SnS_2 on SiO_2 from E1-14. E1-11 (pH 9, 6 h sonication, 2400 rpm) flakes showed a larger size distribution compared to E1-14 (pH 9, 6 h sonication, cascade) flakes. As in the aqueous case, so in the pH 9 case. All other conditions being the same, the difference in the size distribution was attributed to the greater size selectivity of the cascade method.

The UV-vis absorbance evidence suggests that although cascade centrifugation did not result in a greater yield than straight centrifugation at 2400 rpm (given comparable synthetic parameters), the greatest benefit of the method was in its selectivity for monolayers, as evidenced by OM and Raman spectroscopy. The images on the right, from the cascade solution, compare favourably to an example of a good-quality dispersion from the literature:

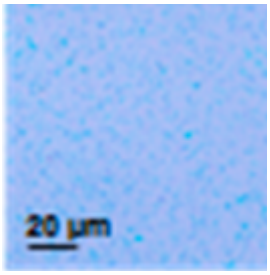

Figure 5.22 *An "ideal" dispersion of WS_2*

Taken from ref. [194], this optical image shows liquid-exfoliated WS_2 drop-casted onto SiO_2/Si in much the same way that was used in the experiments outlined here. Note the contrast of the flakes (blue specks) against the substrate background. This pattern was repeatedly observed in good-quality dispersions of SnS_2 produced herein (Figures 5.20 and 5.21).

According to Backes *et al.*¸flakes with lateral size greater than 150 nm are readily observed by their optical contrast alone, even a low magnifications.[194] Figure 5.22 therefore showed a good dispersion of WS_2 flakes (dark blue) against the brighter substrate surface.

If the solution is thought to contain a large concentration of monolayer flakes, the UV-vis absorbance can be used to calculate the bandgap of the material. The absorption coefficient is calculated by the following relation:[11]

$$\alpha = 2.303\frac{A}{l} \qquad [5.6]$$

where A = absorbance

l = optical absorbance path length/m

The absorption coefficient can be used with the Tauc equation to extract the material bandgap:[11]

$$\alpha h\nu = (h\nu - E_b)^r \qquad [5.7]$$

where $h\nu$ = photon energy

E_b = bandgap energy

r = index dependent on nature of bandgap

Then a Tauc plot is constructed, wherein an exponential function of the absorption coefficient is plotted against the bandgap energy. The exponent depends on the nature of the optical transition and is selected such that the plot shows a linear region that can be extrapolated to show the bandgap. The Tauc plot can be used as a complementary diagnostic tool for the monolayer because a 1L-SnS_2 flake is expected to have a direct bandgap at ~2.68 eV;[285] in contrast, the bulk bandgap lies at 2.18-2.44 eV.[247, 286]

The optical path length was 0.01 m, allowing the absorption coefficient to be calculated at each value of absorbance. A Tauc plot shows $\alpha h\nu^{\left(\frac{1}{r}\right)}$ *vs* $h\nu$ where $h\nu$ is the excitation energy in electron volts. The exponent r is selected from 0.5, 1.5, 2 and 3 with each value corresponding a calculation of the allowed direct, forbidden direct, allowed indirect and forbidden indirect bandgaps respectively. Extrapolation of the linear portion of a resulting Tauc plot (Figure 5.23) to the energy axis leads to the bandgap. For a worked example, see Appendix C3.

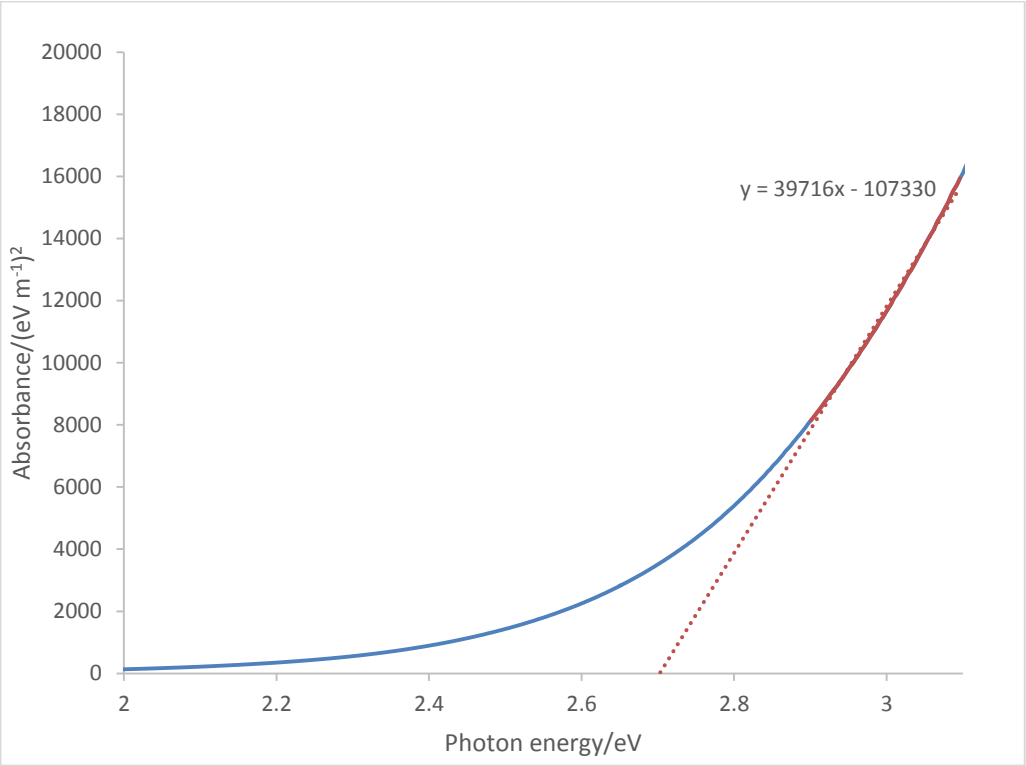

Figure 5.23 *Tauc plot to determine monolayer SnS_2 bandgap*

Plot was derived from UV-vis absorbance of solution E1-14 (pH 9, 6 h sonication, cascade centrifugation). Extrapolation of linear portion confirmed a direct bandgap of ~2.70 eV, demonstrating good-quality monolayers.

Performing this process on the UV-vis absorbance spectrum of E1-14 yielded an allowed direct bandgap of 2.70 ± 0.10 eV, which was corroborated by performing the same calculation on the E0-12 spectrum, leading to a very consistent value of 2.76 ± 0.14 eV. Within their respective margins of error, these values agree exactly with 1L bandgap reported in the literature (2.68 eV).[291]

5.6.5 Effect of pH 13 on exfoliation

The evidence indicated that liquid exfoliation at pH 13 effected a chemical reaction between the material and hydroxide ions in solution. This was evidenced by Raman spectra (Figure 5.24).

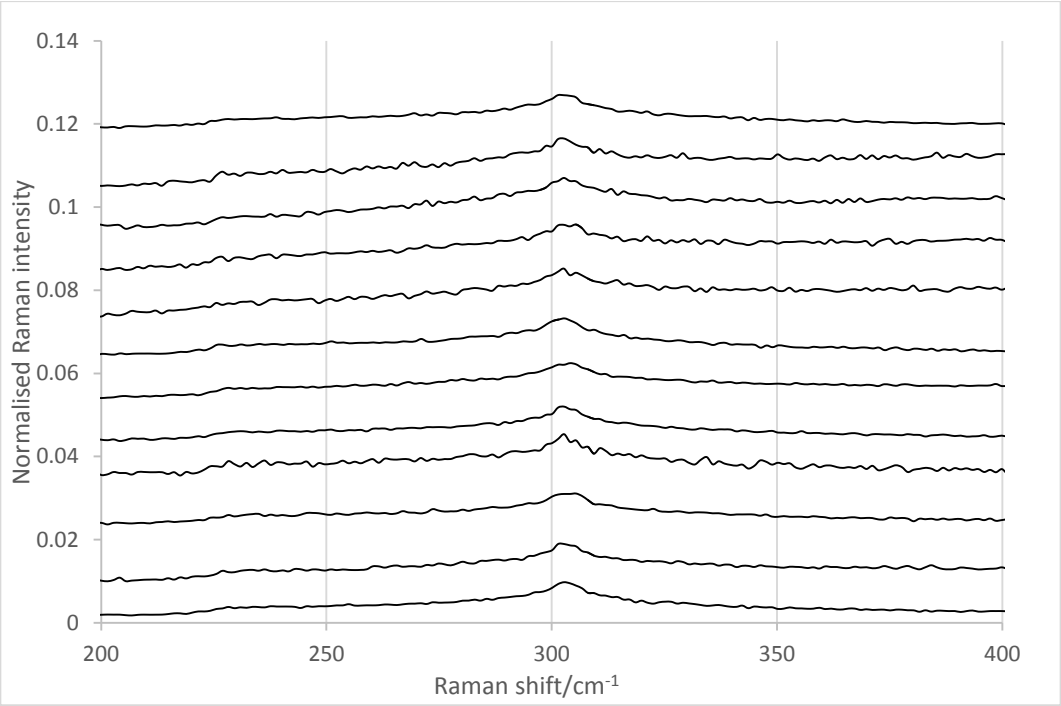

Figure 5.24 *Representative Raman spectra of as-deposited flakes from pH 13 solution*

Spectra were acquired from different samples spanning the full range of parameters used and are thought to be representative of typical results at pH 13. Spectra were normalised to laser power to allow for plotting on the same graph irrespective of acquisition conditions. Note that the absence of an A_{1g} phonon indicates that no SnS_2 was detected at pH 13. The peaks present should not be mistaken for the characteristic vibration; it is an Si-derived vibration at 303 cm^{-1}.

Representative spectra of typical regions of as-deposited flakes from pH 13 solutions showed no A_{1g} peak corresponding to the presence of SnS_2 under any combination of sonication and centrifugation parameters. The peak at ~303 cm^{-1} should not be mistaken for a tin(IV) sulphide peak; it is a substrate peak arising from SiO_2/Si.

Limited spectra did confirm the presence of small flakes of SnS_2, but these were rare and difficult to find. In fact, across many dozens of sampled regions from the pH 13 dispersions, fewer than ten spectra showed the presence of any SnS_2 at all. Figure 5.25 showed optical images (acquired using the viewfinder of the Raman microscope) of selected SnS_2 flakes and corresponding Raman spectra showing 1-3 layer thickness. These were the only surviving examples of few-layer SnS_2 that could be found.

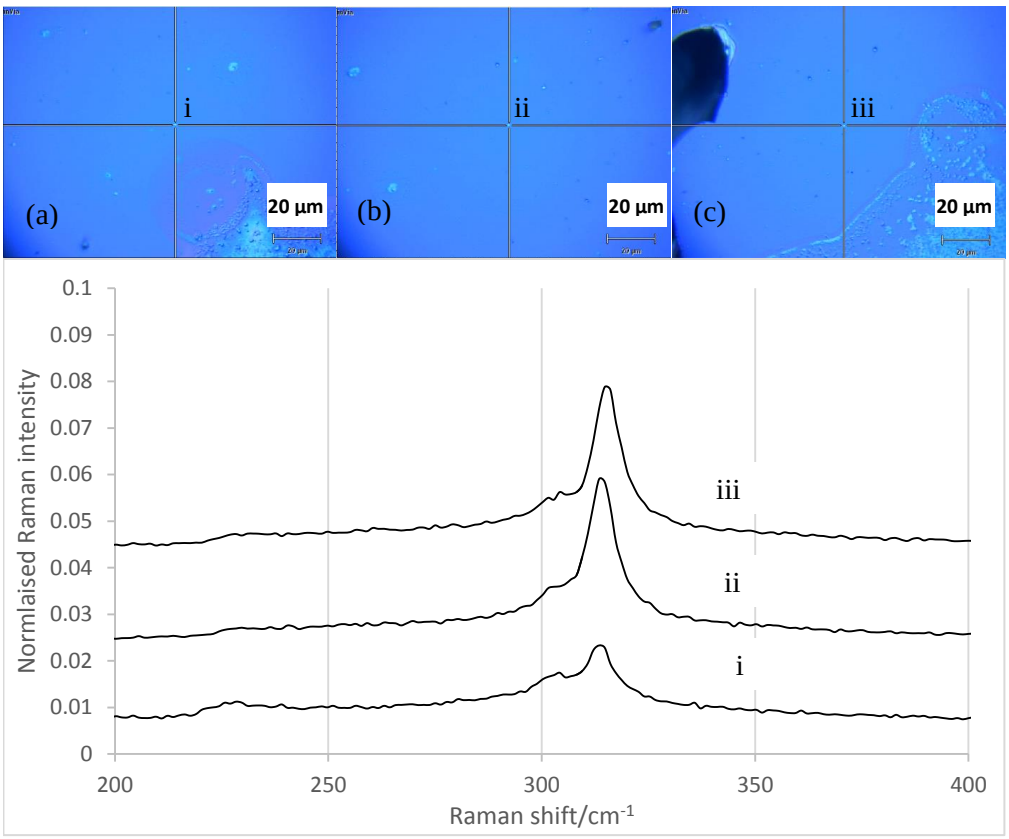

Figure 5.25 *Limited evidence of 1-3L SnS_2 flakes from pH 13 solutions*

The spectra i-iii correspond to the centres of the respective crosshairs in images a-c. The crosshairs were centred on apparent flakes clearly visible against the background. The Raman spectra indicated that only spectrum i was a monolayer with I_A/I_{Si} ratio of 0.02, while ii and iii represented trilayers with ratio around 0.04.

Figure 5.25 shows Raman spectra corresponding to the respective points (i), (ii) and (iii) in images (a), (b) and (c). The A_{1g} peak of spectrum (i) exhibited the ratio $I_A/I_{Si} = 0.02$, which denoted a monolayer. The same peaks of spectra (ii) and (iii) exhibit a ratio of 0.04, which denotes a trilayer.

The difficulty in detecting SnS_2 under any conditions strongly suggested that, in fact, pH was the confounding variable in this case. It is possible that sonication of the material in a concentrated basic solution induced a chemical reaction between the SnS_2 and the hydroxide ions.

Grazing incidence XRD was used to elucidate the product(s) of this reaction. Figure 5.26 shows the acquired XRD pattern from an SiO_2-supported sample of pH 13-exfoliated flakes and the expected SnS_2 spectrum generated using PDXL2 software.

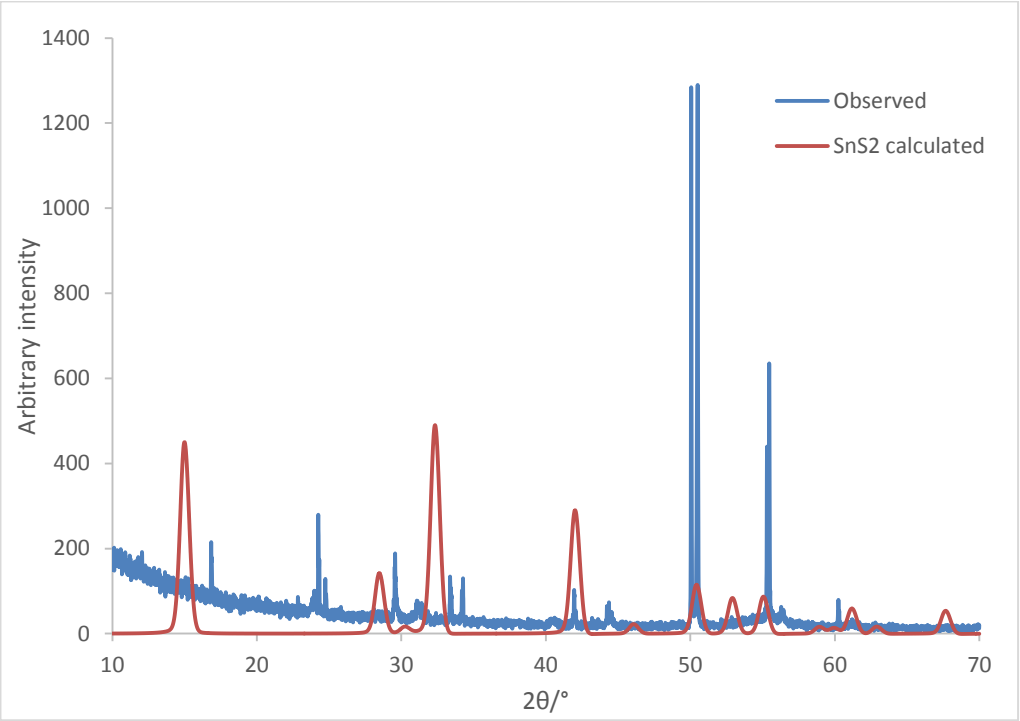

Figure 5.26 *XRD pattern of E2-7 and calculated pattern from SnS_2*

XRD pattern of E2-7 (pH 13, 4 h sonication, 1600 rpm) showed almost no overlap between the observed and calculated (using PDXL2) SnS_2 patterns. This suggested that the crystal structure consistent with SnS_2 was not present in this sample. Information obtained by other characterisation methods suggested that this was not an atypical pattern for a pH 13 sample. The observed spectrum could not be matched to available results in the database, and the exact product observed here remains unknown to the author.

The observed pattern hardly conformed to any of the expected SnS_2 peaks, a stark contrast to the pH 9 case, which showed ample overlap of peaks. This was further confirmation that the conditions effected a chemical reaction at pH 13. However, the nature of the product proved difficult to elucidate as the observed pattern did not fit with calculated patterns corresponding to SnO, SnO_2 or various complexed Sn_xS_y, Sn_xO_y and $Sn_x(OH)_y$ species. Further characterisation work such as elemental analysis could offer a compositional insight into this product, and perhaps TEM could be used to elucidate structural information.

5.7 Conclusion and future work

Exfoliation of SnS_2 (10 g L^{-1}) was performed by a lithium-free intercalation method using hydroxide ions as intercalants in water. Optimal conditions of pH, sonication time and centrifugation speed resulted in a 71% yield of monodisperse monolayers as determined by UV-vis spectrophotometry. This was obtained at pH 9 after 4 h sonication and 800 rpm centrifugation for 20 minutes. The yield represented greater than 26% improvement in yield compared to the

corresponding conditions in water as solvent (which was affected by scattering), confirming the efficacy of hydroxide intercalation as a viable, high-yield method for liquid exfoliation of SnS_2.

The novelty of this method lay in the first application of a lithium-free intercalation method to SnS_2, as well as the first use of aqueous media for SnS_2 exfoliation. This method allows for a safer and less chemically damaging exfoliation method for SnS_2 than the use of lithium.

The monodispersity of solutions was determined by a combination of OM, Raman microscopy and UV-vis absorbance. OM showed the lateral size distribution of flakes deposited on SiO_2 from different solutions. Many monolayer flakes obtained at the optimum conditions of 4 h sonication were of micron-order, and this was an important result. The ability to obtain micron-sized 1L flakes at short sonication times (<7 h) means that the trade-off between sonication time and flake size could be overcome using hydroxide intercalation, and this could be of considerable benefit to the research community in the future. However, further work may be done using higher-resolution imaging techniques such as SEM and TEM to ensure that the smallest monolayer flakes can be detected. This may lead to better assessment of optimal conditions.

A pH of 13 effected a chemical reaction between the material and hydroxide ions, and this suggests that there is an optimum pH. Traces of SnO contaminant were found by XRD even at pH 9, but these were deemed not to have significantly affected the monodispersity, because they were hardly detectable over a range of samples by Raman measurement. Future work may focus on elucidating the optimum pH; it is likely to be either side of pH 9.

Cascade centrifugation was explored as a means of maximising monolayer yield. Although UV-visible spectrophotometry suggested no significant difference between the yield obtained from centrifugation at 2400 rpm and successive centrifugation at 800, 1600 and 2400 rpm, optical and Raman microscopy showed that the monodispersity of the cascaded sample was better than that of the non-cascade case. The quality of monolayers produced both by the cascade and straight centrifugation was demonstrated by the Tauc method, yielding a direct bandgap of 2.70 ± 0.10 eV and 2.76 ± 0.14 eV respectively, which is in strong agreement with the literature on monolayer SnS_2.[286]

The data obtained in this study offer a route towards further parameter optimisation. For instance, it is thought that the starting concentration of material was sub-optimal based on the literature. This study was limited by the amount of starting material that was available. For that reason, it was not possible to investigate higher concentrations, nor was it possible to investigate longer sonication times without diluting the sample further. This presented a trade-off between concentration and sonication time. The possibility of obtaining higher yield at longer sonication times should be explored, provided that a higher concentration be used. In particular, it may be important to consider the difference in sonication quality obtainable by a tip sonicator. There is some evidence

that tip sonication offers more controllable and reproducible conditions.[194] It was also not possible to trial longer or shorter centrifugation times.

Most importantly, this method offers a route towards a low-risk, low-cost and high-yield alternative to lithium intercalation. This study offered no comparison between hydroxide- and lithium-mediated yields. But that was not the explicit intention. The study does show that a safer and more reliable alternative to lithium intercalation is available for SnS_2.

As the field advances towards alternatives to silicon for photonic technologies, the research community will benefit from lithium-free exfoliation offered by the method herein for safely and efficiently producing a high yield of good-quality monolayer SnS_2.

Chapter 6 Summary of Findings, Conclusions and Future Work

The findings presented in this thesis have addressed longstanding concerns in materials synthesis for nanoelectronic devices – particularly issues of industrial scalability, material quality and costs of production. By addressing application-specific challenges, such as the need for semiconducting Si alternatives in optoelectronics and visible absorbers in solar energy harvesting, the thesis provides the research community with an understanding of how research into materials such as MoS_2, WS_2 and SnS_2 can be developed.

Chapter 3 presented the case for new materials to replace silicon in nano- and optoelectronic technologies, due to the limitations imposed on Si by Moore's Law. Briefly, as technologies are continually scaled down to the nanometre scale, the effectiveness of silicon as a semiconductor becomes limited by the material's small indirect bandgap and the fact that silicon is a non-layered material (see Section 3.1). Therefore, the development of layered semiconductors such as the transition metal dichalcogenides (TMdCs) becomes crucial, not only to access atomic layer thickness but to improve electronic performance by accessing a larger, tuneable bandgap.

MoS_2 was presented as a viable alternative to Si for many nano- and optoelectronic properties due to its layered structure, large breakdown field and large, tuneable bandgap (see Section 3.2). Existing synthetic routes to MoS_2 have produced large monolayer films with good crystallinity, but many chemical vapour deposition (CVD) routes are complex, requiring fine control of precursors. CVD tends to produce polycrystalline monolayers, which are affected by electrical resistance at grain boundaries and are therefore not ideal for electronic applications.

The results herein demonstrated large single crystals around 100 μm in lateral size, as demonstrated by optical microscopy (OM) and scanning electron microscopy (SEM) and comparable to prior art (see Section 3.3), using low-temperature liquid atomic layer deposition (ALD) of the molybdenum-containing precursor. Large, well-formed single crystals were obtained from sulphurisation of precursor deposited at 80 ℃ as compared to >500 ℃ for traditional ALD and CVD. These single crystals were monolayer and highly crystalline, as demonstrated by Raman spectroscopy; phase-pure, as demonstrated by photoluminescence (PL); and structurally consistent with the prior art, as demonstrated by transmission electron microscopy (TEM). PL measurements in particular proved that the monolayers exhibited good light emission properties, possessing a bandgap of 1.86 eV and a valley splitting of 140 meV, both values in good agreement with the literature. It is expected that this method will advance the field by providing a new route to the synthesis of optoelectronic-grade single crystals, a good improvement on existing techniques.

The novelty of this new method is that it combined liquid-phase chemistry with layer-by-layer deposition of precursors as seen in ALD to produce monolayers for the first time. The use of a precursor solution to introduce ammonium heptamolybdate was reported for the first time and will lead to reduction in production costs because the system does not need to be maintained at high vacuum and high temperature as in traditional ALD.

Future work may be focussed on incorporation of monolayers produced by this method into devices to test breakdown properties and carrier mobility. To achieve good-quality device properties, it will be crucial to maximise single crystal size beyond that achievable by CVD. Possible routes towards this will include careful choice of substrate, substrate functionalisation and control of annealing and post-annealing parameters. For instance, sapphire could offer an epitaxial substrate to promote merging of well-aligned crystallites without grain boundaries, or hydroxide-etched SiO_2 could promote nucleation on dangling surface bonds. The latter would be a route towards a true ALD in the sense of being surface-limited. Another area of development will be to create a fully liquid-phase process, and this could be achieved using a liquid sulphur precursor, such as CS_2. The advantage of a fully liquid process followed by relatively low-temperature annealing will be to reduce production costs further by eliminating the need for high vacuum and high-temperature annealing. However, such a process will need to be carefully controlled because ensuring a clean interface at the substrate will be a difficult process where solvent is involved. The effect of this can be mitigated by ensuring the closest possible precursor—surface interaction to overcome the solvation energy. Careful control of dip-coating and annealing temperatures will also be important particularly if the solvent is non-volatile.

Chapter 4 presented an application for liquid ALD by using it in the development of an MoS_2—WS_2 heterostructure (see Section 4.1). The MoS_2—WS_2 heterostructure was presented as an ideal proof of concept because of the close lattice-matching between the two materials (see Section 4.2). Furthermore, the band alignment properties present within this heterostructure offer unique electronic properties, such as spatial charge separation, which are not accessible in the monolayer.

Following a discussion of the limitations of exsiting heterostructure synthetic techniques (see Section 4.3), the heterostructure was fabricated by deposition of WS_2 by sputtering and annealing in sulphur, followed by the use of the WS_2 as an epitaxial substrate for the liquid ALD growth of MoS_2, thus conforming to the discrete deposition requirement of ALD. The heterostructure presented herein conformed to the desired vertical rather than lateral configuration, and this was achieved by controlling the order and temperature of material deposition. Characterisation was performed by Raman spectroscopy, PL, as x-ray diffraction (XRD) and energy dispersive x-ray spectroscopy (EDXS). Comparison of optoelectronic properties between the liquid ALD heterostructure and a CVD-grown control sample suggested a cleaner interface in the latter.

This represented a novel approach to heterostructure synthesis in that an ALD-type process for making heterostructures has never previously been reported. This approach will be of benefit in heterostructure research by offering a lower-cost alternative to traditional CVD.

Ensuring a sharp and clean interface remains the primary challenge of this liquid-based approach and is an area for development in future. This will be important in order to make use of the unique interfacial properties of the heterostructure as compared to its constituent monolayers, such as band alignment leading to the spatial separation of charge carriers.

Chapter 5 presented a choice of Si alternatives for photovoltaic applications, with specific focus on visible absorbers as opposed to UV absorbers such as TiO_2 and ZnO_2 (see Section 5.1). The case for SnS_2 was presented, as it is a non-toxic material with inherently favourable electronic properties for solar energy harvesting applications (see Section 5.2)

The challenge of large-scale exfoliation of layered materials has not been met by existing techniques such as the tape method, while lift-off techniques (see Section 5.3) introduce technical complexity. In contrast, liquid-phase exfoliation is high-throughput and practically straightforward.

Liquid exfoliation has previously been combined with lithium ion intercalation to produce monolayers of TMdCs in high yield. However, lithium ion intercalation requires careful safety controls and damages monolayer properties. Therefore, the liquid exfoliation of large flakes of monolayer SnS_2 with the addition of sodium hydroxide ions was presented. The method developed herein offers a route to safe exfoliation of SnS_2 with no effect on material properties at moderate pH. The exfoliated monolayers were of micron scale in lateral size, as determined by OM. Thickness was confirmed by Raman spectroscopy. Yields in excess of 70% were obtainable in under 7 h sonication and with only moderate pH and centrifugation conditions. The use of cascade centrifugation led to improved size selection and monodispersity of exfoliated flakes, as shown by the count of monolayers detected by Raman spectroscopy. The Tauc method demonstrated excellent agreement with the experimentally-obtained bandgaps and theoretical values. These results have never been previously reported and present a yield comparable to literature with shorter sonication time and moderate centrifugation, even at suboptimal starting concentration around 10 g L^{-1}. As the process is developed and optimised in future, it will offer a means of large-scale monolayer production with more moderate conditions than are currently used, which will reduce production costs. This method informs the research community in the rich area of photovoltaics and addresses some of the synthetic challenges therein. This method advances the field by providing a new, safe and high-yield route towards a key photovoltaic material in contrast to existing techniques, which are hazardous, chemically damaging and low-yield.

The novelty of this method lay in the first reporting of an intercalation-based exfoliation of SnS_2 and the first use of aqueous media for SnS_2 exfoliation.

Future work will focus on precisely fine-tuning conditions to determine the optimum parameters not only for maximising monolayer yield, but also for preserving the crystallinity and chemical properties of the material. Device incorporation will allow for probing of photochemical properties of the resultant monolayers

The research in this thesis has addressed key challenges in moving beyond the use of silicon-based technologies. New materials have been considered, and new methods have been proposed for developing them that offer ease of production without compromising quality. These methods are commended to the research community.

Chapter 7 References

1. Centre for International Law, E. E. C. O. f. S. E., and Institute for Applied Ecology Nanomaterials Definition Fact Sheet. http://www.ciel.org/Publications/Nano_definition_Nov2014.pdf (accessed 13th October 2015).

2. Potocnik, J., 2011/696/EU: Commission Recommendation on the Definition of a Nanomaterial. *The OJ EU* **2011, *L 275***, 38-40.

3. Chhowalla, M.; Shin, H. S.; Eda, G.; Li, L. J.; Loh, K. P.; Zhang, H., The Chemistry of Two-Dimensional Layered Transition Metal Dichalcogenide Nanosheets. *Nat. Chem.* **2013,** *5* (4), 263-275.

4. Nicolosi, V.; Chhowalla, M.; Kanatzidis, M.G.; Strano, M. S.; Coleman, J. N., Liquid Exfoliation of Layered Materials. *Science* **2013,** *340* (6139), 1420-1438.

5. Park, J.; Lee, W.; Hwang, S.-H.; Myoung, J. M.; Jung, J.-H.; Kim., S.-Y., Layer-Modulated Synthesis of Uniform Tungsten Disulphide Nanosheets using Gas-Phase Precursors. *Nanoscale* **2015,** *7* (4), 1308-1313.

6. Poudel, B.; Hao, Q.; Ma, Y.; Lan, Y.; Minnich, A.; Yu, B.; Yan, X.; Weng, D.; Muto, A., Vashaee, D.; Chen, X.; Liu, J.; Dresselhaus, M. S.; Chen, G.; Ren, Z., High Thermoelectric Performance of Nanostructured Bismuth Antimony Telluride Bulk Alloys. *Science* **2008,** *320* (5876), 634-638.

7. Splendiani, A.; Sun, L.; Zhang, Y.; Li, T.; Kim, J.; Chim, C.-Y.; Galli, G.; Wang, F., Emerging Photoluminescence in Monolayer MoS_2. *Nano. Lett.* **2010,** *10* (4), 1271-1275.

8. Li, H.; Wu, J.; Zhang, H. Preparation and Applications of Mechanically Exfoliated Single-Layer and Multi layer MoS_2 and WSe_2 Nanosheets. *Acc. Chem. Res.* **2014,** *47* (4), 1067-1075.

9. Lee, K.; Kim, H.-Y.; Lotya, M.; Coleman, J. N.; Kim, G.-T.; Duesberg, G. S., Electrical Characteristics of Molybdenum Disulphide Flakes Produced by Liquid Exfoliation. *Adv. Mater.* **2011,** *23* (36), 4178-4182.

10. Lee, B.; Park, J.; Han, G. H.; Ee, H.-S.; Naylor, C. H.; Liu, W.; Johnson, A. T. C.; Agarwal, R., Fano Resonance and Spectrally-Modified Photoluminescence Enhancement in Monolayer MoS2 Integrated with Plasmonic Nanoantenna Array. *Nano Lett.* **2015,** *15* (5), 3646-3653.

11. Coleman, J. N.; Lotya, M.; O'Neill, A.; Bergin, S. D.; King, P. J.; Khan, U.; Young, K.; Gaucher, A.; De, S.; Smith, R. J.; Shvets, I. V.; Arora, S. K.; Stanton, G.; Kim, H.-Y.; Lee, K.; T., K. G.; Duesberg, G. S.; Hallam, T.; Boland, J. J.; Wang, J. J.; Donegan, J. F.; Grunlan, J. C.; Moriarty, G.; Shmeliov, A.; Nicholls, R. J.; Perkins, J. M.; Grieveson, E. M.; Theuwissen, K.; McComb, D. W.; Nellist, P. D.; Nicolosi, V., Two-Dimensional Nanosheets Produced by Liquid Exfoliation of Layered Materials. *Science* **2011,** *331* (6017), 568-571.

12. An, Y. R.; Fan, X. L.; Luo, Z. F.; Lau, W. M., Nanopolygons of Monolayer MS_2: Best Morphology and Size for HER Catalysis. *Nano Lett.* **2017,** *17* (1), 368-376.

13. Lukowski, M. A.; Daniel, A. S.; English, C. R.; Meng, F.; Forticaux, A.; Hamers, R. J.; Jin, S., Highly Active Hydrogen Evolution Catalysis from Metallic WS_2 Nanosheets. *Energy Environ. Sci.* **2014,** *7* (8), 2608-2613.

14. Withers, F.; Del Pozo-Zamudio, O.; Mishchenko, A.; Rooney, A. P.; Gholinia, A.; Watanabe, K.; Taniguchi, T.; Haigh, S. J.; Geim, A. K.; Tartakovskii, A. I.; Novoselov, K. S., Light-Emitting Diodes by Band-Structure Engineering in van der Waals Heterostructures. *Nat. Mater.* **2015,** *14* (3), 301-306.

15. Zan, W.; Geng, W.; Liu, H.; Yao, X., Electric-Field and Strain-Tunable Electronic Properties of MoS_2/h-BN/Graphene Vertical Heterostructures. *Phys. Chem. Chem. Phys* **2016,** *18* (4), 3159-3164.

16. Britnell, L.; Ribeiro, R. M.; Eckmann, A.; Jalil, R.; Belle, B. D.; Mishchenko, A.; Kim, Y. J.; Gorbachev, R. V.; Georgiou, T.; Morozov, S. V.; Grigorenko, A. N.; Geim, A. K.; Casiraghi, C.; Castro Neto, A. H.; Novoselov, K. S., Strong Light-Matter Interactions in Heterostructures of Atomically Thin Films. *Science* **2013,** *340* (6138), 1311-1314.

17. Kuiri, M.; Chakraborty, B.; Paul, A.; Das, S.; Sood, A. K.; Das, A., Enhancing Photoresponsivity using $MoTe_2$--Graphene Vertical Heterostructures. *Appl. Phys. Lett.* **2016,** *108* (6), 063506 (5 pp.)-063506 (5 pp.).

18. Eda, G.; Maier, S. A., Two-Dimensional Crystals: Managing Light for Optoelectronics. *ACS Nano* **2013,** *7* (7), 5660-5665.

19. Huang, C.; Wu, S.; Sanchez, A. M.; Peters, J. P. P.; Beanland, R.; Ross, J. S.; Rivera, P.; Yao, W.; Cobden, D. H.; Xu, X., Lateral Heterojunctions within Monolayer $MoSe_2$-WSe_2 Semiconductors. *Nat. Mater.* **2014,** *13* (12), 1096-1101.

20. Lee, C.-H.; Lee, G.-H.; van der Zande, A. M.; Chen, W.; Li, Y.; Han, M.; Cui, X.; Arefe, G.; Nuckolls, C.; Heinz, T. F.; Guo, J.; Hone, J.; Kim, P., Atomically-Thin p-n Junctions with van der Waals Heterointerfaces. *Nat. Nanotechnol.* **2014,** *9* (9), 676-681.

21. Bardeen, J., Research Leading to Point-Contact Transistor. *Science* **1957,** *126* (3264), 105-12.

22. Hush, N. S., *An Overview of the First Half-Century of Molecular Electronics*. 2003; Vol. 1006, p 1-20.

23. Tanaguchi, N., On the Basic Concept of Nanotechnology. *Proc. Int. Conf. Prod. Tech. Part II* **1974**.

24. Drexler, K. E., Molecular Engineering: An Approach to the Development of General Capabilities for Molecular Manipulation. *Proc. Nat. Acad. Sci. USA* **1981,** *78*, 5275-78.

25. Binnig, G., and Rohrer, H., Scanning Tunnelling Microscopy. *Surf. Sci.* **1982,** *126*, 236-44.

26. Kroto, H.; Heath, J. R.; O'Brien, S. C.; Curl, R. F.; Smalley, R. E., C60: Buckminster Fullerene. *Nature* **1985,** *318*, 162-163.

27. Binnig, G., Quate, C. F., and Gerber, C., Atomic Force Microscope. *Phys. Rev. Lett.* **1986,** *56* (9), 930-933.

28. Iijima, S., Helical Microtubules of Graphitic Carbon. *Nature* **1991,** *354*, 56-58.

29. Iijima, S., and Ichihashi, T., Single-Shell Carbon Nanotubes of 1 nm Diameter. *Nature* **1993,** *363*, 603-605.

30. Novoselov, K. S.; Geim, A. K.; Morozov, S. V.; Jiang, D.; Zhang, Y.; Dubonos, S. V.; Grigorieva, I. V.; Firsov, A. A., Electric-Field Effect in Atomically-Thin Carbon Films. *Science* **2004,** *306* (5696), 666-669.

31. Novoselov, K. S.; Jiang, D.; Schedin, F.; Booth, T. J.; Khotkevich, V. V.; Morozov, S. V.; Geim, A. K., Two-Dimensional Atomic Crystals. *Proc. Natl. Acad. Sci. USA* **2005,** *102* (30), 10451-10453.

32. Katsnelson, M. I., Graphene: Carbon in Two Dimensions. *Mater. Today* **2007,** *10* (1-2), 20-27.

33. Geim, A. K., Graphene: Status and Prospects. *Science* **2009,** *324* (5934), 1530-1534.

34. Lee, C.; Wei, X.; Kysar, J. W.; Hone, J., Measurement of the elastic properties and intrinsic strength of monolayer graphene. *Science* **2008,** *321* (5887), 385-388.

35. Freitag, M., Graphene Triyalers Unravelled. *Nature Phys.* **2011,** *7* (8), 596-597.

36. Geim, A. K.; Novoselov, K. S., The Rise of Graphene. *Nat. Mater.* **2007,** *6* (3), 183-191.

37. Tan, L. K.; Liu, B.; Teng, J. H.; Guo, S.; Low, H. Y.; Loh, K. P., Atomic Layer Deposition of a MoS_2 Film. *Nanoscale* **2014,** *6* (18), 10584-10588.

38. Radisavljevic, B.; Radenovic, A.; Brivio, J.; Giacometti, V.; Kis, A., Single-Layer MoS_2 Transistors. *Nat. Nanotechnol.* **2011,** *6* (3), 147-150.

39. Li, X., Wang, X.; Zhang, L.; Lee, S.; Dai, H., Chemically-Derived, Ultrasmooth Graphene Nanoribbon Semiconductors. *Science* **2008,** *319* (5867), 1229-1232.

40. Jiao, L., Zhang, L.; Wang, X.; Diankov, G.; Dai, H., Narrow Graphene Nanoribbons from Carbon Nanotubes. *Nature* **2009,** *458* (7240), 877-880.

41. Zhang, Z. P.; Yang, P. F.; Hong, M.; Jiang, S. L.; Zhao, G. C.; Shi, J. P.; Xie, Q.; Zhang, Y. F., Recent progress in the controlled synthesis of 2D metallic transition metal dichalcogenides. *Nanotechnol.* **2019,** *30* (18), 182002.

42. Eda, G.; Fujita, T.; Yamaguchi, H.; Voiry, D.; Chen, M. W.; Chhowalla, M., Coherent Atomic and Electronic Heterostructures of Single-Layer MoS2. *ACS Nano* **2012,** *6* (8), 7311-7317.

43. Wilson, J. A.; Yoffe, A. D., The Transition Metal Dichalcogenides Discussion and Interpretation of the Observed Optical, Electrical and Structural Properties. *Adv. Phys.* **1969,** *18* (73), 193-335.

44. Eda, G.; Yamaguchi, H.; Voiry, D.; Fujita, T.; Chen, M.; Chhowalla, M., Photoluminescence from Chemically-Exfoliated MoS_2. *Nano Lett.* **2011,** *11* (12), 5111-5116.

45. Scheuschner, N.; Ochedowski, O.; Kaulitz, A. M.; Gillen, R.; Schleberger, M.; Maultzsch, J., Photoluminescence of Freestanding Single- and Few-Layer MoS_2. *Phys. Rev. B* **2014,** *89* (12), 125406.

46. Hutchby, J. A., Bourianoff, G. I.; Zhirnov, Z. Z.; Brewer, J. E., Extending the Road Beyond CMOS. *IEEE Circuits Devices Mag.* **2002,** *18* (2), 28-41.

47. Braslavsky, S. E.; Braun, A. M.; Cassano, A. E.; Emeline, A. V.; Litter, M. I.; Palmisano, L.; Parmon, V. N.; Serpone, N.; Alfano, O. M.; Anpo, M.; Augugliaro, V.; Bohne, C.; Esplugas, S.; Oliveros, E.; von Sonntag, C.; Weiss, R. G.; Schiavello, M., Glossary of Terms used in Photocatalysis and Radiation Catalysis (IUPAC Recommendations 2011). *Pure Appl. Chem.* **2011,** *83* (4), 931-1014.

48. Cao, T.; Wang, G.; Han, W. P.; Ye, H. Q.; Zhu, C. R.; Shi, J. R.; Niu, Q.; Tan, P. H.; Wang, E.; Liu, B. L.; Feng, J., Valley-Selective Circular Dichroism of Monolayer Molybdenum Disulphide. *Nat. Commun.* **2012,** *3*.

49. Zeng, H. L.; Dai, J. F.; Yao, W.; Xiao, D.; Cui, X. D., Valley Polarization in MoS_2 Monolayers by Optical Pumping. *Nat. Nanotechnol.* **2012,** *7* (8), 490-493.

50. Mak, K. F.; He, K. L.; Shan, J.; Heinz, T. F., Control of Valley Polarisation in Monolayer MoS_2 by Optical Helicity. *Nat. Nanotechnol.* **2012,** *7* (8), 494-498.

51. Xiao, D.; Liu, G. B.; Feng, W. X.; Xu, X. D.; Yao, W., Coupled Spin and Valley Physics in Monolayers of MoS2 and Other Group-VI Dichalcogenides. *Phys. Rev. Lett.* **2012,** *108* (19).

52. Loh, K. P.; Bao, Q. L.; Eda, G.; Chhowalla, M., Graphene Oxide as a Chemically Tunable Platform for Optical Applications. *Nat. Chem.* **2010,** *2* (12), 1015-1024.

53. Jaramillo, T. F.; Jorgensen, K. P.; Bonde, J.; Nielsen, J. H.; Horch, S.; Chorkendorff, I., Identification of Active Edge Sites for Electrochemical H_2 Evolution from MoS_2 Nanocatalysts. *Science* **2007,** *317* (5834), 100-102.

54. Das, S.; Pandey, D.; Thomas, J.; Roy, T., The Role of Graphene and Other 2D Materials in Solar Photovoltaics. *Adv. Mater.* **2019,** *31* (1).

55. Castellanos-Gomez, A., Why all the Fuss about 2D Semiconductors? *Nat. Photonics* **2016,** *10* (4), 202-204.

56. Chung, I.; Kanatzidis, M. G., Metal Chalcogenides: A Rich Source of Nonlinear Optical Materials. *Chem. Mater.* **2014,** *26* (1), 849-869.

57. Ohmer, M. C.; Pandey, R.; Bairamov, B. H., Emergence of Chalcopyrites as Nonlinear Optical Materials. *MRS Bull.* **1998,** *23* (7), 16-20.

58. Dalton, L. R.; Sullivan, P. A.; Bale, D. H., Electric Field Poled Organic Electro-optic Materials: State of the Art and Future Prospects. *Chem. Rev.* **2010,** *110* (1), 25-55.

59. Ang, P. K., Wang, S.; Bao, Q.; Thong, J. T. L.; Loh, K. P., High-Throughput Synthesis of Graphene by Intercalation -- Exfoliation of Graphite Oxide and Study of Ionic Screening in Graphene Transistor. *ACS Nano* **2009,** *3* (11), 3587-3594.

60. Dreyer, D. R., Todd, A. D., and Bielawski, C. W., Harnessing the Chemistry of Graphene Oxide. *Chem. Soc. Rev.* **2014,** *43* (15), 5288-5301.

61. Liu, Z. P., Ma, R.; Osada, M.; Iyi, N.; Ebina, Y.; Takada, K.; Sasaki, T., Synthesis, Anion Exchange, and Delamination of Co-Al Layered Double Hydroxide: Assembly of the Exfoliated Nanosheet/Polyanion Composite Films and Magneto-Optical Studies. *J. Am. Chem. Soc.* **2006,** *128* (14), 4872-4880.

62. Cravotto, G., and Cintas, P., Sonication-Assisted Fabrication and Post-Synthetic Modifications of Graphene-Like Materials. *Chem. Eur. J.* **2010,** *16* (18), 5246-5259.

63. Hernandez, Y.; Nicolosi, V.; Lotya, M.; Blighe, F. M.; Sun, Z. Y.; De, S.; McGovern, I. T.; Holland, B.; Byrne, M.; Gun'ko, Y.K.; Boland, J. J.; Niraj, P.; Duesberg, G.; Krishnamurthy, S.; Goodhue, R.; Hutchison, J.; Scardaci, V.; Ferrari, A. C.; Coleman, J. N., High-Yield Production of Graphene by Liquid-Phase Exfoliation of Graphite. *Nat. Nanotechnol.* **2008,** *3* (9), 563-568.

64. Bourlinos, A. B.; Georgakilas, V.; Zboril, R.; Steriotis, T. A.; Stubos, A. K., Liquid-Phase Exfoliation of Graphite Towards Solubilised Graphenes. *Small* **2009,** *5*, 1841-1845.

65. Hamilton, C. E.; Lomeda, J. R.; Sun, Z.; Tour, J. M.; Barron, A. R., High-Yield Organic Dispersions of Unfunctionalised Graphene. *Nano Lett.* **2009,** *9* (10), 3460-62.

66. Khan, U.; O'Neill, A.; Lotya, M.; De, S.; Coleman, J., High-Concentration Solvent Exfoliation of Graphene. *Small* **2010,** *6* (7), 864-871.

67. Cui, J.; Song, Z.; Xin, L.; Zhao, S.; Yan, Y.; Liu, G., Exfoliation of Graphite to Few-Layer Graphene in Aqueous Media with Vinylimidazole-Based Polymer as High-Performance Stabiliser. *Carbon* **2016,** *99*, 249-260.

68. O'Neill, A.; Khan, U.; Nirmalraj, P. N.; Boland, J.; Coleman, J. N., Graphene Dispersion and Exfoliation in Low Boiling Point Solvents. *J. Phys. Chem. C* **2011,** *115* (13), 5422-5428.

69. Coleman, J. N., Liquid Exfoliation of Defect-Free Graphene. *Acc. Chem. Res.* **2013,** *46* (1), 14-22.

70. Bracamonte, M. V., Lacconi, G. I.; Urreta, S. E.; Foa Torres, L. E., On the Nature of Defects in Liquid-Phase Exfoliated Graphene. *J. Phys. Chem. C* **2014,** *118* (28), 15455-15459.

71. Han, W.-Q.; Wu, L.; Zhu, Y.; Watanabe, K.; Taniguchi, T., Structure of Chemically Derived Mono- and Few-Atomic-Layer Boron Nitride Sheets. *Appl. Phys. Lett.* **2008,** *93* (22), 223103.

72. Zhi, C.; Bando, Y.; Tang, C.; Kuwuhara, H.; Golberg, D., Large-Scale Fabrication of Boron Nitride Nanosheets and Their Utilisation in Polymeric Composites with Improved Thermal and Mechanical Properties. *Adv. Mater.* **2009,** *21* (28), 2889-+.

73. Gao, G.; Gao, W.; Taha-Tijerina, J.; Balicas, L.; Mathkar, A.; Naravanan, T. N.; Liu, Z.; Gupta, B. K.; Peng, J.; Yin, Y.; Rubio, A.; Ajayan, P. M., Artificially Stacked Atomic Layers: Toward New van der Waals Solids. *Nano Lett.* **2012,** *12* (7), 3518-25.

74. Ma, P.; Spencer, J. T., Non-Covalent Stabilisation and Functionalisation of Boron Nitride Nanosheets (BNNSs) by Organic Polymers: Formation of Complex BNNSs-Containing Structures. *J. Mater. Sci.* **2015,** *50* (1), 313-23.

75. Zhou, K.-G.; Mao, N.-N.; Wang, H.-X.; Peng, Y.; Zheng, H.-L., A Mixed-Solvent Strategy for Efficient Exfoliation of Inorganic Graphene Analogues. *Angew. Chem. Int. Ed.* **2011,** *50* (46), 10839-42.

76. Wang, Y.; Shi, Z.; Yin, J., Boron Nitride Nanosheets: Large-Scale Exfoliation in Methanesulphonic Acid and their Composites with Polybenzimidazole. *J. Mater. Chem.* **2011,** *21* (30), 11371-77.

77. Lin, Y.; Connell, J. W., Advances in 2D Boron Nitride Nanostructures: Nanosheets, Nanoribbons, Nanomeshes, and Hybrids with Graphene. *Nanoscale* **2012,** *4*, 6908-39.

78. Stengl, V., Henych, J., and Kormunda, M., Self-Assembled BN and BCN Quantum Dots Obtained from High Intensity Ultrasound Exfoliated Nanosheets. *Sci. Adv. Mater.* **2014,** *6* (6), 1106-16.

79. Zhou, X.; Hu, X. Z.; Yu, J.; Liu, S. Y.; Shu, Z. W.; Zhang, Q.; Li, H. Q.; Ma, Y.; Xu, H.; Zhai, T. Y., 2D Layered Material-Based van der Waals Heterostructures for Optoelectronics. *Adv. Funct. Mater.* **2018,** *28* (14).

80. Rafiei-Sarmazdeh, Z.; Jafari, S. H.; Ahmadi, S. J.; Zahedi-Dizaji, S. M., Large-Scale Exfoliation of Hexagonal Boron Nitride with Combined Fast Quenching and Liquid Exfoliation Strategies. *J. Mater. Sci.* **2016,** *51* (6), 3162-69.

81. Brent, J. R.; Savjani, N.; Lewis, E. A.; Haigh, S. J.; Lewis, D. J.; O'Brien, P., Production of Few-Layer Phosphorene by Liquid Exfoliation of Black Phosphorus. *Chem. Comm.* **2014,** *50* (87), 13338-13341.

82. Kang, J.; Wood, J. D.; Wells, S. A.; Lee, J.-H.; Liu, X.; Chen, K.-S.; Hersam, M. C., Solvent Exfoliation of Electronic-Grade, Two-Dimensional Black Phosphorus. *ACS Nano* **2015,** *9* (4), 3596-3604.

83. Yasaei, P.; Kumar, B.; Foroozan, T.; Wang, C.; Asadi, M.; Tuschel, M.; Indacochea, J. E.; Klie, R. F.; Salehi-Khojin, A., High-Quality Black Phosphorus Atomic Layers by Liquid-Phase Exfoliation. *Adv. Mater.* **2015,** *27* (11), 1887-+.

84. Hanlon, D., *et al.*, Liquid Exfoliation of Solvent-Stabilised Few-Layer Black Phosphorus for Applications Beyond Electronics. *Nat. Comm.* **2015,** ***6***, 8563.

85. Zhao, W.; Xue, Z.; Wang, J.; Jiang, J.; Zhao, X.; Mu, T., Large-Scale, Highly Efficient, and Green Liquid-Exfoliation of Black Phosphorus in Ionic Liquids. *ACS Appl. Mater. Interf.* **2015,** *7* (50), 27608-27612.

86. Bang, G. S.; Nam, K. W.; Kim, J. Y.; Shin, J.; Choi, J. W.; Choi, S. Y., Effective Liquid-Phase Exfoliation and Sodium Ion Battery Application of MoS2 Nanosheets. *ACS Appl. Mater. Interf.* **2014,** *6* (10), 7084-7089.

87. Varrla, E.; Backes, C.; Paton, K. R.; Harveys, A.; Gholamvand, Z.; McCauleys, J.; Coleman, J. N., Large-Scale Production of Size-Controlled MoS_2 Nanosheets by Shear Exfoliation. *Chem. Mater.* **2015,** *27* (3), 1129-1139.

88. Backes, C.; Szydlowska, B. M.; Harvey, A.; Yuan, S.; Vega-Mayoral, V.; Davies, B. R.; Zhao, P.-L.; Hanlon, D.; Santos, E. J. G.; Katsnelson, M. I.; Balu, W. J.; Gadermeier, C.; Coleman, J. N., Production of Highly Monolayer-Enriched Dispersions of Liquid-Exfoliated Nanosheets by Liquid Cascade Centrifugation. *ACS Nano* **2016,** *10* (1), 1589-1601.

89. Gholamvand, Z.; McAteer, D.; Backes, C.; McEvoy, N.; Harvey, A.; Berner, N. C.; Hanlon, D.; Bradley, C.; Godwin, I.; Rovetta, A.; Lyons, M. E. G.; Duesberg, G. S.; Coleman, J. N., Comparison of Liquid Exfoliated Transition Metal Dichalcogenides Reveals $MoSe_2$ to be the Most Effective Hydrogen Evolution Catalyst. *Nanoscale* **2016,** *8* (10), 5737-5749.

90. Gerchman, D., and Alves, A. K., Solution-Processable Exfoliation and Suspension of Atomically Thin WSe_2. *J. Colloid Interface Sci.* **2016,** *468*, 247-252.

91. Ding, Z.; Bux, S. B.; King, D. J.; Chang, F. L.; Chen, T.-H.; Huang, S.-C.; Kaner, R. B., Lithium Intercalation and Exfoliation of Layered Bismuth Selenide and Bismuth Telluride. *J. Mater. Chem.* **2009,** *19* (17), 2588-2592.

92. Sun, L.; Lin, Z.; Peng, J.; Weng, J.; Huang, Y.; Luo, Z., Preparation of Few-Layer Bismuth Selenide by Liquid-Phase-Exfoliation and Its Optical Absorption Properties. *Sci. Rep.* **2014,** *4*.

93. Ludwig, T.; Guo, L.; McRary, P.; Zhang, Z.; Gordon, H.; Quan, H.; Stanton, M.; Frazier, R. M.; Rogers, R. D.; Wang, H.-T.; Turner, C. H., Mechanism of Bismuth Telluride Exfoliation in an Ionic Liquid Solvent. *Langmuir* **2015,** *31* (12), 3644-3652.

94. Sun, B., and Huang, X. M. H., Mechanical Nano-Resonators at Ultra-High Frequency and Their Potential Applications. *S. Afr. J. Sci.* **2008,** *104* (5-6), 169-171.

95. Lazell, M.; O'Brien, P.; Otway, D. J.; Park, J.-H., Single Source Molecular Precursors for the Deposition of III/VI Chalcogenide Semiconductors by MOCVD and Related Techniques. *J. Chem. Soc. - Dalton Trans.* **2000,** *24*, 4479-4486.

96. Leskela, M., and Ritala, M., Atomic layer deposition (ALD): from precursors to thin film structures. *Thin Solid Films* **2002,** *409* (1), 138-146.

97. Parilla, P. A., Dillon A. C.; Parkinson, B. C.; Jones, K. M.; Alleman, J.; Riker, G.; Ginely, D. S.; Heben, M. J., Formation of Nanooctahedra in Molybdenum Disulfide and Molybdenum Diselenide using Pulsed Laser Vaporisation. *J. Phys. Chem. B* **2004,** *108* (20), 6197-6207.

98. Sneh, O.; Clark-Phelps, R. B.; Londergan, A. R.; Winkler, J.; Seidel, T. E., Thin film atomic layer deposition equipment for semiconductor processing. *Thin Solid Films* **2002,** *402* (1-2), 248-261.

99. Bar Sadan, M.; Enyashin, A.; Gemming, S.; Popovitz-Biro, R.; Hong, S. Y.; Prior, Y.; Seifert, G., Structure and Stability of Molybdenum Sulphide Fullerenes. *Angew. Chem. Int. Ed.* **2007,** *46* (4), 623-627.

100. Bar Sadan, M., *et al.*, Towards Atomic-Scale Bright-Field Electron Tomography for the Study of Fullerene-Like Nanostructures. *Nano Lett.* **2008,** *8* (3), 891-896.

101. Glavin, N. R., *et al.*, Temporally and Spatially Resolved Plasma Spectroscopy in Pulsed Laser Deposition of Ultra-Thin Boron Nitride Films. *J. Appl. Phys.* **2015,** *117* (16).

102. Serrao, C. R.; Diamond, A. M.; Hsu, S.-L.; You, L.; Gadgil, S.; Clarkson, J.; Carraro, C.; Maboudian, R.; Hu, C.; Salahuddin, S., Highly-Crystalline MoS_2 Thin Films Grown by Pulsed Laser Deposition. *Appl. Phys. Lett.* **2015,** *106* (5), 052101.

103. Oldfield, D. T.; McCulloch, D. G.; Huynh, C. P.; Sears, K.; Hawkins, S. C., Multilayered Graphene Films Prepared at Moderate Temperatures using Energetic Physical Vapour Deposition. *Carbon* **2015,** *94*, 378-385.

104. Jamison, P. C.; Tsunoda, T.; Vo, T. A.; Li, J.; Jagannathan, H.; Shinde, S.; Paruchuri, V. K.; Gall, D., SiO_2-Free HfO_2 Gate Dielectrics by Physical Vapor Deposition. *IEEE Trans. Electron Dev.* **2015,** *62* (9), 2878-2882.

105. Rao, C. N. R.; Vivekchand, S. R. C.; Biswas, K.; Govindaraj, A., Synthesis of Inorganic Nanomaterials. *Dalton Trans.* **2007,** *34*, 3728-3749.

106. Rao, C. N. R.; Ramakrishna Matte, H. S.S.; Voggu, R.; Govindaraj, A., Recent Progress in the Synthesis of Inorganic Nanoparticles. *Dalton Trans.* **2012,** *41* (17), 5089-5120.

107. Liu, K.-K.; Zhang, W.; Lee, Y.-H.; Lin, Y.-C.; Chang, M.-T.; Su, C.-Y.; Chang, C.-S.; Li, H.; Shi, Y.; Zhang, H.; Lai, C.-S.; Li, L.-J., Growth of Large-Area and Highly Crystalline MoS_2 Thin Layers on Insulating Substrates. *Nano Lett.* **2012,** *12* (3), 1538-1544.

108. *Modern Trends in Chemical Reaction Dynamics: Experiment and Theory (Part I)*. World Scientific Publishing Co, Pte. Ltd.: Singapore, 2004.

109. Zhang, J.; Xue, D. J.; Zhan, X. J.; Li, Z.; Zeng, D. W.; Song, H. B., Versatile Solution-Processed Synthesis of Two-Dimensional Ultrathin Metal Chalcogenides Following Frank-van der Merwe Growth. *ACS Appl. Mater. Interf.* **2017,** *9* (32), 27102-27110.

110. Rio, E.; Boulogne, F., Withdrawing a solid from a bath: How much liquid is coated? *Adv. Interface Colloid Sci.* **2017,** *247*, 100-114.

111. Winters, H. F., The Role of Chemisorption in Plasma Etching. *J. Appl. Phys.* **1978,** *49* (10), 5165-5170.

112. Sedlacik, M.; Pavlinek, V.; Lehocky, M.; Junkar, I.; Vesel, A., Plasma-Enhanced Chemical Vapour Deposition of Octofluorocyclobutane onto Carbonyl Iron Particles. *Mater. Tehnol.* **2012,** *46* (1), 43-46.

113. Peri, S. R.; Akgun, B.; Satija, S. K.; Jiang, H.; Enlow, J.; Bunning, T. J.; Foster, M. D., Control of Interface Nanoscale Structure Created by Plasma-Enhanced Chemical Vapor Deposition. *ACS Appl. Mater. Interf.* **2011,** *3* (9), 3375-3383.

114. Lin, L. C.; Jing, X. M.; Liu, F. M.; Yin, W.; Yu, D. Q.; Cao, L. Q., Deep Dry Etching of Fused Silica using C_4F_8/Ar Inductively Coupled Plasmas. *J. Mater. Sci. Mater. Electron.* **2017,** *28* (1), 480-486.

115. Kuo, M. S.; Hua, X. F.; Oehrlein, G. S.; Ali, A.; Jiang, P.; Lazzeri, P.; Anderle, M., Influence of C_4F_8/Ar-Based Etching and H_2-Based Remote Plasma Ashing Processes on Ultralow K Materials Modifications. *J. Vac. Sci. Technol. B* **2010,** *28* (2), 284-294.

116. Parker, N. W.; Brodie, A. D.; McCoy, J. H. In *A High-Throughput NGL Electron Beam Direct-Write Lithography System*, Emerging Lithographic Technologies IV, Santa Clara, Ca, Feb 28-Mar 01; Santa Clara, Ca, 2000; pp 713-720.

117. Oshima, C.; Aono, M.; Tanaka, T.; Kawai, S.; Shimizu, R., Thermionic Emission from Single Crystal LaB_6 Tips with (100), (110), (111) and (210) Orientations. *J. Appl. Phys* **1980,** *51* (2), 1201-1206.

118. Futamoto, M.; Nakazawa, M.; Usami, K.; Hosoki, S.; Kawabe, U., Thermionic Emission Properties of Single-Crystal LaB_6 Cathode. *J. Apply. Phys* **1980,** *51* (7), 3869-3876.

119. Storms, E. K.; Mueller, B. A., Study of Surface Stoichiometry and Thermionic Emission using LaB_6. *J. Apply. Phys.* **1979,** *50* (5), 3691-3698.

120. Swanson, L. W., Comparative Study of Zirconiated and Bulit-Up W Thermal-Field Cathode. *J. Vac. Sci. Technol.* **1975,** *12* (6), 1228-1233.

121. Assim, K.; Melzer, M.; Korb, M.; Ruffer, T.; Jakob, A.; Noll, J.; Georgi, C.; Schulz, S. E.; Lang, H., Bis(beta-diketonato)- and Allyl-(beta-diketonato)palladium(II) Complexes: Synthesis, Characterisation and MOCVD Application. *RSC Advances* **2016,** *6* (104), 102557-102569.

122. Du, L. Y.; Wang, H. J.; Ding, Y. Q., A Germanium(II) Aminopyridinato Compound and its Potential as a CVD Precursor. *Polyhedron* **2017,** *134*, 282-286.

123. Du, L. Y.; Yu, S. S.; Liu, X. F.; Ding, Y. Q., An Aminopyridinato Mn(II) Compound as a Novel CVD Precursor for Manganese-Containing Films. *New J. Chem.* **2018,** *42* (6), 4553-4558.

124. Gebhard, M.; Hellwig, M.; Kroll, A.; Rogalla, D.; Winter, M.; Mallick, B.; Ludwig, A.; Wiesing, M.; Wieck, A. D.; Grundmeier, G.; Devi, A., New Amidinate Complexes of Indium(III): Promising CVD Precursors for Transparent and Conductive In2O3 Thin Films. *Dalton Trans.* **2017,** *46* (31), 10220-10231.

125. Merenkov, I. S.; Gostevskii, B. A.; Krasnov, P. O.; Basova, T. V.; Zhukov, Y. M.; Kasatkin, I. A.; Sysoev, S. V.; Kosyakov, V. I.; Khomyakov, M. N.; Kosinova, M. L., Novel Single-Source Precursors for $SiB_xC_yN_z$ Film Deposition. *New J. Chem.* **2017,** *41* (20), 11926-11933.

126. Mayerhofer, T. G.; Popp, J., Beer's Law -- Why Absorbance Depends (Almost) Linearly on Concentration. *ChemPhysChem* **2019,** *20* (4), 511-515.

127. Swinehart, D. F., The Beer-Lambert Law. *J. Chem. Educ.* **1962,** *39* (7), 333.

128. Late, D. J.; Liu, B.; Ramakrishna Matte, H. S. S.; Rao, C. N. R.; Dravid, V. P., Rapid Characterisation of Ultrathin Layers of Chalcogenides on SiO_2/Si Substrates. *Adv. Func. Mater.* **2012,** *22* (9), 1894-1905.

129. Ferrari, A. C.; Basko, D. M., Raman spectroscopy as a versatile tool for studying the properties of graphene. *Nat. Nanotechnol.* **2013,** *8* (4), 235-246.

130. Raman, C. V., A New Radiation. *Indian J Phys* **1928,** *2* (4), 387-398.

131. Strommen, D. P.; Nakamoto, K., Resonance Raman Spectroscopy. *J. Chem. Educ.* **1977,** *54* (8), 474-478.

132. Charbonnier, F., Developing and using the field emitter as a high intensity electron source. *Appl. Surf. Sci.* **1996,** *94-5*, 26-43.

133. Danilatos, G. D., Foundations of Environmental Scanning Electron Microscopy. *Adv. Electron. El. Phys.* **1988,** *71*, 109-250.

134. de Jonge, N.; Ross, F. M., Electron microscopy of specimens in liquid. *Nat. Nanotechnol.* **2011,** *6* (11), 695-704.

135. Suzuki, E., High-resolution scanning electron microscopy of immunogold-labelled cells by the use of thin plasma coating of osmium. *J. Microsc.* **2002,** *208*, 153-157.

136. Scimeca, M.; Bischetti, S.; Lamsira, H. K.; Bonfiglio, R.; Bonanno, E., Energy Dispersive X-ray (EDX) microanalysis: A powerful tool in biomedical research and diagnosis. *Eu. J. Histochem.* **2018,** *62* (1), 88-97.

137. Gavara, N., A Beginner's Guide to Atomic Force Microscopy Probing for Cell Mechanics. *Microsc. Res. Tech.* **2017,** *80* (1), 75-84.

138. Chescoe, D.; Goodhew, P. J., *The Operation of a Transmission Electron Microscope*. Oxford University Press: Oxford, 1984; p 49.

139. Bragg, W. H.; Bragg, W. L., The Reflexion of X-rays by Crystals. *Proc. R. Soc. Lond.* **1913,** *88* (605), 428-438.

140. Hayashi, K., Review of the applications of x-ray refraction and the x-ray waveguide phenomenon to estimation of film structures. *J. Phys. Condens. Matter* **2010,** *22* (47).

141. Moore, G. E., Cramming More Components onto Integrated Circuits. *Proc. IEEE* **1998,** *86* (1), 82-5.

142. Auth, C., 22-nm Fully-Depleted Tri-Gate CMOS Transistors. *IEEE CICC 2012* **2012**, 6 pp.-6 pp.

143. Wang, L. M.; IEEE In *Relationship between intrinsic breakdown field and bandgap of materials*, 25th International Conference on Microelectronics, Belgrade, SERBIA MONTENEG, May 14-17; Belgrade, SERBIA MONTENEG, 2006; pp 615-618.

144. Ding, Y.; Wang, Y.; Ni, J.; Shi, L.; Shi, S.; Tang, W., First principles study of structural, vibrational and electronic properties of graphene-like MX2 (M=Mo, Nb, W, Ta; X=S, Se, Te) monolayers. *Physica B-Condensed Matter* **2011,** *406* (11), 2254-2260.

145. Du, M., Wu, Y., and Hao, X., A Facile Chemical Exfoliation Method to Obtain Large Size Boron Nitride Nanosheets. *CrystEngComm* **2013,** *15* (9), 1782-6.

146. Pak, J.; Jang, Y.; Byun, J.; Cho, K.; Kim, T. Y.; Kim, J. K.; Choi, B. Y.; Shin, J.; Hong, Y.; Chung, S.; Lee, T., Two-Dimensional Thickness-Dependent Avalanche Breakdown Phenomena in MoS2 Field-Effect Transistors under High Electric Fields. *ACS Nano* **2018,** *12* (7), 7109-7116.

147. Lee, B.; Park, J. H.; Han, G. H.; Ee, H.-S.; Naylor, C. H.; Lu, W.; Johnson, A. T. C.; Agarwal, R., Fano Resonance and Spectrally-Modified Photoluminescence Enhancement in Monolayer MoS2 Integrated with Plasmonic Nanoantenna Array. *Nano Lett.* **2015,** *15* (5), 3646-53.

148. Amani, M.; Burke, R. A.; Proie, R. M.; Dubey, M., Flexible Integrated Circuits and Multifunctional Electronics based on Single Atomic Layers of MoS_2 and Graphene. *Nanotechnol.* **2015,** *26* (11), 115202.

149. Nomura, K., Ohta, H.; Ueda, K.; Kamiya, T.; Hirano, M.; Hosono, H., Thin-Film Transistor Fabricated in Single-Crystalline Transparent Oxide Semiconductor. *Science* **2003,** *300* (5623), 1269-72.

150. van der Zande, A. M.; Huang, P. Y.; Chenet, D. A.; Berkelbach, T. C.; You, Y.-M.; Lee, G.-H.; Heinz, T. F.; Reichman, D. R.; Muller, D. A.; Hone, J. C., Grains and Grain Boundaries in Highly-Crystalline Monolayer Molybdenum Disulphide. *Nat. Mater.* **2013,** *12* (6), 554-561.

151. Jeon, J.; Jang, S. K.; Jeon, S. M.; Yoo, G.; Jang, Y. H.; Park, J. H.; Lee, S., Layer-Controlled CVD Growth of Large-Area Two-Dimensional MoS_2 Films. *Nanoscale* **2015,** *7* (5), 1688-1695.

152. Chen, W.; Zhao, J.; Zhang, J.; Gu, L.; Yang, Z.; Li, X.; Yu, H.; Zhu, X.; Yang, R.; Shi, D.; Lin, X.; Guo, J.; Bai, X.; Zhang, G., Oxygen-Assisted Chemical Vapor Deposition Growth of Large Single-Crystal and High-Quality Monolayer MoS_2. *J. Am. Chem. Soc.* **2015,** *137* (50), 15632-15635.

153. Choudhary, N.; Park, J.; Hwang, J. Y.; Choi, W., Growth of Large-Scale and Thickness-Modulated MoS_2 Nanosheets. *ACS Appl. Mater. Interf.* **2014,** *6* (23), 21215-21222.

154. Shi, J. P.; Yang, Y.; Zhang, Y.; Ma, D. L.; Wei, W.; Ji, Q. Q.; Zhang, Y. S.; Song, X. J.; Gao, T.; Li, C.; Bao, X. H.; Liu, Z. F.; Fu, Q.; Zhang, Y. F., Monolayer MoS_2 Growth on Au Foils and On-Site Domain Boundary Imaging. *Adv. Funct. Mater.* **2015,** *25* (6), 842-849.

155. Yu, H.; Liao, M. Z.; Zhao, W. J.; Liu, G. D.; Zhou, X. J.; Wei, Z.; Xu, X. Z.; Liu, K. H.; Hu, Z. H.; Deng, K.; Zhou, S. Y.; Shi, J. A.; Gu, L.; Shen, C.; Zhang, T. T.; Du, L. J.; Xie, L.; Zhu, J. Q.; Chen, W.; Yang, R.; Shi, D. X.; Zhang, G. Y., Wafer-Scale Growth and Transfer of Highly-Oriented Monolayer MoS_2 Continuous Films. *ACS Nano* **2017,** *11* (12), 12001-12007.

156. Fu, D. Y.; Zhao, X. X.; Zhang, Y. Y.; Li, L. J.; Xu, H.; Jang, A. R.; Yoon, S. I.; Song, P.; Poh, S. M.; Ren, T. H.; Ding, Z.; Fu, W.; Shin, T. J.; Shin, H. S.; Pantelides, S. T.; Zhou, W.; Loh, K. P., Molecular Beam Epitaxy of Highly Crystalline Monolayer Molybdenum Disulfide on Hexagonal Boron Nitride. *J. Am. Chem. Soc.* **2017,** *139* (27), 9392-9400.

157. Chen, J. Y.; Tang, W.; Tian, B. B.; Liu, B.; Zhao, X. X.; Liu, Y. P.; Ren, T. H.; Liu, W.; Geng, D. C.; Jeong, H. Y.; Shin, H. S.; Zhou, W.; Loh, K. P., Chemical Vapor Deposition of High-Quality Large-Sized MoS 2 Crystals on Silicon Dioxide Substrates. *Adv. Sci.* **2016,** *3* (8), 1600033.

158. Kim, H. J.; Kim, H.; Yang, S.; Kwon, J. Y., Grains in Selectively Grown MoS_2 Thin Films. *Small* **2017,** *13* (46), 1702256.

159. Liu, L. N.; Qiu, H. L.; Wang, J. Y.; Xu, G. C.; Jiao, L. Y., Atomic MoS2 monolayers synthesized from a metal-organic complex by chemical vapor deposition. *Nanoscale* **2016,** *8* (8), 4486-4490.

160. Bilgin, I.; Liu, F. Z.; Vargas, A.; Winchester, A.; Man, M. K. L.; Upmanyu, M.; Dani, K. M.; Gupta, G.; Talapatra, S.; Mohite, A. D.; Kar, S., Chemical Vapor Deposition Synthesized Atomically Thin Molybdenum Disulfide with Optoelectronic-Grade Crystalline Quality. *ACS Nano* **2015,** *9* (9), 8822-8832.

161. Dumcenco, D.; Ovchinnikov, D.; Marinov, K.; Lazic, P.; Gibertini, M.; Marzari, N.; Lopez Sanchez, O.; Kung, Y.-C.; Krasnozhon, D.; Chen, M.-W.; Bertolazzi, S.; Gillet, P.; Fontcuberta i Moral, A.; Radenovic, A.; Kis, A., Large-Area Epitaxial Monolayer MoS_2. *ACS Nano* **2015,** *9* (4), 4611-4620.

162. Lee, Y. H.; Zhang, X. Q.; Zhang, W. J.; Chang, M. T.; Lin, C. T.; Chang, K. D.; Yu, Y. C.; Wang, J. T. W.; Chang, C. S.; Li, L. J.; Lin, T. W., Synthesis of Large-Area MoS_2 Atomic Layers with Chemical Vapor Deposition. *Adv. Mater.* **2012,** *24* (17), 2320-2325.

163. Zhan, Y. J.; Liu, Z.; Najmaei, S.; Ajayan, P. M.; Lou, J., Large-Area Vapor-Phase Growth and Characterization of MoS_2 Atomic Layers on a SiO_2 Substrate. *Small* **2012,** *8* (7), 966-971.

164. Kang, K.; Xie, S. E.; Huang, L. J.; Han, Y. M.; Huang, P. Y.; Mak, K. F.; Kim, C. J.; Muller, D.; Park, J., High-Mobility Three-Atom-Thick Semiconducting Films with Wafer-Scale Homogeneity. *Nature* **2015,** *520* (7549), 656-660.

165. Azpeitia, J.; Otero-Irurueta, G.; Palacio, I.; Martinez, J. I.; del Arbol, N. R.; Santoro, G.; Gutierrez, A.; Aballe, L.; Foerster, M.; Kalbac, M.; Vales, V.; Mompean, F. J.; Garcia-Hernandez, M.; Martin-Gago, J. A.; Munuera, C.; Lopez, M. F., High-Quality PVD Graphene Growth by Fullerene Decomposition on Cu Foils. *Carbon* **2017,** *119*, 535-543.

166. Li, X. S.; Cai, W. W.; An, J. H.; Kim, S.; Nah, J.; Yang, D. X.; Piner, R.; Velamakanni, A.; Jung, I.; Tutuc, E.; Banerjee, S. K.; Colombo, L.; Ruoff, R. S., Large-Area Synthesis of High-Quality and Uniform Graphene Films on Copper Foils. *Science* **2009,** *324* (5932), 1312-1314.

167. Loh, T. A. J.; Chua, D. H. C., Growth Mechanism of Pulsed Laser Fabricated Few-Layer MoS_2 on Metal Substrates. *ACS Appl. Mater. Interf.* **2014,** *6* (18), 15966-15971.

168. Vlcek, J.; Belosludtsev, A.; Rezek, J.; Houska, J.; Capek, J.; Cerstvy, R.; Haviar, S., High-Rate Reactive High-Power Impulse Magnetron Sputtering of Hard and Optically-Transparent HfO_2 Films. *Surf. Coat. Technol.* **2016,** *290*, 58-64.

169. Alles, H.; Aarik, J.; Aidla, A.; Aurelien, F.; Kozlova, J.; Niilisk, A.; Pärs, M.; Rähn, M.; Wiesner, M.; Hakonen, P.; Sammelselg, V., Atomic Layer Deposition of HfO_2 on Graphene from $HfCl_4$ and H_2 O. *Open Phys.* **2011,** *9* (2), 319-324.

170. Chang, R. J.; Wang, X. C.; Wang, S. S.; Sheng, Y. W.; Porter, B.; Bhaskaran, H.; Warner, J. H., Growth of Large Single-Crystalline Monolayer Hexagonal Boron Nitride by Oxide-Assisted Chemical Vapor Deposition. *Chem. Mater.* **2017,** *29* (15), 6252-6260.

171. Glavin, N. R.; Jespersen, M. L.; Check, M. H.; Hu, J.; Hilton, A. M.; Fisher, T. S.; Voevodin, A. A., Synthesis of Few-Layer, Large-Area Hexagonal-Boron Nitride by Pulsed Laser Deposition. *Thin Solid Films* **2014,** *572*, 245-250.

172. Kim, K. K.; Hsu, A.; Jia, X.; Kim, S. M.; Shi, Y.; Dresselhaus, M.; Palacios, T.; Kong, J., Synthesis and Characterisation of Hexagonal Boron Nitride Film as a Dielectric Layer for Graphene Devices. *ACS Nano* **2012,** *6* (10), 8583-8590.

173. Najmaei, S.; Liu, Z.; Zhou, W.; Zou, X.; Shi, G.; Lei, S.; Yakobson, B. I.; J.-C., I.; Ajayan, P. M.; Lou, J., Vapour-Phase Growth and Grain Boundary Structure of Molybdenum Disulphide Atomic Layers. *Nature Mater.* **2013,** *12* (8), 7754-59.

174. Lee, Y. H.; Yu, L. L.; Wang, H.; Fang, W. J.; Ling, X.; Shi, Y. M.; Lin, C. T.; Huang, J. K.; Chang, M. T.; Chang, C. S.; Dresselhaus, M.; Palacios, T.; Li, L. J.; Kong, J., Synthesis and Transfer of Single-Layer Transition Metal Disulphides on Diverse Surfaces. *Nano Lett.* **2013,** *13* (4), 1852-1857.

175. Boandoh, S.; Choi, S. H.; Park, J. H.; Park, S. Y.; Bang, S.; Jeong, M. S.; Lee, J. S.; Kim, H. J.; Yang, W.; Choi, J. Y.; Kim, S. M.; Kim, K. K., A Novel and Facile Route to Synthesize Atomic-Layered MoS_2 Film for Large-Area Electronics. *Small* **2017,** *13* (39), 1701306.

176. Elias, A. L.; Perea-Lopez, N.; Castro-Beltran, A.; Berkdemir, A.; Lv, R. T.; Feng, S. M.; Long, A. D.; Hayashi, T.; Kim, Y. A.; Endo, M.; Gutierrez, H. R.; Pradhan, N. R.; Balicas, L.; Mallouk, T. E.; Lopez-Urias, F.; Terrones, H.; Terrones, M., Controlled Synthesis and Transfer of Large-Area WS_2 Sheets: From Single Layer to Few Layers. *ACS Nano* **2013,** *7* (6), 5235-5242.

177. Song, J. G.; Park, J.; Lee, W.; Choi, T.; Jung, H.; Lee, C. W.; Hwang, S. H.; Myoung, J. M.; Jung, J. H.; Kim, S. H.; Lansalot-Matras, C.; Kim, H., Layer-Controlled, Wafer-Scale, and Conformal Synthesis of Tungsten Disulfide Nanosheets Using Atomic Layer Deposition. *ACS Nano* **2013,** *7* (12), 11333-11340.

178. Kim, H. G.; Leek, H. B. R., Atomic Layer Deposition on 2D Materials. *Chem. Mater.* **2017,** *29* (9), 3809-3826.

179. Roy, P.; Srivastava, S. K., Chemical Bath Deposition of MoS_2 Thin Film using Ammonium Tetrathiomolybdate as a Single Source for Molybdenum and Sulphur. *Thin Solid Films* **2006,** *496* (2), 293-298.

180. Du, T.; Wang, N.; Chen, H. J.; He, H. C.; Lin, H.; Liu, K., TiO_2-Based Solar Cells Sensitized by Chemical-Bath-Deposited Few-Layer MoS_2. *J. Power Sources* **2015,** *275*, 943-949.

181. Xi, Y.; Serna, M. I.; Cheng, L. X.; Gao, Y.; Baniasadi, M.; Rodriguez-Davila, R.; Kim, J.; Quevedo-Lopez, M. A.; Minary-Jolandan, M., Fabrication of MoS_2 Thin Film Transistors via Selective-Area Solution Deposition Methods. *J. Mater. Chem. C* **2015,** *3* (16), 3842-3847.

182. Worsley, M. A.; Shin, S. J.; Merrill, M. D.; Lenhardt, J.; Nelson, A. J.; Woo, L. Y.; Gash, A. E.; Baumann, T. F.; Orme, C. A., Ultra low Density, Monolithic WS_2, MoS_2, and MoS_2/Graphene Aerogels. *ACS Nano* **2015,** *9* (5), 4698-4705.

183. George, A. S.; Mutlu, Z.; Ionescu, R.; Wu, R. J.; Jeong, J. S.; Bay, H. H.; Chai, Y.; Mkhoyan, K. A.; Ozkan, M.; Ozkan, C. S., Wafer-Scale Synthesis and High-Resolution Structural Characterization of Atomically-Thin MoS_2 Layers. *Adv. Funct. Mater.* **2014,** *24* (47), 7461-7466.

184. Foong, T. R. B.; Shen, Y.; Hu, X.; Sellinger, A., Template-Directed Liquid ALD Growth of TiO_2 Nanotube Arrays: Properties and Potential in Photovoltaic Devices. *Adv. Func. Mater.* **2010,** *20* (9), 1390-1396.

185. Notley, S. M., High-Yield Production of Photoluminescent Tungsten Disulphide Nanoparticles. *J. Colloid Interface Sci.* **2013,** *396*, 160-164.

186. Wang, Y., Cong, C.; Qiu, C; Yu, T., Raman Spectroscopy Study of Lattice Vibration and Crystallographic Orientation of Monolayer MoS2 under Uniaxial Strain. *Small* **2013,** *9* (17), 2857-2861.

187. Korn, T.; Heydrich, S.; Hirmer, H.; Schmutzler, J.; Schuller, C., Low-Temperature Photocarrier Dynamics in Monolayer MoS2. *Appl. Phys. Lett.* **2011,** *99* (10).

188. Ye, L.; Chen, S.; Li, W.; Pi, M.; Wu, T.; Zhang, D., Tuning the Electrical Transport Properties of Multilayered Molybdenum Disulfide Nanosheets by Intercalating Phosphorus. *J. Phys. Chem. C* **2015,** *119* (17), 9560-9567.

189. Shi, J. P.; Zhang, X. N.; Ma, D. L.; Zhu, J. B.; Zhang, Y.; Guo, Z. X.; Yao, Y.; Ji, Q. Q.; Song, X. J.; Zhang, Y. S.; Li, C.; Liu, Z. F.; Zhu, W. G.; Zhang, Y. F., Substrate Facet Effect on the Growth of Monolayer MoS_2 on Au Foils. *ACS Nano* **2015,** *9* (4), 4017-4025.

190. Engelmann, S.; Bruce, R. L.; Sumiya, M.; Kwon, T.; Phaneuf, R.; Oehrlein, G. S.; Andes, C.; Graves, D.; Nest, D.; Hudson, E. A., Plasma--Surface Interactions of Advanced Photoresists with C4F8/Ar Discharges: Plasma Parameter Dependencies. *J. Vac. Sci. Technol. B* **2009,** *27* (1), 92-106.

191. Yatsui, T.; Kuribara, K.; Sekitani, T.; Someya, T.; Yoshimoto, M., Temperature-Modulated Annealing of c-Plane Sapphire for Long-Range-Ordered Atomic Steps. *J. Appl. Phys. D* **2016,** *49* (11).

192. Kovacs, T. N.; Hunyadi, D.; de Lucena, A. L. A.; Szilagyi, I. K., Thermal Decomposition of Ammonium Molybdates. *J. Therm. Anal. Calorim.* **2016,** *124* (2), 1013-1021.

193. Li, X. L.; Li, Y. D., Formation MoS_2 Inorganic Fullerenes (IFs) by the Reaction of MoO_3 Nanobelts and S. *Chem. Eur. J* **2003,** *9* (12), 2726-2731.

194. Backes, C.; Higgins, T. M.; Kelly, A.; Boland, C.; Harvey, A.; Hanlon, D.; Coleman, J. N., Guidelines for Exfoliation, Characterization and Processing of Layered Materials Produced by Liquid Exfoliation. *Chem. Mater.* **2017,** *29* (1), 243-255.

195. Yu, H.; Yang, Z. Z.; Du, L. J.; Zhang, J.; Shi, J. N.; Chen, W.; Chen, P.; Liao, M. Z.; Zhao, J.; Meng, J. L.; Wang, G. L.; Zhu, J. Q.; Yang, R.; Shi, D. X.; Gu, L.; Zhang, G. Y., Precisely Aligned Monolayer MoS_2 Epitaxially Grown on h-BN Basal Plane. *Small* **2017,** *13* (7).

196. Artyukhov, V. I.; Hu, Z. L.; Zhang, Z. H.; Yakobson, B. I., Topochemistry of Bowtie- and Star-Shaped Metal Dichalcogenide Nanoisland Formation. *Nano Lett.* **2016,** *16* (6), 3696-3702.

197. Hui, Y. Y.; Liu, X. F.; Jie, W. J.; Chan, N. Y.; Hao, J. H.; Hsu, Y. T.; Li, L. J.; Guo, W. L.; Lau, S. P., Exceptional Tunability of Band Energy in a Compressively Strained Trilayer MoS_2 Sheet. *ACS Nano* **2013,** *7* (8), 7126-7131.

198. Najmaei, S.; Liu, Z.; Ajayan, P. M.; Lou, J., Thermal Effects on the Characteristic Raman Spectrum of Molybdenum Disulfide (MoS_2) of Varying Thicknesses. *Appl. Phys. Lett.* **2012,** *100* (1), 013106.

199. Chakraborty, B.; Bera, A.; Muthu, D. V. S.; Bhowmick, S.; Waghmare, U. V.; Sood, A. K., Symmetry-Dependent Phonon Renormalization in Monolayer MoS_2 Transistor. *Phys. Rev. B* **2012,** *85* (16), 161403.

200. Zhu, Z. Y.; Cheng, Y. C.; Schwingenschlogl, U., Giant Spin-Orbit-Induced Spin Splitting in Two-Dimensional Transition-Metal Dichalcogenide Semiconductors. *Phys. Rev. B* **2011,** *84* (15), 153402.

201. Buscema, M.; Steele, G. A.; van der Zant, H. S. J.; Castellanos-Gomez, A., The Effect of the Substrate on the Raman and Photoluminescence Emission of Single-Layer MoS_2. *Nano Res.* **2014,** *7* (4), 561-571.

202. Gong, Y. J.; Lin, Z.; Ye, G. L.; Shi, G.; Feng, S. M.; Lei, Y.; Elias, A. L.; Perea-Lopez, N.; Vajtai, R.; Terrones, H.; Liu, Z.; Terrones, M.; Ajayan, P. M., Tellurium-Assisted Low-Temperature Synthesis of MoS_2 and WS_2 Monolayers. *ACS Nano* **2015,** *9* (12), 11658-11666.

203. Gong, Y. J.; Lin, J. H.; Wang, X. L.; Shi, G.; Lei, S. D.; Lin, Z.; Zou, X. L.; Ye, G. L.; Vajtai, R.; Yakobson, B. I.; Terrones, H.; Terrones, M.; Tay, B. K.; Lou, J.; Pantelides, S. T.; Liu, Z.; Zhou, W.; Ajayan, P. M., Vertical and In-Plane Heterostructures from WS_2/MoS_2 Monolayers. *Nature Mater.* **2014,** *13* (12), 1135-1142.

204. Lee, J.; Pak, S.; Giraud, P.; Lee, Y. W.; Cho, Y.; Hong, J.; Jang, A. R.; Chung, H. S.; Hong, W. K.; Jeong, H. Y.; Shin, H. S.; Occhipinti, L. G.; Morris, S. M.; Cha, S.; Sohn, J. I.; Kim, J. M., Thermodynamically Stable Synthesis of Large-Scale and Highly Crystalline Transition Metal Dichalcogenide Monolayers and their Unipolar n-n Heterojunction Devices. *Adv. Mater.* **2017,** *29* (33).

205. Ionescu, R.; George, A.; Ruiz, I.; Favors, Z.; Mutlu, Z.; Liu, C.; Ahmed, K.; Wu, R.; Jeong, J. S.; Zavala, L.; Mkhoyan, K. A.; Ozkan, M.; Ozkan, C. S., Oxygen Etching of Thick MoS_2 Films. *Chem. Commun.* **2014,** *50* (76), 11226-11229.

206. Qi, F.; Li, P. J.; Chen, Y. F.; Zheng, B. J.; Liu, X. Z.; Lan, F. F.; Lai, Z. P.; Xu, Y. K.; Liu, J. B.; Zhou, J. H.; He, J. R.; Zhang, W. L., Effect of Hydrogen on the Growth of MoS2 Thin Layers by Thermal Decomposition Method. *Vacuum* **2015,** *119*, 204-208.

207. Qi, H. M.; Wang, L. N.; Sun, J.; Long, Y.; Hu, P.; Liu, F. C.; He, X. X., Production Methods of Van der Waals Heterostructures Based on Transition Metal Dichalcogenides. *Crystals* **2018,** *8* (1).

208. Novoselov, K. S.; Mishchenko, A.; Carvalho, A.; Neto, A. H. C., 2D Materials and van der Waals Heterostructures. *Science* **2016,** *353* (6298).

209. Dean, C. R.; Young, A. F.; Meric, I.; Lee, C.; Wang, L.; Sorgenfrei, S.; Watanabe, K.; Taniguchi, T.; Kim, P.; Shepard, K. L.; Hone, J., Boron Nitride Substrates for High-Quality Graphene Electronics. *Nat. Nanotechnol.* **2010,** *5* (10), 722-726.

210. Kretinin, A. V.; Cao, Y.; Tu, J. S.; Yu, G. L.; Jalil, R.; Novoselov, K. S.; Haigh, S. J.; Gholinia, A.; Mishchenko, A.; Lozada, M.; Georgiou, T.; Woods, C. R.; Withers, F.; Blake, P.; Eda, G.; Wirsig, A.; Hucho, C.; Watanabe, K.; Taniguchi, T.; Geim, A. K.; Gorbachev, R. V., Electronic Properties of Graphene Encapsulated with Different Two-Dimensional Atomic Crystals. *Nano Lett.* **2014,** *14* (6), 3270-3276.

211. Ceballos, F.; Bellus, M. Z.; Chiu, H. Y.; Zhao, H., Ultrafast Charge Separation and Indirect Exciton Formation in a MoS_2--$MoSe_2$ van der Waals Heterostructure. *ACS Nano* **2014,** *8* (12), 12717-12724.

212. Wang, F.; Wang, Z. X.; Xu, K.; Wang, F. M.; Wang, Q. S.; Huang, Y.; Yin, L.; He, J., Tunable GaTe-MoS_2 van der Waals p-n Junctions with Novel Optoelectronic Performance. *Nano Lett.* **2015,** *15* (11), 7558-7566.

213. Cheng, R.; Li, D. H.; Zhou, H. L.; Wang, C.; Yin, A. X.; Jiang, S.; Liu, Y.; Chen, Y.; Huang, Y.; Duan, X. F., Electroluminescence and Photocurrent Generation from Atomically Sharp WSe2/MoS2 Heterojunction p-n Diodes. *Nano Lett.* **2014,** *14* (10), 5590-5597.

214. Rivera, P.; Schaibley, J. R.; Jones, A. M.; Ross, J. S.; Wu, S. F.; Aivazian, G.; Klement, P.; Seyler, K.; Clark, G.; Ghimire, N. J.; Yan, J. Q.; Mandrus, D. G.; Yao, W.; Xu, X. D., Observation of Long-Lived Interlayer Excitons in Monolayer $MoSe_2$--WSe_2 Heterostructures. *Nat. Commun.* **2015,** *6*, 6242.

215. Hong, X. P.; Kim, J.; Shi, Y.; Zhang, Y.; Jin, C. H.; Sun, Y. H.; Tongay, S.; Wu, J. Q.; Zhang, Y. F.; Wang, F., Ultrafast Charge Transfer in Atomically Thin MoS_2/WS_2 Heterostructures. *Nat. Nanotechnol.* **2014,** *9* (9), 682-686.

216. Hill, H. M.; Rigosi, A. F.; Rim, K. T.; Flynn, G. W.; Heinz, T. F., Band Alignment in MoS2/WS2 Transition Metal Dichalcogenide Heterostructures Probed by Scanning Tunneling Microscopy and Spectroscopy. *Nano Lett.* **2016,** *16* (8), 4831-4837.

217. Yang, W.; Chen, G. R.; Shi, Z. W.; Liu, C. C.; Zhang, L. C.; Xie, G. B.; Cheng, M.; Wang, D. M.; Yang, R.; Shi, D. X.; Watanabe, K.; Taniguchi, T.; Yao, Y. G.; Zhang, Y. B.; Zhang, G. Y., Epitaxial Growth of Single-Domain Graphene on Hexagonal Boron Nitride. *Nat. Mater.* **2013,** *12* (9), 792-797.

218. Miwa, J. A.; Dendzik, M.; Gronborg, S. S.; Bianchi, M.; Lauritsen, J. V.; Hofmann, P.; Ulstrup, S., van der Waals Epitaxy of Two-Dimensional MoS_2--Graphene Heterostructures in Ultrahigh Vacuum. *ACS Nano* **2015,** *9* (6), 6502-6510.

219. Yan, A. M.; Velasco, J.; Kahn, S.; Watanabe, K.; Taniguchi, T.; Wang, F.; Crommie, M. F.; Zettl, A., Direct Growth of Single- and Few-Layer MoS_2 on h-BN with Preferred Relative Rotation Angles. *Nano Lett.* **2015,** *15* (10), 6324-6331.

220. Lin, Y. C.; Chang, C. Y. S.; Ghosh, R. K.; Li, J.; Zhu, H.; Addou, R.; Diaconescu, B.; Ohta, T.; Peng, X.; Lu, N.; Kim, M. J.; Robinson, J. T.; Wallace, R. M.; Mayer, T. S.; Datta, S.; Li, L. J.; Robinson, J. A., Atomically Thin Heterostructures Based on Single-Layer Tungsten Diselenide and Graphene. *Nano Lett.* **2014,** *14* (12), 6936-6941.

221. Liu, X. L.; Balla, I.; Bergeron, H.; Campbell, G. P.; Bedzyk, M. J.; Hersam, M. C., Rotationally Commensurate Growth of MoS_2 on Epitaxial Graphene. *ACS Nano* **2016,** *10* (1), 1067-1075.

222. Azizi, A.; Eichfeld, S.; Geschwind, G.; Zhang, K. H.; Jiang, B.; Mukherjee, D.; Hossain, L.; Piasecki, A. F.; Kabius, B.; Robinson, J. A.; Alem, N., Freestanding van der Waals Heterostructures of Graphene and Transition Metal Dichalcogenides. *ACS Nano* **2015,** *9* (5), 4882-4890.

223. Kang, J.; Tongay, S.; Zhou, J.; Li, J. B.; Wu, J. Q., Band Offsets and Heterostructures of Two-Dimensional Semiconductors. *Appl. Phys. Lett.* **2013,** *102* (1).

224. Deng, Y. X.; Luo, Z.; Conrad, N. J.; Liu, H.; Gong, Y. J.; Najmaei, S.; Ajayan, P. M.; Lou, J.; Xu, X. F.; Ye, P. D., Black Phosphorus--Monolayer MoS_2 van der Waals Heterojunction p-n Diode. *ACS Nano* **2014,** *8* (8), 8292-8299.

225. Chiu, M. H.; Li, M. Y.; Zhang, W. J.; Hsu, W. T.; Chang, W. H.; Terrones, M.; Terrones, H.; Li, L. J., Spectroscopic Signatures for Interlayer Coupling in MoS_2--WSe_2 van der Waals Stacking. *ACS Nano* **2014,** *8* (9), 9649-9656.

226. Jin, C. H.; Kim, J.; Suh, J.; Shi, Z. W.; Chen, B.; Fan, X.; Kam, M.; Watanabe, K.; Taniguchi, T.; Tongay, S.; Zettl, A.; Wu, J. Q.; Wang, F., Interlayer Electron--Phonon Coupling in WSe_2/h-BN Heterostructures. *Nat. Phys.* **2017,** *13* (2), 127-131.

227. Wang, L.; Meric, I.; Huang, P. Y.; Gao, Q.; Gao, Y.; Tran, H.; Taniguchi, T.; Watanabe, K.; Campos, L. M.; Muller, D. A.; Guo, J.; Kim, P.; Hone, J.; Shepard, K. L.; Dean, C. R., One-Dimensional Electrical Contact to a Two-Dimensional Material. *Science* **2013,** *342* (6158), 614-617.

228. Duan, X. D.; Wang, C.; Shaw, J. C.; Cheng, R.; Chen, Y.; Li, H. L.; Wu, X. P.; Tang, Y.; Zhang, Q. L.; Pan, A. L.; Jiang, J. H.; Yu, R. Q.; Huang, Y.; Duan, X. F., Lateral Epitaxial Growth of Two-Dimensional Layered Semiconductor Heterojunctions. *Nat. Nanotechnol.* **2014,** *9* (12), 1024-1030.

229. Fu, L.; Sun, Y. Y.; Wu, N.; Mendes, R. G.; Chen, L. F.; Xu, Z.; Zhang, T.; Rummeli, M. H.; Rellinghaus, B.; Pohl, D.; Zhuang, L., Direct Growth of MoS_2/h-BN Heterostructures via a Sulphide-Resistant Alloy. *ACS Nano* **2016,** *10* (2), 2063-2070.

230. Qiao, H.; Yuan, J.; Xu, Z. Q.; Chen, C. Y.; Lin, S. H.; Wang, Y. S.; Song, J. C.; Liu, Y.; Khan, Q.; Hoh, H. Y.; Pan, C. X.; Li, S. J.; Bao, Q. L., Broadband Photodetectors Based on Graphene--Bi_2Te_3 Heterostructure. *ACS Nano* **2015,** *9* (2), 1886-1894.

231. Levendorf, M. P.; Kim, C. J.; Brown, L.; Huang, P. Y.; Havener, R. W.; Muller, D. A.; Park, J., Graphene and Boron Nitride Lateral Heterostructures for Atomically-Thin Circuitry. *Nature* **2012,** *488* (7413), 627-632.

232. Li, M. Y.; Shi, Y. M.; Cheng, C. C.; Lu, L. S.; Lin, Y. C.; Tang, H. L.; Tsai, M. L.; Chu, C. W.; Wei, K. H.; He, J. H.; Chang, W. H.; Suenaga, K.; Li, L. J., Epitaxial Growth of a Monolayer WSe_2-MoS_2 Lateral p-n Junction with an Atomically Sharp Interface. *Science* **2015,** *349* (6247), 524-528.

233. Zhang, X. Q.; Lin, C. H.; Tseng, Y. W.; Huang, K. H.; Lee, Y. H., Synthesis of Lateral Heterostructures of Semiconducting Atomic Layers. *Nano Lett.* **2015,** *15* (1), 410-415.

234. Lin, Y. C.; Ghosh, R. K.; Addou, R.; Lu, N.; Eichfeld, S. M.; Zhu, H.; Li, M. Y.; Peng, X.; Kim, M. J.; Li, L. J.; Wallace, R. M.; Datta, S.; Robinson, J. A., Atomically Thin Resonant Tunnel Diodes built from Synthetic van der Waals Heterostructures. *Nat. Commun.* **2015,** *6*.

235. Xue, Y. Z.; Zhang, Y. P.; Liu, Y.; Liu, H. T.; Song, J. C.; Sophia, J.; Liu, J. Y.; Xu, Z. Q.; Xu, Q. Y.; Wang, Z. Y.; Zheng, J. L.; Liu, Y. Q.; Li, S. J.; Bao, Q. L., Scalable Production of a Few-Layer MoS_2/WS_2 Vertical Heterojunction Array and its Application for Photodetectors. *ACS Nano* **2016,** *10* (1), 573-580.

236. Wu, W. H.; Zhang, Q.; Zhou, X.; Li, L.; Su, J. W.; Wang, F. K.; Zhai, T. Y., Self-Powered Photovoltaic Photodetector established on Lateral Monolayer MoS_2--WS_2 Heterostructures. *Nano Energy* **2018,** *51*, 45-53.

237. Chen, H. L.; Wen, X. W.; Zhang, J.; Wu, T. M.; Gong, Y. J.; Zhang, X.; Yuan, J. T.; Yi, C. Y.; Lou, J.; Ajayan, P. M.; Zhuang, W.; Zhang, G. Y.; Zheng, J. R., Ultrafast Formation of Interlayer Hot Excitons in Atomically Thin MoS_2/WS_2 Heterostructures. *Nat. Commun.* **2016,** *7*.

238. Berkdemir, A.; Gutierrez, H. R.; Botello-Mendez, A. R.; Prea-Lopez, N.; Elias, A. L.; Chia, C.-I.; Wang, B.; Crespi, V. H.; Lopez-Urias, F.; Charlier, J.-C.; Terrones, H.; Terrones, M., Identification of Individual and Few Layers of WS_2 using Raman Spectroscopy. *Sci. Rep.* **2013,** ***3***, 1755.

239. Chen, S.-Y.; Zheng, C.; Fuhrer, M. S.; Yan, J., Helicity-Resolved Raman Scattering of MoS_2, $MoSe_2$, WS_2, and WSe_2 Atomic Layers. *Nano Lett.* **2015,** *15* (4), 2526-2532.

240. Zhao, W. J.; Ghorannevis, Z.; Chu, L. Q.; Toh, M. L.; Kloc, C.; Tan, P. H.; Eda, G., Evolution of Electronic Structure in Atomically Thin Sheets of WS_2 and WSe_2. *ACS Nano* **2013,** *7* (1), 791-797.

241. Wei, K.; Liu, Y.; Yang, H.; Cheng, X. A.; Jiang, T., Large-Range Modification of Exciton Species in Monolayer WS_2. *Appl. Opt.* **2016,** *55* (23), 6251-6255.

242. Wang, X. H.; Ning, J. Q.; Su, Z. C.; Zheng, C. C.; Zhu, B. R.; Xie, L.; Wu, H. S.; Xu, S. J., Photoinduced Doping and Photoluminescence Signature in an Exfoliated WS_2 Monolayer Semiconductor. *RSC Adv* **2016,** *6* (33), 27677-27681.

243. Huang, C. C.; Al-Saab, F.; Wang, Y. D.; Ou, J. Y.; Walker, J. C.; Wang, S. C.; Gholipour, B.; Simpson, R. E.; Hewak, D. W., Scalable High-Mobility MoS_2 Thin Films Fabricated by an Atmospheric Pressure Chemical Vapour Deposition Process at Ambient Temperature. *Nanoscale* **2014,** *6* (21), 12792-12797.

244. Xu, L. J.; Yin, M. L.; Liu, S. Z., Agx@WO_3 Core-Shell Nanostructure for LSP Enhanced Chemical Sensors. *Sci. Rep.* **2014,** *4*.

245. Wei, K.; Liu, Y.; Yang, H.; Cheng, X. A.; Jiang, T., Large-Range Modification of Exciton Species in Monolayer WS_2. *Applied Optics* **2016,** *55* (23), 6251-6255.

246. Wang, X. L.; Gong, Y. J.; Shi, G.; Chow, W. L.; Keyshar, K.; Ye, G. L.; Vajtai, R.; Lou, J.; Liu, Z.; Ringe, E.; Tay, B. K.; Ajayan, P. M., Chemical Vapor Deposition Growth of Crystalline Monolayer $MoSe_2$. *ACS Nano* **2014,** *8* (5), 5125-5131.

247. Burton, L. A.; Whittles, T. J.; Hesp, D.; Linhart, W. M.; Skelton, J. M.; Hou, B.; Webster, R. F.; O'Dowd, G.; Reece, C.; Cherns, D.; Fermin, D. J.; Veal, T. D.; Dhanak, V. R.; Walsh, A., Electronic and Optical Properties of Single Crystal SnS2: an Earth-Abundant Disulphide Photocatalyst. *J. Mater. Chem. A* **2016,** *4* (4), 1312-1318.

248. Wu, H. W.; Emadi, A.; de Graaf, G.; Leijtens, J.; Wolffenbuttel, R. F., Design and Fabrication of an Albedo-Insensitive Analog Sun Sensor. *Eurosensors* **2011,** *25*.

249. Ram, B.; Singh, A. K., Strain-Induced Indirect-to-Direct Bandgap Transition in Bulk SnS2. *Phys. Rev. B* **2017,** *95* (7).

250. Fu, X.; Ilanchezhiyan, P.; Kumar, G. M.; Cho, H. D.; Zhang, L.; Chan, A. S.; Lee, D. J.; Panin, G. N.; Kang, T. W., Tunable UV-Visible Absorption of SnS2 Layered Quantum Dots produced by Liquid-Phase Exfoliation. *Nanoscale* **2017,** *9* (5), 1820-1826.

251. Su, G. X.; Hadjiev, V. G.; Loya, P. E.; Zhang, J.; Lei, S. D.; Maharjan, S.; Dong, P.; Ajayan, P. M.; Lou, J.; Peng, H. B., Chemical Vapor Deposition of Thin Crystals of Layered Semiconductor SnS2 for Fast Photodetection Application. *Nano Lett.* **2015,** *15* (1), 506-513.

252. Wu, Z. C.; Xue, Y. J.; Zhang, Y. L.; Li, J. J.; Chen, T., SnS2 Nanosheet-Based Microstructures with High Adsorption Capabilities and Visible Light Photocatalytic Activities. *Rsc Adv.* **2015,** *5* (31), 24640-24648.

253. Long, R.; English, N. J.; Prezhdo, O. V., Minimizing Electron-Hole Recombination on TiO2 Sensitized with PbSe Quantum Dots: Time-Domain Ab Initio Analysis. *J. Phys. Chem. Lett.* **2014,** *5* (17), 2941-2946.

254. Dolat, D.; Mozia, S.; Ohtani, B.; Morawski, A. W., Nitrogen, Iron-Single Modified (N-TiO_2, Fe-TiO_2) and Co-Modified (Fe,N-TiO_2) Rutile Titanium Dioxide as Visible-Light Active Photocatalysts. *Chem. Eng. J.* **2013,** *225*, 358-364.

255. Murcia, J. J.; Hidalgo, M. C.; Navio, J. A.; Arana, J.; Dona-Rodriguez, J. M., Study of the Phenol Photocatalytic Degradation over TiO_2 Modified by Sulphation, Fluorination, and Platinum Nanoparticles Photodeposition. *Appl. Catal. B* **2015,** *179*, 305-312.

256. Ma, B. J.; Kim, J. S.; Choi, C. H.; Woo, S. I., Enhanced Hydrogen Generation from Methanol Aqueous Solutions over $Pt/MoO_3/TiO_2$ under Ultraviolet Light. *Int. J. Hydrog. Energy* **2013,** *38* (9), 3582-3587.

257. Planells, M.; Abate, A.; Snaith, H. J.; Robertson, N., Oligothiophene Interlayer Effect on Photocurrent Generation for Hybrid TiO_2/P3HT Solar Cells. *ACS Appl. Mater. Interf.* **2014,** *6* (19), 17226-17235.

258. Zhang, W. P.; Xiao, X. Y.; Li, Y.; Zeng, X. Y.; Zheng, L. L.; Wan, C. X., Liquid Exfoliation of Layered Metal Sulphides for Enhanced Photocatalytic Activity of TiO_2 Nanoclusters and DFT Study. *RSC Adv.* **2016,** *6* (40), 33705-33712.

259. Leijtens, T.; Eperon, G. E.; Pathak, S.; Abate, A.; Lee, M. M.; Snaith, H. J., Overcoming Ultraviolet Light Instability of Sensitised TiO_2 with Meso-Superstructured Organometal Tri-Halide Perovskite Solar Cells. *Nat. Commun.* **2013,** *4*.

260. Eames, C.; Frost, J. M.; Barnes, P. R. F.; O'Regan, B. C.; Walsh, A.; Islam, M. S., Ionic Transport in Hybrid Lead Iodide Perovskite Solar Cells. *Nat. Commun.* **2015,** *6*.

261. Saidaminov, M. I.; Abdelhady, A. L.; Murali, B.; Alarousu, E.; Burlakov, V. M.; Peng, W.; Dursun, I.; Wang, L. F.; He, Y.; Maculan, G.; Goriely, A.; Wu, T.; Mohammed, O. F.; Bakr, O. M., High-Quality Bulk Hybrid Perovskite Single Crystals within Minutes by Inverse Temperature Crystallisation. *Nat. Comm.* **2015,** *6*.

262. Yang, W. S.; Park, B. W.; Jung, E. H.; Jeon, N. J.; Kim, Y. C.; Lee, D. U.; Shin, S. S.; Seo, J.; Kim, E. K.; Noh, J. H.; Seok, S. I., Iodide Management in Formamidinium-Lead-Halide-Based Perovskite Layers for Efficient Solar Cells. *Science* **2017,** *356* (6345), 1376-+.

263. Alberi, K.; Nardelli, M. B.; Zakutayev, A.; Mitas, L.; Curtarolo, S.; Jain, A.; Fornari, M.; Marzari, N.; Takeuchi, I.; Green, M. L.; Kanatzidis, M.; Toney, M. F.; Butenko, S.; Meredig, B.; Lany, S.; Kattner, U.; Davydov, A.; Toberer, E. S.; Stevanovic, V.; Walsh, A.; Park, N. G.; Aspuru-Guzik, A.; Tabor, D. P.; Nelson, J.; Murphy, J.; Setlur, A.; Gregoire, J.; Li, H.; Xiao, R. J.; Ludwig, A.; Martin, L. W.; Rappe, A. M.; Wei, S. H.; Perkins, J., The 2019 Materials by Design Roadmap. *J. Phys. D* **2019,** *52* (1).

264. Lee, J. W.; Kim, H. S.; Park, N. G., Lewis Acid-Base Adduct Approach for High Efficiency Perovskite Solar Cells. *Acc. Chem. Res.* **2016,** *49* (2), 311-319.

265. Bryant, D.; Aristidou, N.; Pont, S.; Sanchez-Molina, I.; Chotchunangatchaval, T.; Wheeler, S.; Durrant, J. R.; Haque, S. A., Light and Oxygen-Induced Degradation Limits the Operational Stability of Methylammonium Lead Triiodide Perovskite Solar Cells. *Energy Environ. Sci.* **2016,** *9* (5), 1655-1660.

266. Juarez-Perez, E. J.; Hawash, Z.; Raga, S. R.; Ono, L. K.; Qi, Y. B., Thermal Degradation of $CH_3NH_3PbI_3$ Perovskite into NH_3 and CH_3I Gases observed by Coupled Thermogravimetry--Mass Spectrometry Analysis. *Energy Environ. Sci.* **2016,** *9* (11), 3406-3410.

267. Matteocci, F.; Cina, L.; Lamanna, E.; Cacovich, S.; Divitini, G.; Midgley, P. A.; Ducati, C.; Di Carlo, A., Encapsulation for Long-Term Stability Enhancement of Perovskite Solar Cells. *Nano Energy* **2016,** *30*, 162-172.

268. Juarez-Perez, E. J.; Ono, L. K.; Maeda, M.; Jiang, Y.; Hawash, Z.; Qi, Y. B., Photodecomposition and Thermal Decomposition in Methylammonium Halide Lead Perovskites and Inferred Design Principles to Increase Photovoltaic Device Stability. *J. Mater. Chem. A* **2018,** *6* (20), 9604-9612.

269. Julien, C.; PerezVicente, C., Vibrational Studies of Lithium-Intercalated SnS_2. *Solid State Ion.* **1996,** *89* (3-4), 337-343.

270. O'Neill, A.; Khan, U.; Nirmalraj, P. N.; Boland, J.; Coleman, J. N., Graphene Dispersion and Exfoliation in Low Boiling Point Solvents. *J. Phys. Chem. C* **2011,** *115* (13), 5422-5428.

271. Backes, C.; Szydlowska, B.; Harvey, A.; Yuan, S.; Vega-Mayoral, V.; Davies, B. R.; Zhao, P.-L.; Hanlon, D.; Santos, E. J. G.; Katsnelson, M. I.; Blau, W. J.; Gadermaier, C.; Coleman, J. N., Production of Highly Monolayer-Enriched Dispersions of Liquid-Exfoliated Nanosheets by Liquid Cascade Centrifugation. *ACS Nano* **2016,** *10* (1), 1589-1601.

272. Voiry, D., Yamaguchi, H.; Li, J.; Silva, R.; Alves, D. C. B.; Fujita, T.; Chen, M.; Asefa, T.; Shenoy, V. B.; Eda, G.; Chhowalla, M., Enhanced Catalytic Activity in Strained Chemically Exfoliated WS_2 Nanosheets for Hydrogen Evolution. *Nature Mater.* **2013,** *12* (9), 850-855.

273. Eng, A. Y. S.; Ambrosi, A.; Sofer, Z.; Simek, P.; Pumera, M., Electrochemistry of Transition Metal Dichalcogenides: Strong Dependence on the Metal-to-Chalcogen Composition and Exfoliation Method. *ACS Nano* **2014,** *8* (12), 12185-12198.

274. Niu, L.; Coleman, J.N.; Zhang, H.; Shin, H.; Chhowalla., M.; Zheng, Z., Production of Two-Dimensional Nanomaterials *via* Liquid-Based Direct Exfoliation. *Small* **2016,** *12* (3), 272-93.

275. Zhou, K.; Si, Y.; Jiang, S.; Song, L.; Hu, Y.; Gui, Z., A Facile Liquid Phase Exfoliation Method to Prepare Graphene Sheets from Different Sizes of Expandable Graphite. *Mater. Res. Bull.* **2013,** *48* (9), 2985-92.

276. Yuwen, L.; Yu, H.; Yang, X.; Zhou, J.; Zhang, Q.; Zhang, Y.; Luo, Z.; Wang, L., Rapid Preparation of Single-Layer Transition Metal Dichalcogenide Nanosheets *via* Ultrasonication-Enhanced Lithium Intercalation. *Chem. Comm.* **2016,** *52* (3), 529-532.

277. Kang, J.; Wood, J. D.; Well, S. A.; Lee, J.-H.; Liu, X.; Chen, K.-S.; Hersam, M.C., Solvent Exfoliation of Electronic-Grade, Two-Dimensional Black Phosphorus. *ACS Nano* **2015,** *9* (4), 3596-3604.

278. Zeng, Z.; Yin, Z.; Huang, X.; Li, H.; He, Q.; Lu, G.; Boey, F.; Zhang, H.., Single-Layer Semiconducting Nanosheets: High-Yield Preparation and Device Fabrication. *Angew. Chem. Int. Ed.* **2011,** *50* (47), 11093-11097.

279. Liu, W. W.; Wang, J. N., Direct Exfoliation of Graphene in Organic Solvents with Addition of NaOH. *Chem. Comm.* **2011,** *47* (24), 6888-6890.

280. Liu, W. Y.; Zhu, Y. B.; Chen, Z. Y.; Lei, J.; Feng, P. Z., Multilayer Black Phosphorus Exfoliated with the Aid of Sodium Hydroxide: An Improvement in Electrochemical Energy Storage. *J. Electron. Mater.* **2018,** *47* (8), 4793-4798.

281. Ricardo, K. B.; Sendecki, A.; Liu, H. T., Surfactant-Free Exfoliation of Graphite in Aqueous Solutions. *Chem. Comm.* **2014,** *50* (21), 2751-2754.

282. Ma, H.; Shen, Z. G.; Yi, M.; Ben, S.; Liang, S. S.; Liu, L.; Zhang, Y. X.; Zhang, X. J.; Ma, S. L., Direct Exfoliation of Graphite in Water with Addition of Ammonia Solution. *J. Colloid Interface Sci.* **2017,** *503*, 68-75.

283. Shen, J. F.; He, Y. M.; Wu, J. J.; Gao, C. T.; Keyshar, K.; Zhang, X.; Yang, Y. C.; Ye, M. X.; Vajtai, R.; Lou, J.; Ajayan, P. M., Liquid Phase Exfoliation of Two-Dimensional Materials by Directly Probing and Matching Surface Tension Components. *Nano Lett.* **2015,** *15* (8), 5449-5454.

284. Huang, Y.; Sutter, E.; Sadowski, J. T.; Cotlet, M.; Monti, O. L. A.; Racke, D. A.; Neupane, M. R.; Wickramaratne, D.; Lake, R. K.; Parkinson, B. A.; Sutter, P., Tin Disulfide -- An Emerging Layered Metal Dichalcogenide Semiconductor: Materials Properties and Device Characteristics. *ACS Nano* **2014,** *8* (10), 10743-10755.

285. Gonzalez, J. M.; Oleynik, II, Layer-Dependent Properties of SnS2 and SnSe2 Two-Dimensional Materials. *Phys. Rev. B* **2016,** *94* (12).

286. Hu, X. H.; Song, G. S.; Li, W. Y.; Peng, Y. L.; Jiang, L.; Xue, Y. F.; Liu, Q.; Chen, Z. G.; Hu, J. Q., Phase-Controlled Synthesis and Photocatalytic Properties of SnS, SnS2 and SnS/SnS2 Heterostructure Nanocrystals. *MRS Bull.* **2013,** *48* (6), 2325-2332.

287. Casiraghi, C.; Hartschuh, A.; Qian, H.; Piscanec, S.; Georgi, C.; Fasoli, A.; Novoselov, K. S.; Basko, D. M.; Ferrari, A. C., Raman Spectroscopy of Graphene Edges. *Nano Lett.* **2009,** *9* (4), 1433-1441.

288. O'Neill, A.; Khan, U.; Coleman, J. N., Preparation of High Concentration Dispersions of Exfoliated MoS_2 with Increased Flake Size. *Chem. Mater.* **2012,** *24* (12), 2414-2421.

289. Marcus, Y., Volumes of Aqueous Hydrogen and Hydroxide ions at 0 to 200 degrees C. *J. Chem. Phys.* **2012,** *137* (15).

290. Sarkar, S.; Gandla, D.; Venkatesh, Y.; Bangal, P. R.; Ghosh, S.; Yang, Y.; Misra, S., Graphene Quantum Dots from Graphite by Liquid Exfoliation showing Excitation-Independent Emission, Fluorescence Upconversion and Delayed Fluorescence. *Phys. Chem. Chem. Phys.* **2016,** *18* (31), 21278-21287.

291. Gonzalez, J. M.; and Oleynik, I., Slice imaging and wave packet study of the photodissociation of CH_3Iin the blue edge of the A-band: evidence of reverse $^3Q_0 \leftarrow {}^1{}_Q1$ non-adiabatic dynamics. *Phys. Chem. Chem. Phys* **2011,** *36*, 16404-16415.

292. Koren, E.; Lortshcer, E.; Rawlings, C.; Knoll, A. W., Adhesion and Friction in Mesoscopic Graphite Contacts. *Science* **2015,** *348* (6235), 679-683.

293. O'Shea, S. J.; Welland, M. E., Atomic Force Microscopy at Solid-Liquid Interfaces. *Langmuir* **1998,** *14* (15), 4186-4197.

294. Bennewitz, R., Friction Force Microscopy. *Mater. Today* **2005,** *8* (5), 42-48.

295. Frisbie, C. D.; Rozsnyai, L. F.; Noy, A.; Wrighton, M. S.; Lieber, C. M., Functional Group Imaging by Chemical Force Microscopy. *Science* **1994,** *265* (5181), 2071-2074.

296. Benedict, L. X.; Chopra, N. G.; Cohen, M. L.; Zettl, A.; Louie, S. G.; Crespi, V. H., Microscopic Determination of the Interlayer Binding Energy in Graphite. *Chem. Phys. Lett.* **1998,** *286* (5-6), 490-496.

297. Liu, Z.; Liu, J. Z.; Cheng, Y.; Li, Z. H.; Wang, L.; Zheng, Q. S., Interlayer Binding Energy of Graphite: A Mesoscopic Determination from Deformation. *Phys. Rev. B* **2012,** *85* (20).

298. Zacharia, R.; Ulbricht, H.; Hertel, T., Interlayer Cohesive Energy of Graphite from Thermal Desorption of Polyaromatic Hydrocarbons. *Phys. Rev. B* **2004,** *69* (15).

299. Colson, J.; Andorfer, L.; Nypelo, T. E.; Lutkemeier, B.; Stockel, F.; Konnerth, J., Comparison of Silicon and OH-Modified AFM Tips for Adhesion Force Analysis on Functionalised Surfaces and Natural Polymers. *Colloids Surf. A* **2017,** *529*, 363-372.

300. Vanossi, A.; Dietzel, D.; Schirmeisen, A.; Meyer, E.; Pawlak, R.; Glatzel, T.; Kisiel, M.; Kawai, S.; Manini, N., Recent Highlights in Nanoscale and Mesoscale Friction. *Beilstein J. Nanotech* **2018,** *9*, 1995-2014.

301. Larson, I.; Drummond, C. J.; Chan, D. Y. C.; Grieser, F., Direct Force Measurements between TiO_2 Surfaces. *J. Am. Chem. Soc.* **1993,** *115* (25), 11885-11890.

302. Finot, E.; Lesniewska, E.; Mutin, J. C.; Goudonnet, J. P., Investigations of Surface Forces between Gypsum Microcrystals in air using Atomic Force Microscopy. *Langmuir* **2000,** *16* (9), 4237-4244.

Appendix A Liquid ALD of Molybdenum Disulphide

A.1 MoS_2 seeding parameters

Table A.1 MoS_2 seeding parameters

Substrate	Seeding method	Conc./ g mL^{-1}	Solvent	Tilt	Temp./℃	Few-layer seed?
S1	a	92	Water	No	70	Yes
S2	a	92	Water	No	70	Yes
S3	a	92	Water	No	25	Yes
S4	a	92	Water	No	25	Yes
S5	a	46	Water	30°	70	No
S6	a	46	Water	30°	70	No
S7	a	46	Water	30°	80	No
S8	a	46	Water	30°	80	No
S9	a	46	Ethanol (50% v/v)	30°	90	No
S10	a	46	Ethanol (50% v/v)	30°	90	No
S11	b	NA	NA	NA	NA	Yes
S12	b	NA	NA	NA	NA	Yes
S13	a	46	Ethanol (50% v/v)	50°	100	Unknown
S14	a	46	Ethanol (50% v/v)	50°	100	Unknown
S15	b	NA	NA	NA	NA	Yes
S16	b	NA	NA	NA	NA	Yes

A.2 Mo precursor dip-coating on bare substrates

In the table, note that substrate **[1]** was SiO_2/Si, and substrate **[2]** was c-cut sapphire. Additional notes about substrate preparation: T23-25 were prepared with 11, 31 and 45 nm channels created by RIE before deposition. T35-36 were prepared by pre-treatment of the substrate by sonication in aqueous KOH (0.2 M) to improve ALD character. A number of solvents were used for the precursor solution, but water was judged the best one. Increasing dip-coating time from 1 min. to 15 min. resulted in a substantial improvement in coverage, but a further increase to 60 min. resulted in only marginal improvement.

Table A.2 Deposition parameters of molybdenum precursor

Sample no. [substrate]	**Solvent**	**Conc./g mL^{-1}**	**Dip-coat t./min.**	**T./℃**
T1 [1]	Water	0.2	1	40
T2 [1]	Water	0.2	15	40
T3 [1]	Water	0.2	60	40
T4 [1]	Acetone	0.2	1	40
T5 [1]	Acetone	0.2	15	40
T6 [1]	Acetone	0.2	60	40
T7 [1]	Water	0.2	1	25
T8 [1]	Water	0.2	15	25
T9 [1]	Water	0.2	60	25
T10 [1]	Acetone	0.2	1	25
T11 [1]	Acetone	0.2	15	25
T12 [1]	Acetone	0.2	60	25
T13 [1]	Water	0.2	15	50
T14 [1]	Water	0.2	15	60
T15 [1]	Water	0.2	15	70
T16 [1]	Water	0.2	15	80
T17 [1]	Water	0.2	15	90
T18 [1]	Water	0.13	15	50
T19-20 [1]	40% acetone	0.2	15	50
T18’ [1]	Water	0.13	15	70
T19’ [1]	40% acetone	0.13	15	70
T20’ [1]	Water	0.13	15	70
T21-21’ [1]	Water	0.13	15	80
T22-25 [1]	Water	0.13	15	70
T26 [1]	Water	0.13	15	80
T27 [1]	Water	0.13	15	70

Sample no. [substrate]	Solvent	Conc./g mL^{-1}	Dip-coat t./min.	T./℃
T28-28' [1]	Water	0.13	15	80
T29 [2]	Water	0.13	15	70
T30 [1]	Water	0.13	15	70
T31 [1]	Water	0.13	15	80
T32 [2]	Water	0.13	15	80
T33-34 [2]	Water	0.13	15	70
T35-38 [1]	Water	0.13	15	80
T39-40 [1]	Water	0.13	Overnight	25
T41-43 [1]	Water	0.13	15	80
T44-47 [1]	Water	0.13	Overnight	80

Table A.3 Dip-coating of sulphur precursor

Sample	Sulphur source	Dip-coating t./min.	T/℃
T41	CS_2	20	30
T42	CS_2	20	35
T43	CS_2	20	35

A.3 Mo precursor dip-coating on seeded substrates

Table A.4 Dip-coating on seeded substrates.

Substrate	Precursor	Solvent	Dip-coat t./min.	T./℃
S1	Ammonium molybdate	Water	2	40
S2	Ammonium molybdate	Water	2	40
S3	Ammonium molybdate	Water	2	40
S4	Ammonium molybdate	Water	2	40
S11	Ammonium molybdate	Water	2	40

A.4 Annealing

For sulphurisation in elemental sulphur, 1600-2000 mg S was used. In experiments in a smaller tube furnace, the amount was reduced to 1200 mg then 200 mg to mitigate blockage of the exhaust. Where 5% H_2 is shown, the sample was annealed in a 95:5 mixture of argon (57 sccm) and hydrogen (3 sccm) up to 500 ℃, and thereafter in argon.

Table A.5 Sulphurisation, annealing and post-annealing in elemental sulphur

Sample	Sulphur/ mg	Gas	Gas flow/ sccm	T./℃	t./min.	Post-anneal T./℃	Post-anneal t./min.
T1-18	1600	N_2	100	800	10		
T19	1600	N_2	100	800	10	1000	60
T18'-20'	1600	N_2	100	800	10		
T21	1200	5% H_2	60	800	10		
T21'	200	5% H_2	60	800	10		
T22	2000	N_2	100	800	10	1000	60
T23-26	2000	N_2	100	800	10		
T27	2000	N_2	100	800	10	1000	60
T28	1200	5% H_2	60	800	10		
T28'	200	5% H_2	60	600	10		
T29-30	2000	N_2	100	800	10		
T33-34	2000	N_2	100	800	10	1000	60

Table A.6 Sulphurisation, annealing and post-annealing in CS_2

Sample	T/℃	t/min.	Gas, flow rate/sccm	Post-anneal T./℃	Post-anneal t./min.	Gas, flow rate/sccm
T31	800	10	N_2, 100			
T32	800	10	N_2, 100			
T35	800	240	N_2, 100	1000	60	Ar:H_2, 50:10
T36	800	240	N_2, 100	1000	60	Ar:H_2, 50:10
T37	800	60	N_2, 100			
T38	800	60	N_2, 100			
T39	800	60	N_2, 100	1000	60	Ar:H_2, 54:6
T40	800	60	N_2, 100	1000	60	Ar:H_2, 54:6
T41	450	60	Ar, 60			
T42	800	60	Ar:H_2, 54:6			
T43	800	60	Ar:H_2, 54:6			
T44	800	60	N_2, 100			
T45	800	60	N_2, 100			
T46	800	60	N_2, 100			
T47	800	60	N_2, 100			

A.5 Calculation of interplanar d-spacing

See below for calculations corresponding to TEM images of MoS_2 domains as discussed in Section 3.6.3 in the main body.

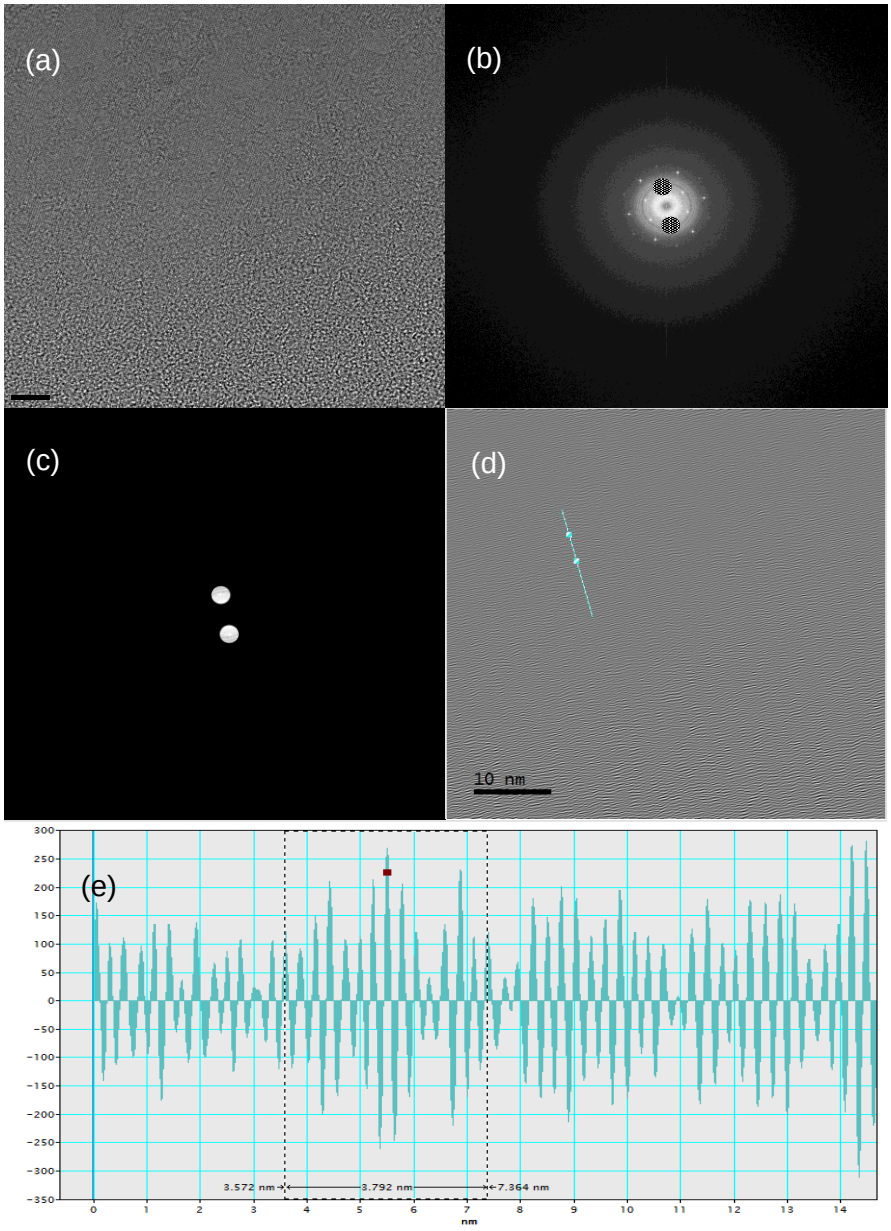

Figure A.1: *Calculation of interplanar d-spacing*

(a) *TEM image of a crystalline region of a sample grown at 80 ℃ dip-coating and ten minutes of annealing at 800 ℃ sulphurisation with sulphur flakes.* ***(b)*** *FFT of the whole region showing the six-fold-symmetrical diffraction spots of the (100) and (110) lattice planes.* ***(c)*** *Mask applied over the top of two diametrically-opposite spots in the inner ring.* ***(d)*** *Inverse FFT of the masked area showing clearly the lattice planes in the crystal. A line profile is drawn over the top, perpendicular to the lattice planes.* ***(e)*** *Line profile of the highlighted region in (d).*

References

The characteristic d-spacing of the (100) lattice plane can be calculated by appropriate analytical software. We used GMS Digital Micrograph. The procedure is outlined below:

- A region of interest (Figure A.1(a)) is selected and an FFT taken (Figure A.1(b)).
- Two diametrically-opposite spots in the same diffraction pattern are masked and the unmasked areas removed from the image (Figure A.1(c)).
- An inverse FFT of the masked area is taken to yield an image of the lattice planes in the crystal (Figure A.1(d)). A line profile is taken perpendicular to the lattice planes.
- The line profile is plotted (Figure A.1(e)). To determine the d-spacing, two points are selected that are of roughly equal height on the +y-axis. The distance in +x between these two points is read as 3.792 nm. The number of "spaces" between the two points is counted (14). Dividing the distance by the number of spaces gives the d-spacing between two adjacent lattice planes.

  (3.792 nm)/14=0.271 nm

A.6 Dip-coating of CS_2 – variable quality

A representative Raman spectrum below, obtained from samples T42 and T43, showed scant evidence of the characteristic peaks of mono-/few-layer MoS_2 (*cf.* Section 3.6.6). Similar spectra were obtained from several regions across the two substrates.

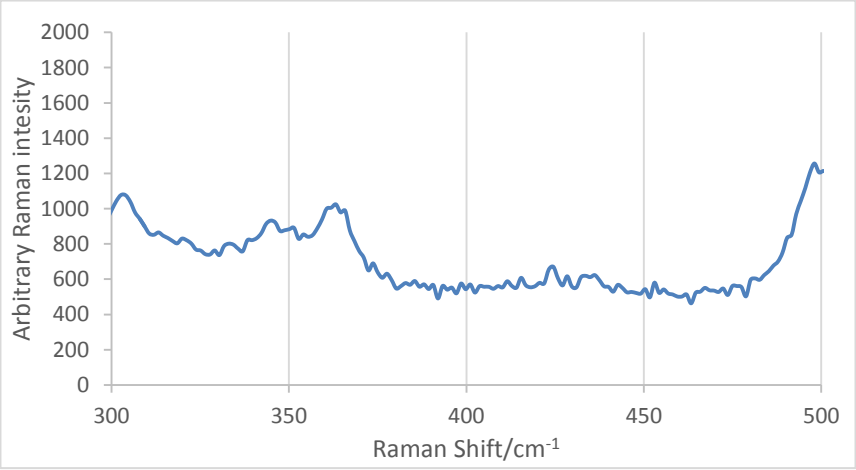

Figure A.2 *Representative Raman spectrum of CS_2-grown samples T42 and T43*

The absence of any peaks at the characteristic positions of the E_{2g} and A_{1g} modes suggested, across a range of regions sampled, that the CS_2 dip-coating method produced inconsistent quality of material.

Appendix B Liquid Exfoliation of Tin(IV) Disulphide

B.1 UV-vis absorbance data for molar extinction coefficient determination

Below is the output of regression analysis performed on the plot shown in Figure 5.7. The molar extinction coefficient is the gradient of the line, which is described as the "coefficient". The upper and lower 95% confidence levels are shown.

SUMMARY OUTPUT

Regression Statistics	
Multiple R	0.999062
R Square	0.998124
Adjusted R Square	0.997499
Standard Error	0.037985
Observations	5

ANOVA

	Df	*SS*	*MS*	*F*	*Significance F*
Regression	1	2.303476	2.303476	1596.456	3.45E-05
Residual	3	0.004329	0.001443		
Total	4	2.307804			

	Coefficients	*Standard Error*	*t Stat*	*P-value*	*Lower 95%*	*Upper 95%*
Intercept	-0.02371	0.031946	-0.74233	0.511727	-0.12538	0.077953
X Variable 1	2078.874	52.02951	39.95568	3.45E-05	1913.293	2244.455

The error in the molar extinction coefficient is calculated by worst-case scenarios using the upper and lower 95% confidence intervals. This method accounts for all volumetric errors accumulated during the preparation of the various concentrations used for UV-vis absorbance measurements in Section 6.6.1.

$(2244.4 – 2078.9)\ g^{-1}\ cm^{-2} = 165.5\ g^{-1}\ cm^{-2}$

$(2078.9 – 1913.3)\ g^{-1}\ cm^{-2} = 165.6\ g^{-1}\ cm^{-2}$

The error in the molar extinction coefficient was 170 $g^{-1}\ cm^{-2}$ to two significant figures.

B.2 Determination of scattering in UV-vis spectra

B.2.1 2h-Sonicated aqueous solutions

SUMMARY OUTPUT

Regression Statistics	
Multiple R	0.9984
R Square	0.996803
Adjusted R Square	0.996798
Standard Error	0.01604
Observations	601

ANOVA

	Df	*SS*	*MS*	*F*	*Significance F*
Regression	1	48.05347	48.05347	186780.4	0
Residual	599	0.154106	0.000257		
Total	600	48.20757			

	Coefficients	*Standard Error*	*t Stat*	*P-value*	*Lower 95%*	*Upper 95%*
Intercept	14.53909	0.031315	464.2795	0	14.4775907	14.600593
X Variable 1	-4.81703	0.011146	-432.181	0	-4.83892245	-4.795143

Error in coefficient n was 0.02.

B.3 Bandgap determination using Tauc plot

Solution E1-14 was taken as a sample with an apparently good degree of monolayer monodispersity. The UV-vis spectrum is reproduced below:

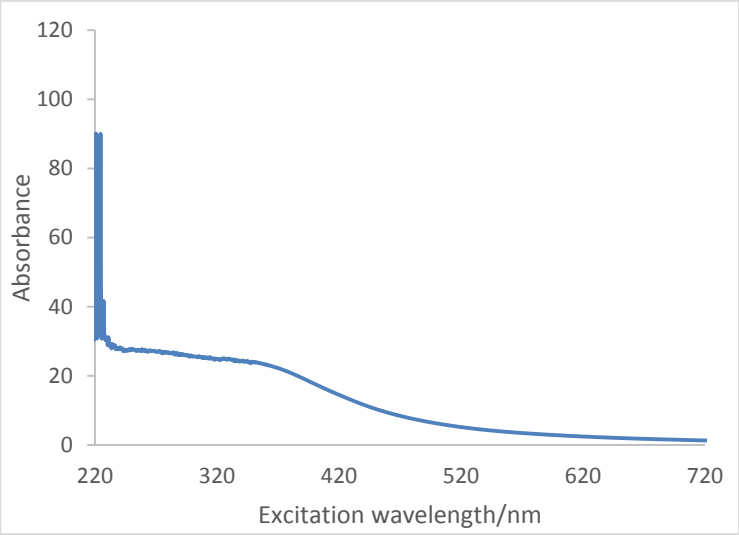

Figure C.1 *UV-vis absorbance spectrum of E1-14*

This spectrum was acquired by broadband scanning across the range 800-750 nm. Analysis of scattering suggested minimal scattering and OM analysis suggested a good dispersion, while Raman showed monolayer signals. Therefore, this sample was taken as an example of high-yield, monodisperse monolayers.

To calculate the bandgap, one first converts all absorbance values to the absorption coefficient at a given wavelength. This is done simply using Equation 6.2:

$$\alpha = 2.303\left(\frac{A}{l}\right)$$

where A = absorbance

l = optical absorbance path length/m

Each excitation wavelength in nanometres is converted to its corresponding value in electron volts:

$$E_{h\nu} = \frac{1240\ \text{eV nm}}{\lambda}$$

Then, the Tauc plot is constructed as $(\alpha h\nu)^{\frac{1}{r}}$ *vs* bandgap energy in hν, where r = 0.5, 1.5, 2 or 3 depending on the nature of the transition. The plot below chooses r = 0.5, corresponding to the allowed direct transition:

References

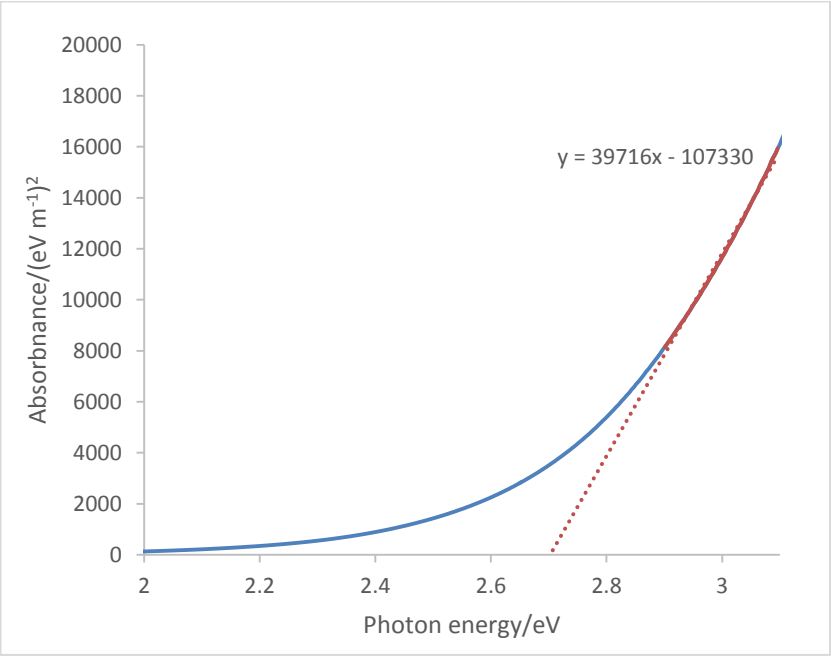

Figure C. 1 *Tauc plot to determine allowed direct bandgap of 1L-SnS_2*

The Tauc plot shows the bandgap at the x-intercept of the linear portion of the absorbance. In this case, a value of 2.70 eV is obtained.

The largest linear region of the graph is selected and a line-of-best-fit is extrapolated to the energy axis. Then a regression analysis on the linear portion can be performed to find the corresponding error. Thus, the bandgap energy is obtained: $E_b = 2.70 \pm 0.10$ eV.

SUMMARY OUTPUT

Regression Statistics	
Multiple R	0.99823
R Square	0.996464
Adjusted R Square	0.996397
Standard Error	138.5152
Observations	55

ANOVA

	df	*SS*	*MS*	*F*	*Significance F*
Regression	1	2.87E+08	2.87E+08	14934.06	1.19E-66
Residual	53	1016882	19186.45		
Total	54	2.88E+08			

	Coefficients	*Standard Error*	*t Stat*	*P-value*	*Lower 95%*	*Upper 95%*
Intercept	-107330	973.945	-110.201	2.79E-64	-109283	-105376
X Variable 1	39715.73	324.9926	122.205	1.19E-66	39063.87	40367.58

Considering the upper and lower 95% confidence limits yielded an error of 0.10 eV.

Interestingly, performing the same method on another sample, E0-12 for confirmation produced a very agreeable bandgap value of 2.76 ± 0.14 eV.

Appendix C Liquid Atomic Force Microscopy – Graphene as Proof of Concept

C.1 Background

Koren *et al.* investigated the strength of interlayer vdW adhesion forces in graphite. They welded an AFM cantilever tip to the platinum-coated surface of highly-oriented pyrolytic graphite (HOPG) pillars produced by EBL. They had determined the force constant of the cantilever tip by force curve measurements. With this information, they applied a known lateral shearing force to the AFM tip, and determined the force at which the interlayer interaction in the graphite basal plane was overcome.[292]

In the Koren study, the authors made no deliberate attempt to obtain monolayers. In fact, the group's method only yielded multilayer graphene. Thus, it might be possible to apply a modification to the method, marrying the technique of liquid exfoliation to the Koren technique with the aim of producing monolayer graphene.

AFM has been used to probe short-range solvation forces acting near the surface of graphite,[293] and this presents a way of advancing the Koren method. SPM-based techniques for elucidating friction and adhesion forces also exist, and the leading ones are the two advanced methods of AFM known as friction force microscopy (FFM) and chemical force microscopy (CFM). FFM detects lateral force variations on the atomic scale by sliding the tip over a flat surface and measuring torsion in the cantilever.[294] CFM can be used in either constant force mode or constant height mode to map vdW forces at the atomic level between a gold-coated tip and the surface. This technique is sufficiently powerful to detect changes in functional group.[295] However, FFM and CFM are tools primarily used in engineering. Although CFM lends itself well to measurements in liquid media – suggesting that AFM-based liquid exfoliation is plausible – neither technique is ideal for studying interlayer forces during exfoliation, because they do not utilise shearing.

Efficient exfoliation methodologies benefit greatly from an understanding of the energies involved in shearing. For instance, is there a reduction in the layer-to-layer cohesion energy in the mechanical *vs.* liquid case wherein an adhesive solvent—nanosheet interaction is introduced? If so, this could lead to a simple method for quantitatively elucidating solvent—nanosheet interactions in liquid exfoliation. In this mini-project, graphite pillars were produced and sheared using an AFM cantilever tip. If successful, the technique could be applied to MoS_2.

The present gap in knowledge about adhesive forces during liquid exfoliation provided the motivation for this fundamental study.

C.2 Materials

Having considered motivations, one considers what materials could be insightful and relevant to the field. In order for the lateral shearing process to work, the material is required to be layered. Much has been said about graphene in this thesis (see Section 1.1.5). For reasons previously described, other layered materials have been explored such as MoS_2, WS_2 and SnS_2. However, for a study that is more fundamental in nature rather than application-driven, graphene is an acceptable choice. That is because the use of graphene would offer a direct comparison between these findings and those of Koren *et al.* Little is already known about the interlayer binding energy governing exfoliation of graphene, and that is because direct measurement has rarely been possible. Experimental observations range from 0.14 J m^{-2} to 0.35 J m^{-2}.[296-298] Koren *et al.* obtained a value of 0.23 J m^{-2}, in good agreement with other studies. There is a large body of literature on graphene exfoliation. This will not be discussed here, but some examples can be found in Table 1.3, refs. [63] to [70] (Section 1.3.1).

Once the proof of concept is established using graphene, then the known method will be more easily adapted to suit other layered materials, including those on which a body of literature is not yet available.

C.3 Synthesis

The conditions in this study closely follow those used by Koren *et al.* This is to ensure that difference in findings can be attributed to liquid *vs.* mechanical exfoliation. They fabricated samples featuring cylindrical and complex pillars with a typical height of 50 nm from high-quality HOPG substrates by RIE, using structured Pd-Au metal layers as masks. For shearing, they used a Pt/Ir metal-coated AFM tip with the metal mask on top of the structures. The tip apex was cold-welded to the metal by applying a force of 50 nN and electrical current pulse 1 mA for 1 s. The resulting mechanical contact between the tip and the metal mask allowed for the application of lateral shear forces of up to 200 nN, inducing a shear glide along a single basal plane in the HOPG structure.[292]

The novelty of this appraoc hwill be in the first reported application of an AFM-driven study to the liquid exfoliation case, marrying the two techniques of AFM and liquid exfoliation with a view to understanding the forces at work during liquid exfoliation and potentially advancing the field by opening up an easy route to determine solvent—nanosheet interactions.

C.4 Experimental details

C.4.1 Etching of pillars

All work was performed in a Class 100 cleanroom. The surface of a 1×1 cm substrate of Grade 2 HOPG (purchased from SPI Supplies) was smoothened by mechanical exfoliation of the uppermost layers using the Scotch-tape method. In addition, the bottom of the substrate was flattened by the application of pressure by hand. This smoothening was to ensure that the vacuum did not break during the e-beam lithography process. The substrate was baked at 180 ℃ for 70 s. A resist comprising a 1:1 ratio of PMMA-950 and anisole (2 drops) was spin-coated onto the substrate at 3000 rpm for 90 s. A uniform region of resist in the centre of the substrate was identified by optical microscopy.

The e-beam system was an Elonix ELS-1000, the voltage used for patterning was 100 kV, the current was 100 pA, and the dose was 960 μC cm^{-2}. EBL was used to pattern the selected region of the resist with three 15×15 arrays of circles with diameters of 200, 400 and 600 nm and a pitch of 500 nm. In order to facilitate characterisation, large triangular markers were patterned to point to the arrays.

PMMA is a positive resist, so the region exposed to the e-beam becomes soluble in the developer. The regions of exposed resist were removed using a 1:3 ratio of methyl isobutyl ketone (MIBK) developer and IPA. The substrate was dipped in the developer solution and mildly agitated by hand for 45 s. After development, the substrate was dried with nitrogen, yielding a patterned resist surface with circular holes for metal deposition by thermal evaporation.

Thermal evaporation was used to deposit 10 nm Pt on the substrate surface, followed by 15 nm Au. The process is non-selective, so it deposits the metals over the entire wafer surface and not just in the holes created by resist development. The Pt acted as an adhesion layer for Au, while the Au layer was intended as an electrical contact for the AFM cantilever tip.

Following the thermal evaporation, the remaining resist was removed by lift-off using oxygen plasma, thus removing the unwanted metal coating along with the resist. The lift-off proceeded at a rate of 11 nm min^{-1}, etching into the graphite substrate to a depth of 50 nm. The result was a substrate with three arrays of metal-coated graphite pillars, in accordance with the e-beam lithography pattern. It was expected that the rough height of the pillars including the metal coatings be 65 nm.

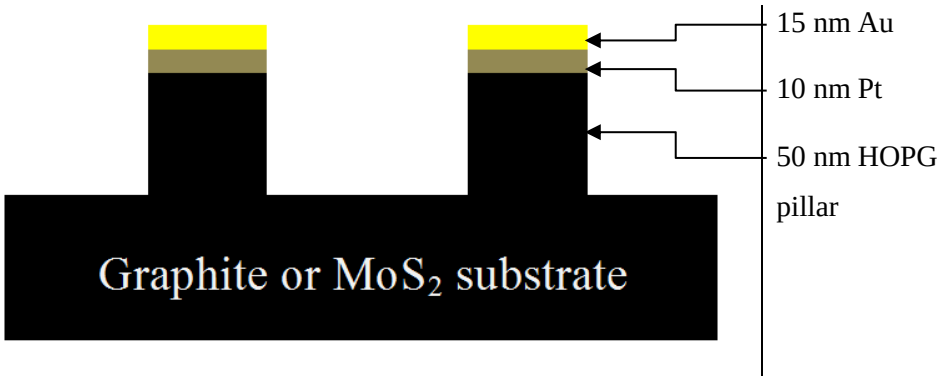

Figure C.1 *Cross-section of pillars after photolithography and lift-off*

PMMA-950 resist was spin-coated onto a graphene wafer. EBL was performed at 100 kV, 100 pA and 960 μC cm^{-2}. 15 × 15 arrays of pillars with diameters of 200, 400 and 600 nm were patterned the surface. Following development of the resist, 10 nm Pt and 15 nm Au were deposited on the pillar surfaces by thermal evaporation. Lift-off proceeded at 11 nm min^{-1}, removing the remaining resist and etching the surface to a depth of 50 nm, producing metal-topped pillars as above.

Figure C.1 depicts the expected cross-sectional view of a pillar after deposition with a 10 nm Pt layer and 15 nm Au and subsequent plasma lift-off. Viewed in plan, the pillars might look as in Figure C.2:

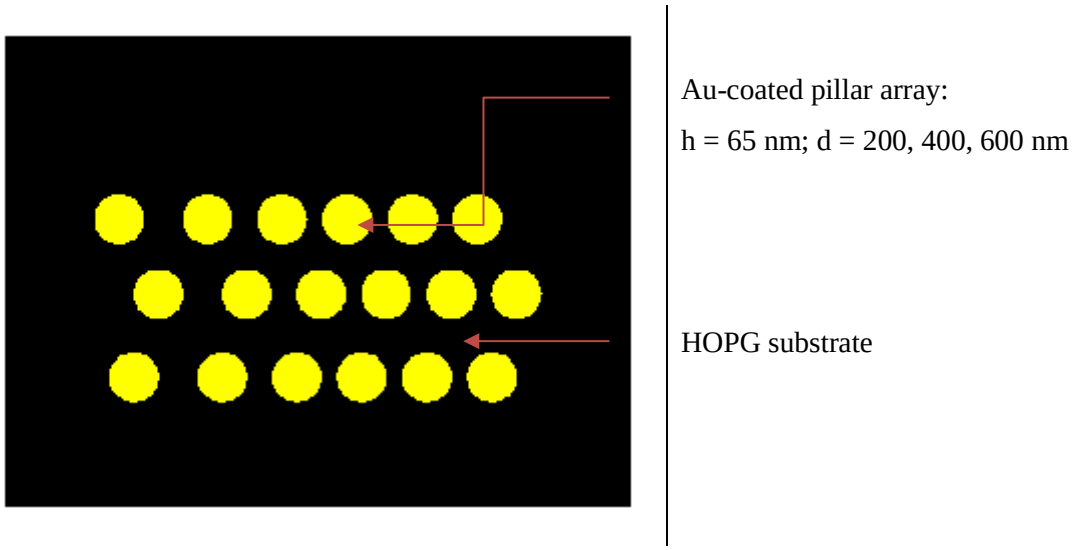

Figure C.2 *Top-down depiction of Au surface on top of pillars (not to scale)*

The figure illustrates the appearance of the pillars when studied from above. The gold surfaces are visible and would act as contact points for the cantilever tip.

Figure C.2 shows a top-down view of the Au/Pt-coated pillars etched into the HOPG surface. Three regions were created, each comprising a 15×15 square array of pillars. The first array contained pillars of diameter 200 nm, the second of 400 nm and the third of 600 nm. Each pillar had a target height of 65 nm.

C.4.2 Force curve measurement

The first step of any AFM procedure is to calibrate the cantilever deflection sensitivity by taking a force curve. In this case, that process was performed in force modulation mode. The target amplitude was set throughout the procedure as 1 V. A run without a sample in place determined that the resonance of the Si cantilever tip occurred at 280.4 Hz. This determined the eventual drive frequency of the cantilever at 279.5 Hz.

C.4.3 Cold-welding

To achieve cold-welding to the pillar surface, a current pulse of a 1 mA was applied for 1 s between the cantilever tip and surface, as in Figure C.3. This was first performed without a solvent present in the system as it was not required.

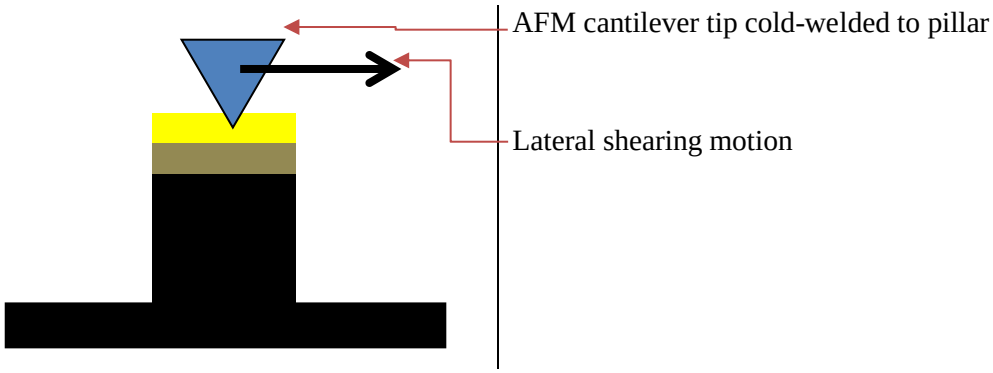

Figure C.3 *AFM setup for cold-welding tip to pillar surface*

The gold surface acted as a contact point for the Si tip, allowing for the tip to be cold-welded to the pillar by the application of a bias voltage.

The cantilever was driven to the surface of the pillar, again in force modulation/tapping mode. When the two surfaces were in contact, the welding current was applied.

C.5 Results and Discussion

The force curve measurement depends on a number of interacting parameters. The exact shape of the force curve is determined by tip characteristics such as composition and radius, and environmental parameters such as humidity, the surrounding medium and temperature.[299] That is to say, there is a large degree of variability in the force curve measurements that is dependent on factors that are extremely difficult to control, and it is expected that the introduction of a liquid medium would therefore be a particular challenge. As a result of this, most obtained values are specific to a single tip—sample configuration. It is one of the major drawbacks in determining absolute values by AFM.

To determine the interlayer attractive force, the tip cold-welded to the uppermost layer of graphene can be modelled as a spring. At a basic level, the lateral shearing force applied by a stiff cantilever can be approximated as a function of the force constant of the tip and the lateral displacement, as per Hooke's Law:

$$\Delta F \propto k\Delta x \qquad [C.1]$$

where ΔF = lateral shearing force/N

k = tip force constant/N m^{-1}

Δx = lateral displacement/m

A spring has an elastic limit, which is the force at which the linear relationship of Hooke's Law breaks down. Beyond the elastic limit, the spring does not return to its original position when the force is removed. This is why a spring could be a good analogy for the AFM—graphene system. The elastic limit could be thought of as the interlayer vdW force. Application of a force that exceeds the interlayer attraction would lead to exfoliation. The method may not give an exact value but could afford a relative comparison between the dry and liquid cases, which is likely to be within the limitations of the AFM. Further calculations using the method derived by Koren *et al.* then lead to a more accurate figure, but this stage was hidnered here due to practical difficulties.

The figure shows an AFM image of selected etched pillars on the graphene surface. Note the line profile showing a step height of ~65 nm.

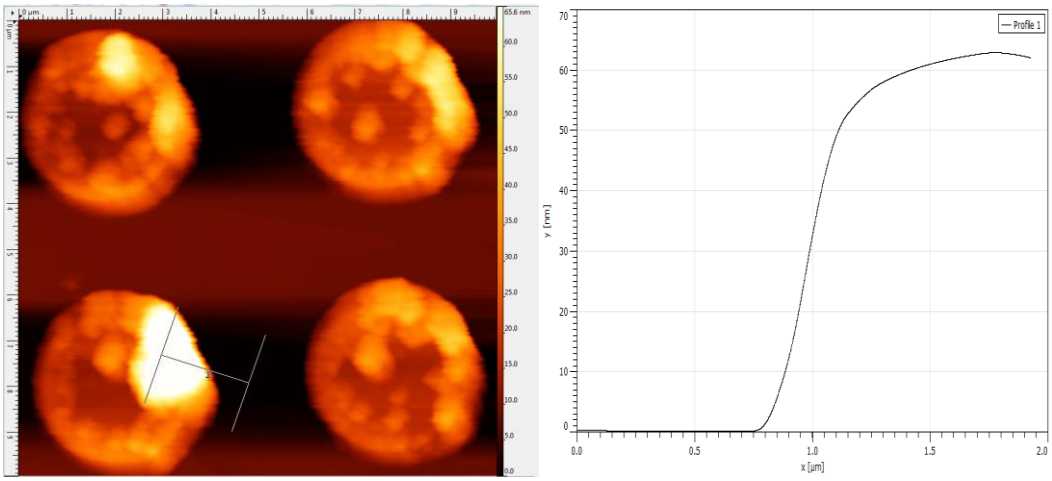

Figure C.4 *Morphology and height of RIE pillars on graphene surface*

The line profile shows that the expected pillar height of 65 nm was achieved, but the intensity bar suggests a rough surface possibly arising from a rough wafer to begin with. This implies that a smoothing process was necessary before the EBL process. The author is grateful to Sean O'Shea for his assistance with acquiring these data.

Cold-welding proved to be difficult to achieve. The cantilever repeatedly slipped and dragged over the surface, leading to considerable damage to the tip and ineffective shearing. Figure C.5 shows a false-colour 3D map of the pillar surfaces. It is clear that the surface height varied considerably, by as much as 20 nm.

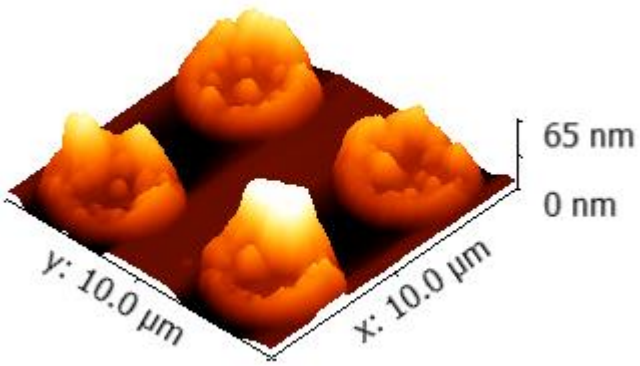

Figure C.5 *3D AFM map of coated graphene pillars shows rough surface*

The 3D profile of the AFM image in Figure C.5 illustrates the surface roughness of the pillars. This is one explanation for the poor contact between the AFM tip and the gold surface layer. The author is grateful to Sean O'Shea for his assistance with acquiring these data.

The 3D map shows that the pillar surfaces were rather rough. This is one possible explanation for the difficulty in cold-welding the tip to the surface. The surface roughness is likely to have compromised the quality of the contact between the tip and the pillar surface. It is important to achieve good cold-welding in order to reduce the risk of the tip slipping and dragging over the surface rather than shearing.

One possible method for improving the cold-welding process would be to use a flat-plate cantilever tip. In contrast to the typical cantilever tip, which is a pyramidal structure that tapers to a sharp apex, the flat-plate tip is cylindrical. The contact point of the flat-plate tip is the circular face of the cylinder. This type of tip presents a large surface area over which adhesion might occur, and it has been particularly effective in vacuum conditions. However, vacuum conditions are impractical, and this would clearly present a problem were a solvent to be introduced to the system, as in the liquid AFM case.

It is possible that the cold-welding difficulties arose because of the inherent properties of the metal mask. AFM studies have previously been confounded by the interactions of the mask surface with the silicon tip. Indeed, there is evidence that cold-welding works best when the two contacting surfaces are of the same material. A recent promising area has been the development of coated cantilever tips to overcome this issue. Vanossi *et al.* described coating Cu cantilever tips with a

conformal layer of graphene.[300] This created a tip that controlled for the interactions that previously affected AFM-based graphene studies. The coating process restricted the resolution of the subsequent AFM process by blunting the tip. However, it is not necessarily the case that this would be an issue in a cold-welding setup, in which the resolution of the tip is not as important as control over the lateral shearing motion.

Some groups have used cruder methods to adhere a tip to a sample, such as gluing or mounting a crystal directly to the cantilever using epoxy glue.[301, 302] However, this method is not expected to be useful for sub-micron pillars, due to the level of precision required in practice. In fact, in a study where lateral shearing direction is particularly important, the gluing method does not offer a sufficiently reliable way of maintaining the cantilever in such a way that its lateral force remains parallel to the basal plane.

C.6 Conclusion and future work

The aim of this study was to elucidate the fundamental effects of solvent—material interactions on liquid exfoliation. A significant hurdle was the determination of the appropriate bias voltage for cold-welding the AFM tip to the target material's surface, which is a non-trivial process. Different approaches were proposed to overcome this issue, which included the use of a flat-plate AFM tip or a graphene-coated AFM tip. Both of these methods are not without problems, but they present a rich area to explore in future work.

Once practical issues have been overcome, this technique may prove particularly useful to the community as a reliable method for directly measuring the effects of solvent interactions on liquid exfoliation. This technique, when fully developed, could represent a method for elucidating the most appropriate solvent to use in liquid exfoliation without the need for time-consuming trials.

To achieve the ambitious aims of this technique, the generality of liquid AFM will need to be demonstrated. That will require the application of this method to MoS_2 and other layered materials once the graphene case is settled.